ADDIS ABABA UNIVERSITY

COLLEGE OF NATURAL AND COMPUTATIONAL SCIENCES

SCHOOL OF EARTH SCIENCES

CHARACTERIZATION AND EVALUATION OF STRUCTURAL PERMEABILITY OF THE NORTHERN LAKE ABAYA GEOTHERMAL FIELD, SOUTHERN MAIN ETHIOPIAN RIFT

BY

YAFET GEBREWOLD BIRHANE

A thesis submitted to the School of Graduate Studies of Addis Ababa University in partial fulfillment of the requirements for the degree of Master of Science in Resource Geology (Geothermal Energy)

May 2019

ADDIS ABABA UNIVERSITY
COLLEGE OF NATURAL AND COMPUTATIONAL SCIENCES
SCHOOL OF EARTH SCIENCES

CHARACTERIZATION AND EVALUATION OF STRUCTURAL PERMEABILITY OF THE NORTHERN LAKE ABAYA GEOTHERMAL FIELD, SOUTHERN MAIN ETHIOPIAN RIFT

BY

YAFET GEBREWOLD BIRHANE

A thesis submitted to the School of Graduate Studies of Addis Ababa University in partial fulfillment of the requirements for the degree of Master of Science in Resource Geology (Geothermal Energy)

May 2019

Addis Ababa, Ethiopia

ADDIS ABABA UNIVERSITY

COLLEGE OF NATURAL AND COMPUTATIONAL SCIENCES

SCHOOL OF EARTH SCIENCES

CHARACTERIZATION AND EVALUATION OF STRUCTURAL PERMEABILITY OF THE NORTHERN LAKE ABAYA GEOTHERMAL FIELD, SOUTHERN MAIN ETHIOPIAN RIFT

BY

YAFET GEBREWOLD BIRHANE

Approved by the Examining Committee

Dr. Balemwal Atnafu	_____	_____
Head, School of Earth Sciences	Signature	Date
Prof. Gezahegn Yirgu	_____	_____
Advisor	Signature	Date
_____	_____	_____
Examiner	Signature	Date
_____	_____	_____
Examiner	Signature	Date

Declaration of Originality

I hereby declare that the thesis "*Characterization and Evaluation of Structural Permeability of the Northern Lake Abaya Geothermal Field, Southern Main Ethiopian Rift*" is my original master's degree work under the supervision of Prof. Gezahegn Yirgu and has not been presented to any other university or institution for the award of any degree or diploma. All sources and materials used for the thesis have been duly acknowledged.

Yafet Gebrewold _____ _____

Signature Date

This is to certify that the above declaration made by the candidate is correct to the best of my knowledge and it has been submitted for examination with my approval as university advisor.

Prof. Gezahegn Yirgu _____ _____

Advisor Signature Date

Abstract

Lake Abaya geothermal field is located on the axis of the Southern Main Ethiopian Rift (SMER), near the western margin where the plateau transitions into the rift floor. The study area is located approximately 275 km south from Addis Ababa. The main objective of the research study is to evaluate the structural permeability and characterize the geothermal system in the Northern Lake Abaya Geothermal Field. To meet the objectives, different methods have been applied. The methods are; remote sensing, geological field mapping and sampling, field soil CO_2 flux and temperature measurements and petrographic and laboratory fluid analysis. The results of geological investigations are summarized in a geologic map (scale, 1:50,000) that shows various lithologies, recent to very young eruptive features, dense fault systems and active geothermal activities. The exposed volcanic and sedimentary lithologic units are ignimbrite, trachyte, pumiceous pyroclastic flow and fall deposits, basalts, scoria, rhyolitic and obsidian lava flows and alluvial and lacustrine sediments. The volcanic products, except the very recent once, are affected by extensional tectonics which is manifested by the occurrence of joints, fissures and extensive normal faulting, all trending NNE-SSW. The thermal fluid analysis results indicate the thermal waters are primarily of near neutral pH and are primarily of the sodium- bicarbonate type. The high silica concentration measured in all springs result in estimated reservoir temperatures of greater than 140°C. The average cation and gas geothermometers suggest reservoir temperatures of greater than 200°C. The soil CO_2 flux measurement results show elevated fluxes (>>100 g m^{-2} d^{-1}) along major faults and surface manifestations. The total CO_2 released from the Abaya fault has a total degassing amount of 282.274 ton d^{-1}. The results of soil temperature survey indicate a higher temperature anomaly up to 98.5 °C. The structurally controlled surface thermal manifestation, the presence of low resistivity zones inferred from geophysical data, the anomalous absolute temperatures interpreted from the thermal imagery, the anomalous soil CO_2 flux and temperatures all suggest that the Abaya geothermal system has favorable deep-seated permeable zones for the fluids to accumulate and continuously feed the surface thermal emissions.

Key words: Lake Abaya Geothermal Field; Enhancement; Thermal Imagery; Soil CO_2 Flux; Permeable Zone

Acknowledgment

This research work is done by contribution of different organizations and individuals. I am greatly indebted to Addis Ababa University for providing an opportunity to study my master‘s degree. For the invaluable academic support, an enormous thank you is owed to my advisor Prof. Gezahegn Yirgu and My Co-Advisor Dr .Snorri Gudbrandsson. Their follow up, constructive comment, valuable suggestion, encouragement and tireless support was throughout the life time of this thesis work. Intense gratitude goes to all lecturers. I would also like to thank Dario Ingi Di Rienzo and Hjalmar Eysteinsson for their needed support and shearing knowledge and experiences during different field trips.

The CO_2 flux measurment instrument presented in this paper was provided by the Reykjavik Geothermal Ltd, Iceland. Jon Orn Jonsson, the country manager of the Reykjavik Geothermal Ltd here in Ethiopia, is thanked for permission to study in the area licensed to the company, use the instrument, financial support during the field work and for extending all kinds of supports. Thanks are due to the University of Iceland and the University of New Mexico, Albaquerque for conducting the fluid chemical analysis of the major and minor ion compositions and for steam composition of fluid samples.

I acknowledge Chelsea Cervantes, Sydney Gunnarson and Daniel Ben Yahoshua, as anonymous reviewers for their suggestions that greatly improved an earlier version of the paper. Thanks are also to Abate Assen, Amdemichael Zafu, Samuel Getachew, Solomon Kebede and Salhadin Ali for their insightful reviews.

My very sincere gratitude goes to my beloved friends and AAU MSc fellows, I am so thankful for the good time we spent together and for your encouragement, collaboration and motivation. Thanks are due to friends especially to Yared sinetibeb, Getnet Gezahegn and Biniam Fentie.

My deepest gratitude goes to my family, dad, sisters and brothers for their unflagging love and unconditional support throughout my life and my studies. Your prayers, love, support and encouragement was worth more than I can express on paper.

The last but not the least my sincerely thanks goes to the administrators of the Humbo Woreda and the community in Abela and Abaya area for their cooperation during the field work.

Dedication

This work is dedicated to my beloved Father.

Table of contents

List of Figures

List of Tables

List of Acronyms

AAU	Addis Ababa University
AddMWL	Addis Ababa Meteoric Water Line
AfrMWL	African Meteroic Water Line
ANS	Arabian Nubian Shield
a.s.l	above sea level
DDS	Diffuse Degassing Structures
DEM	Digital Elevation Model
E.A.P	East African Plateau
EARS	East African Rift System
EGI	Energy and Geosciences Institute
ELC	Italian electroconsult
EMA	Ethiopian Mapping Agency
ENVI	Environment for Visualizing Images
EPA	Environmental Protection Authority
EPRI	Electric Power Research Institute
GM	Groundmass
GMWL	Global Meteoric Water Line
GPS	Global Positioning System
GSA	Graphical Statistical Approach
GSE	Geological Survey of Ethiopia
GSD	Ground Sampling Distance
JPL	Jet Propulsion Lab
MB	Mozambique Belt
MER	Main Ethiopian Rift
MT	Magnetotelluric
NASA	National Aeronautics and Space Administration
NDVI	Normalized Difference Vegetation Index
NGA	National Geospatial-Intelligence Agency
NIR	Near infrared
OLI	Operational Land Imager
PPL	Plane Polarized Light
RG	Reykjavík Geothermal

SDFZ	Silti Debre Zeyt Fault Zone
SRTM	Shuttle Radar Topography Mission
SMER	Southern Main Ethiopian Rift
SNNPR	Southern Nations, Nationalities and Peoples' Region
SWIR	Short wave infrared
TDS	Total Dissolved Solids
TG	Temperature Gradient
TIRS	Thermal Infrared Sensor
UNDP	United Nations Development Program
USGS	United States Geological Survey
UTM	Universal Transverse Mercator
WFB	Wonji Fault Belt
WODA	Wolaita Development Association
WGS	World Geodetic System
XPL	Cross Polarized Light
YTVL	Yerer-Tullu Wellel Volcano-tectonic Lineament

1. Introduction

Humans have always been depended on energy and mineral resources for its technological and cultural evolution**.** Currently and in the near future, energy and environmental issues will be two of the biggest challenges that mankind faces this century. Population levels are increasing globally and energy consumption is rising rapidly as the economies of the developing world industrialize, whilst traditional resources are being exhausted.

Non-renewable energy is energy from a natural resource such as coal, gas, or oil that, once consumed, cannot be replaced. Wind power, solar power (thermal and photovoltaic), hydro power, tidal power, biomass and geothermal energy are considered as renewable energy sources (Martina, 2009). Most of today's primary energy requirements are met by utilizing of non-renewable sources of energy causing significant damage to the environment (Weiss, 2003).

Renewable sources of energy are essential alternatives to currently widely utilizing fossil fuels. Geothermal resource contributes both to energy supply, with electrical power generation and for non-electricity generation applications such as horticulture, animal breeding, aquaculture, agro-industry, health and recreation, mineral water bottling, mineral extraction, space cooling and heating. Geothermal energy is considered as indigenous and environmentally benign energy sources that provide base-load power (Martina, 2009; EGI, 1997). It is a renewable source of energy formed and stored underground as hot water/steam (DiPippo, 2005 cited in Yosef Mengistuet al., 2019). Because of their independence from weather conditions, their constant output and availability around the clock geothermal resources are advantageous compared to other renewable sources such as wind, solar and hydropower sources (Samrock et al., 2015).

The principal sources of energy in Ethiopia are represented by traditional (biomass) energy sources. This happens because more than 80 % of the country's population is engaged in the small-scale agricultural sector and lives in rural areas (Solomon Kebede, 2014). The continuous economic growth has brought about a significant growth of energy demand including electricity. Currently, all the energy to be produced in the country will focus in renewable energy resources centered on hydropower, with complementary geothermal energy (Solomon Kebede, 2014). It helps to meet the planned climate resilient green economy of the country (EPA, 2011). Ethiopia benefits from hydro resources based on its

energy development upon hydropower plants. Although the energy from hydropower is renewable and environmental friendly, power plant operation is affected by seasonal rainfall fluctuations, expected to increase in the future due to climate change (Varet et al., 2012). In such context, geothermal energy will play a role in strengthening the energy sectors in Ethiopia.

Geothermal resource exploration and study in Ethiopia started in 1969 with a collaboration work of the Ethiopian Geological Survey and the United Nations. Over the years, an inventory of the possible resource areas within the Ethiopian sector of the East African Rift system, as reflected in surface hydrothermal manifestations has been built up. A regional reconnaissance work was conducted in the whole rift, including Geological, geochemical and hydrological surveys (UNDP, 1973). Lake Abaya geothermal prospect was one of the selected areas as the most promising geothermal fields.

In the present work, evaluation of structural permeability and their control on the thermal manifestations are tested using soil temperature and CO_2 flux measurement. This is to sum up in the characterization of the geothermal system of the Northern Lake Abaya geothermal field. The research project is conducted on the western rift margin close to the town of Wolaita Soddo, North of Lake Abaya in the central Ethiopia, along the southern sector of the Main Ethiopian Rift.

1.1. Geographic setting of the Study Area

1.1.1. Location and Accessibility

The proposed research study area is located in the southern part of the Main Ethiopian Rift (MER) about 275 km south southwest of Addis Ababa. It is directly above Lake Abaya, in the Southern Nations, Nationalities and Peoples' Region (SNNPR). The study area is accessible by the Asphalt-weather Addis Ababa – Arba Minch road, only 30 km drive from Soddo. Secondary road such as the Humbo – Abela Fericho – Bilate farms road provide reasonable access within the study area with many other secondary roads in the intensely cultivated parts along the escarpments. It is more specifically located in the Tebele map sheet with the sheet number 0637B4 according to the Ethiopian Mapping Agency (EMA). The study area has coverage of approximately 205km^2. The UTM (Universal Transverse Mercator) coordinates shows that the area is bounded by 373640 to 386540 m E and 728205 to 744405m N.

The main road that runs from Wolayita Soddo (or Soddo) to the town of Arba Minch is found asymptotic to the southwestern part of the study area which makes the study area easy to access using a vehicle. The gravel roads constructed for raw material transportation from quarries of scoria and pumices creates more accessible in the area. These roads pass through Abela village in the western part of the study area towards Abaya state farm dividing the area into two parts. The truck continues northwards towards Bilate state farm and Tobacco monopoly farm.

To the northeast and central part of the study area, there are foot trails developed by the local peoples for their day to day activity. This foot trails create additional access to the portion of the study area that is located far away from the main and gravel roads towards the Hobicha caldera, Hako and Salwa Dore Mountains that are found northeast of Abela Village.

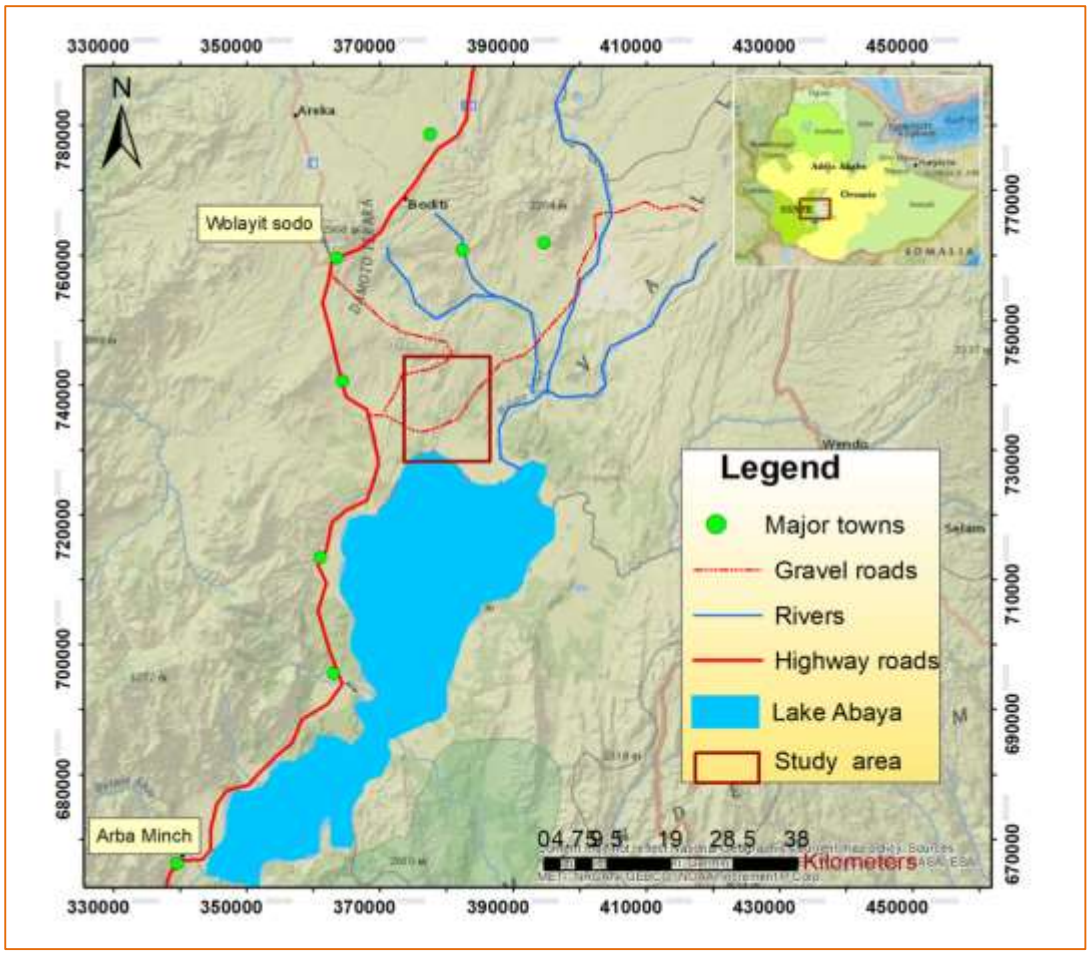

***FIGURE 1.1**: Location and accessibility map of the study area*

1.1.2. Physiography and Drainage

As it is discussed in section 1.1.1, the research study area is located on the western flank of the Southern Main Ethiopian Rift (SMER), where the plateau transitions into the rift floor (Figure 1.2). It is characterized by an absence of a major rift escarpment. Instead, the topographic transition between the rift floor and the plateau is gentle and accommodated by numerous roughly NNE-SSW-trending normal faults (Minissale et al., 2017). The topography gently slopes from Wolayita Soddo (2165 m a.s.l.) south and southeast towards the axis of the rift (Figure 1.2). At Humbo town which is around 30 km NW of Abela village, there exist faults exposed on older basalts (Zanettin et al., 1978). Young and distinct tectonic structures start appearing near the Abela village. From here, eastwards up to the lake, one comes across a series of young faults which have produced small horst-graben structures. The study area is the setting for two prominent graben structures. One is the Salewa-Dore graben, which is the host for an array of scoria cones and active fissures and the second is the Chewkare graben. Rhyolitic lava domes, scoria cones and calderas are also the most notable features within the study area. Various volcanic centers such as Doguna, Salewa-Dore, Hako, Chericha, Hobitcha and Donga Surrounding and within the study area represent the elevated topographies with altitudes ranging from 2090 to 1450m a.s.l. The tectonic lake of Abaya makes the southern boundary of the study area.

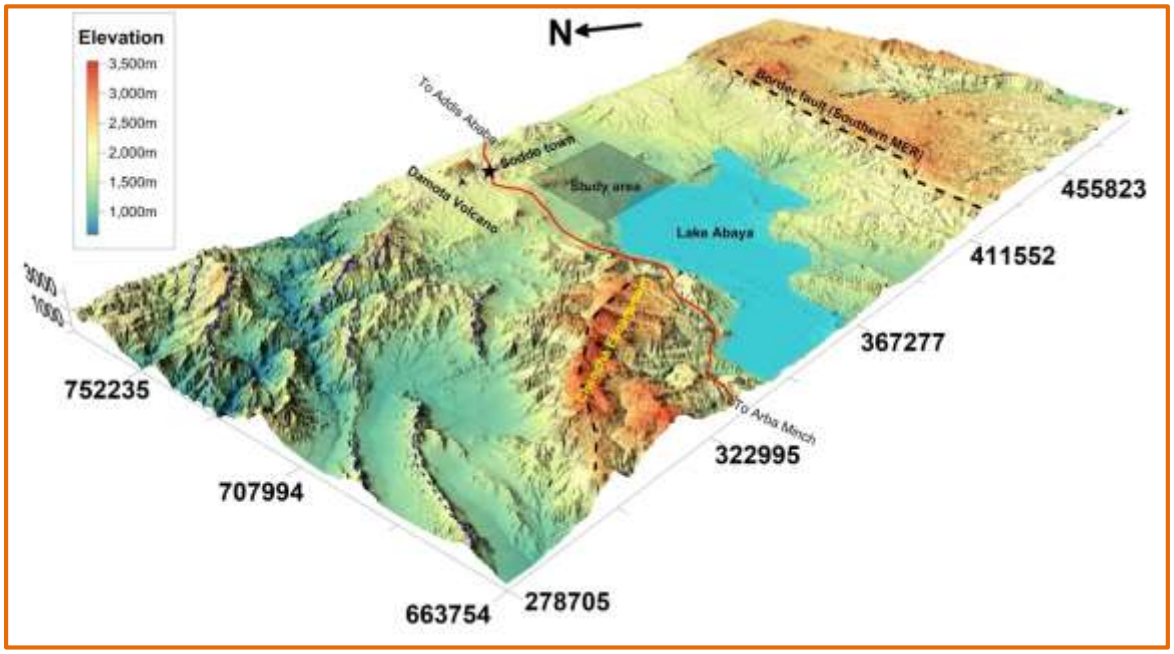

***FIGURE 1.2**: Physiographic makeup of the study area*

1.1.3. Climatic conditions and Vegetation

The climate condition of the research study area is explained by taking the average temperature and precipitation of the neighboring town (Soddo). This town is located in the tropics at high altitude possessing a well-moderated Subtropical highland climate with a pronounced pattern of wet summers and dry winters (Köppen climate classification, Koppen Cwb, 2018). Despite being located in the Northern Hemisphere, Sodo is actually cooler in the "summer" than the "winter" due to much higher rainfall in the high-sun season.

According to climate-data.org in https://en.wikipedia.org/wiki/Sodo, the climate around the area of the study is classified as warm and temperate. The rainfall is significant, with precipitation even during the driest month. The average temperature in Soddo is 19.3 °C and Precipitation averages 1484 mm. The temperature is highest on average in February, at around 21.2 °C and July is the coldest month of the year at 16.8 °C on average. The least amount of rainfall occurs in December with an average of 23 mm. In July, the precipitation reaches its peak, with an average of 223 mm. The variation in the precipitation between the driest and wettest months is 200 mm while the variation in annual temperature is around 4.4 °C.

The strong topographic characteristics control the expected tropical climate and soils in the study area. The vegetation distribution is mainly dependent on the climatic condition of the area. The natural vegetation consists of savannah-type and deciduous vegetation on the Rift floor and the lower slope and afromontane forests on the upper slope and the highlands (Westphal, 1975). Agriculture is mainly rain fed and dominated by mixed systems with both crop and livestock (Amare Getahun, 1978). The study area is suitable for agricultural activities having various climatic conditions, variety soil profiles, 12,000 hectares of reproductive land for irrigation and intense water bodies. The common types of crops cultivated in the area are production of legumes, root crops, Teff and some cereals – predominantly Maize (Takele Bassa, 2017). Agricultural investment sectors include Bilate state farm and Tobacco monopoly farm to the north east part of the study area.

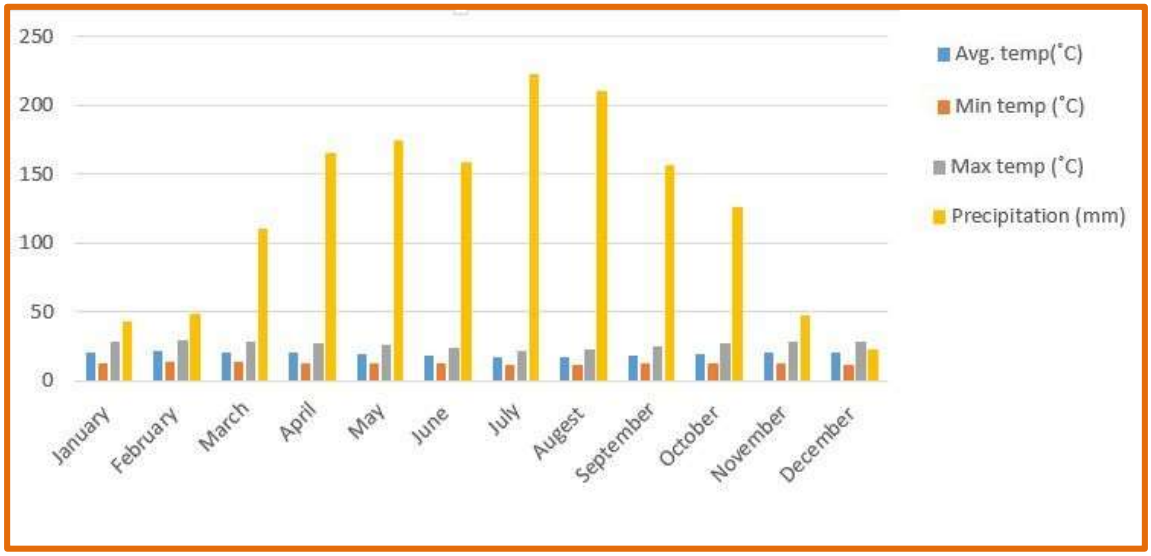

***FIGURE 1.3**: Climate bar chart showing Average climatic conditions (by month) of the Soddo area (sourced from* https://en.wikipedia.org/wiki/Sodo**)**

1.1.4. Population and Settlement

The average population density around the study area (Wolaita Zone) overs 385 people per square kilo meter making it one of the most densely populated areas in the country (Takele Bassa, 2017). The density in some parts of the Zone is as high as 781 ppkm² in Damot Gale Wereda; and as low as 168 ppkm² in Humbo Woreda. According to the data gathered by Wolaita Development Association (WODA) in 2009 the population size and structure, the current total population of the zone is 1,906,244 of which 795,950 are children (0-14years) 901,276 are working age population and 29,352 are old age (65+1) population, women of reproductive age (15-49) are 42,572. Wolaytta is spoken as a first language by between 1.6 and 2 million people (Compiled from Wikipedia as a source). Amharic, Sidamigna and Oromiffa are also spoken sparsely. The majority of the people are Protestant Christians, some are orthodox Christians and the rest are Muslims and other Christian denominations (https://joshuaproject.net/people_groups/15835).

1.2. Statement of the Problem

The Main Ethiopian Rift is an area which is studied a lot with respect to its volcanism and tectonism. The geothermal resource in the Ethiopian rift is being studied. Recently the studies have increased with increased interest from universities in structure, volcanism and interest in geothermal harvesting. In different geothermal fields of the MER like Aluto-Langano geothermal field a detailed study of; hydrothermal alteration, water-rock interaction process (Brhanu Gizaw, 1985, Meseret Teklemariam, 1996), Structural controls on fluid pathways (Hutchison et al., 2015) and detailed characteristics of the geothermal resource is conducted.

The Northern Lake Abaya Geothermal Field, as one of the geothermal prospects identified by the Geological Survey of Ethiopia following several geoloscientific works in the outhern Main Ethiopian Rift (e.g., UNDP, 1973; Tadiwos Chernet, 2011; Minissale et al, 2017), which should be given the proper attention considering the amount of information it can offer about geothermal energy potential in the area. Although the geothermal resource in the Northern Lake Abaya Geothermal Field, the system associated with the rift volcanism and tectonic environment, is thought to exist; only limited geological studies are available in explaining its potential. No sufficient work is found to exist that describes the general characteristics of the resource. There is no established geothermal conceptual modeling which is used to identify promising areas of the thermal anomaly. According to Corti et al., (2014), the distribution of the recent volcano-tectonic activity in the southern MER, where the proposed study area is found, is poorly known. The relations between volcanism and recent, rift-related faulting are less straightforward, and so are the possible implications for geothermal research.

The most recent and notable study regarding the Northern Lake Abaya Geothermal Field is the work of Minissale et al, (2017). In this study, the occurrence, chemical composition, origin and geothermal significance of thermal springs and fumaroles naturally discharging in the area are reviewed in relation with recent tectonics. Most of the thermal springs are dominated by a CO_2-rich gas phase and discharge along the active faults bordering the western edge of the Main Ethiopian Rift valley. However, Structural permeability is not evaluated with the help of soil temperature and CO_2 flux measurement yet. In addition to this, despite of regional correlations of the volcanic products and lacustrine deposits and construction of the stratigraphic outlines in the region were done by using isotopic dating

(Tadiwos Chernet, 2011), still a lot remains to be done due to strong lateral variations and petrographic similarity of the lithology.

The current study is motivated by the gap related to structural permeability evaluation and relationship between soil gas emission and the tectonic structural features. Moreover, the exploration of geothermal resource in the Northern Lake Abaya Geothermal Field is in nascent stage and that motivated to look into the aspect in detail.

1.3. Research Objectives

1.3.1. General Objective

The main objective of the present research study is evaluation of structural permeability and characterization of the geothermal system in the Northern Lake Abaya Geothermal Field.

1.3.2. Specific Objectives

The Specific objectives of the research are to:

- Establish the relationships between the young volcanic centers, active extensional structures and the distribution and types of the thermal manifestations.
- Determine the locations and trends of geological structures and deduce the major structures controlling fluid movement in the geothermal field.
- Quantify the natural CO_2 soil flux emissions.
- Establish the relationships between soil gas emissions and the geological structures in order to evaluate the structural permeability (subsurface fault characterization) of the area.
- Determine the chemistry of the thermal waters and estimate sub-surface temperatures.

1.4. Research Methods

In order to accomplish the stated objectives above, the following research methods and approaches have been followed.

1.4.1. Remote Sensing and GIS methods

Analyses of remote sensing data provide some insight into how the structural fabric had a control on the distribution of the hydrothermal manifestations identified as hydrothermal fields (Tadiwos Chernet, 2011).

In the present remote sensing-based analysis, two types of satellite data were used: optical and elevation data. The optical and elevation data comprise Landsat image and Shuttle Radar Topography Mission (SRTM) Digital Elevation Model (DEM) respectively. Landsat 8 data LC08_L1TP_169055_20171203_20171207_01T1 was accessed from the image courtesy of the U. S. Geological Survey Earth Resources Observation and Science Centre (http://earthexplorer.usgs.gov). Data with a path/row of 169/056 were obtained from the Landsat 8 Operational Land Imager (OLI) and Thermal Infrared (TIR) sensors for December 03, 2017. This specific image was chosen because the study area receives no/less rainfall during December, which enhances the impact of solar radiation on the land surface. The Raw Landsat 8 data is presented in Appendix VI.

During the study, data analysis were carried out using ERDAS 2014 and Arc GIS 10.2 by juxtaposing the imageries with geological map (1:50,000) of the study area and a 30 m resolution digital elevation model (DEM). During the preprocessing, all images were geo-referenced into one projection system where they were projected to Universal Transverse Mercator (UTM) zone 37N projection using World Geodetic System WGS84 datum. Images were clipped within the boundary of the study area. The satellite images were then layer stacked. These layers-stacked images were processed and analyzed using the software packages ERDAS IMAGINE 2014 and ArcGIS suite of geospatial processing program Arc Map version 10.4. The actual processing comprises band combination and band ratioing. Band ratioing between different band ranges is taken in order to enhance the spectral contrast. It is found helpful in mapping of hydrothermal alteration zones successfully.

In the present study remote sensing and GIS is mainly applied to delineate various geological and structural features of the area and hydrothermal alteration zones distribution.

All bands from 1 to 9, except band 9 and 1 were used in remote sensing data analysis. The cirrus band (Band 9) and Band 1 were excluded as they were mainly designed to support atmospheric correction and for studies of coastal water and aerosols respectively.

The elevation data used in this research study were obtained from Shuttle Radar Topography Mission (SRTM) Digital Elevation Model (DEM). Elevation data of 30m spatial resolution was obtained from NASA`s Jet Propulsion Lab (JPL) through USGS's Earth Explorer website (http://www.jpl.nasa.gov/srtm).

Primary data of thermal imagery was captured with a drone having a thermal camera. It was acquired during the second phase of field work (November 25 to December 07/2018) by RG Geothermal.

The effect of sunlight on the thermal dataset becomes too strong after 8:00 AM, therefore flying the area at night or at the latest around sunrise was found to be ideal. Thermal imagery data capturing was over the area of approximately 13.4 km^2. The resolution or average Ground Sampling Distance (GSD) for the thermal and RGB map is 67 cm and 32 cm respectively. The raw data was then georeferenced and the RGB and thermal orthomosaic were created finally. The data needs no temperature calibration because the types of camera that were used compensates for internal changes in the camera temperature after every few image and readjusts accordingly. When data processing, radiometric images (rjpgs) is used in which the absolute temperature is supposedly preserved.

Individual images were georeferenced using the GPS onboard the drone, which records the location and camera angles of each photo. These photos are then stitched together using photogrammetry software (no corrections applied). Therefore, the accuracy of the dataset geolocation is no more than that of the GPS onboard the drone, estimated to be within several meters.

FIGURE 1.4: *The drone used for thermal mapping (Source: RG Geothermal Ltd*)

1.4.2. Field geological and structural mapping and sampling of rocks and fluids

The main aim of this field work was to look for faults and collection of structural data measurements, to know the distribution of the lithologies and take representative samples for further laboratory analysis (especially for petrographic thin section analysis). The lithology variation and geological structures are transferred to a geological and structural map of scale 1:50,000. The field investigation was carried out systematically following predetermined traverse routes. Traverses where also focused on visible outcrops and associated structures (faults). Intern, this is based on spots taken from satellite images

during the pre-field phase of the present research activity. Water samples were also collected for chemical analysis.

The second phase of the field work was done in between November 25 to December 02/2018. These fieldworks were with the major objective of geochemical sampling of thermal manifestations for fluid and gas geochemical analysis. Hot grounds, hot springs and fumarole temperatures were measured using thermocouple thermometer and readings recorded in the field note book. Geographical coordinates of all stations studied and points of sampling were also marked and recorded using the hand held GPS. For purposes of conformity, the reference datum used in making all maps in this study was WGS 1984 Zone 37N.The field observations were also used to identify and verify the features displayed on satellite imagery, collection of structural data measurements, and documentation of hydrothermal area. The structural data are mainly measured for structures such as faults, joints and fractures/fissures by using Brunton (Brunton Pocket Transit) compass and clinometer. Structural measurements from the field were synthesized by a software package called Stereonet and analysed using the stereographic projection technique in GeoRose software.

The third and fourth phase of the field works were done in between January 11 to January 18/2019 and February 07 to February 21/2019 respectively. These fieldworks are targeted at collection of data about the soil CO_2 flux measurement and soil temperature surveys. Gas sampling from gas rich spings and weak fumaroles, geological mapping and structural data measurement has been also done in parallel.

1.4.3. Field geochemical methods: Soil CO_2 flux and temperature measurements

Soil gas flux and temperature measurements were conducted in the third and fourth phase of the field work which is discussed in section 1.5.3. The soil gas flux and temperature survey consist of 756 direct measurement points. The soil gas flux and temperature measurements were conducted in a selected area of the research study area at predefined profiles and fixed intervals, perpendicular to the fault structure and systematic sampling method. The CO_2 flux through the soil was measured over a rectangular grid with intervals of 50 m E-W and 200 m N-S with some exclusion in areas not suitable for measurement. Areas covered by younger lava flow were almost impossible to sample and few samples thus represents such areas, as was seen within the Hako lava dome were only possible to

sample. For areas that show variation in the measurement the sample spacing is made closer up to 20 m. The target area for the soil gas and temperature survey was based on the surface studies result (remote sensing analysis, structural mapping) conducted earlier than the survey and previous literatures done on the same geological environment (e.g. Hutchison et al., 2015). Diffuse degassing structures (DDS) constitute drilling targets for geothermal resource exploitation, and can be accurately mapped by CO_2 flux measurements.

For the CO_2 flux measurement, Portable flux equipment designed for surveying CO_2 flux is used. Terms of reference specify the method to be used; the closed chamber flux measurement techniques (Bloomberg et al., 2012; Lewicki et al., 2005; Chiodini et al., 1998). For the present study a flux-meter from Westsystems supplied by Reykjavik geothermal was used (http:www.westsytems.com/portable.html). This method involves placing an accumulation chamber on the ground and an air pump circulates air from the chamber through a LICOR-LI820 CO_2 sensor, an infrared (NDIR) gas analyzer based upon a single path, dual wavelength infrared detection system (Figure 1.5). The system uses an inverted chamber placed on the soil surface. The accumulation method calculates CO_2 flux by placing a 200 mm diameter accumulation chamber on the soil surface and pressing it into the soil to obtain a seal (Chiodini et al., 1998).

The sensor signals the concentration of the CO_2 (in ppm) to a palm computer, and then the gas is delivered again to the accumulation chamber. As the flow of the soil gas is constant in to the chamber the concentration of CO_2 will raise with time until a level is reached where the CO_2 escaping is equal to the CO_2 inflow. The results are plotted in time versus ppm CO_2. In the field, the slope and calculated residual mean square (r^2) of the selected section of the concentration/time curve (black vertical line in figure 1.5B). The co-efficient (r) is a measurement of the accuracy, value close to 1 shows very good accuracy. The field work shows that the accuracy is very high ($r > 0.95$). Measuring location (the GPS position) as well as the barometric pressure and air temperature are recorded. The flux measurement is based on the rate of CO_2 increase in the chamber; the measurement lasts for approximately 2 minutes at each location.

The CO_2 soil flux and concentration is influenced by external factors, such as the barometric pressure (atmospheric pressure P_{atm}), the air and soil temperature and humidity, the wind speed, the amount of rain and vegetation (Reimer, 1980). The influence of rainfall and soil humidity can be avoided through working in dry periods where the possible

changes in soil CO_2 flux induced by variable P_{atm} are almost inevitable (Chiodini et al. (1998). In the study area, the month January and February has low humidity and precipitation. Those months is selected for the survey in order to minimize the effect of the environmental factor on the CO_2 soil flux and concentration. The variation that can come from the wind speed can be minimized by carefully placing the chamber in the soil during measurement that does not allow exchange of air with atmosphere during the measurement. The increment in instrument reading that comes from vegetation abundance is minimized by taking measurement far from vegetated areas.

Soil temperature measurement is conducted simultaneously with soil flux using a 1 m long Digi-Sense Type K heavy-duty thermocouple probe from Cole-Parmer and an Oakton Temp 10 Thermocouple Thermometer (Figure 1.6A). It is measured at 0.5 m depth usually at the same location as the soil flux. The metal bar was driven with a custom-made sledge (figure 1.6B) to 50 cm depth at the same location after measuring the soil gas flux and the probe inserted and pushed to reach the required measuring point location. The penetration through the soil causes friction heat, the probe was therefore left in place until the temperature device shows that a stable reading had been reached. In the cases when the 50 cm depth could not be reached due to strong basement rocks the temperature and depth of the probe was reported as well as the temperature.

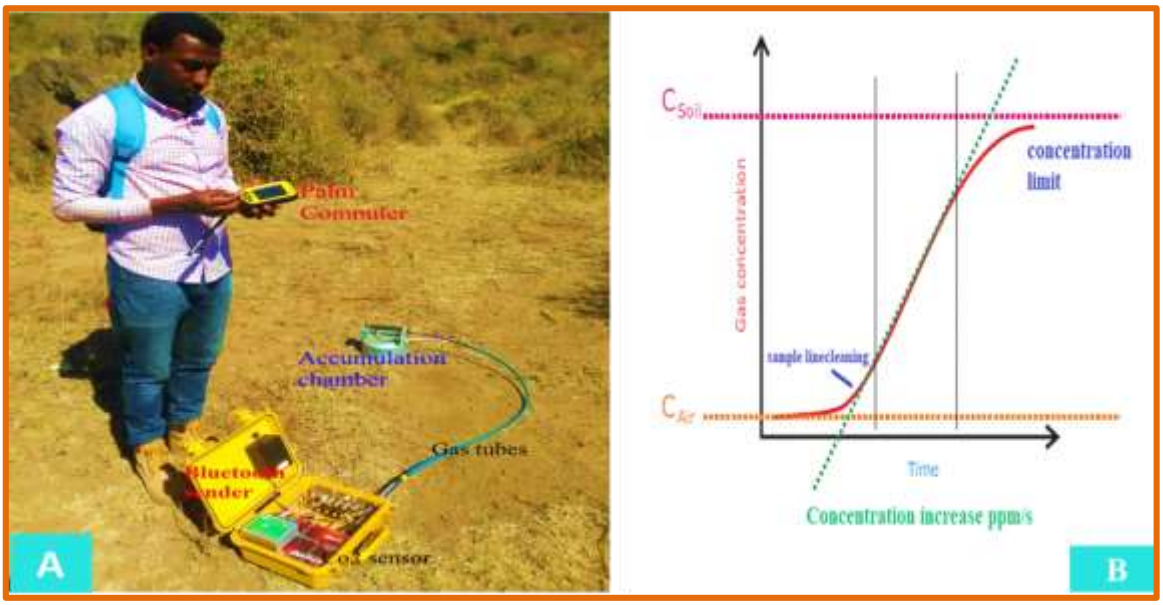

FIGURE 1.5: A. *Setup of the soil flux equipment in the field* ***B.*** *Time versus ppm for the accumulation chamber (from the instrument manual; supplied by RG Geothermal Ltd)*

FIGURE 1.6: A. *thermocouple probe and thermometer used for soil temperature measurements* ***B.*** *Custom-made sledge hammer used to inject iron rod into 50 cm depth for temperature measurements (properties of RG Geothermal Ltd)*

1.4.4. Laboratory methods: petrographic and fluid analysis

For observation and characterization of micro textures and mineral assemblage in the surface lithologies and determination of geothermal fluid chemistry, different analytical methods were used. The methods included petrography microscope thin section analysis and fluid analysis (Titrimetery and Spectrophotometers).

1.4.4.1. Petrographic analysis

Petrography microscope analysis was very helpful to identify/confirm rock types, texture, porosity, vein fillings, and alteration of primary and secondary minerals and to identify additional minerals not seen in the field by binocular lenses.

In the present research, thin sections of 12 representative samples from study area were made at the Institute of the central Geological Laboratory of the Geological Survey of Ethiopia. The thin section samples are selected based on the variety of the lithologies, their importance and their ambiguities to identify while in the field work. Inspection of the prepared thin section was conducted at the AAU petrography laboratory with the use of Lecia Petrographic Microscope for determination of modal composition (modal proportion of minerals in each rock type,) and micro-textures of rocks. Images of minerals under thin sections at different sites of observation are also taken using the camera on Lecia Petrographic Microscope. In petrography microscope analysis, minerals are identified according to their properties in plane-polarized and cross-polarized light. It includes cleavage, colour, pleochroism, twinning and the interference properties.

1.4.4.2. Fluid analyses

The assessment of the chemistry of the thermal water features helps in understanding the water type as well as an estimation of the deep temperature of the geothermal system with the application of chemical geothermometers (Giggenbach and Goguel 1989).

A total of nine water samples and twelve dry gas samples were collected in the study area from thermal springs. Spring samples were collected from relatively appreciable flows that remain constant throughout the year with relatively high flow rate and high temperature. The distributions of the thermal manifestations where samples are taken are in the Wache and Boramitta; Chewokare graben, North West of Lake Abaya (Abaya fault).

Chemical analysis of the major and minor ion compositions were carried out at the Institute of Earth Sciences, the University of Iceland and the steam composition at the University of New Mexico, Albaquerque. All major cations were analysed by Atomic Absorption Spectroscopy. Carbonate and bicarbonate determined by HCl acid titration to pH 8.23 and 3.8 respectively using pH-meter to control the end point of the titration. Chloride was determined by Argentiometric titration using potassium chromate as an indicator for the end point of the titration. Sulphate was determined by turbidimetry and gravimetry where the sample concentration is low or high respectively. Fluoride was determined by specific ion electrode. Silica and Boron were determined by spectrophotometery, using Molybdate blue and carmenic acid methods respectively.

The reliability of major cations and anions analysis of the water samples was evaluated, using the standard relative analytical error estimation method. The results were found to full fill the standard relative analytical error estimation of –5% and +5%, which suggest that the analytical results are reliable for interpretation.

1.4.4.2.1. Data analysis tools

The standard instruments used in the analysis of the thermal samples include:

- The double-beam or modern single-beam atomic absorption spectrophotometer for the determination of cations, as well as boron (> 10 mg/kg) and silica
- The ionic chromatograph for the analysis of most anions.
- The visible-UV spectrophotometer for the colorimetric determination of boron (curcumine method) and silica (ammonium molybdate method).
- The automatic titrator for the determination of alkalinity.
- The pH-mV-meter equipped with glass-electrodes for pH determination and fluoride- and ammonia- specific electrodes.

1.5. Expected outcomes and research relevance

As it is discussed in the problem statement the Lake Abaya has not been studied in the aspect of resource potential characterization and structural permeability evaluation in detail. This research study will be the very first detail study on its structural permeability evaluation and relationship between soil gas emission and the tectonic structural features. The main expected research outputs will be as follows:

- Gives insight knowledge to understand role of the tectonic structures in creating permeable reservoir to the geothermal system.
- Provides better scientific understanding to characterize the geothermal production potential of the area.
- There is an increase in the interest of natural sources of energy probably primarily geothermal energy. Contribution of this research will means a lot to promote interest in geothermal energy.

The research study is carried out in partial fulfillment of a Master's Degree in resource geology (geothermal energy) at the Addis Ababa University, Ethiopia.

2. Literature review

2.1. Overview of the concepts of geothermal system

The geothermal system can be described as ‘convecting water in the upper crust of the Earth, which, in a confined space, transfers heat from a heat source to a heat sink, usually the free surface’ (Hochstein, 1990). It has three basic components namely; the fluid, the heat source and the reservoir (Figure 2.1). The steam or hot water contained in the reservoirs can be tapped by drilling to deliver heat to the surface for thermal use or generation of electricity and other direct applications.

Geothermal energy is the vast reservoir of heat energy in the earth’s interior , whose surface manifestation are fumaroles, geysers, steaming grounds, mud pools and hot springs (Dickson and Fanelli, 2004; Manzella, 2006 **)**. It consists of all the thermal energy stored in the earth’s crust. Thermal energy in the earth is distributed between the constituent host rock and the natural fluid that is contained in its fractures and pores at temperatures above ambient levels. These fluids are usually water with various amounts of dissolved salts and are typically present as liquid or supercritical fluid phase but may sometimes consist of a saturated or superheated steam vapor phase (Hochstein, 1990).

The different forms of geothermal energy resources; hydrothermal, hot dry rock, geopressured, magma, and earth heat; all result from this concentration of earth's heat in discrete regions of the subsurface (Bertani, 2008). Temperature within the earth increases with increasing depth. Highly viscous or partially molten rock at temperatures between 650 to 1,200°C is assumed to exist everywhere beneath the earth's surface at depth of 80 to 100 kilometers. The temperature at the earth's center, nearly 6,400 kilometer deep, is expected to be 4,000°C or higher. Heat flows constantly from its sources within the earth to the surface (EPRI, 1978). Hydrothermal geothermal resource can be found in same places as volcanoes, as magma/volcanic activity are most often the heat source of a geothermal system. Most geothermal resources presently usable for electric power generation result from the intrusion of magma at great depths into the earth’s crust. These intrusions usually reach depths of 0 to 10 km (Tester et al., 2005).

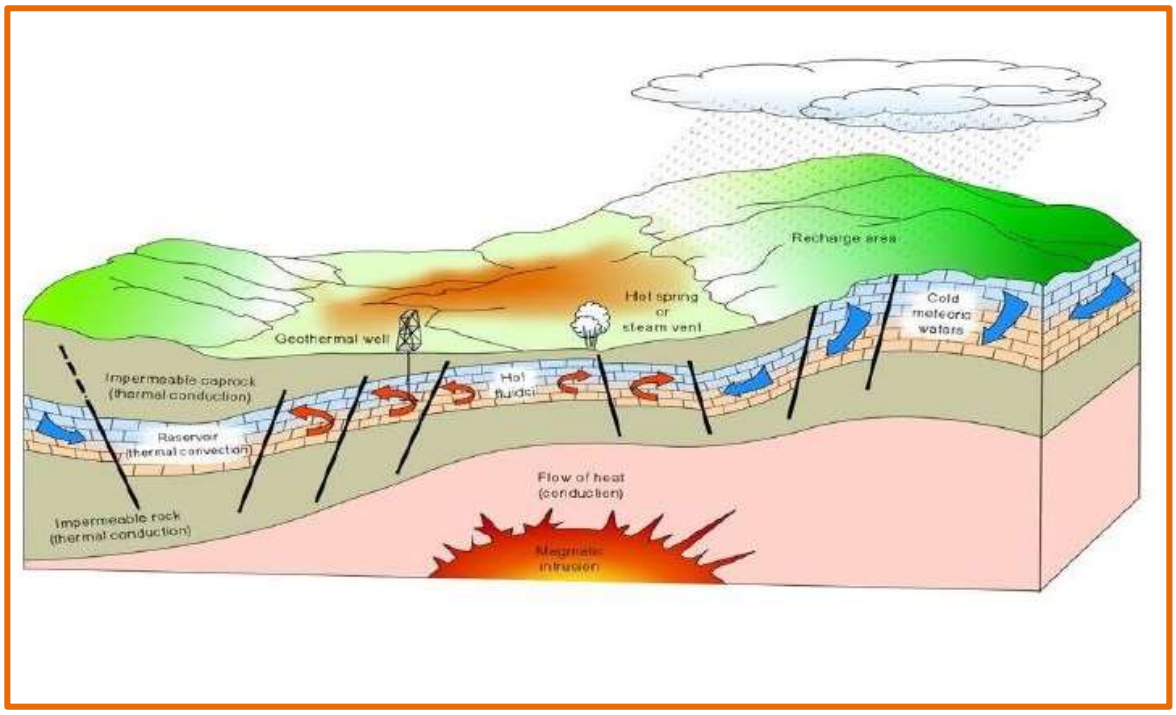

FIGURE 2.1: *A schematic representation of an ideal geothermal system (Hochstein, 1990)*

2.2. Geothermal resources in Ethiopia

The EARS provides a unique opportunity to meet future growth with renewable sources like geothermal energy. High-enthalpy geothermal reservoirs that form over magmatic intrusions are found abundantly along the EARS (Samrock et al., 2018**)**. Utilization of this renewable energy resource is currently increasing and could contribute to a low-carbon sustainable energy mix for the emerging and fast-growing economies of East African countries (Solomon Kebede, 2016; Younger, 2014 cited in Samrock et al., 2018).

The Quaternary-recent volcano-tectonic activity of the MER makes it the host for enormous geothermal resources. After an initial phase of basin subsidence related to slip along large boundary faults, the Quaternary-recent volcano-tectonic activity of the MER is typically associated with dense fault swarms, referred to as Wonji Fault Belt (WFB). The dense fault network characterizing the WFB allows deep fluid circulation at major volcanic centers, and development of promising geothermal resources (Corti et al., 2014). Many studies in the rift, are also suggest that existing fault structures can play a significant role in the development of a volcanic complex, ultimately providing high permeability pathways for magma, hydrothermal fluids, and gas to ascend to the surface (e.g., Arnórsson, 1995; Rowland and Sibson, 2004; Caliro et al., 2005; Fridriksson et al., 2006 cited in Hutchison et al., 2015). According to Hutchison et al., (2015), understanding of how pre-existing

structures such as regional tectonic faults and caldera ring faults affect fluid flow to the surface has important implications for geothermal exploration. Geothermal exploration in Ethiopia started in 1969 but so far only limited geothermal development has taken place. In the whole MER about 120 geothermal sites, mainly surface hydrothermal manifestations, have been identified with an estimated overall potential for power generation of around 5000MWe (UNDP, 1973; Meseret Teklemariam and Solomon Kebede 2010 cited in Samrock, 2015). UNDP in (1973) conducted detailed descriptions of hydrothermal features in the Ethiopian rift on selected targets namely; Tendaho Graben, Danakil Depression and Aluto Volcanic Center. This was accompanied by detailed mapping of the main hydrothermal areas employing photogeologic interpretations and field observations. The primary objective of this work was identifying and evaluating local regions of anomalous heat flow. Ground investigation and infrared photography within 150,000 km^2 of the rift of Ethiopia along with geologic, geochemical and hydrologic techniques were utilized. In addition, analysis of hot spring, surface and well waters and fumarole gas samples were employed. This work identified more than 500 hydrothermal features.

The highest geothermal potential is expected in the northernmost part of the MER where it shows the most advanced stage of rift evolution. However, detailed surface exploration and feasibility studies have been focused on the central MER geothermal sites due to easier access to infrastructure (Meseret Teklemariam and Solomon Kebede 2010 cited in Samrock, 2015). Here, prioritization for geothermal exploration has been given to eight sites, namely Tendaho, Corbetti, Aluto-Langano, Tulu Moye, Gedemsa, Kone, Fantale and Gedemsa (Figure 2.2). A description of the better known geothermal resource which has received more attention in recent years is reviewed below.

2.2.1. The Tendaho geothermal field

The Tendaho graben is found further north in the Afar depression. It is a NW-SE trending graben about 50 km wide and is the southern extension of the afar active spreading zones where the active Erta Ale-Manda Hararo volcanic ranges are situated.

According to the Italian electroconsult (ELC), (2015) the youngest rocks of the region are Quaternary axial fissural basalts, subordinate rhyolites and associated products of central volcanoes (Upper Extrusive Complex). In the grabens these volcanic products are interbedded with the fluviolacustrine sediments that are washed from the surrounding

highlands and horsts, therefore, most of the rock fragments that constitute the sediments are of volcanic origin. From the structural point of view, normal faults and open fissures are the principal elements of the Afar tectonics observed in Tendaho geothermal field. The Alalobeda manifestations are located in the NW trending Tendaho Graben.

At Tendaho, between 1993 and 1998, three deep (to a maximum depth of 2100 m) and three shallow explotatory wells (up to 500 m) were drilled that found a temperature of over 270°C. Preliminary production test and techno-economic study indicated that the shallow productive wells in Tendaho is about 5 MWatt and the potential of the deep reservoir is estimated about 20 MWatt (Aquater, 1996a; 1996b cited in Meseret Teklemariam and Kibret Beyene 2005).

2.2.2. The Tulu Moye - Gedemsa geothermal prospect area

Tulu Moye is one of the lakes district geothermal prospects, which is located about 200 km south east of Addis Ababa, the Main Ethiopia Rift. Different literature sources suggested that the topographic setting, quaternary faulting and magmatism in Tulu-Moye make it a promising geothermal prospect (e.g., UNDP, 1973; Abebe Ayele, Meseret Teklemariam and Solomon Kebede 2002; Engdawork Admassu and Selamawit Worku 2015; Yosef Mengistu et al., 2019). The area is characterized by volcanism dating from Recent (0.8-0.08 Ma) to historical times depicting the presence of young eruptive centers (ELC, 1987). It hosts three major quaternary felsic centers namely; Tulu Moye, Bora and Bericha. The main hydrothermal manifestations are weak fumaroles, altered grounds and active steaming grounds having temperature ranging from 70 - 80 °C. Five temperature gradient wells (TG wells) have been drilled to depths ranging from 133- 179 meter; having temperature of 78°C. Deep reservoir temperature of hot springs and Well TG-1 as estimated by chemical geothermometer shows an average of 194°C confirming the existence of potential geothermal reservoirs with high temperature (Asfaw Teclu and Taffesse Gizaw 2001).

2.2.3. The Aluto-Langano geothermal field

Aluto-Langano geothermal field is located on the floor of the Ethiopian Rift Valley about 200km south-east of Addis Ababa. The Aluto volcanic complex is a Quaternary volcanic center located along the Wonji Fault Belt in the central sector of the MER (Meseret Teklemariam 1986; Ernst et al., 2010). The geology of this complex is mainly volcanic along with some lacustrine sediment (Meseret Teklemariam 1986).

Most advanced studies have been carried out at the Aluto- Langano geothermal field. It is the first geothermal field in Ethiopia to be exploited where the only electricity producing geothermal power plant in the country is located (Meseret Teklemariam and Kibret Beyene, 2000). Within the Aluto- Langano geothermal field, eight exploration wells have been drilled reaching depths of 2500 m and temperatures up to ∼350 ◦C during the 1980s (Abebaw Endeshaw 1988 cited in Samrock et al., 2015). Six of the wells are located in the Centre of the volcanic complex with two of them, LA3 and LA6, being productive. Four of them, LA4, LA5, LA7 and LA8, have been drilled into the outflow zone and show a temperature reversal with depth. The productive wells are drilled into the upflow zone, which is located under an NNE tending fault system that intersects the volcanic complex. Two other wells located west and south outside of the complex are non-productive. A pilot power plant was installed at Aluto in 1999 with an overall capacity of 7MWe. However, due to operational difficulties it only produced 3MWe (UNDP, 1973; Meseret Teklemariam 1986; Meseret Teklemariam et al 1996; Meseret Teklemariam and Solomon Kebede 2010: Samrock et al., 2015).

2.2.4. The Corbetti geothermal prospect area

The Corbetti geothermal prospect area is located about 250 km south of Addis Ababa. Corbetti is a Holocene volcanic complex found in the central sector of the MER (Martin-Jones et al., 2017). The area comprises both sedimentary and volcanic rocks (Elias Altaye 1984). The most abundant volcanic rocks are peralkaline pyroclastics (ignimbrite and pumice) which are attributed to central-type eruptions with subsequent volcano-tectonic collapse. Corbetti is a silicic volcano system within 12 km wide caldera that contains extensive thermal activity such as fumaroles and steam vents associated with The Quaternary volcanism (Tadesse Mamo and Zewdu Abtew 2011). An integrated Geological, geochemical and geophysical investigations conducted in Corbetti area indicated the presence of potential geothermal reservoirs with temperature in excess of 250°C. Six temperature gradient wells (shallow drill holes) have been drilled to depths ranging from 93- 178 meter; a maximum temperature of 94°C was recorded (UNDP 1973; Lloyd, 1977; Solomon Kebede and Mohammedberhan Abdulkadir 1987). From these sources, the intrusion beneath the Corbetti caldera is old to provide enough heat sources for the system (results of shallow drilled holes). Rather local intrusions associated with the eruption of Chebbi and Urji volcanoes are probably inducing the high thermal anomaly.

It is important to consider that, apart from the favorable geological conditions; geothermal resources in the Ethiopian rift are primarily controlled by rift structures. Therefore, understanding the way in which rift faults influence subsurface thermal fluid flows plays a key role. Bruhn et al., (1994) has noted the close interaction between fluid circulation and faults. The theoretical background behind evacuation of structural permeability in the current work is that structures may act as strong water passage zones and hence would be potential drill targets.

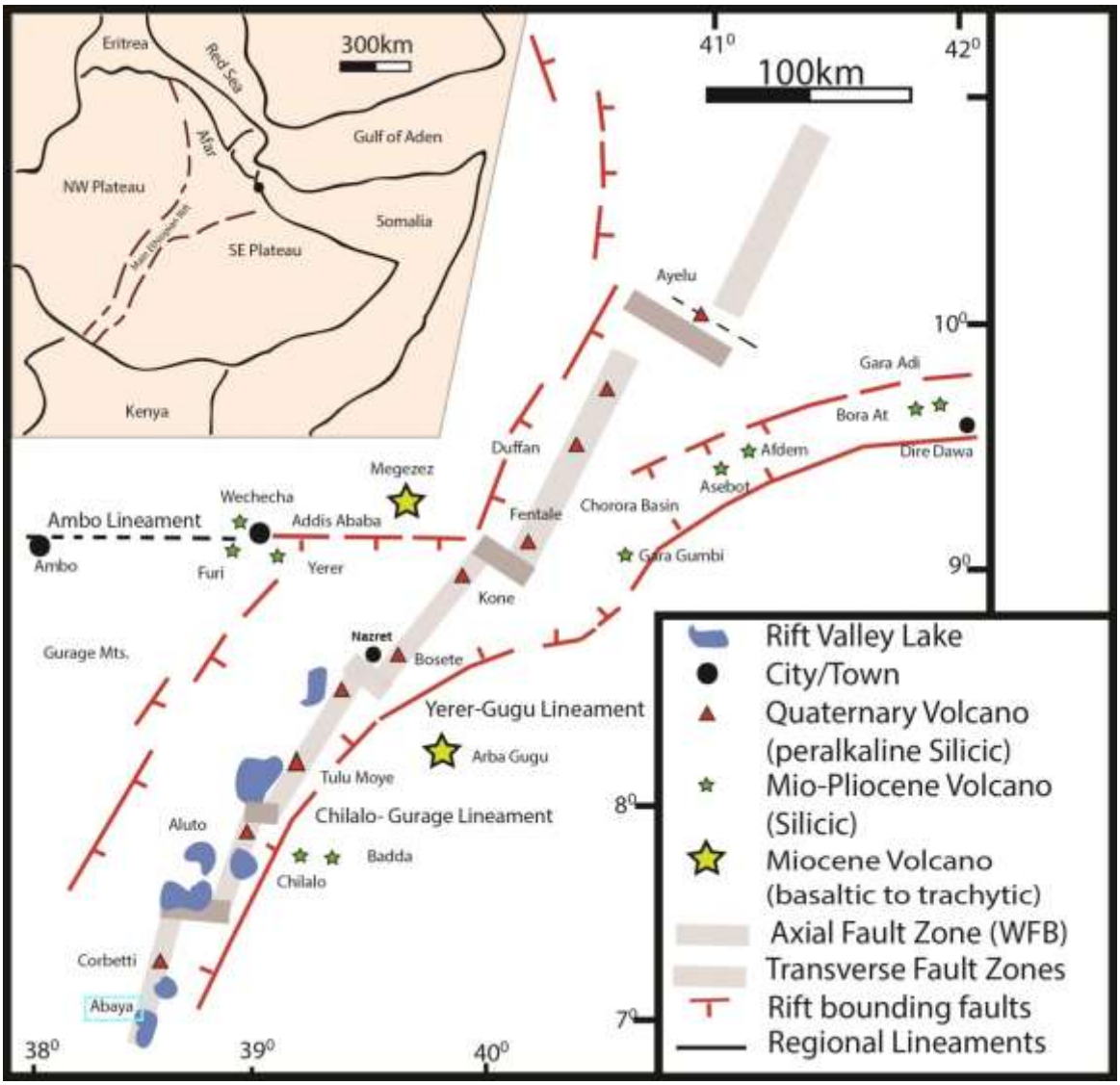

FIGURE 2.2: *Location map of the Northern Lake Abaya Geothermal field in the Ethiopian Rift (adopted after Geological Survey of Ethiopia)*

2.3. Application of soil CO_2 flux and temperature measurement in geothermal resources exploration

2.3.1. Soil CO_2 flux measurement

Volcanic and hydrothermal gases are of interests to geothermal and volcanic studies. The term volcanic gas defines a gas exsolved from a magmatic source of an active volcano whereas hydrothermal gas defines a gas exsolved from the envelope of hot water that surrounds the magmatic environment. Volcanic gases have composition different from the hydrothermal gases, the first is richest in sulfur dioxide (SO_2) and the second in hydrogen sulfide (H_2S) (Giggenbach, 1996). Carbon dioxide (CO_2) occurs in both hydrothermal and magmatic gases and is the most abundant gas after water vapor (Giggenbach and Goguel, 1989).

High amounts of CO_2 are released to the atmosphere from active volcanic areas, not only during eruptions but also during quiescent periods (Allard et al., 1991; Baubron et al., 1990 cited in Chiodini et al., 1998). This volcanic CO_2 discharge occurs from both active craters, as plumes and fumaroles, and the flanks of volcanic edifices, as diffuse soil emanations. The deep-seated faults in the crust tap magmatic CO_2, which is transmitted to the surface where it is naturally lost through the soil (Giggenbach and Goguel, 1989). CO_2 of magmatic origin is normally channeled through deep-seated tectonic structures close to the surface of the earth and then seeps out of the ground through the soil.

The soil CO_2 flux is an interest to a number of research disciplines (e.g. geology, ecosystem ecology, climate and atmospheric science). Geologists are usually interested in CO_2 originating from deeper layers associated with magmatism (Harvey et al., 2015). This is because, preexisting faults in volcanically and seismically active rift systems may control the rise and eruption of magma (Hutchison et al., 2015). It also directs the flow of hydrothermal fluids and gas in the subsurface. The study of soil CO_2 flux measurement helps to explore how preexisting tectonic and volcanic structures control fluid pathways and degassing.

Portable equipment designed for surveying CO_2 flux in geothermal prospects has been commercially available since the late 1990's. Soil gas mapping is an important geothermal exploration tools because distribution of geothermal gases such as H_2S and CO_2 in the soil can elucidate pathways (structures) of steams to the surfaces (Fridricksson et al., 2016). Geothermal gasses are transported with steam to the surface through point sources (steam

vents, gases bubbles through water) and some of it is released diffusely through soil (diffuse degassing). Concentration of some of the geothermal gases in the steam can be used for geothermometry. Other gases can simply suggest geothermal activity by their present.

The diffuse flux of CO_2 through the soil in geothermal fields can provide important information on the nature of the geothermal system. Open fractures and faults, with respect to fluid flow, are the preferential pathways for CO_2 escaping from a geothermal reservoir (Figure 2.3). If such a structure is buried in the subsurface it may be located based on mapping of a linear CO_2 flux anomaly on the surface (Fridricksson, 2009). According to Hutchison et al., (2015), areas which have highly affected by brittle structure will have high measurement result because of those structures will act as a conduit and make the lithology plus the soil more permeable and finally enable us to get high value of diffuse degassing structures. But local variations of the CO_2 degassing may occur. The permeability variations at local scale may come from lithological and topographic controls (Tamiru Alemayehu and Vernier, 1997, Schöpa et al., 2011, Hutchston et al 2015). The diffuse degassing structures (DDS) constitute drilling targets for geothermal energy exploitation, and can be accurately mapped by CO_2 flux measurements.

After any survey of soil CO_2 flux in geothermal area, a key task is the identification of the biogenic component of the total CO_2 flux, so this "background" can be accounted for. A review of geothermal publications shows that the statistical methods are commonly used to identify and quantify background (biogenic CO_2 components) flux (Chiodini et al., 1998, Fridriksson et al., 2006, Harvey et al., 2015). The graphical statistical approach (GSA) is one of the statistical methods that partitions separate log-normally distributed populations using cumulative probability plots (Chiodini et al., 1998). Inflection points in cumulative probability plots can be used to distinguish the presence of multiple populations (Sinclair, 1974). It is through the above theoretical backgrounds that the current study is conducted.

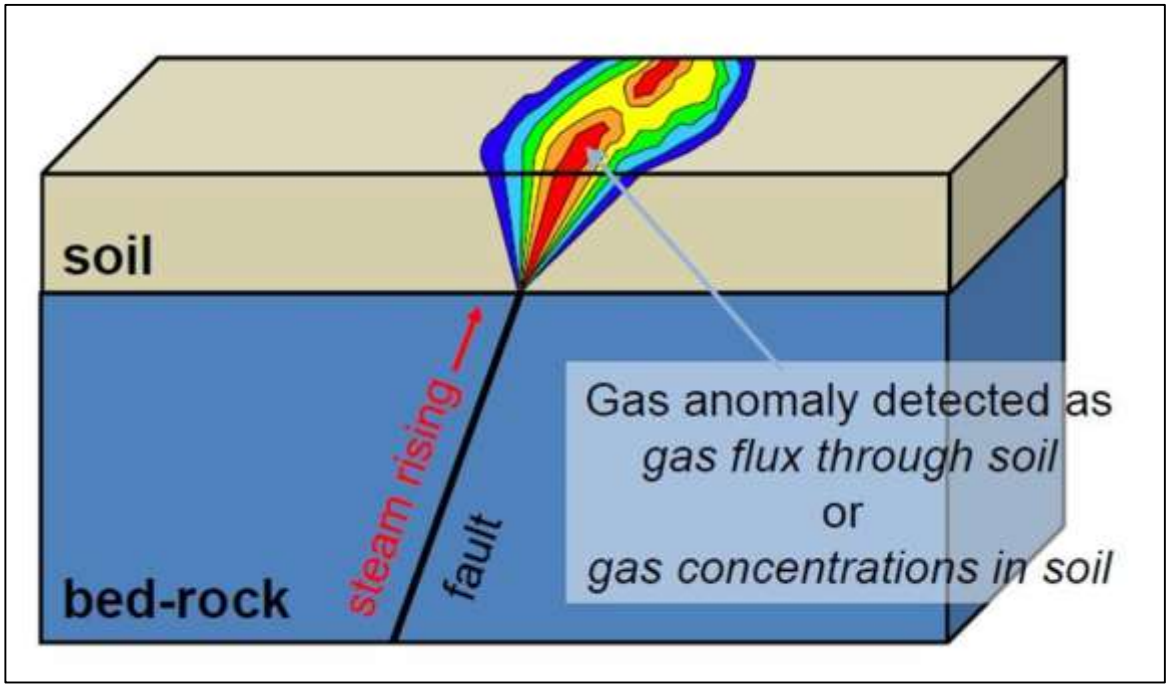

FIGURE 2.3: *Model for defused degassing of geothermal gases (Adopted after Oskarsson, 2016)*

2.3.2. Soil temperature survey

Temperature survey is an important geothermal exploration tool. Shallow temperature surveys are coast effective, portable, quick and potential. It is used to locate and map thermal anomalies and aquifers in details (Sladek et al., 2012).it is also important to identify and delineate geothermal outflow zones in a very lower coast prior to temperature gradient drilling and other exploration techniques (Zehner et al., 2012).

2.4. Overview of Previous Works in Northern Lake Abaya area

Previous geological, geochemical and geophysical works in the MER that are related to geothermal disciplines are reviewed and presented in this section.

Geological investigations provide basic information into the relations between faulting and magma/fluids migration. This in turn yields basic information for geothermal prospection. Many geological, geochemical and few geophysical works in the MER have been done for the last decades. Tadiwos Chernet, (2011) has a study on the geology and hydrothermal resources in the northern Lake Abaya area. Corti et al., (2013) studied the Quaternary volcano-tectonic activity in the Sodo region. A year later, Corti et al., (2014) examined the Volcano-tectonic and hydrothermal activity in the Soddo area.

Hutchison et al., (2015) studied Structural controls on fluid pathways in an active rift system, where the case study was the Aluto volcanic complex. Soil-gas CO_2 degassing surveys were among the methods adapted to explore how preexisting tectonic and volcanic structures control fluid pathways and spatial patterns of volcanism, hydrothermal alteration and degassing. The result of this work shows that there is an estimated total CO_2 emission of 250–500 t d^{-1} from Aluto volcanic complex.

Previous works, specifically focused on hydrothermal venting and volcanic degassing (Schöpa et al., 2011; Pantaleo and Walter, 2013 cited in Hutchison et al., (2015), has also shown that while preexisting structures may control permeability at the edifice scale, at smaller scales these structural controls may be hidden by localized near-surface permeability variations. These local influences may include (1) lithological variations, where fluids will preferentially migrate along high permeability layers (e.g., poorly consolidated tephra layers) and (2) topographic controls, where the stress fluid induced by gravitational loading causes fracturing parallel to topography, and focuses pathways for steam and other gases toward topographic highs (Schöpa et al., 2011 cited in Hutchison et al., (2015). Geothermal activities in the Main Ethiopian Rift (Purschel et al., 2013); Geothermal potential and origin of natural thermal fluids of the northern Lake Abaya area (Minissale et al., (2017) are also some examples of previous work on geothermal resource of the MER.

Gravity analysis in Duguna volcano, SMER (Mahatsente et al., 1999); vertical electrical sounding and magnetic geophysical survey on the Boku thermal field (Tigistu Haile et al. 2000); Geophysical investigations beneath the Wonji magmatic segments in the northern MER (Keranen et al., 2004); MT soundings around the Lake Abaya geothermal field (Mohammednur Desissa and Yohanes Lema 2006); Geophysical investigation in the northern MER (Keranen and Klemperer 2008); Magnetotelluric (MT) measurements to investigate the electrical conductivity structure under the Aluto volcanic edifice (Samrock et al., 2015) and magnetotelluric image of transcrustal magmatic system beneath the Tulu Moye Geothermal Prospect (Samrock et al., 2018) are some examples of previous geophysical works in the MER.

The Quaternary-recent volcano-tectonic activity of the MER is typically associated with dense fault swarms affecting the rift floor (Corti, 2009; Corti et al., 2014, Hutchison et al., 2015). These dense fault networks characterizing the WFB allow deep fluid circulation at

major volcanic centers, and development of promising geothermal resources. In the MER, most of the rift floor and margins are covered by volcanic and volcano-sedimentary rocks (Mohr and Zanettin, 1988; Tadiwos Chernet, 2011; Corti et al., 2013). Volcanic sequences are a result of the typical bimodal volcanism (Tadiwos Chernet, 2011 cited in Corti et al., 2014). The shallow crustal magma chambers hosted in these axial volcanic centers delivers heat sources for the existence of geothermal resources whereas the lacustrine and volcanoclastic graben infill sediments may serve as the cap rock (Tadiwos Chernet, 2011).

Tigistu Haile et al., (2000) did vertical electrical sounding and magnetic geophysical survey on the Boku thermal field, near Adama (Nazareth) town. This work showed that there exist vapor-dominated geothermal fields located on or close to volcanoes. The volcanoes may host shallow magma chamber beneath it which could be the heat source for the geothermal fields in the area. An integrated geophysical study in the Boko geothermal area, MER by Tamiru Alemayehu and Tigistu Haile (2008) involves thermal, magnetic, electrical, electromagnetic and gravimetric surveys. This geophysical investigation have clearly mapped the shallow low resistivity zones that are likely to indicate the presence of thermal aquifers and the location of major faults that allow downward and upward fluid flow. Samrock et al (2015) conducted magnetotelluric (MT) measurements to investigate the electrical conductivity structure under the Aluto volcanic edifice in order to put constraints on the source of unrest and to advance knowledge about the distribution of melt. Samrock et al., (2018), presented a crustal-scale electrical conductivity model for a magmatic segment in the Ethiopian Rift, derived from magneto telluric data.

3. Regional Tectonics and Geology

3.1. The East African Rift System

The East African Rift System (EARS) is the classical example of a seismically and volcanically active continental rift, extending for about 6,500 km from the Dead Sea Rift in the north to Mozambique in the south. This rift is a mobile volcanic belt under constant motion. The movement causes deformation of the lithosphere resulting in propagation of fractures and faults, reactivation of buried inactive faults and in some cases, arrest or closure of previously active geological structures. It is divided into an eastern branch and western branch, and is composed of several interacting segments.

3.2. The Main Ethiopian Rift (MER)

3.2.1. Tectonics of the Main Ethiopian Rift (MER)

The Ethiopian Rift system is located in the eastern branch of EARS, and started to develop during Miocene time ( ). This rift is basically a very large graben formed by tensional movements as a result of drifting of the Nubian and Somalian plates with a concomitant domal uplift (Figure 3.1). It extends about 1000 km in a NE-SW to N-S direction from Afar southwards to the Turkana Depression (Corti, 2009; Pürschel et al., 2013; Samson Tesfaye et al., 2003).

The MER extends some 500km NNE from just south of latitude 6 degrees N near Lake Chemo to latitude 9 degrees N where it meets the complex Afar triple junction. The MER separates the Nubian and the Somalian plate, its trough is between 35 and 85 km wide and bounded by large normal boundary faults, which developed during the Miocene. The major escarpment between the rift floor and the flanking southern and northern Ethiopian plateaus is built by steep NE striking normal boundary faults and the relative displacement reaches overall differences in height of up to 2000m (Corti, 2008).

The MER in East Africa records a transition from early fault-dominated morphology in the South to axial magma assisted-rifting, typical of continental break-up in the North. This makes the rift as one of the few locations on Earth offering a complete picture of the evolution of continental rifting (Molin and Corti, 2015). It is an ideal place to analyze the evolution of continental rifting since it exposes, along-strike, several sectors of

asynchronous rift development from continental rifting in the south, to incipient oceanic spreading in the north. This rift allows analyzing the time-space variations in deformation, volcanism during extension and associated hydrothermal activity (Corti et al., 2014).

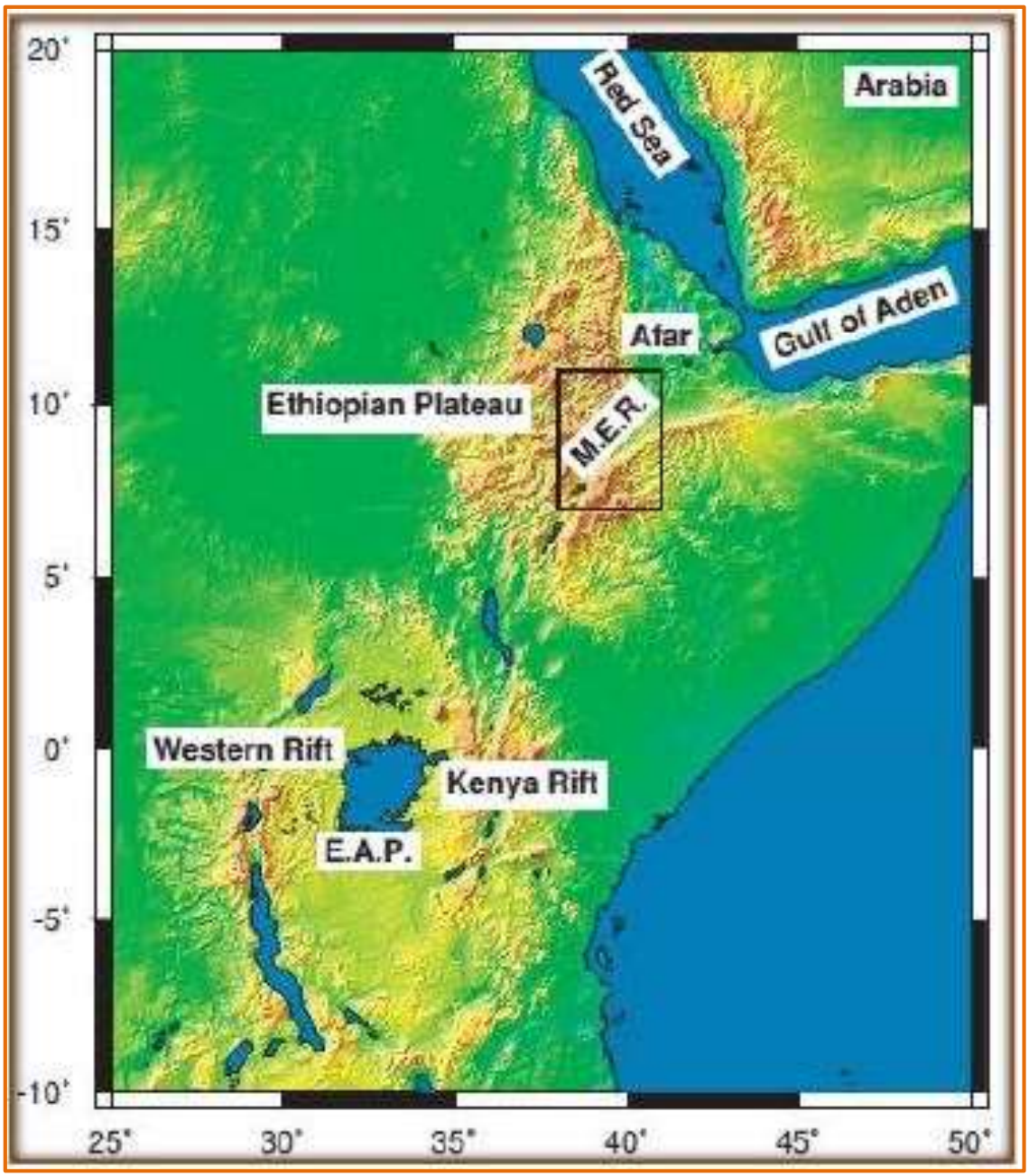

FIGURE 3.1: *Regional map of the East African Rift. E.A.P stands for East African Plateau and M.E.R for Main Ethiopian Rift on which the study area is located (Maguire et al., 2006)*

The MER is composed of three main different segments (Northern, Central and Southern), differing in terms of fault timing and patterns, and lithospheric characteristics (Mohr, 1983; Hayward and Ebinger, 1996; Bonini et al., 2005; Corti, 2009 cited in Corti, 2013). These segments of the MER are characterized by the occurrence of a typical bimodal magmatic

activity and two distinct systems of extensional structures: a system of NE-SW to N-S trending border faults and a system of NNE-SSW to N-S trending Wonji Fault Belt (WFB), which is en echelon arranged faults obliquely affecting the rift floor (e.g. Mohr, 1962, 1967, 1987; Gibson, 1969; Gidey Woldegabriel et al., 1990 and Corti, 2009). These faults developed in response to Miocene-recent motion between Nubia and Somalia plates (Corti et al., 2009). WFB is the active spreading axes formed during the Quaternary episode of tectonism after the development of the MER (Tadiwos Chernet, 2011). Boundary fault activity and absent axial volcano-tectonic activity are believed to mark an initial stage of rifting in the Southern MER, whereas inactive rift margins and focused tectono-magmatic deformation at the rift axis are thought to indicate an incipient break-up in the Northern MER (e.g., Agostini et al., 2011a; Corti, 2009; Hayward and Ebinger, 1996; Keir et al., 2013 cited in Molin and Corti, 2015). With more emphasis giving to the southern part of MER, which is a sector consisting of the study area, these different attributes of the three MER segments are discussed in the following sections.

The Northern MER is well thought-out to extend from the true Afar depression up to the Lake Koka region, where it is separated from the Central MER by the Boru Toru Structural high (Bonini et al., 2005). Although Northern MER, is thought to be magma-dominated showing how rift morphology develops through time (Corti, 2009); it is characterized by two distinct fault sets. These are NE–SW trending border faults on the boundaries of the rift, and a set of closely spaced NNE–SSW-trending faults (Hutchison et al., 2015). The main boundary faults in this region formed at about 10-11 Ma ago (Kazmin et al., 1980; Mohr, 1983).

The Central MER contains most of the Lakes Region, up to the Lake Hawassa area. It is bounded by the Yerer-Tullu-Wellel volcano tectonic lineament to the north and the Goba–Bonga lineament to the south and by the fault escarpments such as Munesa and Guraghe rift margins to the east and west (Tsegaye Abebe et al., 2010). The main boundary faults in the Central MER are well developed at the age of late Miocene–Pliocene age (Bonini et al., 2005; Tsegaye Abebe et al., 2010 cited in Molin and Corti, 2015) and are still seismically active (Hutchison et al., 2015, Samrock et al., 2018). In this sector of the rift, much of the active tectonic deformation occurs in the magmatic segments through NNE–SSW Wonji faults (Keir et al., 2006).

With respect to rift morphology, the southern MER, the focus of this study, is fault-dominated and the few geophysical data indicate the absence of significant magmatic modification of the crust/lithosphere in the sector. This rift margin is characterized by Scattered Quaternary volcanic activity (Corti et al., 2013; Ebinger et al., 1993; Dugda et al., 2005 cited in Molin and Corti, 2015). It extends south of Lake Hawasa into the ~300-km -wide system of basins and ranges. It is characterized by the major fault escarpments of Chencha to the western margin and Agere Selam to the eastern margin (Figure 3.2).

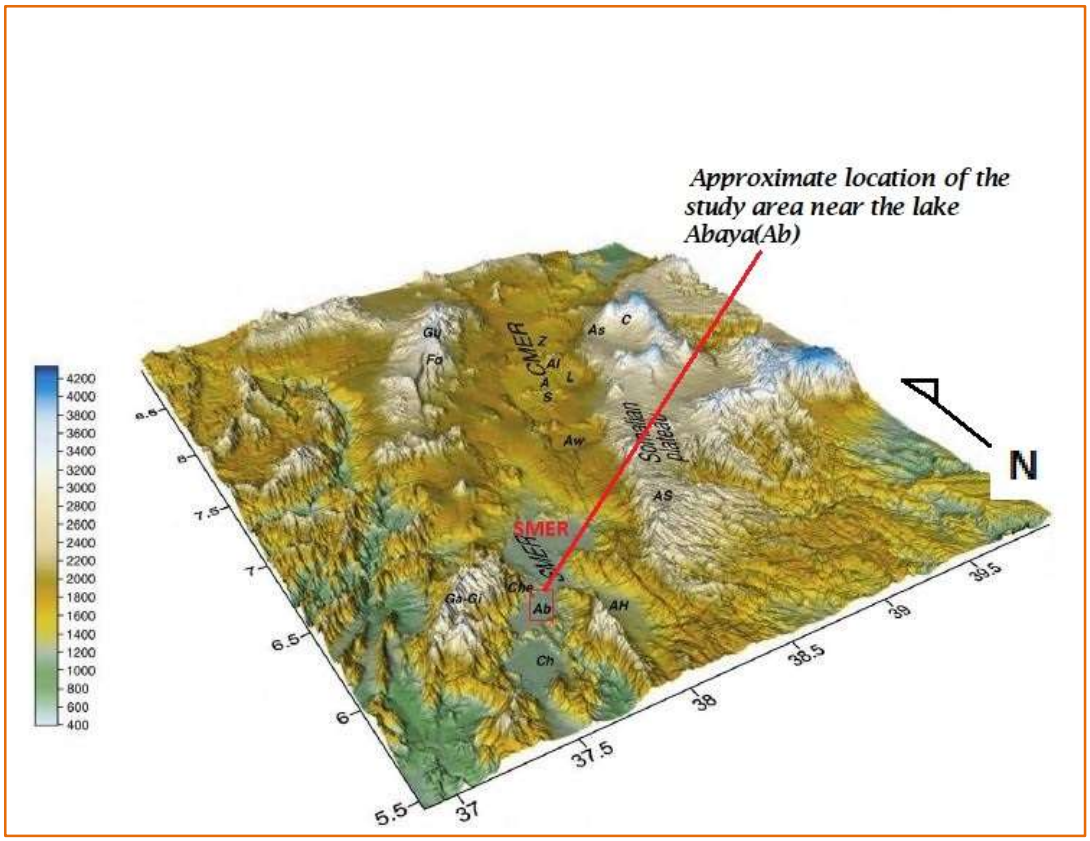

FIGURE 3.2: *Three-dimensional representation of the rift topography comprising SMER and showing the relative location of the study area (red polygon), the border faults (Che= Chencha, AS= Asela, GU= Guraghe and FO= Fonko escarpments) and Lake (Ab: Lake Abaya, Ch: Chamo); (adapted from Corti, 2009)*

The first extensional structures in Southern MER is developed as N-S trending Kenya Rift related structures at about 20–21 Ma and lasted up to 11 Ma (Corti, 2009). In the Southern MER, a few major boundary faults accommodate the largest part of recent and active deformation (Ebinger et al., 1993; Hayward and Ebinger, 1996 cited in Molin and Corti, 2015). In this rift sector, the Wonji faults are comparatively less developed than in the

Central and Northern MER, oriented around N–S, i.e. roughly parallel to the boundary fault systems.

Numerous quaternary rhyolitic volcanic centers are aligned along the WFB. Salwa Dore and Hako are thought to be the youngest volcanic centers in the southern main Ethiopian rift (Tadiwos Chernet, 2011).

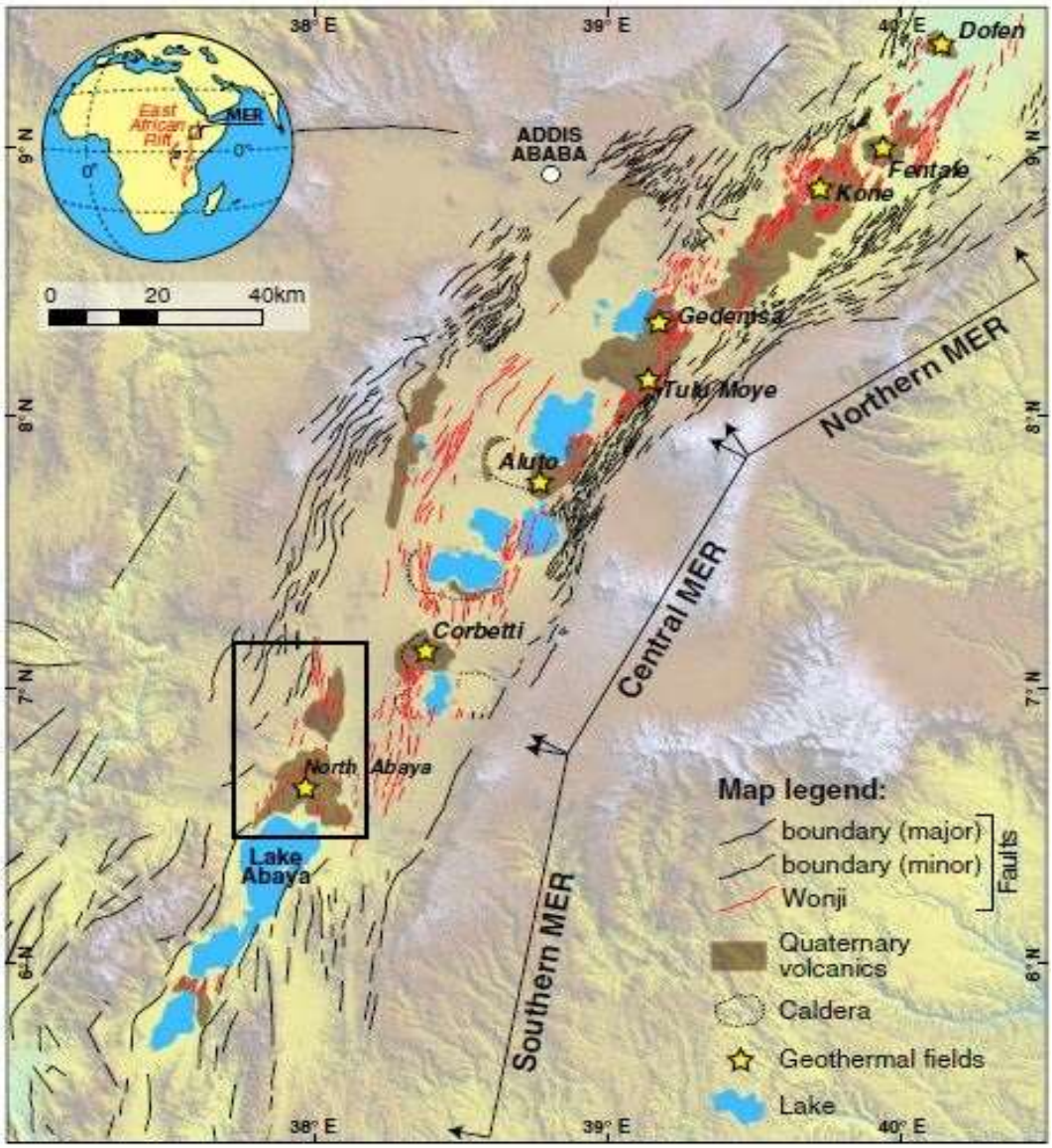

FIGURE 3.3: *Tectonic setting of the Main Ethiopian Rift; the black rectangle represent the current study area (Adopted from Minissale et al., 2017)*

3.2.2. Volcanism of the MER

An episodic magmatic activities has been took place in the MER that is mainly within the two geologic periods; Late Tertiary and Quaternary (Gidey Woldegabriel et al., 1990). The two main phases of volcanic episodes are experienced in the Southern sector of the MER. The pre-rift flood-basalt event is dated at about 45 Ma confirming that the Tertiary volcanic activity in the Southern MER started earlier than in the other MER sectors (Zanettin et al., 1978, Ebinger et al., 1993; Gidey Wolde Gabriel et al., 1990; Ebinger et al., 2001). During the Eocene to late Oligocene, volcanism started by the eruption of flood basalts that have generally been attributed to either one or two mantle plumes affecting the base of the lithosphere under Afar or the Afar to Northern Kenya rifts (Ebinger et al., 1993; Gezahegn Yirgu et al., 2006; Tadesse Alemu, 2012). This initial, mainly basaltic activity ended around 30 Ma (Zanettin et al., 1978). This was followed by a complex shield volcano activity (Kieffer et al., 2004). Many large shield volcanoes developed on the surface of the volcanic plateau after the peak of flood basalt emplacement from 30 to 23Ma (Ring, 2014).

After volcanic eruption that developed large shield volcanoes on the surface of the volcanic plateau, a second episode of flood basalt volcanism has been described in southern Ethiopia at 18 to 11Ma and in MER to Afar at about 11 to 10Ma (Bonini et al., 2005). This volcanic activity continued in the SMER during the Miocene up to 11 Ma, with eruption of basalts, trachyte, ignimbrite and rhyolites (Levitte et al., 1974; Zanettin et al., 1978 and Ebinger et al., 1993). Extensive late Miocene-Pliocene rhyolitic ignimbrites (~7-3 Ma) with intercalated minor mafic lavas were emplaced throughout the northern and central MER (Kazmin et al., 1980).

Cenozoic age in Ethiopia is of potential economic importance. Geothermal activity and groundwater resources are associated with the Cenozoic deposits (Ernst et al., 2010). More recent volcanism is associated with the development of the Rift Valley. Volcanic activity is concentrated within this structure and along the edge of the adjoining plateau. Volcanism has continued into the present time in the Afar region within small eruptive centers. The composition of the lavas produced ranges from basalt to siliceous types (Kazmin, 1980). Bimodal volcanic rocks with widespread flood basalts and subordinate felsic products such as lavas and pyroclastic strata were closely related with the WFB that formed in the rift floor during the Quaternary about ~ 1.6-1.8 Ma ago (Gidey WoldeGabriel et al., 1990). The presence of a complete magmatic differentiation series extending from a mildly

alkaline basaltic parental magma to comenditic and pantelleritic end members is seen in some segments of the WFB (Paola, 1986). This indicates the existence of magma beneath the WFB.

The volcanic activity in and around the Abaya geothermal field is typically marked by bimodal activities (Minissale et al., 2017). The first volcanic activity is constituted by rhyolitic centers characterized by the emission of large volumes of peralkaline lava flows, domes and pyroclastic deposits. These volcanic centers are common along the western rift margin at Hobitcha and Doguna volcanoes, although some acidic volcanoes are observed at the rift axis; Chericha volcano is an example (Figure 3.4). Very recent obsidian and pitchstone flows are located near the southern edge of the Hobitcha caldera, at Salewa-Dore and Hako volcanic centers. These latter centers probably represent the youngest rhyolitic activity in the area and are characterized by ongoing steam vents and steaming ground activity (Tadiwos Chernet, 2011 cited in Minissale et al., 2017). These are thought to host a shallow magma chamber that serve as the heat source for geothermal resource existing in the area. The second stage of volcanic activity is characterized by basaltic lava flows, scoria cones and phreatomagmatic deposits. The basalts are associated with the recent faults located in the western part of the rift valley. These faults are documented by NNE-SSW alignments of numerous scoria cones marking the main fault swarms (Corti et al., 2013 cited in cited in Minissale et al., 2017).

3.3. Geology of the Northern Lake Abaya area

The outcropping rocks in and around the Abaya geothermal field are mainly volcanic and volcano-sedimentary formations, mostly associated with the main rifting events (Tadiwos Chernet 2011; Corti, et al., 2013; corti et al., 2014; Minissale et al., 2017). The oldest volcanic products are represented by Oligocene (30–36 MA years old), pre-rift basalts of the Trap Series (Zanettin et al., 1978; Mohr and Zanettin, 1988 cited in Minissale et al., 2017). These units are overlain by Pliocene peralkaline pantelleritic Nazret ignimbrites and trachytic lava flows. These units are in turn overlain by sequences made of alluvial and rare lacustrine sediments, with interbedded pyroclastics and basalt flows of Pleistocene-Holocene age (De la Torre et al., 2007 cited in Minissale et al., 2017). According to Corti (2014), the Quaternary volcanic sequences are mainly composed of acidic rocks (e.g., pantelleritic ignimbrites, peralkaline lava flows and domes, obsidian and pitchstone flows)

and basic rocks. Basic products includes basaltic lava flows, scoria and phreatomagmatic deposits (Figure 3.4).

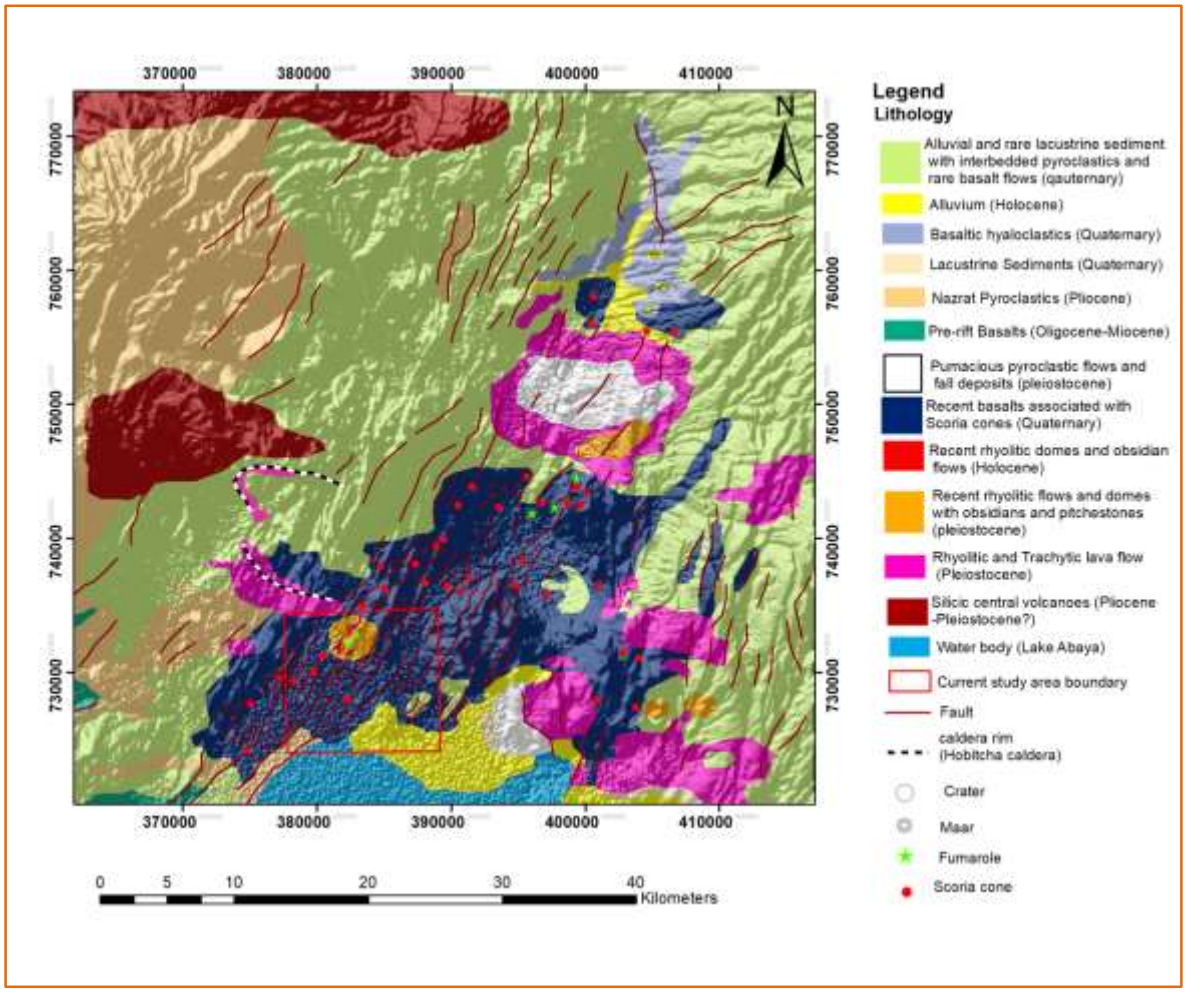

FIGURE 3.4: *Simplified geological map of the Wolaita Soddo area after Corti et al., (2014).*

3.4.Hydrogeological setting

The tectonic lake of Abaya makes the southern boundary of the study area. This lake has an area of about 1140 km^2 and mean depth of 8.6 m (Seleshi Bekele, 2001). The river Bilate to the northeast, Hamassa to the west, Gidabo to southeast, and Galana are the main perennial rivers entering Lake Abaya (Fassil Teffera et al., 2018). The Bilate which rises on the southern slopes of Mount Gurage runs mostly southward to drain into Lake Abaya at its northern shore. The Gidabo, which rises on the western slopes of the Bale Mountains, runs mostly southwards to drain into Lake Abaya at its northeastern tip after having passed the Gidabo flood plains. A third river is the Gelana, which rises at the western escarpment of the Rift Valley northwest of Bule Hora Town. The Gelana flows northwards through the Gelana Graben in the middle between eastern and northern slopes of the Amaro Mountains, before it enters the Bore swamps. It finally drains on the eastern side into the Lake Abaya.

These rivers carry from the adjoining highlands a lot of sediments into the lake as evidenced by the suspended clay and silt in the lake water which has given it the peculiar reddish-brown color (Fassil Teffera et al., 2018).

Groundwater flux ensures steady steam supply to maintain geothermal production in any geothermal field. Therefore, understanding the mechanisms enabling movement of groundwater from the recharge zone to and out of the reservoir system needs to be an important part of geothermal study. Geothermal fluids originate from groundwater moves through complex geological structural channels to reach the hot reservoir rocks. Though, the modes and mechanisms of flow of both steam in the geothermal system and groundwater are different due to their changes in physical state and pressure (Todd and Larry, 2005).

Groundwater flow is dependent on hydraulic gradient and intrinsic permeability of the transmitting medium. Groundwater moves through rocks which contain different transmissivity and porosity values that directly affect their water retention and transmission capacities. Many faults and fractures have been buried by either lacustrine sedimentary material or have been filled up during subsequent eruptions, reducing their transmissivities. The burying material always reduces the hydraulic conductivity causing ground water to move very slowly as compared to surface water. Aquifereous strata may be offset by fault systems making them barriers or channels of groundwater flow (Heath, 1983).

The domal uplift in Ethiopia created high hydraulic gradient from recharge areas to the rift floor (Tesfaye Tessema, 2017) where most of the geothermal fields are located. These are mountain Ranges located to the northwest and southwestern of Ethiopian rift that form the main recharge channels to the floor of the rift. The formation of water catchment areas in eastern and western escarpments has ensured a constant fluid supply to the geothermal areas. This is because both the eastern and western escarpment areas have high precipitation. The channels of this recharge system in the study area are regarded to be the NNE-SSW and the transverse NW-SE tectonic structures (Corti et al., 2013). The geological structures and volcanic series associated with the extensional tectonics are important for groundwater occurrence in the region due to their high permeability. The hydrography of the Soddo area appears to be strongly influenced by tectonics, in terms of both structure location as well as variations in tectonic rates (Corti et al., 2013). It is characterized by the channels both parallel and perpendicular to tectonic structures. The

hydrography is not yet developed in correspondence to fault scarps, likely as a consequence of recent scarp growth.

The study area is located on the western margin of the southern MER between the major escarpments of Chencha and Fonko-Guraghe (Corti et al., 2014). Therefore, Groundwater in the area is received from these catchment regions to the west of the rift. Water movement is mainly through underground channels formed by enhanced permeability of the regional faults. The main source of fluids in Lake Abaya geothermal system is therefore considered probably to be meteoric in origin (Minissale et al., 2017).

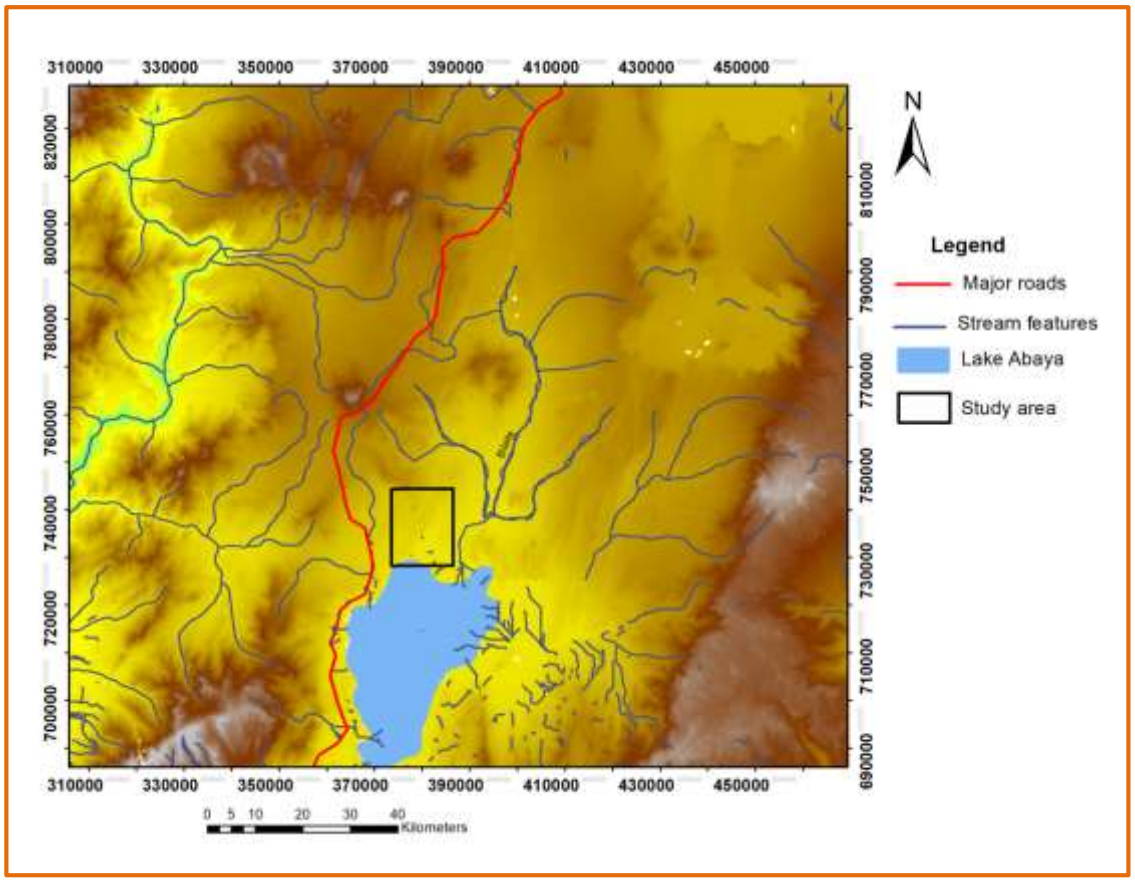

FIGURE 3.5: *Hydrogeological map of Abaya geothermal field*

3.5. Geophysical Background of the Northern Lake Abaya area

Geophysical investigation in the northern MER has pointed that there exists a strong tectono-magmatic modification of the crust and lithosphere beneath the WFB segments (e.g., Keir et al., 2006; Keranen and Klemperer, 2008 cited in Corti 2013). It highlights the Strong relations between the architecture and characteristics of the WFB and voluminous middle-to-lower crustal magma intrusion. The lithosphere in the northern sector of the MER, at the depth of immediately beneath the Moho has a low velocity and low density (Mackenzie et al., 2005). This is interpreted as the presence of hot rocks containing a small percentage of melt which may be the heat source for the geothermal fields in the area.

According to Samrock et al. (2015), the 3-D inversions of the observed Magnetotelluric (MT) data from Aluto reveal the typical electrical conductivity distribution of a high-enthalpy geothermal system, which is mainly governed by the hydrothermal alteration mineralogy. From this source, no evidence has been found for an active deep magmatic system under Aluto rather the occurrence of melt is predominantly at lower crustal depths

along an off-axis fault zone a few tens of kilometers west of the central rift axis. This is interpreted as the deforming source is most likely situated within the shallow hydrothermal system of the Aluto-Langano geothermal field. MT data from the work of Samrock et al., (2015) concluded that the main occurrence of magma and melt in the Lake District of the MER is prevalently at lower crustal depths along the Silte-Debre_Zeyit fault zone (SDFZ) west of the main rift axis and not at the seismically active faults along the central rift axis. Samrock et al., (2018), presented a crustal-scale electrical conductivity model for a magmatic segment in the Ethiopian Rift, derived from magnetotelluric data. From this source, the electrical conductivity model presents the 3-D image of a magmatic-hydrothermal system in the MER. This model shows that melt migrates along preexisting weak structures (fault-controlled transport of melt) and is stored in different concentrations on two major interconnected levels, facilitating the formation of a convective hydrothermal system.

Gravity analysis in Donga volcano, close to the study area indicated the existence of a large magmatic intrusion at a depth of 10 km (Mahatsente et al., 1999 cited in Minissale et al., 2017). The study was found to be analogous with what was observed beneath the Wonji magmatic segments in the northern MER (Keranen et al., 2004 cited in Minissale et al., 2017).

Mohammednur Desissa and Yohanes Lema **(**2006) did MT soundings around the Lake Abaya geothermal field. These surveys were conducted to outline the regional and subsurface structure plus the possible heat source for the geothermal resource in and around the Lake Abaya geothermal field.

Modeling and interpretation of the work of Mohammednur Desissa and Yohanes Lema (2006) was with the 1-D inversion method. Modeling is considered up to a depth of about 3km, where best fit between the data and model parameters were observed for all sites. The geo-electrical models are presented at two different depth levels 500m and 2000 m for each line. MT survey measurement points on geophysical profile lines one and two lies exactly on the current study area (Figure 4.16). Line one is on the southernmost part of the study area close to the geothermal manifestation at the lake shore of Abaya. Line two is on the northernmost part of the study area close to the young silicic centers (Salewa Dore rhyolitic dome). Coordinates for the MT survey lines and points are presented in Appendix VIII.

Profile line one has four sites (Figure 3.6) namely; site 001, site 002, site 003 and site004. Site 001 is characterized by low resistivity starting from surface and getting wider at around 1200m depth. The site was observed between hot springs which are favored by structurally weak zone (low resistivity). According to this work; the very low vertical resistivity along the profile line one, could indicate the up flow zone through which hydrothermal fluids migrate to the surface. Site 002 shows relatively low resistivity (10-15Ωm) up to a depth of around 500-600m and then it gets very low up to 1500m. Resistivity signature below 1500m is relatively high, which could be due to volcanic intrusion. Sites 004 and 003 are characterized by very high resistivity starting from surface up to 500m depth, which could be due to extrusive volcanic rocks. Below this depth, resistivity under site 004 becomes relatively low while under site 003 it is very low, which might be related to extremely altered rocks or related to magmatic brine (saline water).

Profile Line two has three sites (Figure 3.7) namely; site005, site006 and site007. Resistivity signature along line two shows different characteristics compared to line one. The shallower part is mapped by relatively high resistivity except at site 005, where low resistivity is observed up to 100 m. The conductive anomalous zone is mapped at central part of the line below 1 km depth under sites 005 and 007. This is interpreted as the conductive anomalous zone show the existence of deep seated heat source. Relatively low resistivity value between 500 and 1000m depth is observed at site 006.

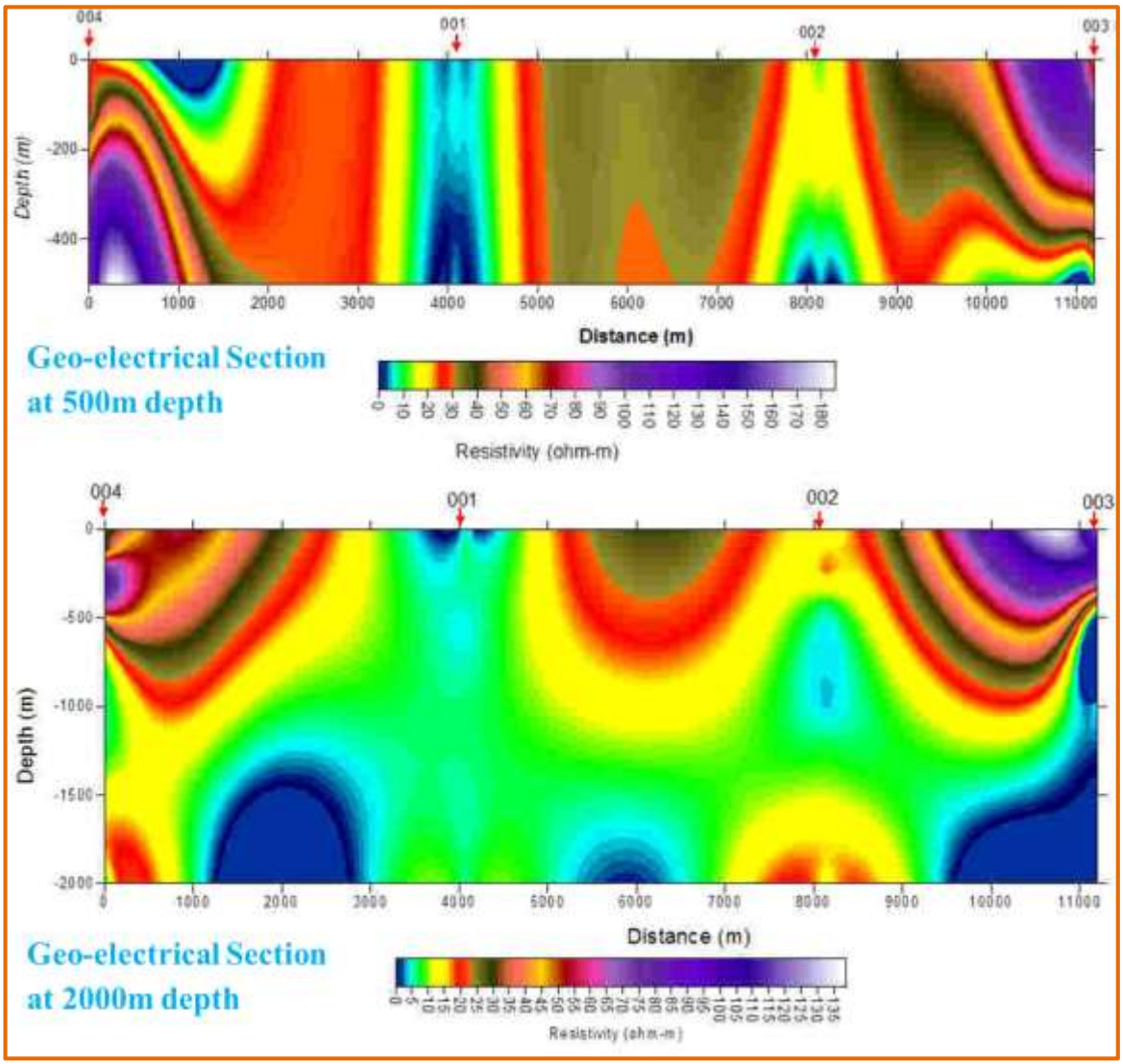

***FIGURE: 3.6**: Geoelectric section along profile line one (Mohammednur Desissa and Yohanes Lema 2006)*

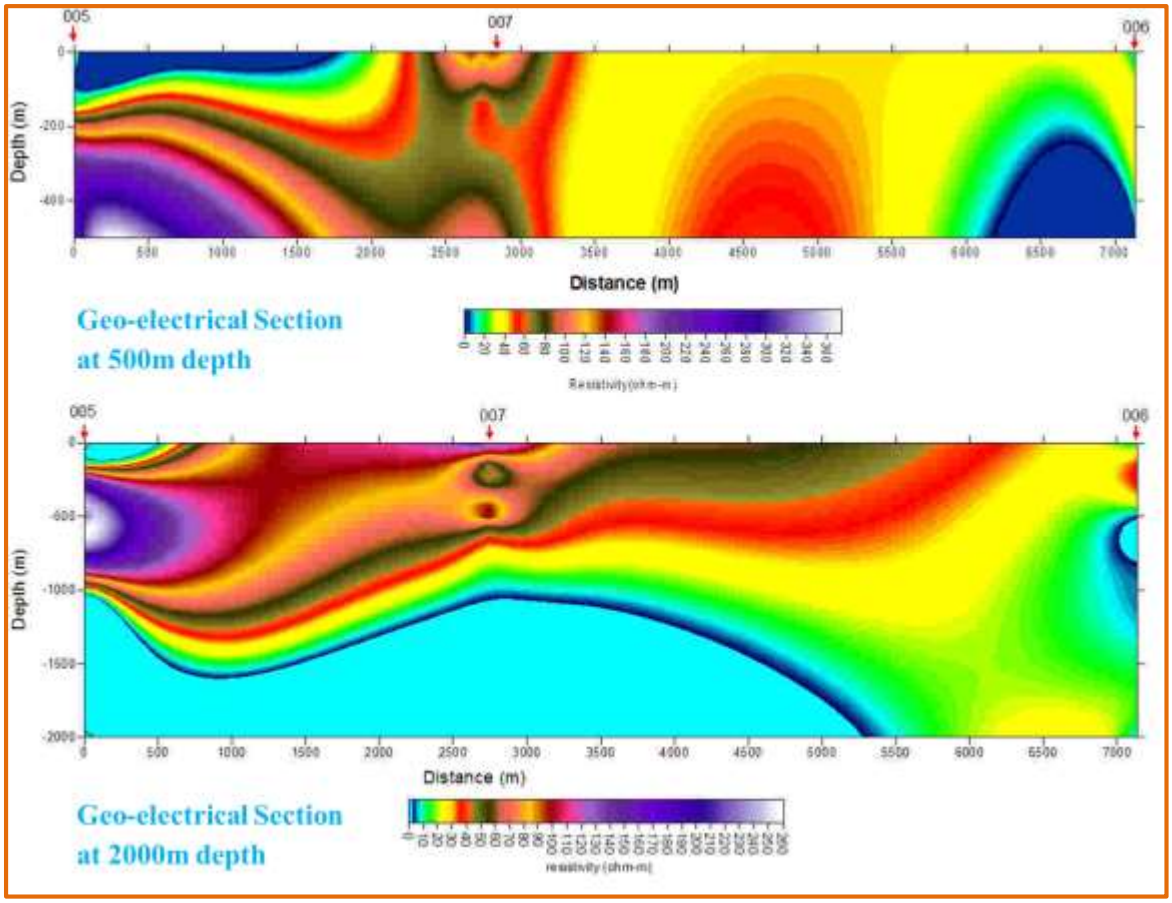

***FIGURE 3.7**: Geoelectric section along profile line two (Mohammednur Desissa and Yohanes Lema 2006)*

4. Research results and interpretations

4.1. Geology of the Northern Lake Abaya geothermal field

The local stratigraphy (Figure 4.17) in the area includes both volcanic rocks and continental sedimentary rocks. The exposed volcanic units are ignimbrites, trachyte, pumiceous pyroclastic rocks, basalts and rhyo-obsidian flows. The pyroclastic rocks, basaltic lava flows and sedimentary deposits form flat lying layers in the faulted terrain while the more silicic lavas form high standing volcanic eruptive centers. The sedimentary units include Pleistocene volcano-sediments, Holocene lake sediments and recent alluvium and fluvial deposits (Tadiwos Chernet, 2011). The youngest basalts occur along the Wonji Fault Belt which is associated with scoria cones.

4.1.1. Lithology and Petrographic Descriptions

As it has been discussed above, different lithologies are identified according to field mapping and the analysis from petrography methods. Rock units that were identified accordingly ignimbrite, trachyte, pumiceous pyroclastic flow and fall deposits, basalts, scoria, rhyolitic lava dome and obsidian flows and alluvial and lacustrine sediments. A detail description of the rock units follows.

4.1.1.1. Ignimbrite

The ignimbrite unit is exposed in northern (Hobitcha Caldera), south and southeast (Chewkare Graben) of the study area.

A succession of ignimbrites outcropped on south part of the study area (the west of Lake Abaya) is fault forming defining the western margin of the Chewkare Graben (Figure 4.1A). Chewkare Graben is an approximately 10km wide axial graben partly occupied by the northern tip of Lake Abaya (Tadiwos chernet, 2011). This Ignimbrite rock unit is brownish- grayish green in color and crystal rich. It contains rhyolitic and basaltic fragments of reddish and grey color, probably of xenocrysts. This unit undertakes heavy alterations associated with hydrothermal activities. It is found overlain by pumice fall deposits and lacustrine sediments. In some outcropped part, the topmost part of this unit is covered by recent basaltic flow (intruded by basalts). Here recent basalts have a continuous cover and faults are not large enough to expose what is below.

The succession of ignimbrite unit exposed in the southeastern part is a greyish to black in color and shows fiamme. It appear vesiculated in its upper part and compact near the base. This unit grades upwards into a dark brown tuff and the uppermost part is constituted totally of poorly consolidated ash and pumice. Pumiceous deposits is found overlain this unit where there exist no clear separation between them.

Another variety of ignimbrite is found in the northern most part of the study area. This unit is associated with Hobitcha Caldera which is brown, lithic rich and weakly welded ignimbrite. It is exposed interstratified with basalts. Such varieties of ignimbrite also crop out on the south eastern part of the study area. The fractures and minor joints are observed in this rock formation. An average thickness of 150 m is recorded from field observation.

Three samples that are collected from the outcropping ignimbrite are prepared for thin section petrographic analysis (ABD-13; Figure 4.2, F118; Figure 4.3 and F1110; Figure 4.4). Accordingly, the rock is with abundant phenocrysts and clasts. Sanidine is the most abundant phenocryst that is shiny, lath-shaped with perpendicular cleavage (Figure 4.2A). Numerous clasts of various origin and color are also exists which are mostly predominated by grey-white and black.

On sample number ABD-13, phenocrysts, lithic fragments, opaque minerals, volcanic glass and trace amount of mafic minerals are present. 3- 4 % Quartz and 9-10 % sanidine exists as phenocrysts. Quartz show fracture system and overgrowth of it on sanidine is also observed (Figure 4.2A). Twinned sanidine exists both as phenocrysts and as lithic fragment. Volcanic glasses constitute the high percentage composition (72-75%) being the groundmass and shows flow pattern under PPL. Lithic fragments (10-12 %) contain mafic minerals (trace amount of pyroxene and amphibole, Figure 4.3), quartz, opaque minerals (2-3%), volcanic glass and sanidine.

On sample number F1110, volcanic glasses are the groundmass of the rock sample with high percentage of modal composition (67-73%). The phenocrysts are 8-10% sanidine, 4-5% opaque minerals and 3-4% quartz. The lithic fragments (9-10%) constitutes of opaque minerals, fine grained sanidine, quartz and trace amount of mafic minerals. Phenocryst of amphibole is found in trace amount probably is from xenocrysts observed in hand specimen of this rock sample (Figure 4.1).

Abundant amounts of volcanic glass as ground mass (70-75%), phenocrysts, lithic fragments, opaque minerals and trace amount of mafic minerals are found to exist in the rock sample number F118 under thin section. The phenocrysts are 10% sanidine, 3-4% Quartz, 2-3% alkali feldspar. Trace amount of large mafic minerals which is amphibole (Figure 4.3A and 4.4D) is also present. This minute amount of amphibole is slender shape surrounded by groundmass of volcanic glass. This crystal shows dark to brownish extinction color. The crystal is the host for quartz and other mafic minerals.

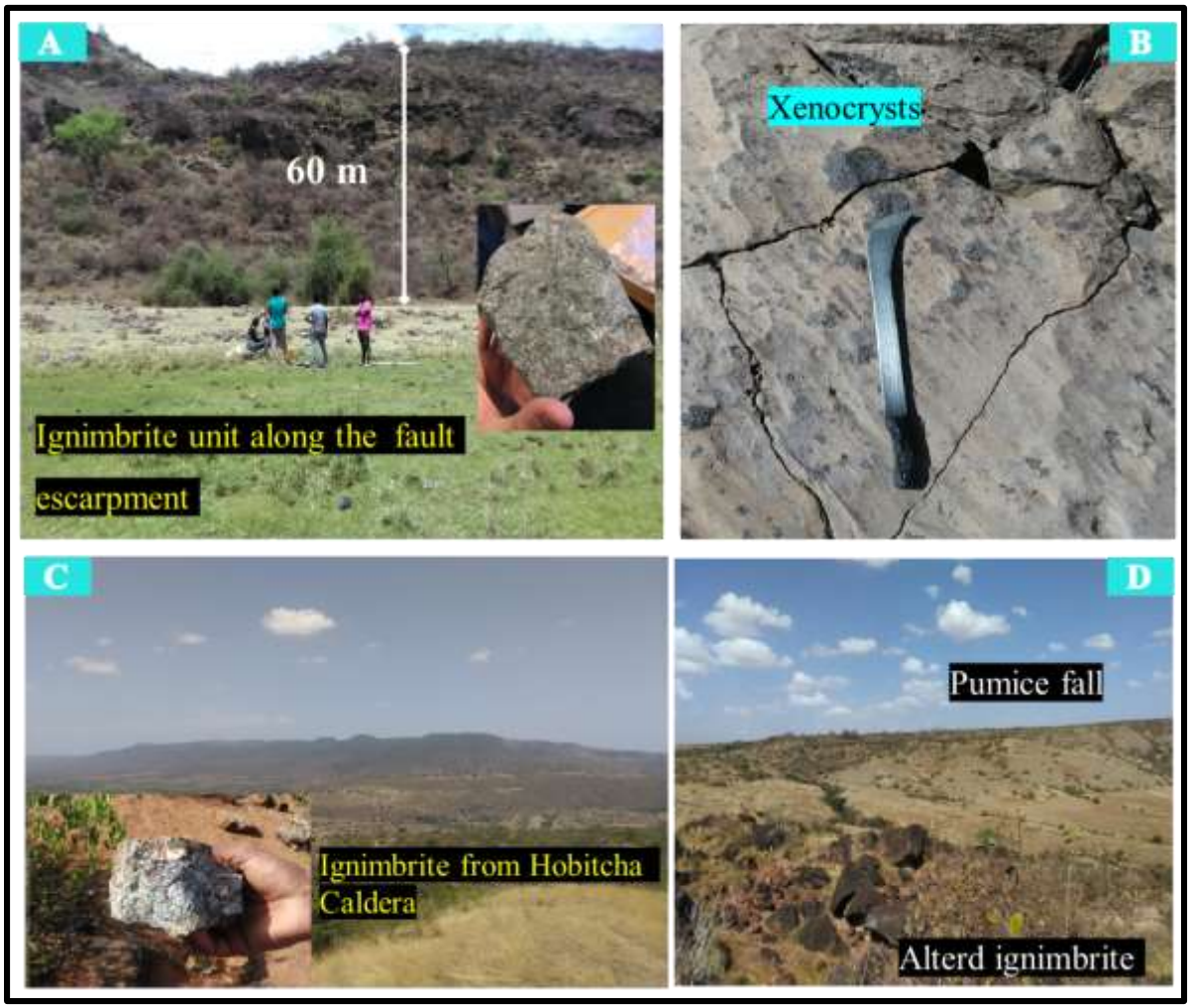

FIGURE 4.1: *varieties of Ignimbrite units from the study area* ***A.*** *Dark grey dense ignimbrite along the fault escarpment* ***B.*** *Ignimbrite exposed on river cut close to hot springs containing xenocrysts* ***C.*** *Ignimbrite from Hobitcha with abundant rock fragment (basalts) and* ***D.*** *Ignimbrite from the main thermal manifestations that is heavily altered to reddish-orange color and cover by pumice fall on top*

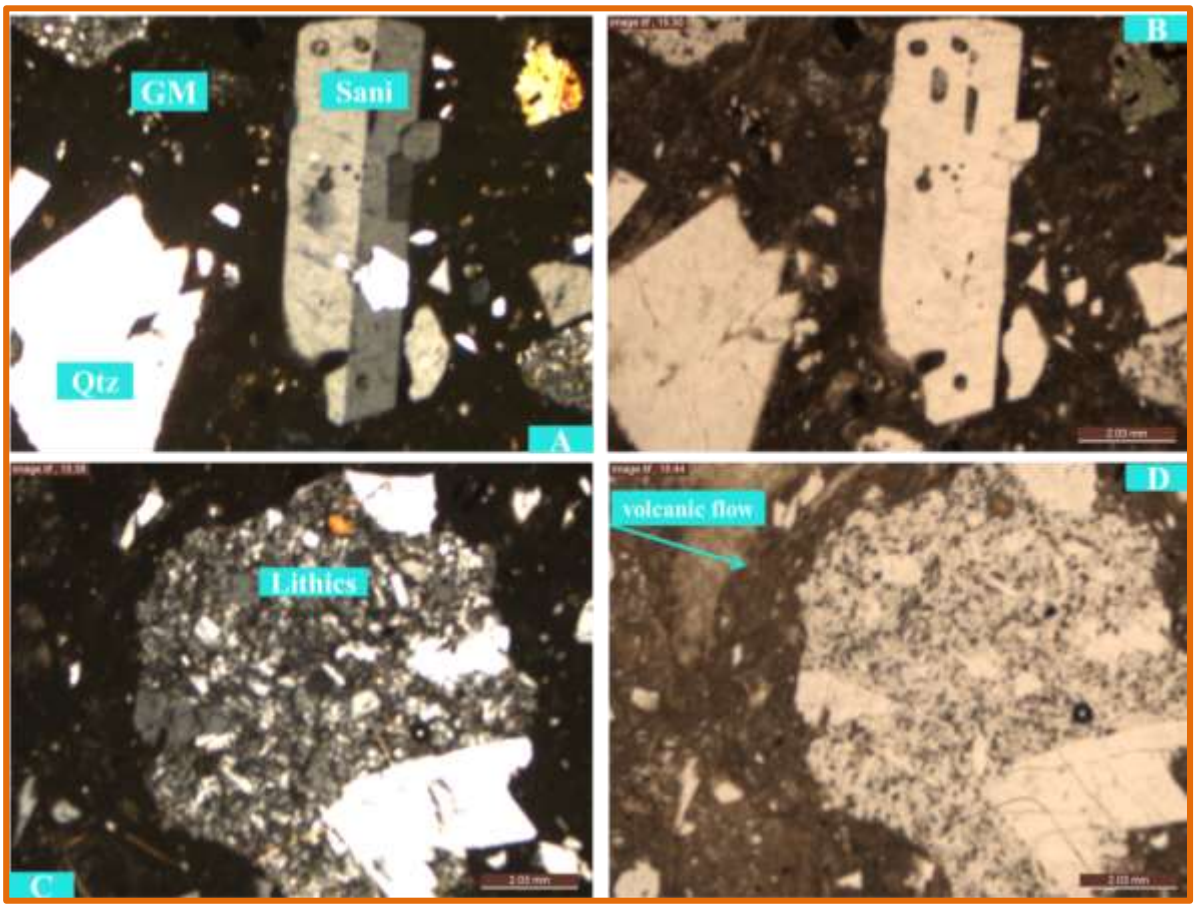

***FIGURE 4.2**: Microphoto picture of Ignimbrite sample; ABD-13 under optical microscope in XPL (**A & C**) and PPL (**B & D**) view. The labels stands for; GM – groundmass, Sani- sanidine and Qtz - Quartz; The photo taken at 4X magnification*

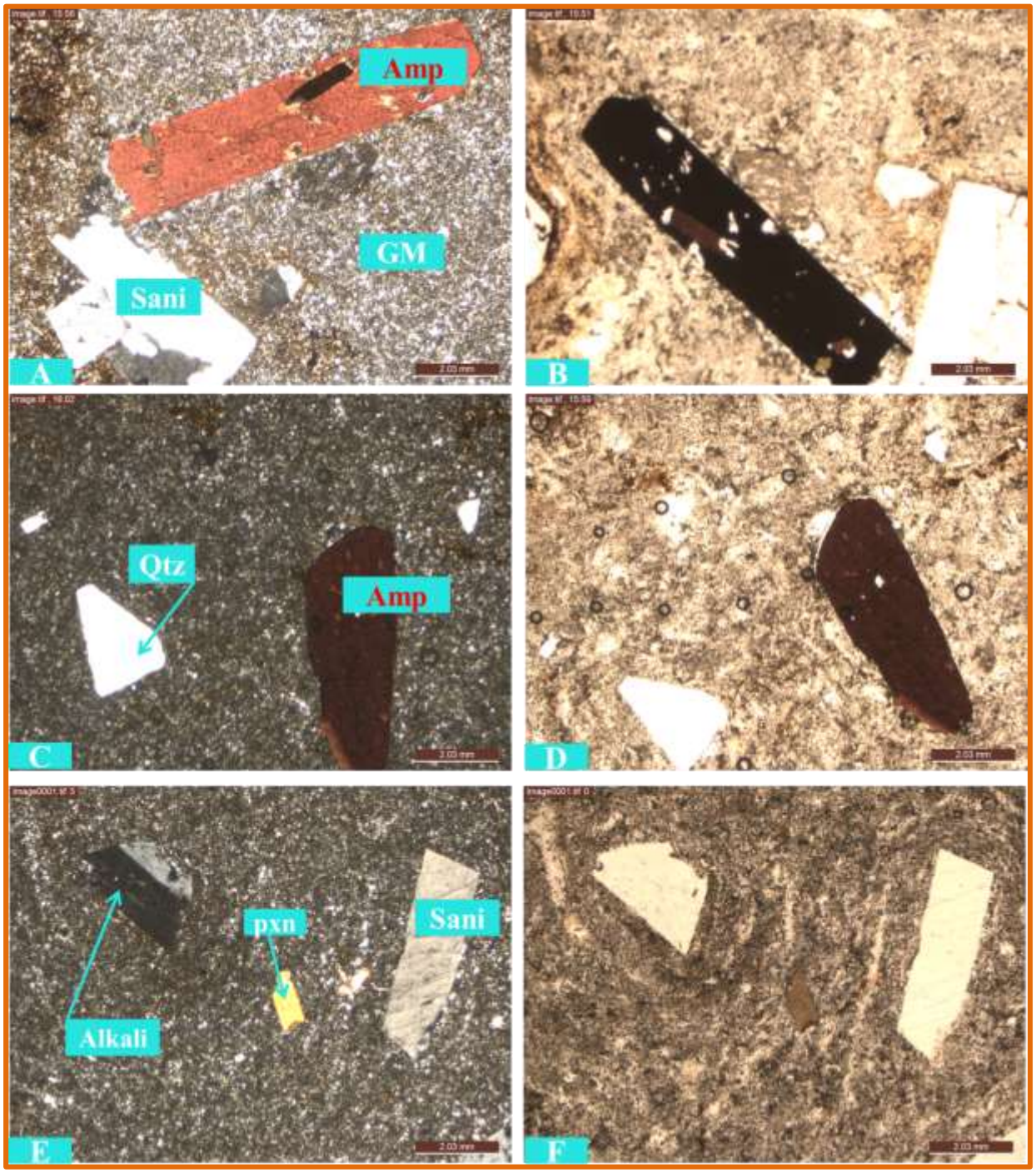

FIGURE 4.3: *Microphoto picture of Ignimbrite sample; F118 under optical microscope in XPL (**A, C & E**) and PPL (**B, D & F**) view. The labels stands for; GM – groundmass, Sani- sanidine, Pxn – clinopyroxene, Amp – amphibole, Alkali- alkali feldspar and Qtz - Quartz; The photo taken at 4X magnification*

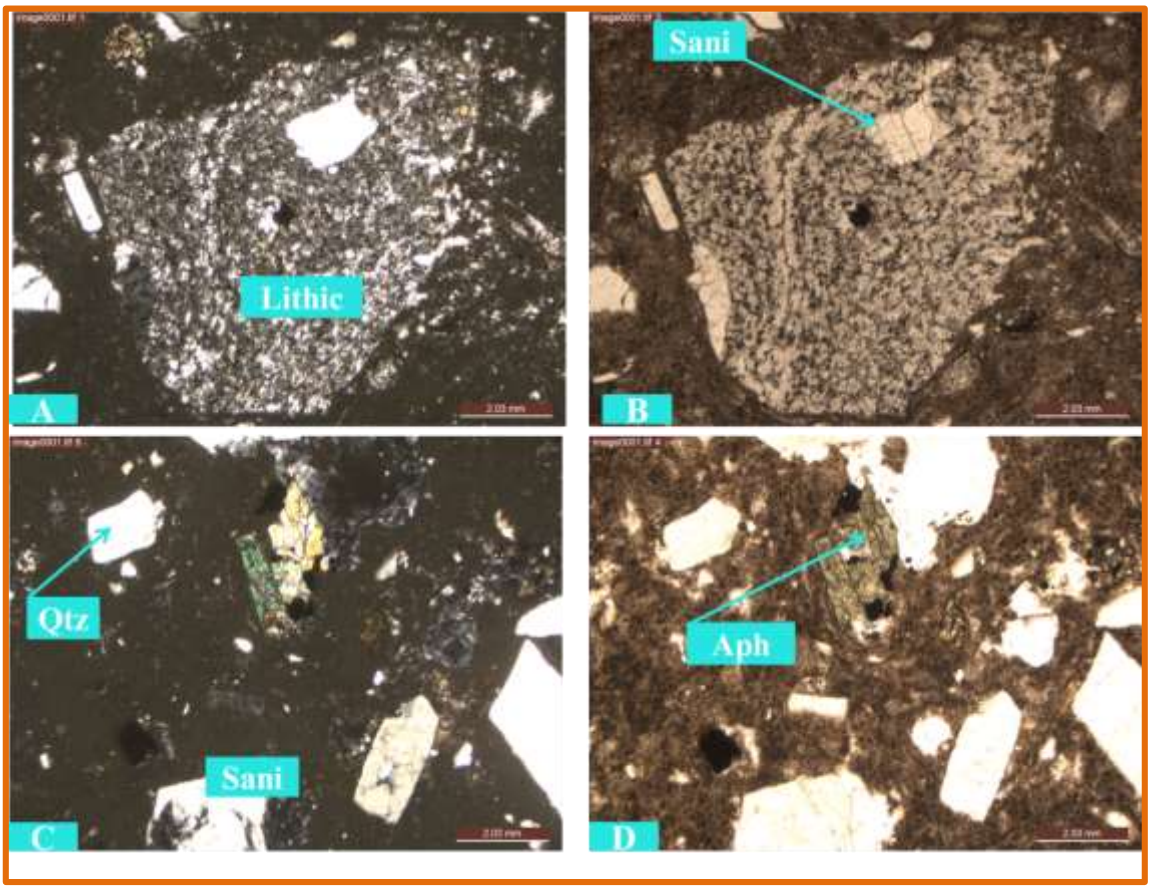

***FIGURE 4.4**: Microphoto picture of Ignimbrite sample; F1110 under optical microscope in XPL (**A & C**) and PPL (**B & D**) view. The labels stands for; Sani- sanidine, Lithic-lithic fragment, Aph- amphibole and Qtz - Quartz; The photo taken at 4X magnification*

4.1.1.2. Trachytic lava flow

Trachyte is exposed in between the Hobitcha caldera and the recent rhyolitic domes (Hako and Salewa Dore). On the hand specimen, this rock unit is pale grey-pink in color (Figure 4.5) with really shiny when exposed to light source. Reddish to pinkish color of this rock is probably associated with hydrothermal alteration. It is very crumbly, not well consolidated and thus easily brakes into pieces.

***FIGURE 4.5**: Trachyte from the study area*

Two samples collected from the outcropping trachyte are prepared for petrographic analysis (ABD-01; Figure 4.6 and ABD-06; Figure 4.7). Accordingly, the rock show abundantly large phenocrysts of feldspar, lath-shaped and with a well-defined cleavage. The phenocrysts are up to 3-4mm in size surrounded with fine grained groundmass.

On sample number ABD-01, Sanidine is abundantly (37-40%) found as both phenocrysts and groundmass. This mineral shows Carlsbad twinning as it is demonstrated by the contrasts of light and dark color in crossed polarized light (Figure 4.6A). The fine grained matrix surrounding it allows clear distinction of its boundaries and shape. The groundmass in this rock sample constitutes sanadine, 2-3% quartz, 4-7% opaque minerals (Fe-Ti oxides), 11-14% orthoclase (k-feldspar), 5-6% plagioclase and 5-6% volcanic glass. Trace amount of Pyroxene and Olivine microcrystals are also present. Pyroxene shows a clear zonation. Intergrowth of olivine on sanidine is found showing random fracture system with no cleavage (Figure 4.6F).

Sanidine mineral is abundantly found as large phenocryst (high modal abundance 37-40 %) on sample number ABD-06. At 10x magnification some crystals of the sanidine is too large for a complete view but the fine grained matrix surrounding it allows clear distinction of

its boundaries and shape. It shows brownish-pink color (Figure 4.7A) under crossed polarized light probably associated with hydrothermal alteration. Other phenocrysts are 11% orthoclase (k-feldspar), trace amount of pyroxene and plagioclase. Orthoclase shows simple twinning. Plagioclase shows polysynthetic twinning and slightly alteration on the crystal surface of the mineral as it is seen under XPL (Figure 4.7E). The groundmass contains 11-15% volcanic glass, 7-8% quartz, 6-7% opaque minerals and trace amount of plagioclase. Pyroxene and Olivine microcrystals are also found in minute amount. Pyroxene shows intergrowth on existing phenocrysts of orthoclase (Figure 4.7G).

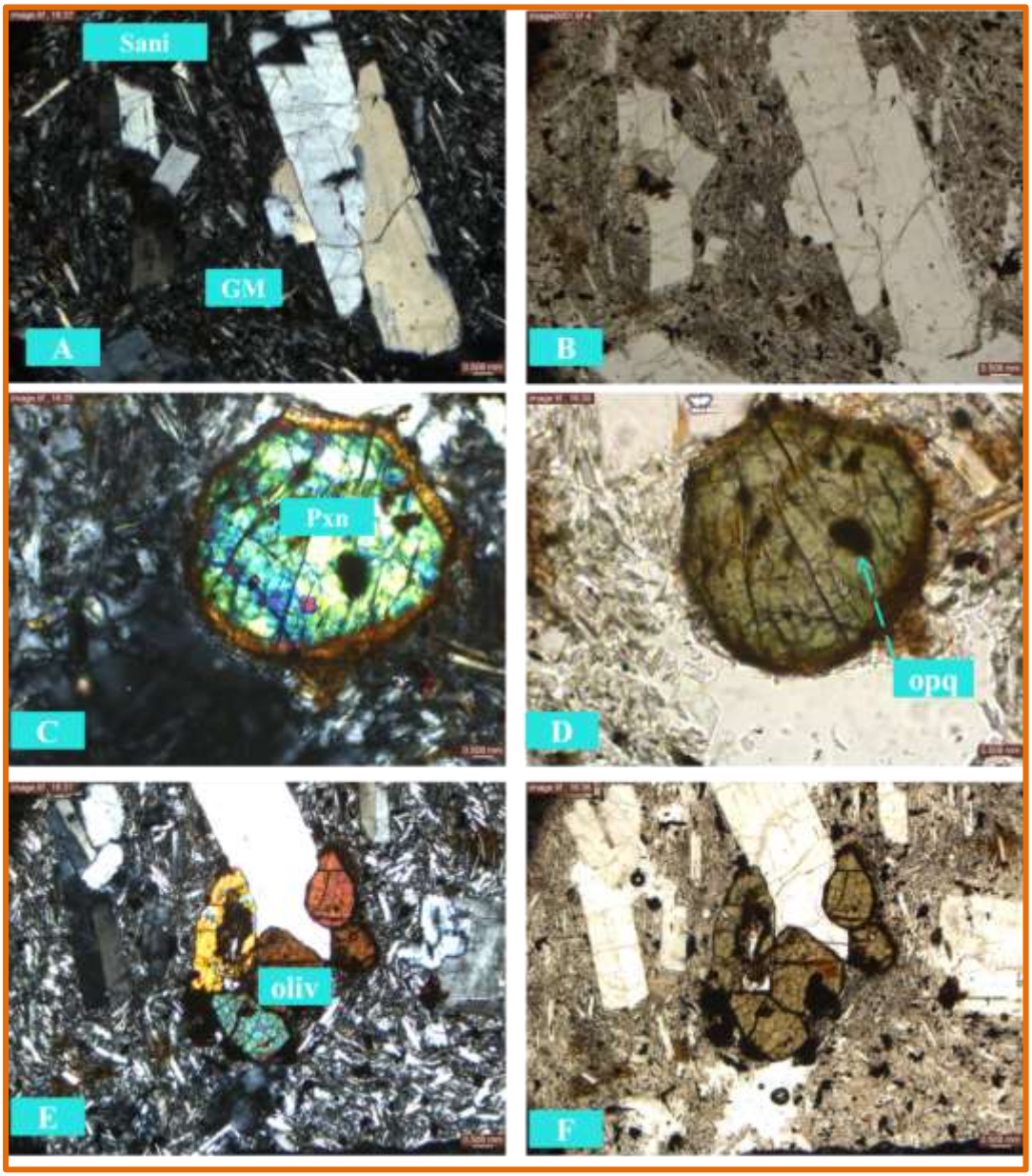

***FIGURE 4.6**: Microphoto picture of Trachyte sample; ABD-01 under optical microscope in XPL (**A, C & E**) and PPL (**B, D & F**) view. The labels stands for; Sani- Sanidine, GM-groundmass, Oliv – Olivine, Pxn - pyroxene and Opq -Fe-Ti Oxides; The photo taken at 4X magnification*

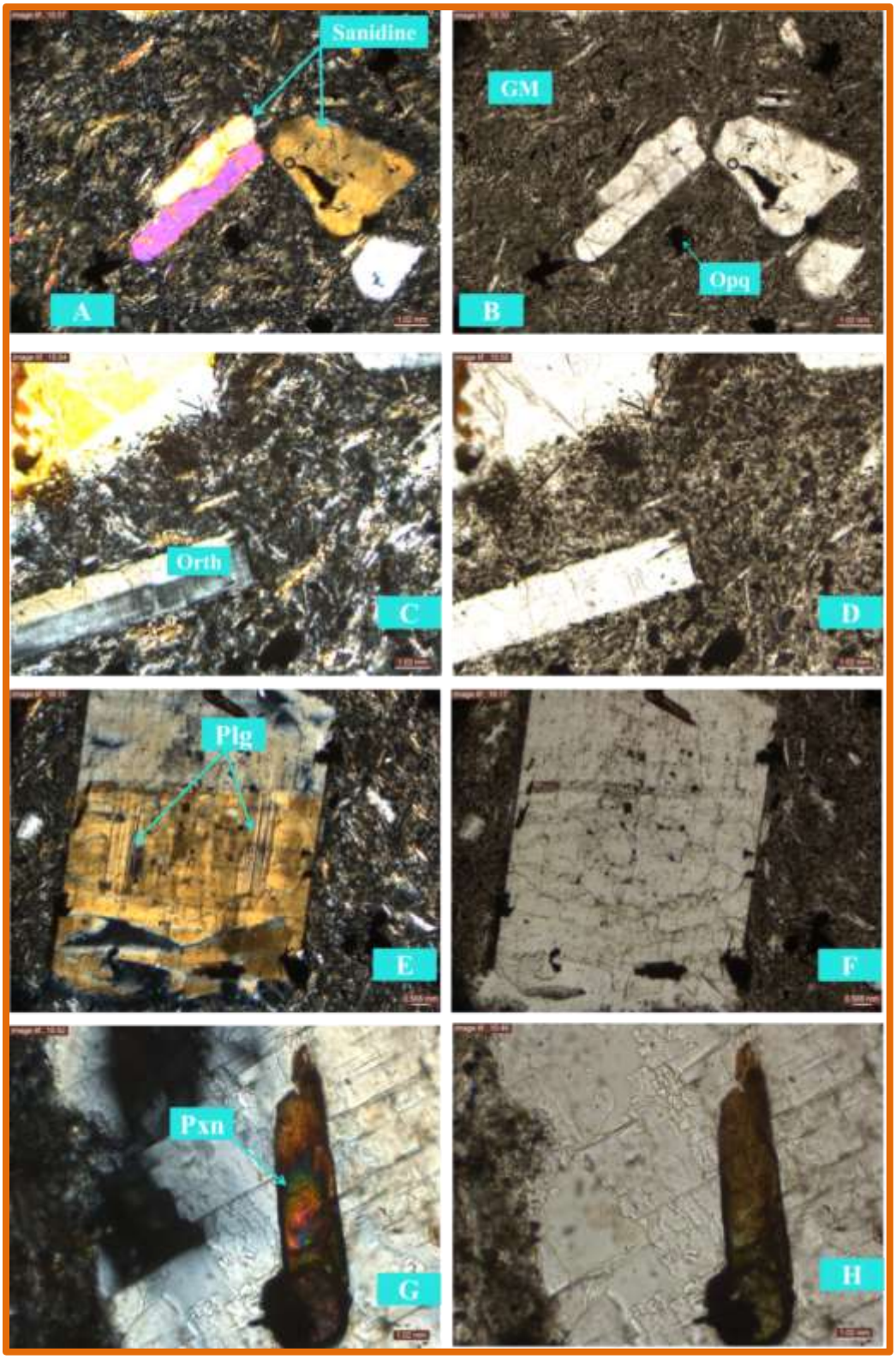

***FIGURE 4.7**: Micrographic pictures of sample ABD-06, in pane polarized (**B, D, F and H**) and crossed polarized (**A, C, E and G**) light magnified 4X. Plg = plagioclase, Opq = opaque minerals, GM = groundmass, Pxn = pyroxene and Orth = orthoclase*

4.1.1.3. Pumiceous pyroclastic flow and fall deposits

The pumiceous pyroclastic rocks consist of flow deposits with different grain size from very coarse grained pumiceous blocks of lava to fine grained ash deposits with minute amounts of rock fragments. The rock fragments include fragmented obsidians, basalt and lacustrine sediments (siltstones, claystones and sandstones). Many layers of fall deposits can be found intercalated with fragmented obsidians. They are exposed in the north, south and south eastern part of the study area overlying the ignimbrite units. These units are characterized by pale grey color, moderately welded, slightly-heavily weathered and show variations in vertical thickness.

Field observations made at different outcrops of this unit have shown that the unit is composed of several diverse layers. Thin layer of ash deposits are found interlayered with pumice units exposed by a quarry southeast of the study area (Figure 4.8A). This quarry is found helpful to measure a 17m thickness of layered pumiceous pyroclastic rocks. The lowest layer is about 12m thick and is composed of coarse unwelded pumice which sometimes measures to 2cm in grained size. Overlying this is a thin layer of ash deposits. Then, the pumice with 4m thickness comes on top. This last pumice layer is slightly weathered and intercalated with lacustrine sediments.

On the way to Salewa Dore road cut, pyroclastic flow deposits are outcropped stratified with different rocks. A thickness of approximately 20m layering of pumice, ash and basalt is observed (Figure 4.8B). The lowest layer is about 14 m thick basaltic lava flow exposed by river cut. The next layer is a 5m thick layer of massive gray to reddish ash containing minor amounts of pumice fragments. The topmost layer consists of 11m thick, poorly sorted and unwelded pumice with other rock fragments (obsidians, scoria).

The pyroclastic flow deposits are also exposed around the recent rhyolitic domes (Hako and Salewa Dore) stratified with pitchstones, obsidian lava flows, basalts and lacustrine sediments. Stratification of this unit with ignimbrite is also common around the main thermal manifestation close to the Lake Abaya (Figure 4.8 C and D). This unit is observed forming pumice cone in some area south of the Hako dome and south most of the study area as well.

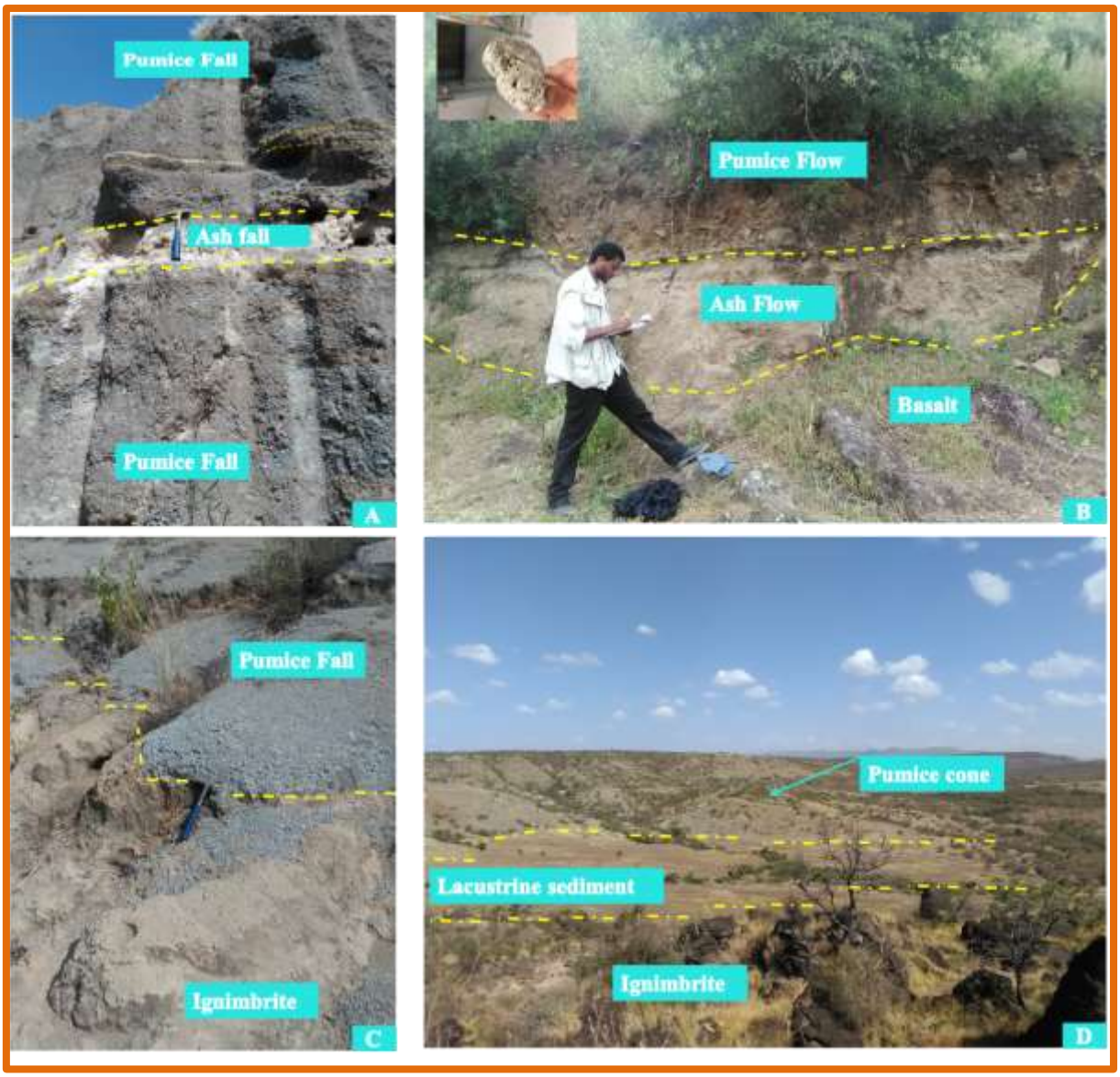

FIGURE 4.8: *pumice and Ash deposits showing interbedding with different types of rock units. The ash flow that overlay the basalt show increment in vertical thickness from 0.4 m to 1 m*

4.1.1.4. Basaltic lava flows

Basaltic lava flows covers larger portion of the study area. It forms both the gentle slope and steep cliffs along fault exposures. These units are the results of fissural eruption of low viscosity magma (Tadiwos Chernet, 2011) which overlie the pumice and ash deposits and underlie intensely denuded lacustrine sediments in some the study area. It is clearly observed that the whole formation has been intensely affected by extensional tectonic activities.

Two varieties of basaltic unit are found in the study area. One is very fine grained (aphyric texture), massive and hard which is mostly dissected by dense faults (Figure 4.9B). This variety of basaltic unit is probably from the first basaltic eruptions at least in some part of the studied area. Thickness of 30 to 40 m is measured for this unit in some parts of the area exposed by faults. The thickness of these basaltic formation decreases away from the Salewa Dore -Hoko area both in the east and west directions.

The other varieties of basalt (porphyritic basalt flow) are associated with scoria cone. It is highly vesicular in texture and large vesicles with irregular shapes on the surface of the flow are common features to this variety (Figure 4.9A). Abundant and randomly distributed feldspar phenocrysts measured up to 8mm are observed. Some vesicles have been partly filled with minerals most likely calcite. This flow is separated from the underlying one by a 2-3 m layer of scoriaceous material at the western and eastern faults bounding the Salewa Dore -Hoko graben.

On hand specimen this rock sample is fine grained dark/black igneous unit with large stretched vesicles. Five samples that are collected from the outcropping basalts in the study area are prepared for petrographic analysis (ABD-16, Figure 4.10). Accordingly, the rock shows dark/black fine groundmass with large phenocrysts (up to 8mm in size) of plagioclase. Under optical microscope thin section sample number ABD-16, the groundmass consists of olivine, plagioclase, opaque minerals and void spaces. The phenocrysts are large crystal of plagioclase and moderate size olivine and pyroxene. Trace amount of sanidine is also found. Few phenocrysts are visible with anhedral habit. The mineralogy of most of the basaltic samples suggests an olivine composition except for their different degree of porphyricity.

***FIGURE 4.9**: varieties of basaltic units from the study area*

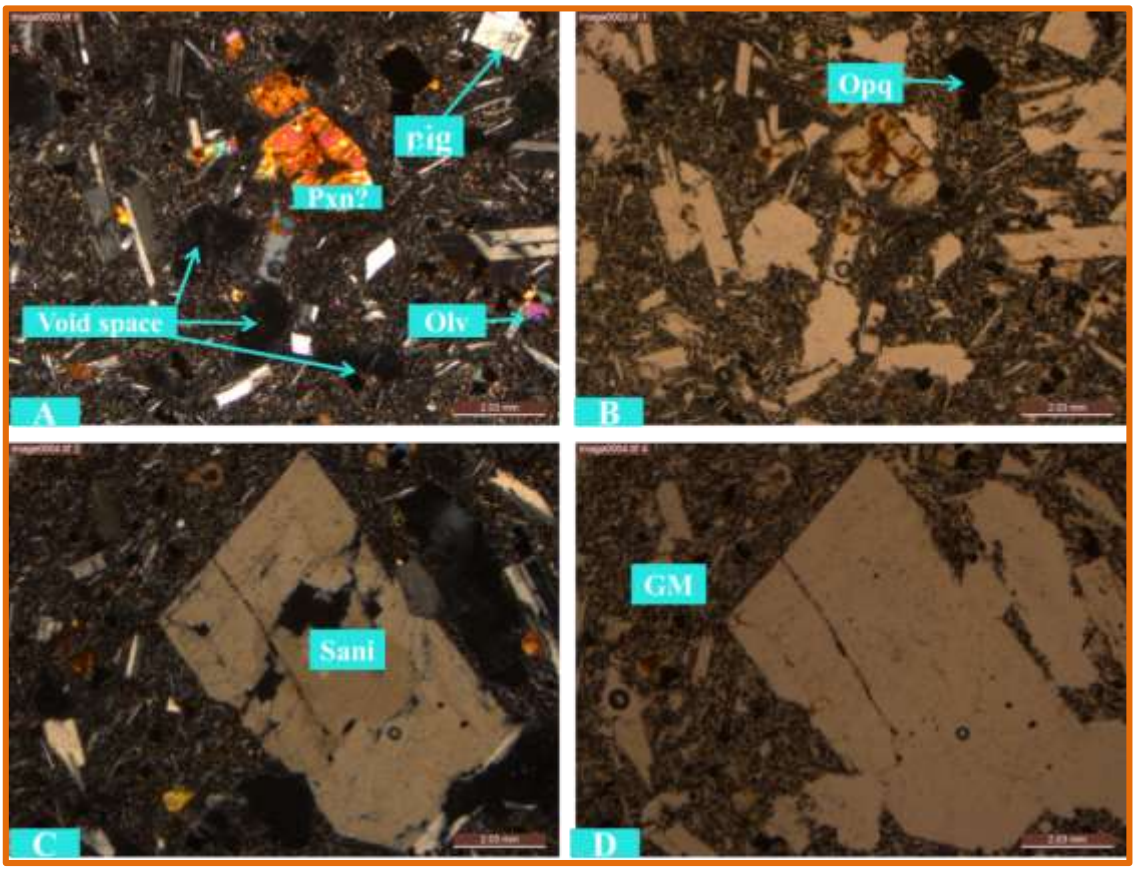

***FIGURE 4.10**: Microphoto picture of Basalt sample; ABD-16 under optical microscope in XPL (**A & C**) and PPL (**B & D**) view. The labels stands for; Sani- Sanidine, GM-groundmass, Olv – Olivine, Pxn – pyroxene, plg- plageoclase and Opq -Fe-Ti Oxides; The photo taken at 4X magnification*

4.1.1.5. Scoriaceous products and Scoria cone

Scoriaceous products (bombs and lapilli) are the other igneous unit outcropped in the study area. These units probably represent the last basaltic activity in the study area. It is observed that these units form the volcanic landform structures such as scoria cones. Scoria cones have been observed to underlie the next volcanic episode which is the eruption of rhyolitic lavas resulted in rhyolitic products and obsidians. However, basaltic lavas and associated spatters which seem to be relatively younger than those described above are found in some places. Even though the scoria cones are not distinguished to be separate, they differ in their degree of freshness and preservation of volcanic structures. Therefore, they may belong to a later episode of basaltic eruptions separated from the earlier ones. Numerous scoria cones are found in the obvious alignment with NNE- SSW fault systems probably indicating they are of fissural in origin. Scoriaceous products are partly oxidized and moderately altered. Alterations are yellowish to brownish in color (Figure 4.11). Weathering and oxidation processes have also played to change scoria in to reddish color.

***FIGURE 4.11**: Scoriaceous products and Scoria cone from the study area*

4.1.1.6. Rhyolitic lava domes and Obsidian flows

Rhyolite is the youngest product among the major lithological units found in the study area. It is a dome forming unit where a sequence of rhyolitic lavas is distributed at the youngest silicic centers (Figure 4.12A and B). Previous works (e.g., Tadiwos Chernet, 2011, Corti et al., 2014) also revealed that the Salewa Dore – Hako rhyolitic center have produced very

recent obsidian and Pitchstone flows probably representing the youngest rhyolitic activity in the study area.

The rhyolites are light grey to reddish brown; the color varies due to alteration intensity associated with fumarolic activity as it is seen on the top of the Hako and to the bottom side of Salwa Dore rhyolitic domes. Alteration of these rocks is slight at their bottom parts and showing a bit increase towards top parts of the centers. This is because fumarolic activity is more common on the top of these domes. Some of the rock sample from this unit (the unit nearest to Hobitcha rhyolites) is with beautiful flow banding structures. Here, there exist two predominant colored flow bands: grey and reddish brown. Aphyric texture to the naked eye, small minerals aligned along flow bands.

The rhyolitic lava dome is affected by minor faults probably being the passageway for the fumarolic activity around. These rhyolitic lava flows are greyish in color and porphyritic in textural character. The upper portions are made up of less porphyritic (phenocrysts of quartz and alkali feldspar noticeable in the microscope) that shows weak banding.

The rhyolite unit is seen coated by Obsidian flows at its exterior surface. These obsidian flows is characterized by crystal rich, irregular shaped unit likely to be pitchstones. Two categories of obsidians are identified based on physical difference. The first one is massive obsidian that is exposed on top to bottom of the Salwa Dore and Hako domes coating it. The second variety is fragmented obsidian exposed together with pumiceous pyroclastic rocks. Stratified ash and pumice deposits intercalated with lacustrine sediments forms the bottom of the rhyolitic domes, the base of the volcano being composed of rhyolite flows. Thick flows of obsidian and a few pumice and ash falls are probably resulted from the last products of volcanic activity in the study area. The obsidians are found on the central vents of the rhyolitic domes. The largest volume of extrusion is from Salwa Dore (meaning "obsidian" in local language) where a conical dome is built. These obsidians are black with slight amounts of phenocrysts visible on hand specimen. Obsidians from Hoko are less porphyritic than that of Salwa Dore.

Two samples that are collected from the outcropping rhyolitc lava flow/obsidian are prepared for petrographic analysis (ABD-04; Figure 4.13 and ABD-11; Figure 4.14). Accordingly, the rock shows large phenocrysts of sanidine locked within a glassy matrix

and with numerous glass inclusions. This rock show radiate texture probably is formed by overgrowth of alkali feldspar and quartz on existing phenocryst (Figure 4.13A).

Crystal rich obsidian is another igneous unit observed in the field. This unit is coarse grained, dark-green/black in colour with the exterior surface of obsidian (glassy texture) and shiny appearance (Figure 4.12C). On sample ID ABD-04, the volcanic glass constitutes most percentage compositions (85-92%) forming the ground mass of the rock. The phenocrysts are 8- 9% twinned Sanidine, 4-5 % opaque minerals and 3- 4 % quartz. Sanidine is large, elongated and with maximum grain length of 10mm. Minor amount of mafic minerals (clinopyroxene and olivine) is observed in this thin section sample (Figure 4.13A and C). Intergrowth of olivine on deformed sanidine is also present (Figure 4.13A). On sample ID ABD-11, volcanic glass is present throughout the whole sample in the groundmass taking higher percentage (89-93%). The phenocrysts are 5- 7 % sanidine, 4-5 % opaque minerals and 2- 3 % quartz (Figure 4.14). Quartz is present as a glass inclusion and sanidine is characterized by contrasting interference colour between pink and dark/black color under XPL (Figure 4.14E). Interesting crystal of alkali-feldspars with variety color dominantly greenish surrounded by volcanic glass is present (Figure 4.14C).

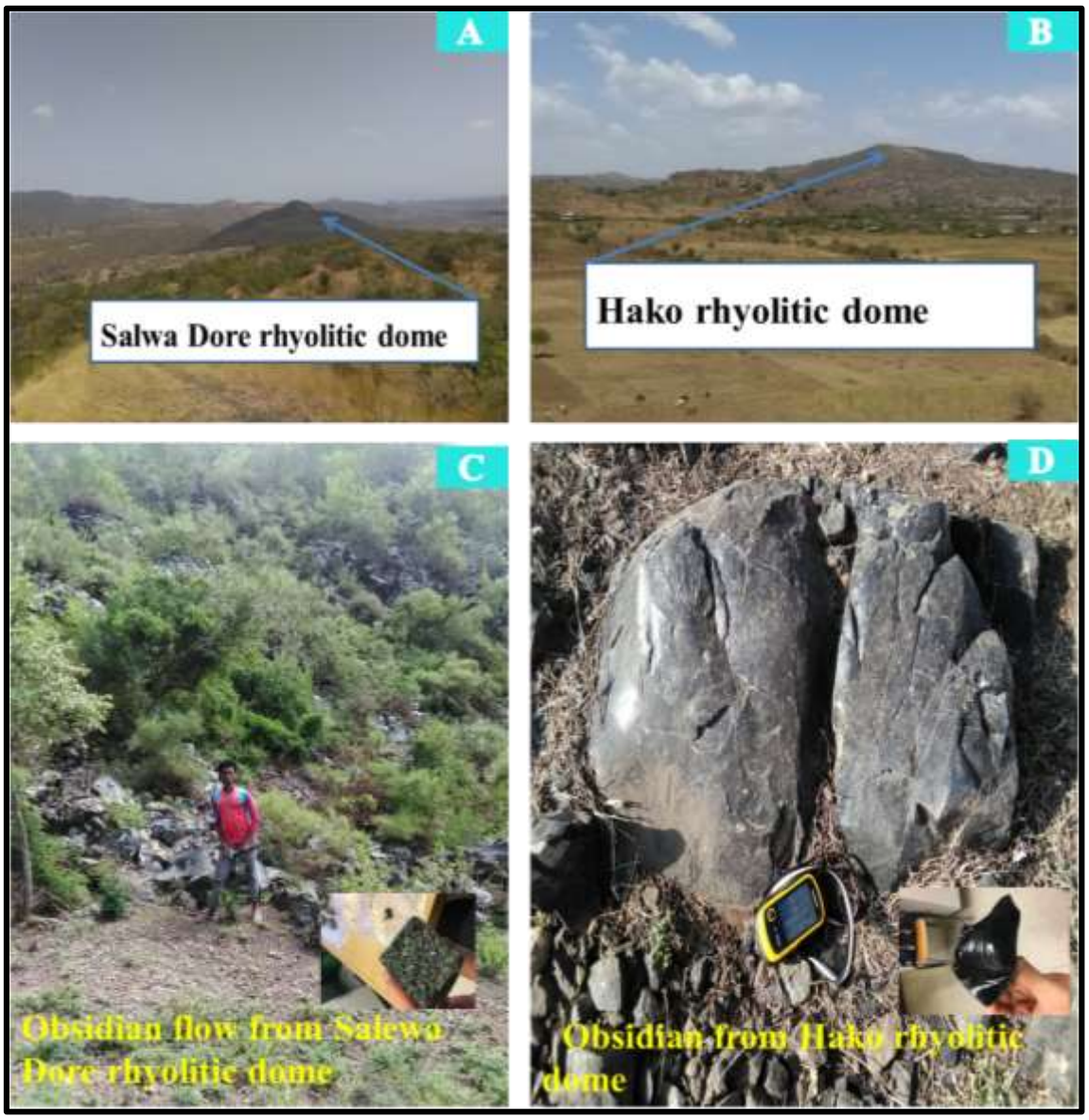

***FIGURE 4.12**: Rhyolitic domes and massive Obsidian exposed on top to bottom of the domes*

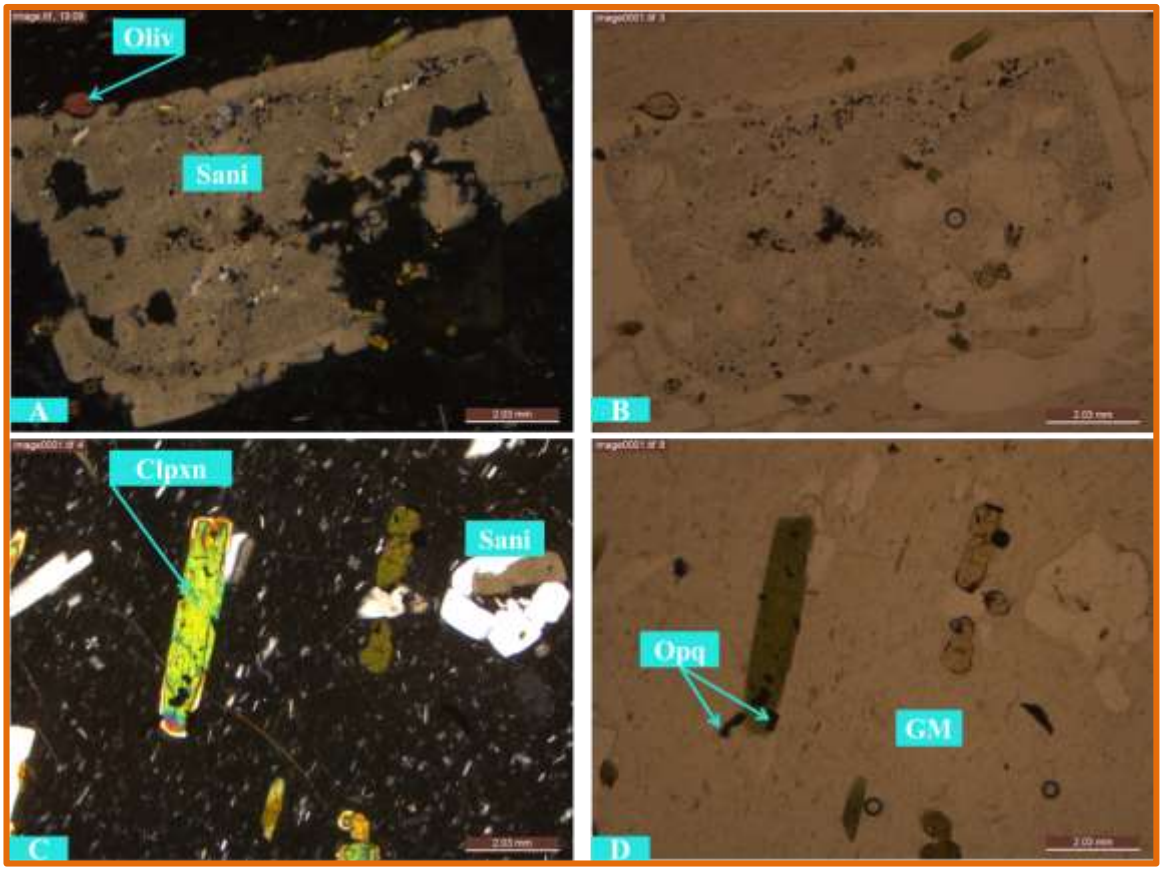

***FIGURE 4.13**: Microphoto picture of Obsidian/pitchstone sample; ABD-04 under optical microscope in XPL (**A & C**) and PPL (**B & D**) view. The labels stands for; GM – groundmass, Sani- sanidine, clpxn- clinopyroxene and Opq- opaque minerals; The photo taken at 4X magnification*

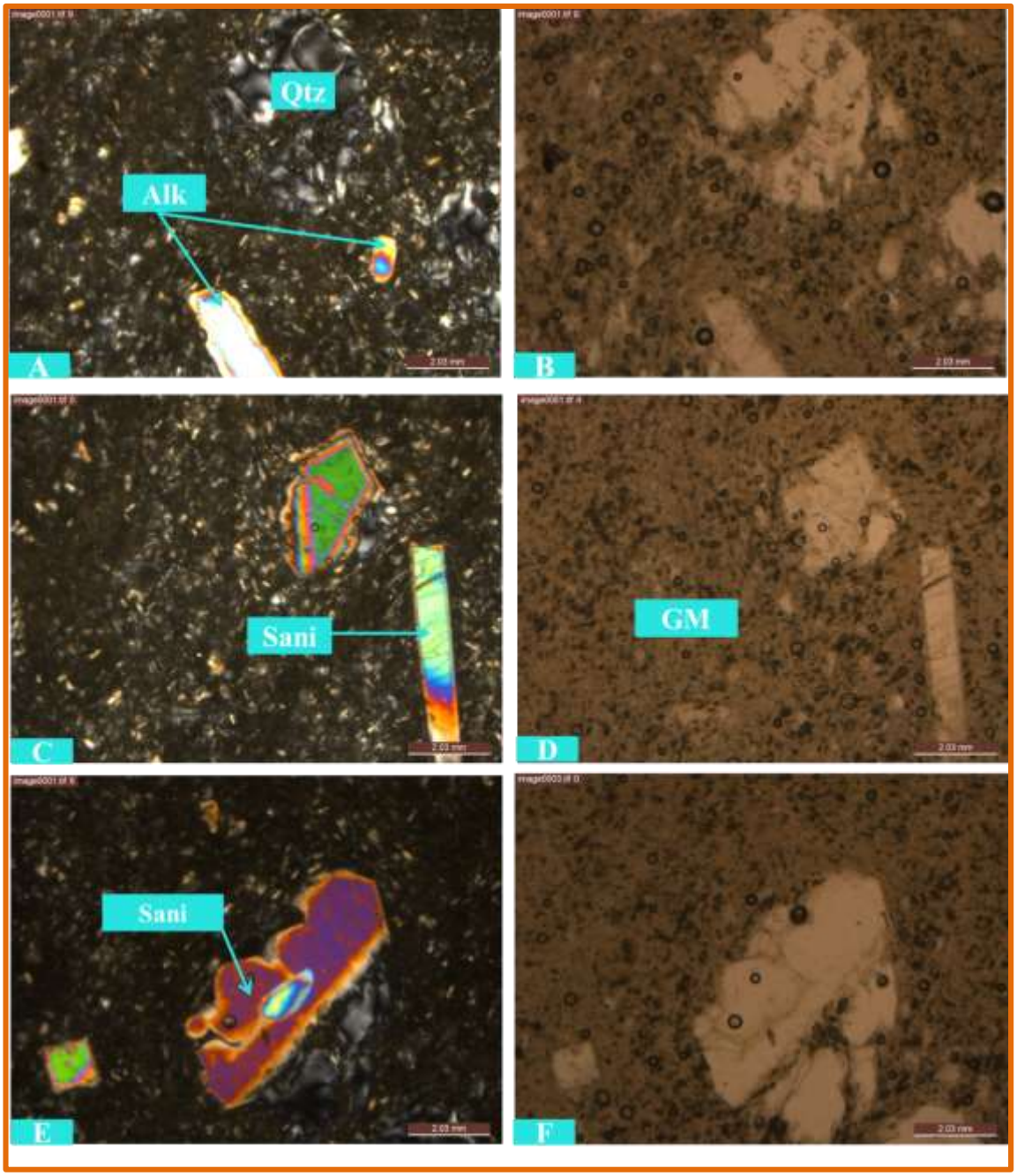

***FIGURE 4.14**: Microphoto picture of Obsidian sample; ABD-11 under optical microscope in XPL (**A, C & E**) and PPL (**B, D & F**) view. The labels stands for; GM – groundmass, Sani- sanidine, Alk – Alkali-feldspar and Qtz - quartz; the photo taken at 4X magnification*

4.1.1.7. Alluvial and Lacustrine sediments

These sediments are dark grey to yellowish brown, fine grained units exposed largely at chewkare graben (southeast most part of the study area). These units are also found interbedded with pumiceous pyroclastic rocks, sometimes underlain the basalts in some part of the study area. Some part of the area covered with these sediments is permanently water-logged partly due to continuous inflow of water from the surrounding springs. This marshy land is found to surround the small faulted block of the Ignimbrite formation. The materials forming these sediments consist mainly of clay and silt with some minor sand and conglomerate.

A variety of lacustrine sediments are found restricted to the lake level. These varieties include unconsolidated silty clay, conglomerates and sandstone with minor ash and pumice flow intercalation.

Alluvial sediments seem to be related with the major river (the Bilate River) which is the main source of recharge to Lake Abaya. The Bilate River carries a considerable amount of sediments to the Lake during heavy rainy seasons. Consequently, a large delta and floodplains have been built at the inlet of the river to the lake where silt to clay sediment deposition is observed. Minor joint are observed to intersect the alluvial sediments in some part of the study area (Figure 4.15).

***FIGURE 4.15**: Exposure of lacustrine sediments that is located southeastern part of the study area.it is crossed by minor joint with spacing of 30 cm*

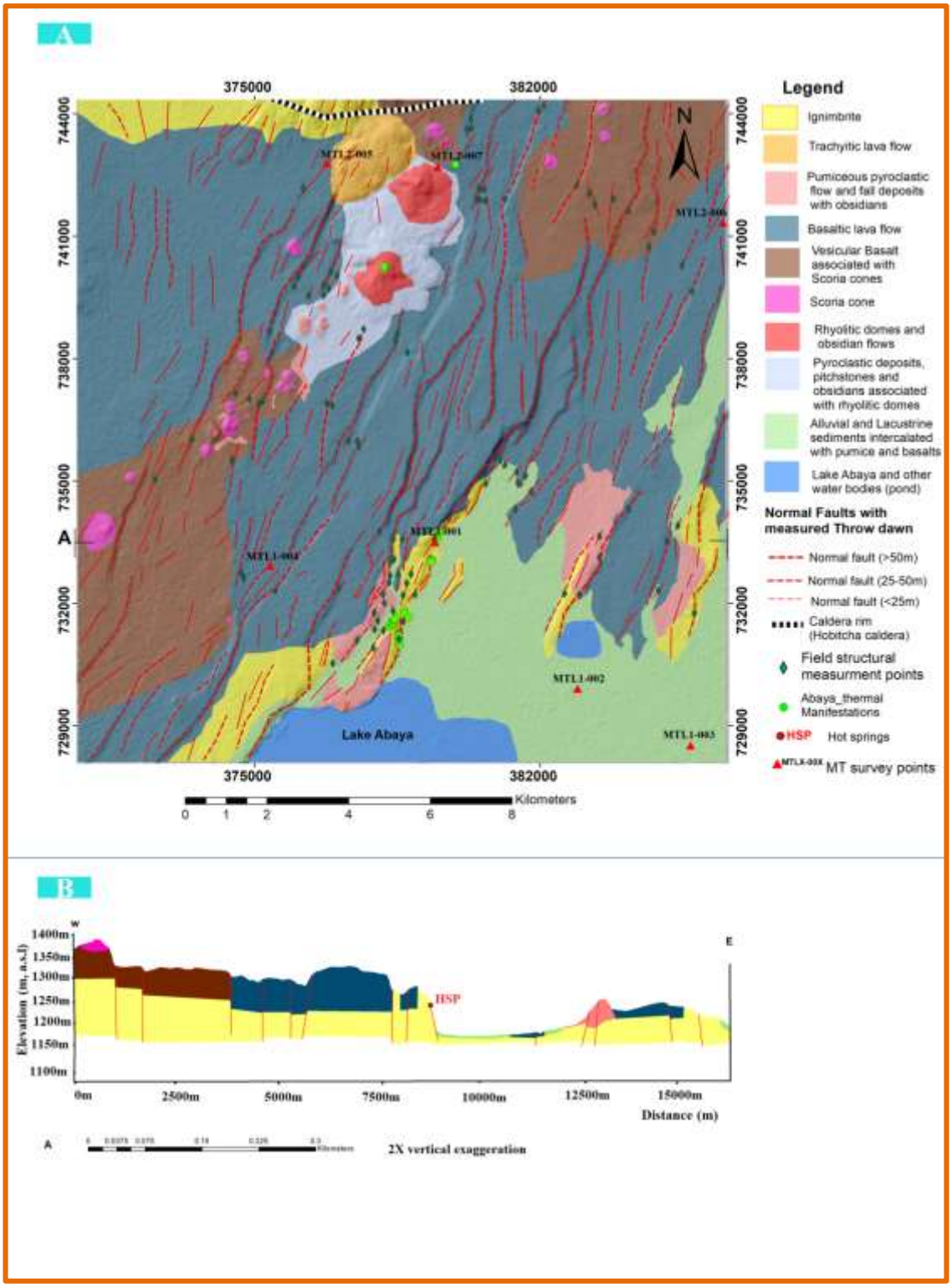

FIGURE 4.16: A. *Geological map of the study area and* ***B.*** *geologic cross section along A (w-E) traverse line*

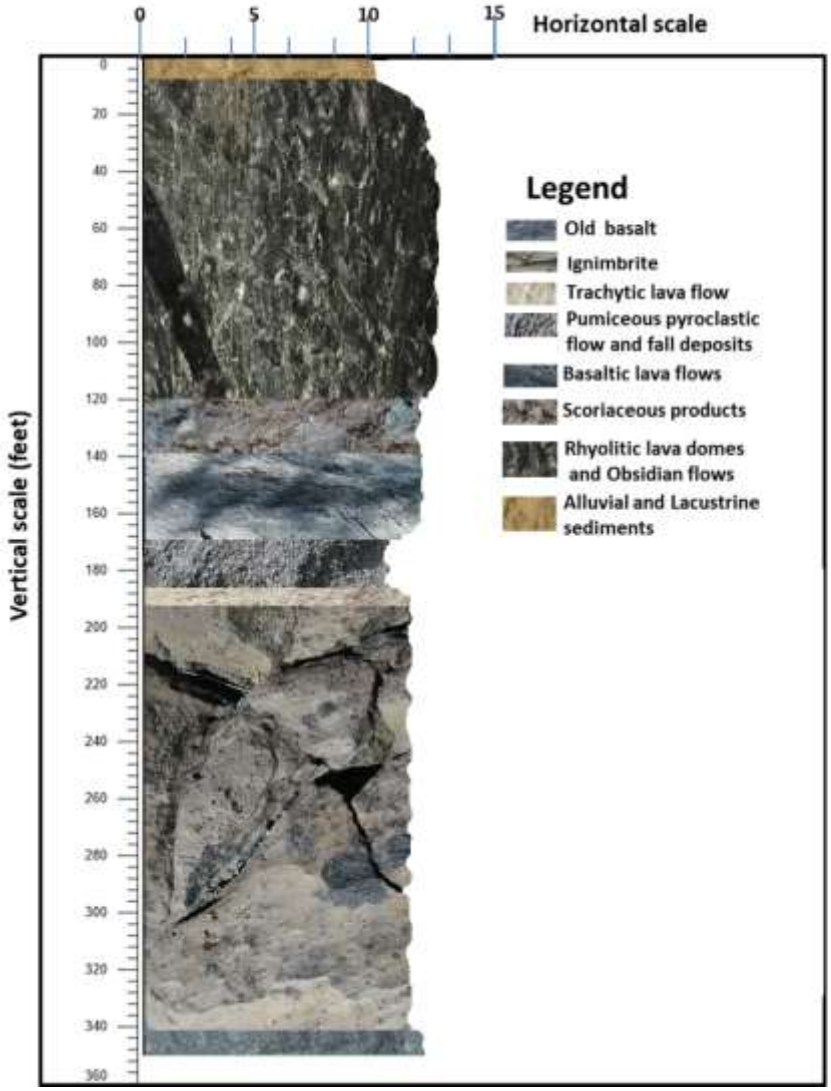

***FIGURE 4.17**: Composite stratigraphy of the study area. The scale labeled vertically shows the thickness (feet). Horizontal scale is based on rocks resistance to weathering.*

4.2. Geological structures and permeability

Geothermal fluid flow along the Ethiopian rift system is greatly influenced by the system of normal faulting, en echelon rift shoulder faulting and the rift floor basin (Hutchison et al., 2015). The faults may facilitate geothermal fluid flow by providing channels of high permeability or they may create barriers to flow by offsetting areas of high permeability. Previous studies to evaluate geothermal resources within the MER have indicated that Quaternary extensional tectonic movements along the axis of the rift have evidently created wide spread secondary permeability and faulted the cap rock thereby a supply of hydrothermal fluid to surface manifestations (e.g., Lloyd, 1977).

Field structural observation in this study shows the presence of series of intense normal faulting and volcanism in the area. Here, detailed structural mapping and structural analysis (the trend of the structures) of field data using the stereographic projection technique in GeoRose software is conducted and presented. Relationship and contribution of these structures to the geothermal field of the area is interpreted by integrating with the remote sensing work, Landsat imagery of the study area, along with field observation. This is found helpful in delineating the various geological and structural features of the area.

4.2.1. Normal faults

Normal Fault is the predominant structure mapped during the field activity (Figure 4.18). Faults were identified mostly on the base of morphological criteria. Faults are expressed in general by the occurrence of steep slopes, separating rocky ridges with steep sides usually covered by basalt and Ignimbrite blocks from flat, narrow plains underlain by volcano-sedimentary deposits. The throw of the faults within the basaltic and ignimbrite portion of the study area can be estimated to be in the order of 10-180 m based on the morphological criteria (the difference of elevation between top of the ridges and bottom valleys). Based on general considerations, faults are inferred to be sub-vertical.

The observed faults have no perfect planar surfaces thus several strike and dip measurements are taken to describe the attitude of the faults. It is noted that the faults change its attitude both along strike and dip. Most of the geological structures observed and measured in the field are high-angle normal faults where their dips ranging from 75° to 85° to the northwest and the southeast. Fault strikes vary from N-S, NNE-SSW, NE-SW.

Central part of the study area has a high density of NNE-SSW faults. The orientation measurements of all faults are presented on Appendix II.

4.2.2. Joints and cracks

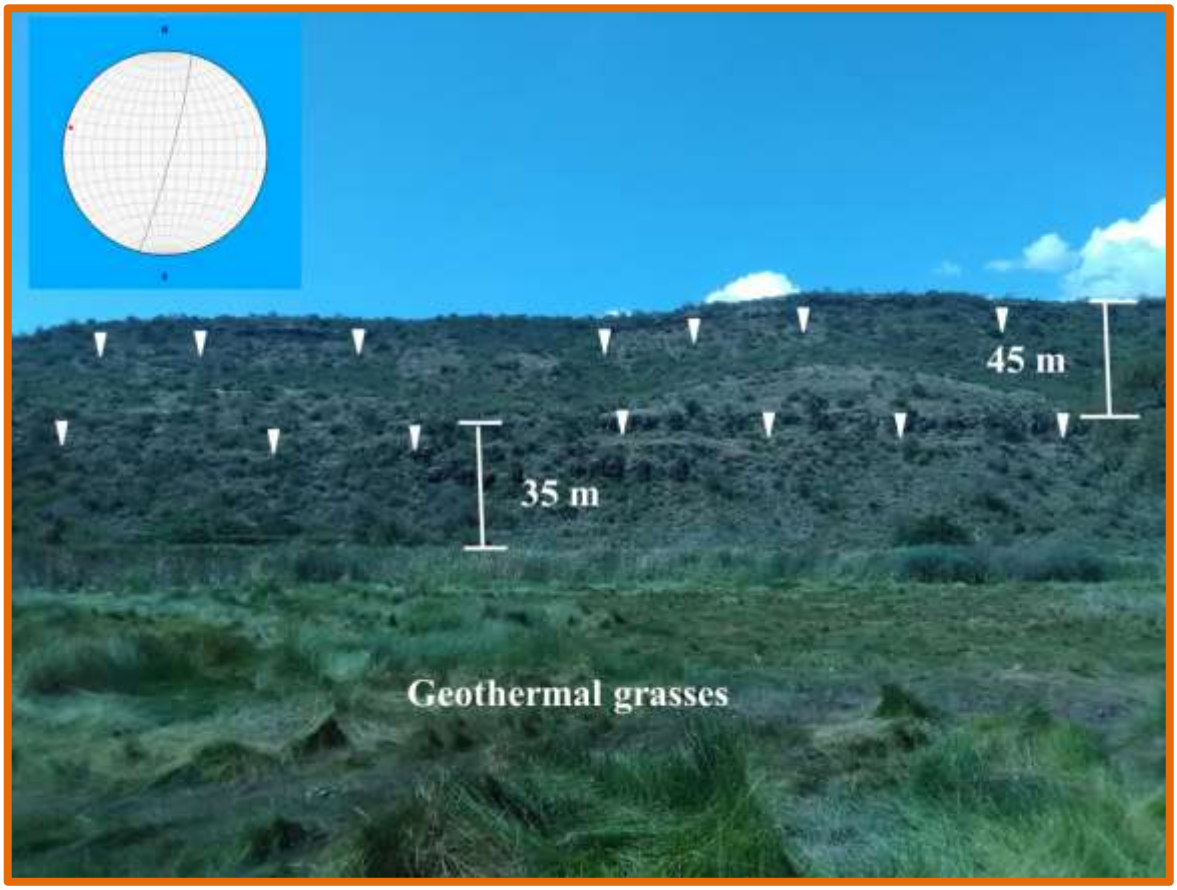

***FIGURE 4.18**: Field Photo of the step faults cutting ignimbrite close to the hot springs at Chewkare graben, the fault dip direction is SE. Top-left plot display the fault data analysis (stereoplot of fault at F003 measurement point with GeoRose) which shows orientation of 015 strikes and 85^0 dip.*

Joint is fracture which has no or insignificant relative displacement between the blocks found on the two side of the fracture. This structure is predominantly observed on basalt units, rhyolitic lava flow and pumice fall. The joint that is present on the basaltic block (Figure 4.19) has a general orientation of NE-SW strike and vertical to sub vertical dip amount. Cracks are more common to the lacustrine sediments close to the Lake Abaya. The orientation measurements of all joints and cracks are presented on Appendix II. Maximum aperture for the joints measured in the field is 15 cm. Ground cracks have a bit wider average spacing of up to 15 m.

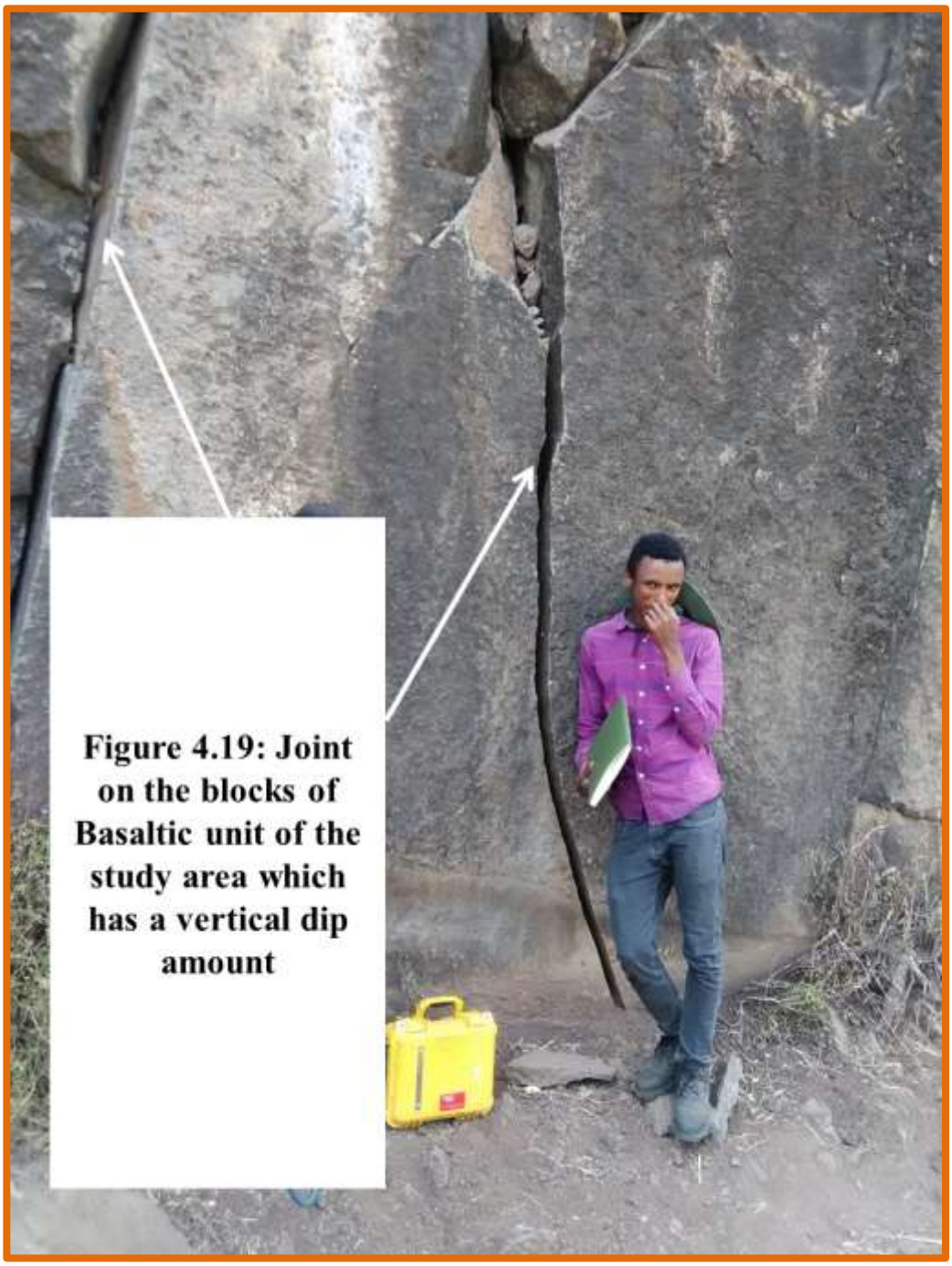

Figure 4.19: Joint on the blocks of Basaltic unit of the study area which has a vertical dip amount

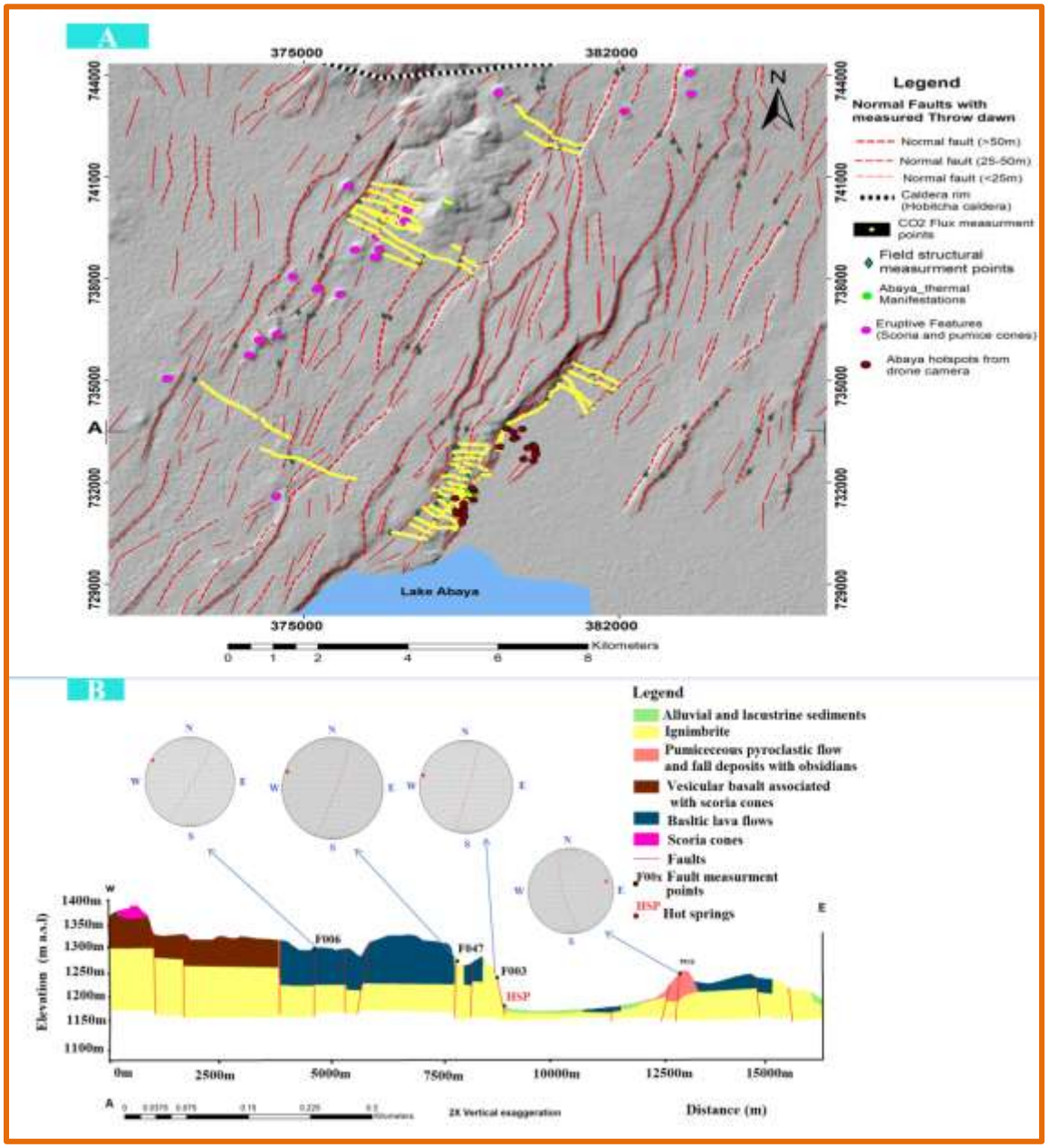

***FIGURE 4.20: A**. Structural map of the study area with sites of structural measurements overlaid on hill shade as a background; mainly interpreted from Google earth, SRTM DEM, Landsat 8 and field mapping **B.** Structural-geological cross section along A traverse line and Stereographic projections (GeoRose) display the fault planes and the collected associated fault-slip vectors.*

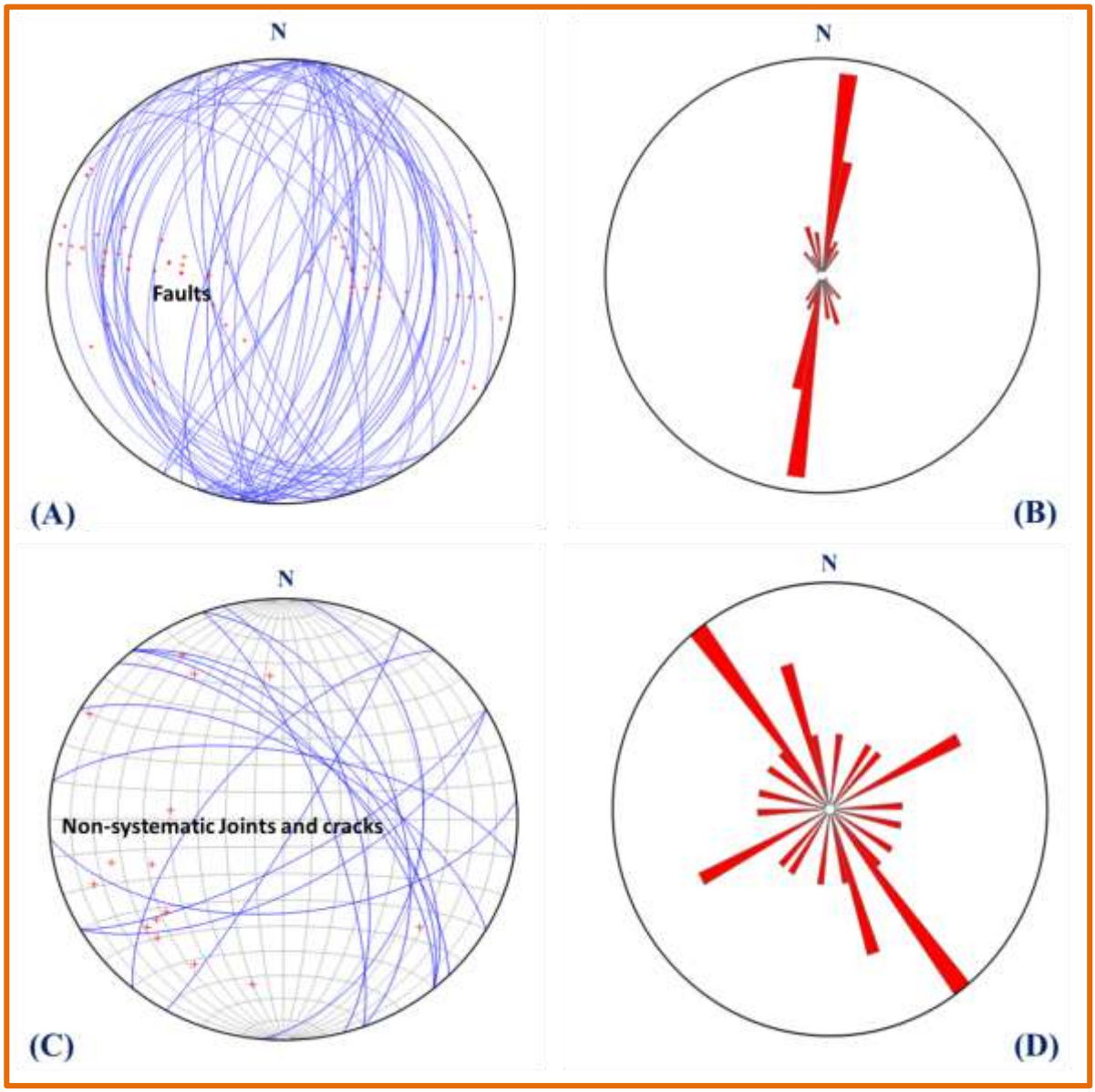

***FIGURE 4.21**: Schmidt net lower hemisphere plot of structures measured in the field **A**. stereoplot of faults **B**. Rose plots comprising fault trends **C**. stereo plot of non-systematic joints and cracks **D**. Rose diagram of joints and cracks*

4.2.3. Geothermal Manifestations

Hydrothermal Manifestations in the geothermal fields are surficial evidence for the possible existence of geothermal fluids at depth (Hochstein, 1990). Their occurrence and physical character can give some indication of conditions at depth.

Most hydrothermal features in the study area are concentrated along the dense NNE-SSW trending fault system; on the Abaya fault, a large ignimbrite escarpment on the western part

of the Chewkare graben. Minute amounts of geothermal manifestations are also found in the Salewa-Dore and Hako (SD-H) felsic centers (Figure 4.24). Previous works also reveals that distribution of hydrothermal active zones is strongly controlled by tectonics and geological structures (e.g, Tadiwos Chernet, 2011). These manifestations are natural thermal springs (ranging from 40°C to 90°C), steaming ground/fumarolic activity (close to 100 °C at 50 cm depth), mud pools, hot and warm ground and altered surface rocks. Most strong hot spring is found along the margins of the swampy ground in the Chewkare graben. It is due to the fact that this area of discharge is at a lower elevation relative to the surrounding areas, and therefore nearer to the groundwater. This makes, it easier for the groundwater to be discharged upwards through the fault fracture. Ignimbrite unit is the host rock for most surface hydrothermal manifestations although some present in the basaltic fissure and in association with rhyolitic lava flows. An eruptive steam is present close to the lake shore that is released at about 3 m above the lake level suggesting that reservoir pressures may exceed hydrostatic pressure (Figure 4.22B).

Hot grounds and hydrothermal alterations are related to fumarole vents and hot springs. The hot ground exists in wider area with temperature close to 100 °C at 70 cm depth where the steam vent is present. These hot grounds are covered with a thin film of bicarbonate salts and are for the most part heated by conduction indicating subsurface boiling (Tadiwos chernet, 2011). Alteration related to hot spring activity is commonly represented as superficial deposition of siliceous sinter and travertine (Figure 4.22C and 4.23D).When carbonate bearing water around the hot spring are exposed to the air; the water evaporates leaving a small deposit of calcium carbonate that form travertine. Deep rooted alteration is present in association with fumarolic activity that pervasively affects the ignimbrite with wide spread exposed surfaces of altered rock to reddish and yellowish color (Figure 4.22 D). Zones of oxidized products stained reddish- black colors on some altered ground and native mineral sublimates such as sulfur are also present (Figure 4.23B and C). Geochemical characteristics of the thermal manifestations, fluid sample analysis and results are presented on chapter 5 of this thesis work.

FIGURE 4.22: *photo picture of the hydrothermal manifestations found predominantly at the shore of Lake Abaya* ***A.*** *Hot spring with hydrothermally deposited crust of sulphides settled at the bottom* ***B.*** *Eruptive steam (weak geyser activity) from fissures on ignimbrite* ***C.*** *Silica sinter deposition associated with Hot Springs* **D**. *Alteration associated with the fumaroles.*

***FIGURE 4.23**: photo picture of the hydrothermal alteration and oxidation processes of the study area **A.** siliceous sinter deposition **B.** oxidation associated with fumaroles (black color) **C.** Native sulfur mineral deposition; yellowish in color **D.** Travertine deposition associated with fossil hot springs.*

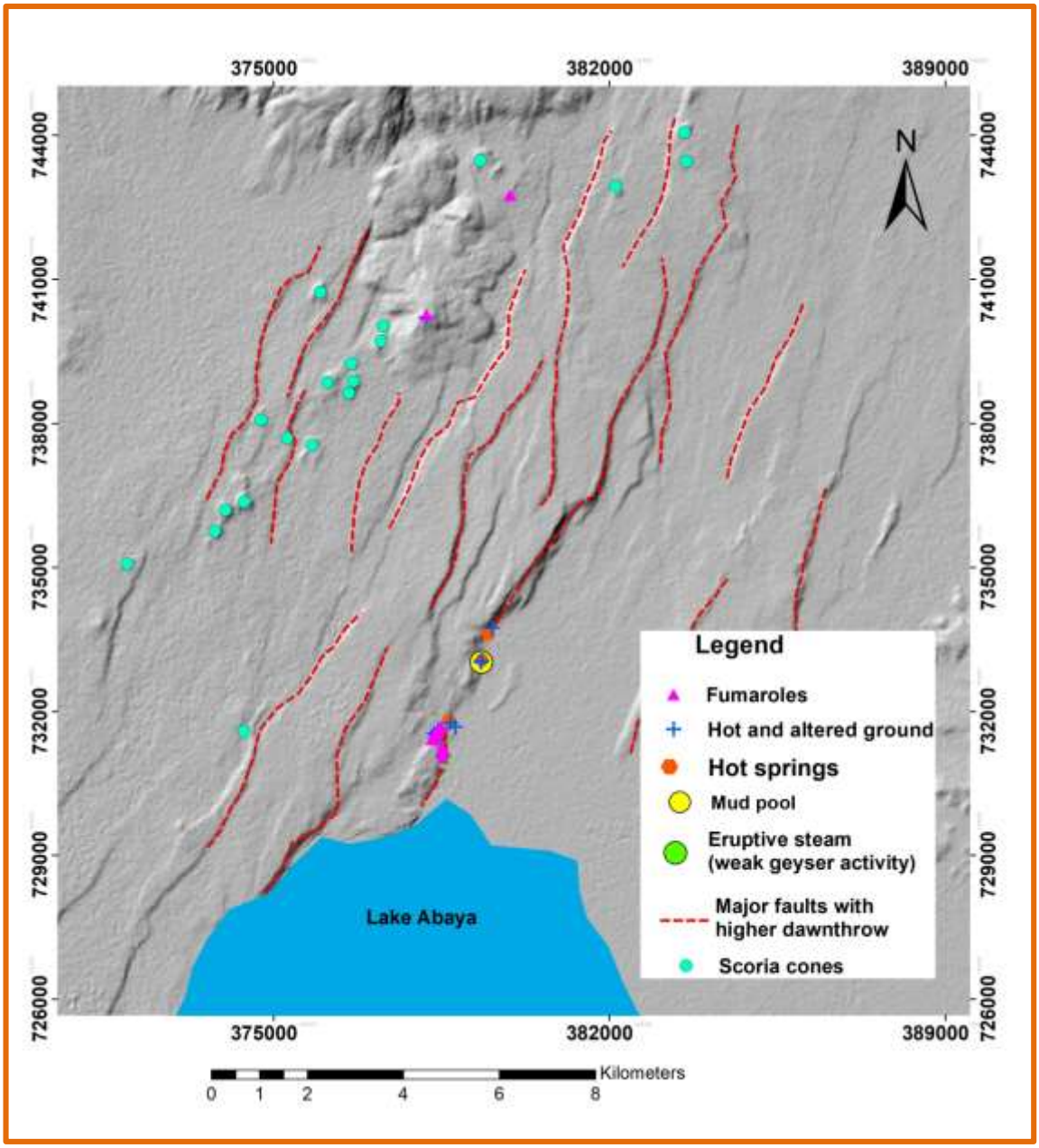

***FIGURE 4.24**: Distribution of hydrothermal manifestations and their relationship with fault and volcanic centers in the study area*

4.3. Geochemistry of the Thermal Manifestations

Geochemistry is one of the most effective ways of studying geothermal resource, both in the exploration and exploitation stages (Charles Wanjie, 2012). Chemical composition of the thermal water has proven very useful in evaluating subsurface temperature, determining water origin, observing mixing and predicting scaling and corrosion. The study of the origin and evolution of volcanic and geothermal fluids is one of the main concerns of geothermal resource study (Craig, 1963**;** Ellis and Mahon 1964; Marini, 2000). Possible sources contributing major and trace elements to these discharges include the magma, the host rocks and the fluids circulating in the subsurface.

Prior to the current study, the Abaya region was known as a potential area storing high enthalpy geothermal reservoir. Several previous geochemical works have been carried out in the Abaya region, collecting samples in and around the geothermal fields of the current study (UNDP, 1973, Craig et al., 1977, ELC, 1987, Darling, 1990, GSE, 2000, Abebe Ayele et al., 2002, Asfaw Teclu, 2003, Salahadin Ali and Lemma Kassa, 2007, Reykjavík Geothermal, 2011 and Minissale et al., 2017). The location and names of the springs within the current study area were obtained from these various databases. The chemical composition of the spring water has been reported in the above sources but no gas chemistry from the area has been found in literature so far.

The visited and sampled geothermal manifestations in this study are classified into two different types; water samples and gas samples. The hot springs and steaming ground (weak fumarolic activity) are mostly located on the Abaya fault, a large escarpment of the NNE-SSW trending fault, stretching from Lake Abaya to the north. The geothermal manifestations in the area are mainly the thermal springs, boiling mud pools and fumaroles with temperatures from 40 °C to 100 °C, generally with temperatures increasing to the south (Table 4.1). Also found in the area are the steaming ground, high surface temperature anomalies with temperatures ranging up to 100 °C at 50 cm depth. These temperature anomalies are mostly located on a horst west of the Abaya fault were a large area of surface alteration with several steam vents, springs and audible boiling at shallow depths exists. There are other hydrothermal manifestations in the Salewa Dore-Hako complex in the form of steam vents (Table 4.2). The locations with the thermal anomalies are not always suitable for sampling but from most of them, a dispersed weak steam rises that is likely to be steam

from the boiling water below that can be easiy heard. The three locations of these anomalies from SD-H graben, all have temperatures of 50 °C or less.

During the first, second and third phase of the field works, most of the springs were visited and a total of nine water samples and twelve dry gas samples were collected from the springs and steam vents. The spring's temperature can reach 100°C on the surface and to 50 cm depth. The area where the highest temperature is recorded shows extensive surface alteration, as expected with the high surface temperatures. The geographic location of each sample spot was recorded with GPS equipment.

Physico-chemical parameters such as discharge temperature and pH were determined in the field. The water samples were filtered and treated. Filtration was done using a hand pump-syringe, which operates manually. The acid treatment with 1% HNO_3 is conducted in situ for the metals remain in solution. The filtered and treated samples were stored in polyethylene double cap plastic and glass bottles that have different volume (50-500ml). Untreated and unfiltered samples were also collected and stored in double cap polythene bottles (for anions and boron determination) and in amber glasses (for CO_2 and H_2S titration done in the field and for stable isotopes). For SiO_2 determination, 10ml of sample was taken for each samples and was diluted to a volume of 100ml (1:10) with distilled (deionized) water in order to avoid polymerization that may occur between the period of sampling and analysis due to cooling of the sample. 50ml water samples and condensate were collected for stable isotope determination. After sampling all sample bottles were properly double capped. The samples were collected according to standard practice and analysed at the University of Iceland.

The gas samples were collected from gas rich springs and weak fumaroles on the southern part of the northwest Abaya fault. The samples are split into three types. (A) Dry gas; collected in Vacuettes (Vacuum gas tubes) and in flow through gas tubes and analysed for steam composition at the University of New Mexico, Albaquerque, (B) Dissolved gases; Collected in bulb and analysed for H_2S and CO_2 in the field laboratory of RG geothermal Ltd (C) Major gases; Sample collected in a vacuumized Giggenbach flask, dissolved gases removed and analysed in field laboratory of RG geothermal Ltd, head space gases analysed at Iceland Geosurvey (ISOR) using a gas chromatograph for the volatile components in the samples.

Interpretation of the results of fluid sample analysis is conducted with AquaChem software package. AquaChem is a software package developed specifically for graphical and numerical analysis and modeling of water quality data (From the software manual). It features a fully customizable database of physical and chemical parameters and provides a comprehensive selection of analysis tools, calculations and graphs for interpreting water quality data. In the current study; plotting techniques available in AquaChem used to represent the chemical characteristics of fluids includes sample plots (pie), ternary plots (ternary, piper and giggenbach) and geothermometer plot. Each of these plots provides a unique interpretation of the many complex interactions between the fluids (subsurface water) and rocks (aquifer materials). Ternary and piper diagrams are the most commonly used diagrams to classify water types in the geothermal waters (Giggenbach, 1998). Ternary plots are used to determine the relationship between the concentrations of three different parameters in multiple samples. Piper plots are used to show clustering nature between multiple samples and trends in major ions.

Table 4.1*: Name, location and field measurement of the physical properties of the thermal water samples collected from the study area.*

Sampling							**Sampling location [WGS 84 datum]**		
Spring (This study)	**Spring (previous study)**	**Date**	**Time**	**T (^{o}c)**	**PH**	**T [(^{o}c,amb)**	**X**	**Y**	**Elevation [a.s.l]**
AB-18-W01	SP-16	2.10.2018	12:33	41	6.39	28	380514	734766	1191
AB-18-W02	SP-15	2.10.2018	14:48	67	5.94	35	379475	733674	1181
AB-18-W03	N.a	3.10.2018	14:23	88	5.40	33	378524	731134	1199
AB-18-W04	SP-8	3.10.2018	17:40	67	6.08	35	378667	731880	1191
AB-18-W05	SP-15	25.11.2018	18:40	67	6.27	34	379474	733676	1185
AB-18-W06	SP-15	26.11.2018	15:03	67	6.23	33.4	379457	733671	1189
AB-18-W07	SP-15	26.11.2018	15:04	68	6.40	33.4	379475	733676	1188
AB-18-W08	SP-13	26.11.2018	16:02	57	6.55	33	379346	733135	1182
AB-18-W09	SP-8	27.11.2018	15:55	67	6.84	31	378667	731880	1191

Table 4.2: *Geothermal manifestations for the study area in the form of the steaming ground (surface temperature anomalies)*

Steaming ground	**Temperature [°C]**	**Location [WGS 84 datum]**		
		X	Y	Elevation (m a.s.l.)
SG_1	37	379929	742830	1430
SG_2	84	378489	731743	1225
SG_3	48	378188	740324	1596
SG_4	50	378188	740324	1595
SG_5	74	378532	731301	1202
SG_6	74	378532	731301	1201
SG_7	87	378532	731290	1198
SG_8	95	378532	731268	1199
SG_9	98	378532	731080	1198
SG_10	94	378423	731655	1246
SG_11	88	378521	731179	1206

Table 4.3: *The names and location of the gas sampling in the study area*

Sampling				**Sampling location [WGS 84 datum]**		
Sample name	**Date**	**Time**	**T °C**	**X**	**Y**	**Elevation**
AB-18-G01	29.11.2018	11:50	94	378353	731590	1243
AB-18-G02	29.11.2018	11:50	94	378353	731590	1243
AB-18-G03	29.11.2018	11:50	94	378353	731590	1243
AB-18-G04	29.11.2018	13:04	58	379479	733655	1182
AB-18-G05	29.11.2018	13:04	58	379479	733655	1182
AB-19-G01	12.1.2019	13:07	50	378192	740329	1601
AB-19-G02	14.1.2019	12:39	97	378387	731603	1264
AB-19-G03	15.1.2019	13:13	97	378572	731024	1185
AB-19-G04	15.1.2019	13:13	97	378572	731024	1185
AB-19-G05	16.1.2019	11:51	95	378337	731548	1252
AB-19-G06	16.1.2019	12:05	100	378354	731586	1249
AB-19-G07	16.1.2019	13:10	94	378462	731729	1248

4.3.1. Chemistry of the thermal waters and gas samples

Geothermal fluids contain a wide variety and concentration of dissolved constituents. The chemical parameters often cited to characterize geothermal fluids are total dissolved solids (TDS) and pH (Arnorsson et al., 1990). The TDS gives a measure of the amount of chemical salts dissolved in the waters and the pH is a measure of the acidity or alkalinity of the fluid. These two parameters can be measured in the field by use of a conductivity meter and a pH meter. The conductivity meter measures the TDS of a fluid by measuring its electrical conductivity. The more the dissolved salts, the higher the electrical conductivity. The TDS of the geothermal fluids are usually composed mainly of sodium (Na), calcium (Ca), potassium (K), chlorine (Cl), silica (SiO_2), sulfate (SO_4), and bicarbonate ($HC0_3$) and minor amount of fluorine (F) and boron (B) (Giggenbach, 1988).

The chemical composition of geothermal fluids such as water, steam and dry gas are used to constrain parameters such a reservoir temperature, type of water, salinity, and extent of fluid–rock interactions (Fridricksson et al., 2016). The amount and nature of dissolved chemical species in geothermal fluids are functions of temperature and of the local geology. Most of the time, lower-temperature resources usually have lower amount of dissolved solids than do higher temperature resources. Prolonged water-rock interaction liberates ionic species and produces a saturated silica solution (Arnorsson et al., 1990). As geothermal fluids move through rocks, they react chemically with the rocks, which themselves are usually chemically complex. Minerals in the reservoir rocks may be selectively dissolved by the fluids while other minerals may be precipitated from solution or may substitute for certain elements within a mineral. These mineralogical changes in the reservoir rocks may cause volume changes that affect the permeability and porosity of the rocks. The volume changes are at the expense (if the volume decrease) of open space in the rock which caused a decrease in permeability. In locations where pressure, temperature, or rock chemistry change abruptly, minerals may be precipitated into the open spaces. SiO_2 and calcium ($CaCO_3$) are the principal minerals usually involved in precipitation (Giggenbach and Goguel, 1989). The solubility of SiO_2 decreases with a decrease in temperature (Fournier and Potter, 1982). SiO_2 can be precipitated into open spaces such as fractures or pores in the rock. It is in the regions of the subsurface temperature changes abruptly where most hot springs discharge. $CaCO_3$ is more soluble at low temperatures than at high temperatures (retrograde solubility).

Previous studies in the Abaya region were used to obtain a lot of information's about the chemical compositions of water samples that can be compared. This includes the regional high silica concentrations, greater than 180 ppm on average, the low salinity and the temperature of most of the springs greater than 50°C. Constantly, Spring-6 (labelled Spring-5 in 2000) shows the highest SiO_2 concentration, 200 ppm in 1977 but greater than 400 ppm in 2000, 2007 and 2011(Craig et al., 1977, GSE, 2000, Salahadin Ali and Lemma Kassa, 2007, Reykjavík Geothermal, 2011). This difference is quite possibly as a result of sample handling, with SiO_2 precipitating in the sample before analysis is performed.

The review of the chemical composition from the springs in and around the Abaya regions and sampled in the year 2000, 2003, 2007 and 2011 are presented in Table 4.4. These data bases cover all known springs in the area. Accordingly, the waters collected from the springs (labelled as Sp-XX) show high SiO_2, from 107 in Sp-2 to 512 ppm in Sp-6. All springs (SP-#) have high CO_2 concentration and relatively low SO_4 (4-89 ppm), and chlorine (8-762 ppm).

***Table 4.4**: Chemical composition of water samples collected in Abaya geothermal field obtained from previous studies. Samples collected in 2000 were collected by GSE, in 2003 by Asfaw Teclu, in 2007 by Salahadin Ali and Lemma Kassa and in 2011 by Reykjavík Geothermal. N.a. = not analyzed*

Sample name	**pH**	**T °C**	**Cond (µS/cm)**	**H_2S**	**CO_2**	**CO_3^{2-}**	**HCO_3^-**	**SO_4^{2-}**	**Cl^-**	**F^-**	**Na^+**	**K^+**	**Ca^{2+}**	**Mg^{2+}**	**B**	**SiO_2**	**Year**
SP-1	6.7	35	166	N.a.	172	0.11	154	4	8	1.55	49	9.3	20	7	0.19	144	2000
SP-1	N.a.	N.a.	N.a.	N.a.	N.a.	N.a.	N.a.	4	8	1.7	N.a.	N.a.	N.a.	N.a.	N.a.	144	2003
SP-1	6.9	36.5	427	N.a.	N.a.	N.a.	N.a.	N.a.	N.a.	N.a.	52	11	21	8	0.1	118	2007
SP-2	7.6	39	609	N.r.	559	2.62	668	22	104	2.71	223	26	34	40	0.04	107	2000
SP-2	N.a.	N.a.	N.a.	N.a.	N.a.	N.a.	N.a.	22	104	2.60	N.a.	N.a.	N.a.	N.a.	N.a.	110	2003
SP-3	6.9	41	669	N.r.	640	0.88	645	24	103	2.78	213	26	53	56	0.22	123	2000
SP-3	N.a.	N.a.	N.a.	N.a.	N.a.	N.a.	N.a.	24	103	2.8	N.a.	N.a.	N.a.	N.a.	N.a.	123	2003
SP-4	6.4	43	996	N.r.	997	0.48	776	13	72	15	530	41	16	55	0.24	155	2000
SP-4	N.a.	N.a.	N.a.	N.a.	N.a.	N.a.	N.a.	13	72	15	N.a.	N.a.	N.a.	N.a.	N.a.	156	2003
SP-5	9.5	58	2860	N.r.	1208	339	1328	89	762	46	1370	174	0.2	0.1	3.13	433	2000
SP-5	9.6	N.a.	N.a.	N.a.	728	N.a.	N.a.	89	734	44	N.a.	N.a.	N.a.	N.a.	N.a.	433	2003
SP-6	9.7	98	5820	N.a.	N.a.	N.a.	N.a.	N.a.	N.a.	N.a.	1370	187	0.4	0.1	2.8	412	2007

SP-6	9.68	21.2	3850	0.1	1173	285	1334	88.5	697	40.8	1280	177	0.45	0.19	3.70	512	2011
Sp-7	7.1	40	N.a	N.a	N.a	N.a	514	N.a	N.a	N.a	192	16	12.8	3.00	N.a	N.a	2000
Sp-7	7.2	68	2210	N.a.	N.a.	N.a.	N.a.	N.a.	N.a.	N.a.	530	30	16.5	7.7	0.1	134	2007
SP-8	6	86.5	505	N.a.	N.a.	N.a.	N.a.	N.a.	N.a.	N.a.	37	19	10	20	0.1	214	2007
SP-8	6.91	24.3	1492	0	1220	1.11	1347	10.8	52.1	13	540	33.9	19.7	9.85	0.77	151	2011
SP-11	7.5	46	560	N.r.	488	2.44	614	10	50	20	280	13.1	6.4	1.5	0.04	128	2000
SP-13	8.2	46	623	N.r.	598	6.49	780	9	40	16	342	18.1	5.2	3.3	0.04	144	2000
SP-13	N.a.	N.a.	N.a.	N.a.	N.a.	N.a.	N.a.	30	40	16	N.a.	N.a.	N.a.	N.a.	N.a.	144	2003
SP-14	8.2	92	4470	N.a.	N.a.	N.a.	N.a.	N.a.	N.a.	N.a.	1150	64	1.6	0.2	1	219	2007
SP-15	5.2	20	60	N.a.	N.a.	N.a.	N.a.	N.a.	N.a.	N.a.	5	3	1.6	0.4	0	124	2007
SP-15	7.29	23.7	1500	0	1137	2.52	1418	10.7	63	13.7	495	31.7	16.6	6.51	0.79	144	2011
SP-16	7.56	23.5	868	0	586	2.08	748	17	94.5	2.17	206	27.4	38.5	44.3	0.59	114	2011

Not all springs from the literature (Table 4.4) have been located during this survey. Therefore, the samples collected in this survey are from the springs in the Abaya fault. Sample AB-18-W03 is collected from a hot spring, not previously sampled. It is in the large hydrothermally altered area on the Abaya fault within a larger area where several springs, some gas rich others only water are present.

The Chemical composition of water samples from the current survey show concentrations of sodium that ranges from 5 to 540 mg/kg, potassium 9-55 mg/kg, calcium 2 to 90 mg/kg and magnesium 0.5 – 65 mg/kg. The analysis result of the chemical compositions of water samples (in mg/kg) from current survey is presented in Table 4.5. The major chemical constituents in the collected samples are presented in a pie plot (Figure 4.25).

The molecular ratio from the chemical concentration of water samples is used to elucidate whether the different water features originate from the same source or not and to determining the system temperature as high or low qualitative (Arnórsson, 2000). Water samples with similar molecular ratio of Cl/SO_4 and Cl/B will show as they might have originated from the same source with similar rock environment. Water samples which have a relatively high Na/Mg ratio and low Na/K ratio might indicates high deep temperature being closest to the major upflow zone (Ellis and Wilson, 1963 cited in Arnórsson, 2000). Accordingly, water samples AB-18-W05, AB-18-W06 and AB-18-W07 have shown similar Cl/SO_4 and Cl/B ratio, which might indicate that they have originated from same source with similar rock environment. The water samples AB-18-W05, AB-18-W06 and AB-18-W07 have also shown high Na/Mg ratio which might indicate high deep reservoir temperature. One sample, AB-18-W03 shows very low Na/K ratio that may also indicate high deep reservoir temperature. The molecular ratio from the chemical concentration of water samples in the current study is presented in Table 4.6.

The stable isotope composition of water samples from the study area is presented in Table 4.7 and displayed along Global Meteoric water lines (GMWL), Addis Ababa (AddMWL) and African Meteoric Water Lines (AfrMWL) all from (Levin, et al., 2004) in Figure 4.26. The analysis result of the gas samples from the current survey show that they have very low H_2S concentrations and high concentrations of CO_2. The chemical composition of the gases is presented in Table 4.8.

Table 4.5: *Chemical composition of water samples collected in Abaya from the current survey, in mg/kg.*

Sample ID	pH	T(°C)	SiO_2	Na	K	Ca	Mg	Fe	Al	B	CO_2	SO_4^{2-}	HCO_3^-	CO_3^{2-}	Cl^-
AB-18-W01	6.39	41.4	119.1	219.5	30.55	39.45	43.29	0.092	0.127	0.140	542.8	20.97	397.32	0.18	99.69
AB-18-W02	5.94	67	138.6	523.8	33.80	18.31	6.049	1.362	0.377	0.291	948.9	16.79	422.77	0.08	55.33
AB-18-W03	5.4	88.1	116.8	5.987	9.301	2.235	0.544	0.079	0.063	0.007	10.2	104.8	1.43	0	1.573
AB-18-W04	6.08	67.2	147.1	492.7	34.32	19.22	8.373	0.239	0.173	0.293	865.9	18.45	571.43	0.22	50.63
AB-18-W05	5.94	67	142.9	533.5	34.20	16.51	5.857	0.088	0.074	0.286	N.a.	14.51	0	0	54.52
AB-18-W06	6.23	67.3	142.9	526.6	33.60	16.66	5.603	1.278	0.186	0.291	1395.5	14.79	938.48	0.38	52.69
AB-18-W07	6.4	67.7	142.5	530.4	33.70	16.38	5.622	1.355	0.150	0.296	1356.7	14.17	1092.39	0.65	53.21
AB-18-W08	6.55	56.8	189.1	431.5	51.29	87.65	61.86	1.104	0.033	0.309	1730.4	11.07	1471.86	1.48	51.79
AB-18-W09	6.84	67.2	149.5	522.3	35.41	19.71	8.712	0.462	0.119	0.295	1294.7	14.00	1397.17	2.31	53.35

***Table 4.6**: Molecular ratio of water samples from the study area*

Sample Name	Na/Mg(mg/kg)	Na/K(mg/kg)	Cl/SO4(mg/kg)	Cl/B(mg/kg)
AB-18-W01	5.070	7.183	4.754	714.392
AB-18-W02	86.597	15.498	3.295	190.259
AB-18-W03	11.007	0.644	0.015	239.243
AB-18-W04	58.837	14.356	2.745	173.044
AB-18-W05	91.078	15.600	3.757	190.750
AB-18-W06	93.987	15.676	3.564	181.191
AB-18-W07	94.346	15.738	3.756	179.791
AB-18-W08	6.976	8.413	4.678	167.616
AB-18-W09	59.954	14.750	3.809	180.607

***Table 4.7:** Analytic results of stable isotope composition of water samples from the study area; Water samples collected in 1977 were by Craig, in 2011 were by RG geothermal Ltd*

Sample	□ $^{18}O/^{16}O$	Stdev	□ $^{3}H_2/^{2}H_2$	Stdev	Date
AB-18-03	8.21	0.03	20.49	0.17	This paper
AB-18-04	-3.02	0.05	-7.34	0.38	This paper
AB-18-W06_1	-3.11	0.02	-6.9	0.71	This paper
AB-18-W06_2	-3.12	0.02	-7.7	0.57	This paper
AB-18-W09_1	-3	0.05	-7.48	0.81	This paper
AB-18-W09_2	-3.01	0.05	-6.86	0.36	This paper
Boloche-14	-0.13	N.a.	0.1	N.a.	2011
SP-15	- 2.98	N.a.	-9.4	N.a.	1977
SP-15	-3.07	N.a.	-8.16	N.a.	2011
SP-16	-2.9	N.a.	-7.1	N.a.	1977
SP-16	-2.74	N.a.	-6.99	N.a.	2011
SP-6	-1.06	N.a.	-11.3	N.a.	2011
SP-8	-2.88	N.a.	-8.7	N.a.	1977
SP-8	-3.01	N.a.	-9.64	N.a.	2011

***Table 4.8**: Chemical composition of gas samples (in mmol/kg) collected from the study area*

Sample name	H_2 [mmol/kg]	N_2 [mmol/kg]	CH_4 [mmol/kg]	O_2 [mmol/kg]	Ar [mmol/kg]	H_2S [mmol/kg]	CO_2 [mmol/kg]
AB-19-G04	N.a	N.a	N.a	N.a	N.a	1.19	11223
AB-19-G05	N.a	N.a	N.a	N.a	N.a	2.64	72414
AB-19-G06	N.a	N.a	N.a	N.a	N.a	3.40	106894
AB-19-G02	0.005	1.16	0.543	0.44	0.02	0.14	43560
AB-19-G04	0.005	2.83	0.0.15	1.37	0.06	0.14	13640
AB-19-G06	0.003	15.8	9.000	5.91	0.33	0.31	93148

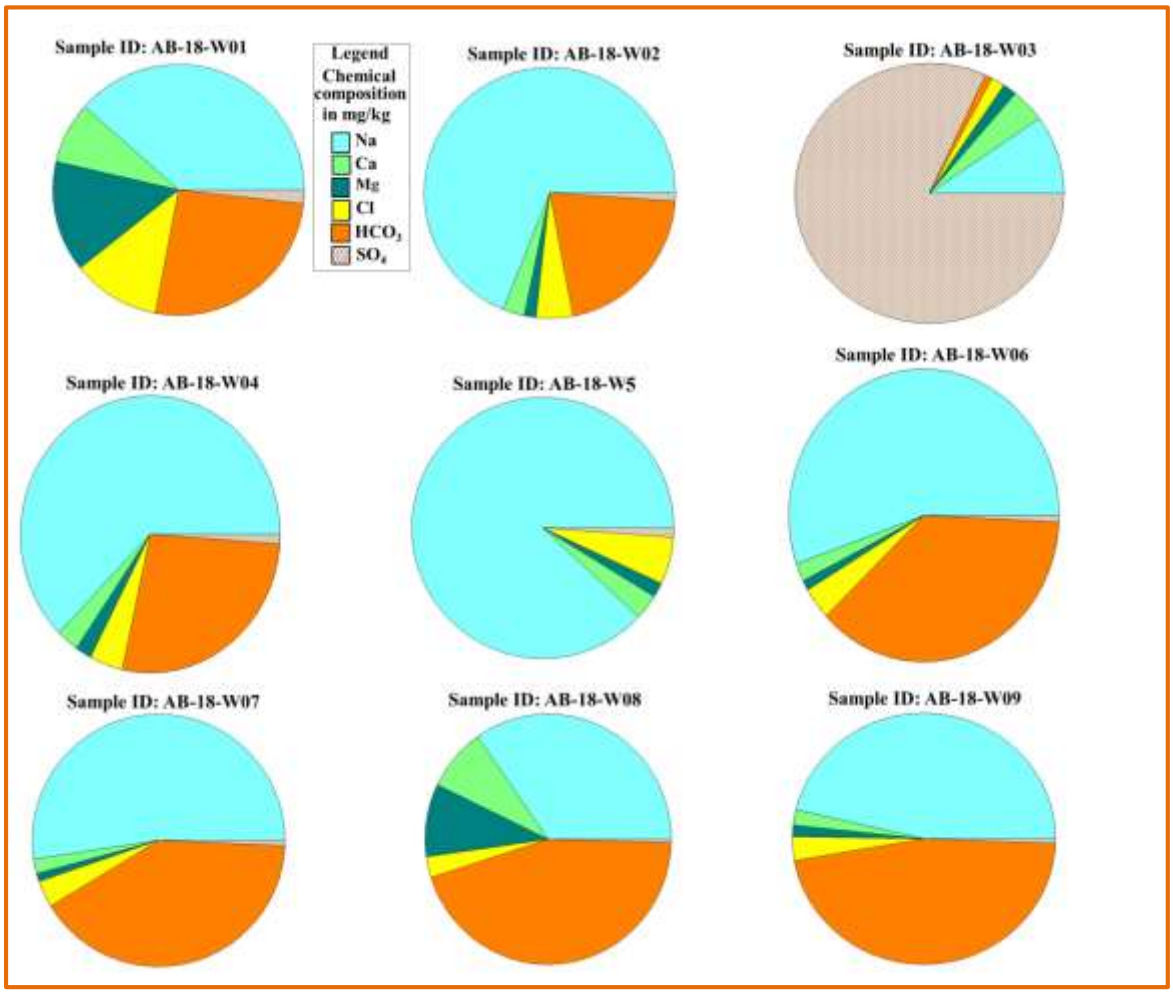

***FIGURE 4.25**: Pie plot showing the major chemical constituents in analyzed water samples from study area*

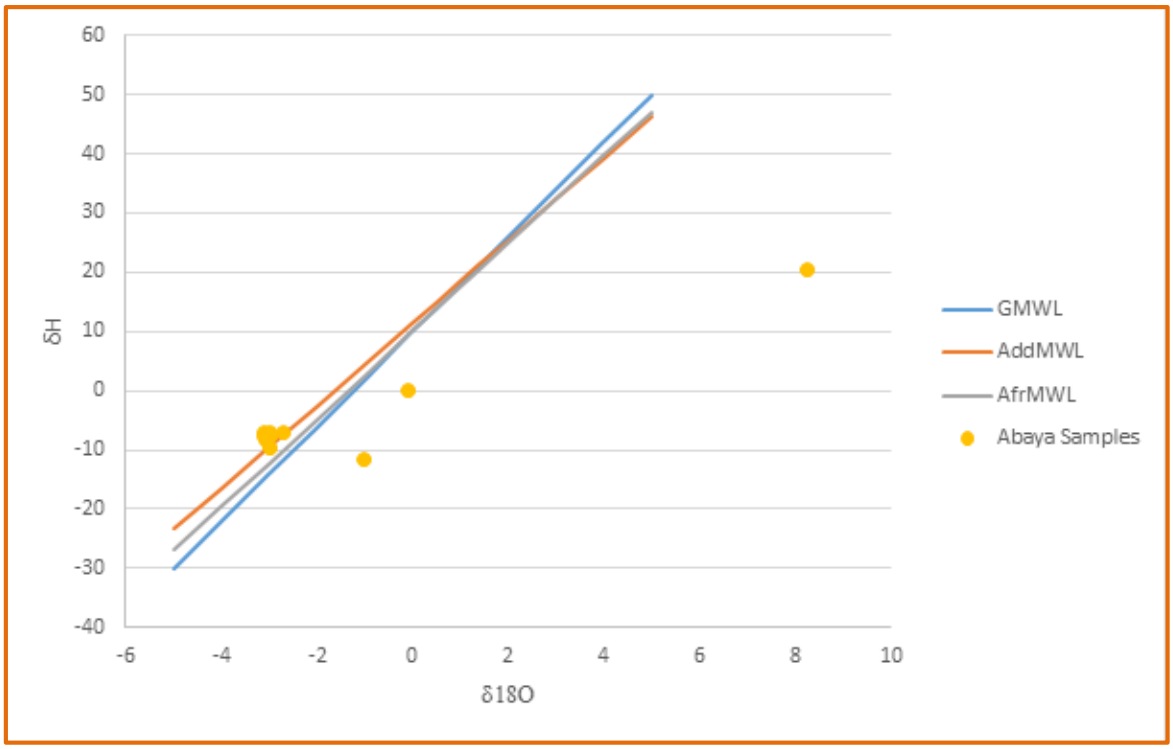

***FIGURE 4.26**: Plots of isotopic fractionation of waters collected in the study area (yellow circles) displayed with reference to the Global Meteoric Water Line (GMWL) in blue, Addis Ababa Meteoric Water Line (Orange) and African Meteroic Water Line (Grey). Most samples show strong agreement to the AddMWL and one sample, AB-18-W03 shows an enriched isotopic compoostion*

4.3.2. Chemical classifications of waters

The classification water type in geothermal system is to see if they are suitable for the application of chemical geothermometers (Giggenbach and Goguel, 1989). Near neutral to slightly alkaline pH samples with relatively low SO_4 and high chloride are important for applications of chemical geothermometers. Samples which are more alkaline with high SO_4 are not suitable for the application of chemical geothermometers. The classification is made upon the basis of contents of the major dissolved chemical species in the water samples. Such chemical species includes Ca, Mg, Na, K, HCO_3, CO_3, SO_4 and Cl.

The waters in the study area are primarily of near neutral pH and are primarily of the sodium bicarbonate types. The major types of water identified are presented in Table 4.9.

The anion ternary diagram plots using the sample results from current study shows that most water samples as peripheral water, with only two water samples suggested to be steam heated and mature waters (Figure 4.27). The Giggenbach ternary diagram (Figure 4.28) suggests most spring water to be immature and or partially equilibrated waters. The piper diagram is plotted using milliequivant percentage of cations (Na, Ca and Mg) and anions (SO_4, HCO_3 and Cl) therefore suggest clustering nature between most of the water samples (Figure 4.29).

Table 4.9: *The water types identified for the study area*

Sample Name	**Location**	**Sample date**	**water type**
AB-18-W01	AB Fault	2.10.2018	Na-Mg-HCO3-Cl
AB-18-W02	AB Fault	2.10.2018	Na-HCO3
AB-18-W03	AB Fault	3.10.2018	SO4
AB-18-W04	AB Fault	3.10.2018	Na-HCO3
AB-18-W05	AB Fault	25.11.2018	Na-
AB-18-W06	AB Fault	26.11.2018	Na-HCO3
AB-18-W07	AB Fault	26.11.2018	Na-HCO3
AB-18-W08	AB Fault	26.11.2018	Na-HCO3
AB-18-W09	AB Fault	27.11.2018	Na-HCO3

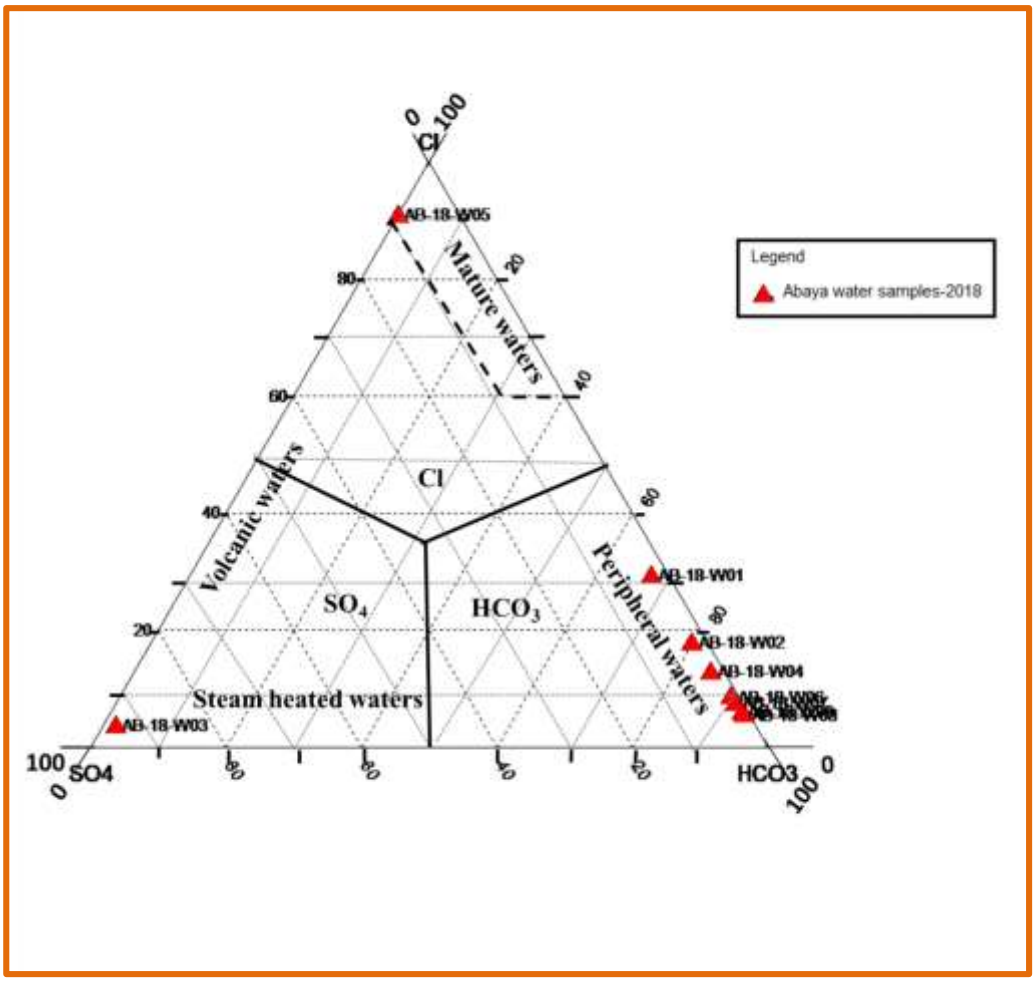

***FIGURE 4.27**: Anion diagram of the thermal waters sampled from the springs in the study area. All waters, apart from two, are suggested to be surface waters with CO_2 dominant species*

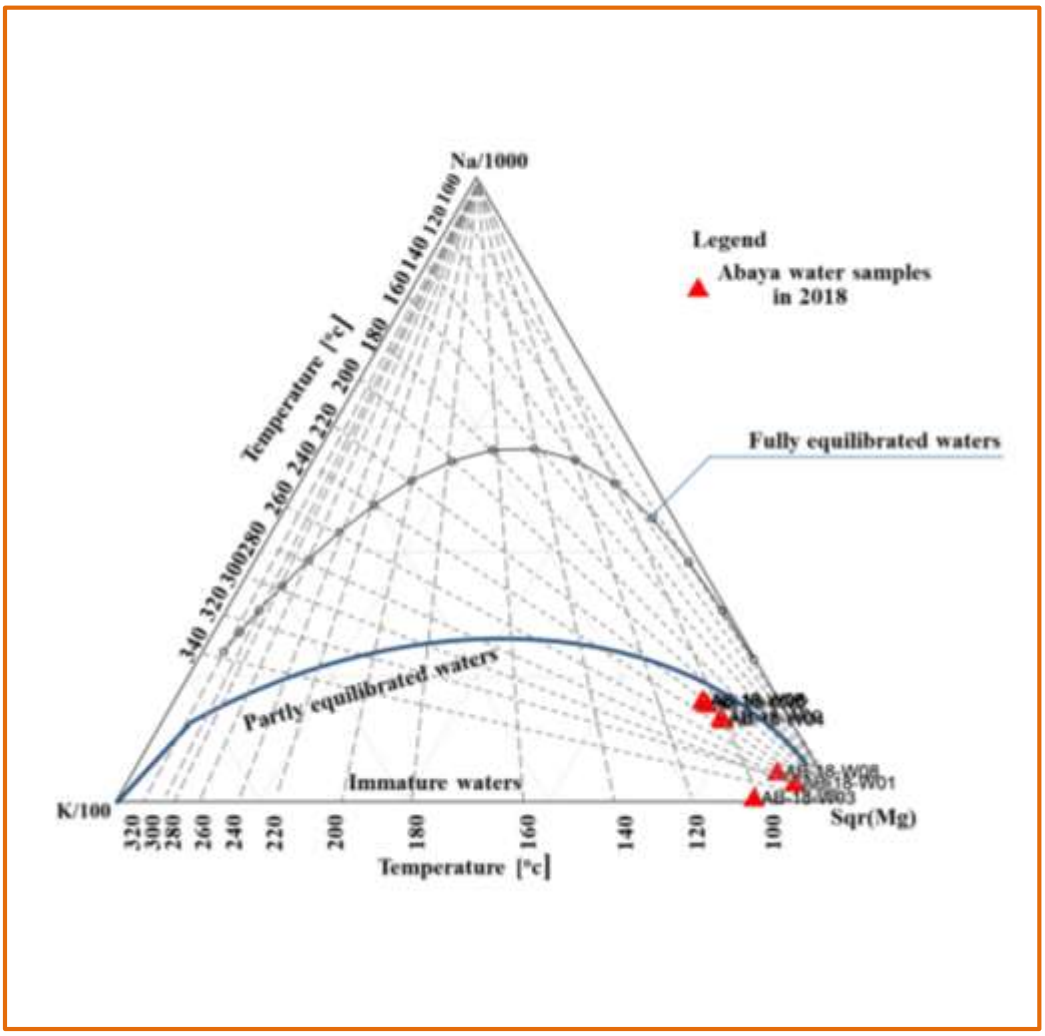

FIGURE 4.28: *Giggenbach diagram suggests most water samples collected in the area are of unequilibrated to partially equilibrated waters*

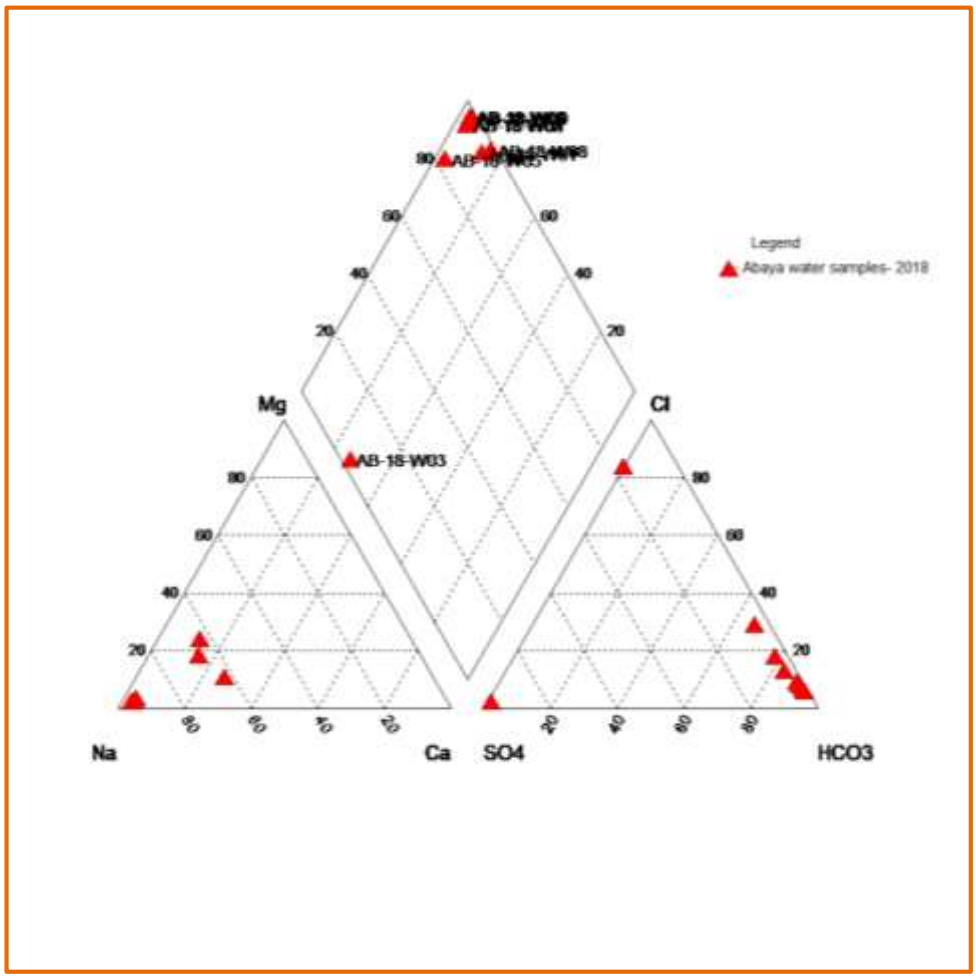

FIGURE 4.29: *Piper diagram of ion contents for water samples in the study area*

4.3.3. Estimates of deeper reservoir temperatures

Chemical Geothermometers are developed on the basis of temperature dependent chemical equilibrium between the water and the minerals at the deep reservoir conditions (Arnórsson, 2000). They are all also based on the assumption that there is adequate supply of solid phases for the fluid to be adequately saturated with the constituents used for geothermometry and no mixing of hot and cold water occurs as water flows to the surface. Therefore, the water preserves its chemical composition during its ascent from the reservoir to the surface (Giggenbach, 1988, Arnórsson, 2000, Murithi, 2012). But the assumption of the preservation of water chemistry may not always hold, because the water composition may be affected by processes such as cooling and mixing with waters from different

reservoirs. During the ascent of geothermal waters from a deep reservoir to the surface, they may cool by conductive heat loss as they travel through cooler rocks (conductive cooling) or by boiling because of decreasing hydrostatic head (adiabatic cooling). The conductive cooling can bring about some modification in the chemical composition of the ascending water by mineral dissolution or precipitation (Arnórsson, 2000). This is because cooling by conduction does not by itself result in any changes in the chemical and isotopic composition of the water rather it may change the degree of saturation with respect to both primary and secondary minerals. Boiling invariably causes changes in the composition of rising geothermal waters. These include degassing and an increase in the solute content of the water due to steam loss.

Geothermometers are used to estimate subsurface temperatures (temperature expected to be encountered by drilling) and to predict changes in a reservoir during utilization (Arnórsson, 2000, Murithi, 2012, Wanjie, 2012). Geothermometers have been classified into three groups; liquid geothermometers (silica and cation geothermometers), gas geothermometers and isotope geothermometers. The most important chemical geothermometers are the silica (quartz and chalcedony) and Na/K geothermometers (Fournier and Potter, 1982, Arnórsson et al., 1983, Giggenbach, 1988 and Arnórsson, 2000). The limitations to these thermometers are that other elements can influence the accuracy such as Ca and Mg for the Na-K-Ca thermometers. The silica geothermometer depends on equilibrium between the reservoir rock and the fluid at the reservoir temperature (Arnórsson, 2000). The stable silica mineral varies with temperature. At temperatures higher than 180 °C quartz is the stable form of SiO_2 whereas at temperatures below 120 °C the chalcedony is the stable form of SiO_2. The silica level in the fluid where equilibrium reigns is used to predict the temperature.

In a place where the shallow ground water table is deep in the subsurface, springs are not available; water geothermometers cannot be used to predict the subsurface temperatures. This has called the early scientists for the development of gas geothermometers from mainly of fumaroles (e.g. D'Amore and Panichi, 1980). Based on the concentrations of CO_2, H_2S, and H_2 and gas concentration ratio of CO_2/H_2 and H_2S/H_2, Arnorsson and Gunnlaugsson (1985) proposed temperature functions for gas geothermometers applicable to fumarolic steam.

The chemical data on hydrothermal waters in the Ethiopian Rift and probable deep-water temperatures deduced from silica and Na-K geothermometers were reported by UNDP (1973). Accordingly, subsurface temperatures of more than 200°C have been estimated. Birhanu Gizaw (1985) identified and evaluated the mixing processes by chemical means and mixing models; applied newly calibrated chemical geothermometers; and made preliminary solution-mineral equilibria studies based on the existing database. As a result, the estimated temperature for the northwest Abaya area springs based on mixing models is in excess of 200°C. The reserviour temperature estimated from samples collected in and around the Abaya region is reviewed from various data bases. It shows that samples collected from Spring 5 and spring 6 show water of partially to fully equilibrated waters with reservoir temperature greater than 200 °C (Table 4.10).

Based on the fluid and gas chemistry of the samples collected and analysed in this study, the estimated equilibrium temperature was calculated.The chemical geothermometers show high temperatures from all samples (Table 4.11).

The concentrations and concentration ratios of various geothermal gases are used to estimate the temperature of the geothermal reservoir, assuming certain equilibrium between mineral and steam (Arnórsson and Gunnlaugsson, 1985). Based on the gas concentrations from the current survey, the estimated reservoir heat was calculated using geothermometers from Arnorsson (2000) and thermometers therein. The extremely high CO_2 concentration evidently indicates very high reservoir temperatures, greater than 400 °C. These values are almost certainly too high. But the average of the geothermometers, column AVE in Table 4.12 suggest reservoir temperatures of greater 200 °C.

Table 4.10: *Reservoir temperature based on silica and cation geothermometers from different literature sources according to (Fournier, 1977, Truesdel, et al, 1977, Tonani, 1980, Giggenbach, 1988). Quartz-no steam loss (conductive cooling), (Giggenbach) TQC, toC= (1309)/(5.19-logSiO2)-273.15, t=0-250. Quartz-maximum steam loss (adiabatic cooling), (Giggenbach) TQA, t oC = (1522)/(5.75-logSiO2)-273.15, t=0-250. Na/K (Fournier) TNa/K-F, toC = (1217)/(log(Na/K)+1.483)-273.15,t>150. Na/K (Truesdel), TNa/K-T, toC = (855.6)/(log(Na/K)+0.8573)-273.15 , t>150. K/Ca (Tonani), T K/Ca-T = (1930)/ (3.861-log (K/Ca) -273.15. Sample collected in 2003 was collected by Asfaw Teclu, in 2007 by Salahadin Ali and Lemma Kassa, and in 2011 by RG Geothermal Ltd.*

Sample Name	**T_{QC} [ºc]**	**T_{QA} [ºc]**	**$T_{Na/K-F}$ [ºc]**	**$T_{Na/K-T}$ [ºc]**	**$T_{K/Ca-T}$ [°C]**	**Year**
Sp-1	159	151	279	269	295	2000
Sp-1	147	141	291	285	193	2007
Sp-2	34	43	231	205	212	2000
Sp-3	149	142	235	210	189	2000
Sp-4	163	154	196	162	364	2000
Sp-5	240	216	238	215	N.a	2000
Sp-5	240	216	250	N.a.	N.a.	2003
Sp-6	141	136	231	205	212	2000
Sp-6	235	212	245	224	N.a.	2007
Sp-6	252	226	246	225	N.a.	2011
Sp-7	154	147	173	133	472	2007
Sp-8	185	172	413	473	266	2007
Sp-8	162	153	180	143	258	2011
Sp-14	186	173	171	132	580	2007
Sp-15	70	75	441	520	264	2007
Sp-15	159	151	182	145	266	2011
Sp-16	145	139	244	222	183	2011

Table 4.11: *Reservoir temperature based on silica and cation geothermometers from the current study according to (Fournier, 1977, Truesdel, et al, 1977, Tonani, 1980, Giggenbach, 1988). Quartz-no steam loss (conductive cooling), (Giggenbach)* T_{QC}*,* $t^oC = (1309)/(5.19-\log SiO_2)-273.15$*, t=0-250. Quartz-maximum steam loss (adiabatic cooling), (Giggenbach)* T_{QA}*,* $t\ ^oC = (1522)/(5.75-\log SiO_2)-273.15$*, t=0-250. Na/K (Fournier)* $T_{Na/K-F}$*,* $t^oC = (1217)/(\log(Na/K)+1.483)-273.15$*,t>150. Na/K (Truesdel),* $T_{Na/K-T}$*,* $t^oC = (855.6)/(\log(Na/K)+0.8573)-273.15$ *, t>150. Na/K (Giggenbach),* $T_{Na/K-G}$*,* $t^oC = 1390/(1.750+(\log(Na/K))-273.15$*. K/Ca (Tonani),* $T_{K/Ca-T} = (1930)/(3.861-\log(K/Ca)-273.15$*.*

Sample ID	T_{QC} [°c]	T_{QA} [°c]	$T_{Na/K-F}$ [°c]	$T_{Na/K-T}$ [°c]	$T_{Na/K-G}$ [°c]	$T_{K/Ca-T}$ [°C]
AB-18-W01	147	141	247	225	260	213
AB-18-W02	156	149	182	145	200	194
AB-18-W03	146	140	669	1011	619	322
AB-18-W04	160	152	188	152	205	322
AB-18-W05	158	150	180	142	199	271
AB-18-W06	158	150	181	320	199	269
AB-18-W07	158	150	181	143	199	271
AB-18-W08	176	165	232	207	246	199
AB-18-W09	161	153	186	149	203	262

Table 4.12: *The calculated estimated reservoir temperatures based on gas geothermometer from Arnorsson (2000);* $T^oc = 304.1-39.48log(H_2S/H_2)$, $T^oc = 227.2+20.99log(H_2)$, $T^oc = 311.7-66.72log(CO_2/H_2)$, $T^oc = 246.7+44.8log(H_2S)$, $T^oc =44.1+269.25log(CO_2)-76.88\ [log(CO_2)]^2 + 9.52[log(CO_2)]^3$. *The gas and gas concentration ratio is given in mmol/kg of steam. N.c = not calculated*

Sample name	**H_2S/H_2**	**H_2**	**CO_2/H_2**	**H_2S**	**CO_2**	**AVE**	**STDEV**
AB-19-G04	**N.c**	**N.c**	**N.c**	**250**	**418**	**N.c**	**N.c**
AB-19-G05	**N.c**	**N.c**	**N.c**	**266**	**541**	**N.c**	**N.c**
AB-19-G06	**N.c**	**N.c**	**N.c**	**271**	**576**	**N.c**	**N.c**
AB-19-G02	**249**	**229**	**144**	**208**	**501**	**266**	**122**
AB-19-G04	**247**	**229**	**158**	**208**	**428**	**254**	**92**
AB-19-G06	**226**	**225**	**128**	**224**	**564**	**273**	**150**

4.4. Remote Sensing, Soil CO_2 Flux and Temperature Measurement

In this section, different analyses (remote sensing and geophysical data) and the measurement data analysis of the soil CO_2 flux and soil temperature from field work is presented. Remote sensing analyses are employed in order to examine the different lithological units and structural elements in the area. Secondary geophysical data analysis is to understand the subsurface layers according to their resistivity characteristics (e. g. low resistivity implies weak zone) and to elucidate the possible reservoir and heat source for the geothermal field of the area. Soil gas flux measurements are for the purpose of identification of subsurface/hidden faults. These faults allow greater fluid flow than elsewhere.

4.4.1. Remote Sensing Data Analysis

Currently, most of the Earth surface is covered by digital elevation model (DEM) data, Landsat, Aster and other satellite imagery, which are freely available. The aim of this contribution is to provide basic information on data types, which could be used for geological interpretation.

Implementation of remote sensing data and their interpretation can provide useful geological and structural information. Morphology can be easily visualized using DEMs in the form of colored elevation maps combined with shaded relief. Some lithologies (rock types) can be identified from morphology, but the main usage of DEM is in structural interpretation. Best approach for identification of lithological features such as lithological boundaries or hydrothermal alteration zones is to combine RGB composites from visible and infrared bands of optical satellite imagery such as Landsat.

According to Tadiwos Chernet, (2011), analyses of remote sensing data provided some insight into how the structural fabric had a control on the distribution of the hydrothermal manifestations identified as hydrothermal fields. These satellite image processing methods are widely used in lithological and structural mapping (e.g., Solomon kebede and Gebreab Melke, 2006; Mwaniki et al., 2015; Ali and Pour, 2014; Raharimahefa and kusky, 2006; Chatterjee, 2003; Al-Shumaimri, 2012; Ali et al., 2012).

Extrusive igneous rocks (lavas and domes) pose a huge problem for image analysis because they are usually interbedded with sediments and pyroclastic rocks. The differentiation between sediments and volcanic rocks can be solved if we can observe associated volcanic landforms such as relics of cones or lava flows. A larger problem is the discrimination between the pyroclastic products and the volcanic rocks themselves. The exact determination of pyroclastic rocks from their volcanic counterparts typically requires verification in the field. Areas covered by volcanic rocks display dendritic pattern of drainage system and stand out as positive topographic features (Martínek, 2018).

Remote sensing imagery at the scale of 1: 50,000 can significantly help with mapping unit boundaries. Details on units/structures and particular lithologies must be checked in the field as it is discussed in the above paragraph. But spectral mapping has limits. It is quite common that high lithological contrast of two rocks with similar composition but different texture (e.g. granite – rhyolite) is not visible in the images (they can appear with similar colors because of similar composition). On the other hand, very significant spectral expression of two rocks may represent only minor change in mineralogy (e.g. clayey sandstone, Fe-oxide rich sandstone, organic rich sandstone). For the purposes of geological mapping, it is best if the rocks are part of a single unit (Gad and Kusky, 2006).
The study area has considerable vegetation cover which imposes a significant effect up on using remote sensing method. However, such problem is tackled to some extent by using the method in combination with field observations. In the current study, different remote sensing techniques; pre-processing, band combination and band ratio are applied on Landsat 8 OLI data to stand out the different features; lithological units, alteration minerals, geologic structures and vegetation.

4.4.1.1. Pre-processing

Images used for geological interpretation usually underwent several phases of pre-processing. These include georeferencing and/or map transformation to reduce spatial distortion and to fit to available map data; spatial filtering to “clean” poor quality data or to sharpen image.

Remote sensing data were pre-processed where layer stacking and image subset were performed before proceeding to the main processing techniques: band combination and band ratioing. This pre-processing makes satellite image interpretable for a specific use. Landsat 8 image has 11 bands which are of 30 m resolution except band 8, which is of 15 m resolution. In this study, only bands 1 to 7 were stacked because the other bands are not useful for distinguishing lithologies and delineating structures.

4.4.1.2. Enhancement

Enhancement is a technique/method which can be used to identify lithologies and structures from optical imagery. Enhancements are used to make image easier for visual interpretation and thus analysis and extraction of more (geological) information is possible. These techniques modify attributes of an image to make it more suitable for a given task and a specific observer; for geological interpretation in this case, by maximizing clarity, sharpness and details of features of interest.

Contrast enhancement involves changing the original values so that more of the available range is used, thereby increasing the contrast between targets and their backgrounds. There are many different techniques and methods of enhancing contrast and detail in an image. Filtering and stretching are the enhancement techniques applied in this study.

4.4.1.3. RGB (Band Combination) Combination

There are just a few spectral bands in multispectral images; there are many minerals and rocks, therefore it is not usually possible to precisely identify lithology. The basic approach for multispectral analysis is to try various band combinations to map lithological boundaries – different color often represents different lithology (Madani, 2014).

In this study, to enhance different lithologies and structures most used band combinations as RGB are Landsat 8 432,762,754 and 543, which enables identification of several lithologies. Lithological and structural identification is achieved by juxtaposing the data obtained from field observations with Landsat 8 image band combinations. Lava flows, pumiceous pyroclastic rocks (pumice and ash), hydrothermally altered rocks, lacustrine sediments, basalts and several normal faults. The nature of pyroclastic rocks may interfere with sedimentary rock. These are however mostly discernible by their proximity to volcanic

centers or volcanic rocks (Figure 4.30). Pyroclastic rocks such as pumice fall in the study area seem to be associated with centers such as Chericha, found outside the study area. Unsupervised classification of the Landsat 8 OLI image (Figure 4.30) depicts pumice fall and lacustrine sediments as whitish to grey (represented in circle). Vegetation is in green and water in white. Dark black color represents rhyolitic dome, scoriaceous lava flow and swampy area.

Landsat 8 image spectral bands 4, 3, 1 (natural color) as RGB composite, are used for recognizing different lithologies (Figure 4.31A). Fault patterns of the study area are also visible. Here each observed different colors represent different lithology. Rhyolitic lava flow is represented by red circles, (B) hydrothermally altered ignimbrite and pumiceous pyroclastic rocks are represented in cyan color rectangles, lacustrine deposits are represented by fire red rectangles and swamp areas are pink polygons. Vegetation appears dark green and water white. The composite RGB images of bands 7, 6, 2 also depicts various lithologies and structures (Figure 4.31A)**.** It works with bands sensitive to clay minerals. These are good for soil mapping, e.g. hydrothermal alteration zones are expressed here in yellow and brownish-yellow colors because they are abundant in clay minerals and Fe oxides**.** Recent rhyolitic lava flow appears dark brown; pumiceous pyroclastic rocks are shown as light yellow to white, Vegetation is in green and water is in blue.

Landsat 8 7, 5, 4 RGB band combination (Figure 4.31B) show recent rhyolitic lava flow as dark brown (represented in circle, A), hydrothermally altered ignimbrite and pumiceous units are in dark pink (represented in rectangle, B), lacustrine sediments are in white to grey (represented in polygon, C). Vegetation is in green and water in blue. Visible and near infrared bands (VNIR) Landsat 8 5, 4, 3 as RGB false color composite are used for understanding and mapping of vegetation cover (Figure 4.31B). Vegetation density in the study area is represented in red and water as cyan. This RGB combination highlights the boundaries between vegetated and outcrop areas. Higher values of the red color tone represent more densely vegetated areas, while lower values represent no vegetation or bare areas.

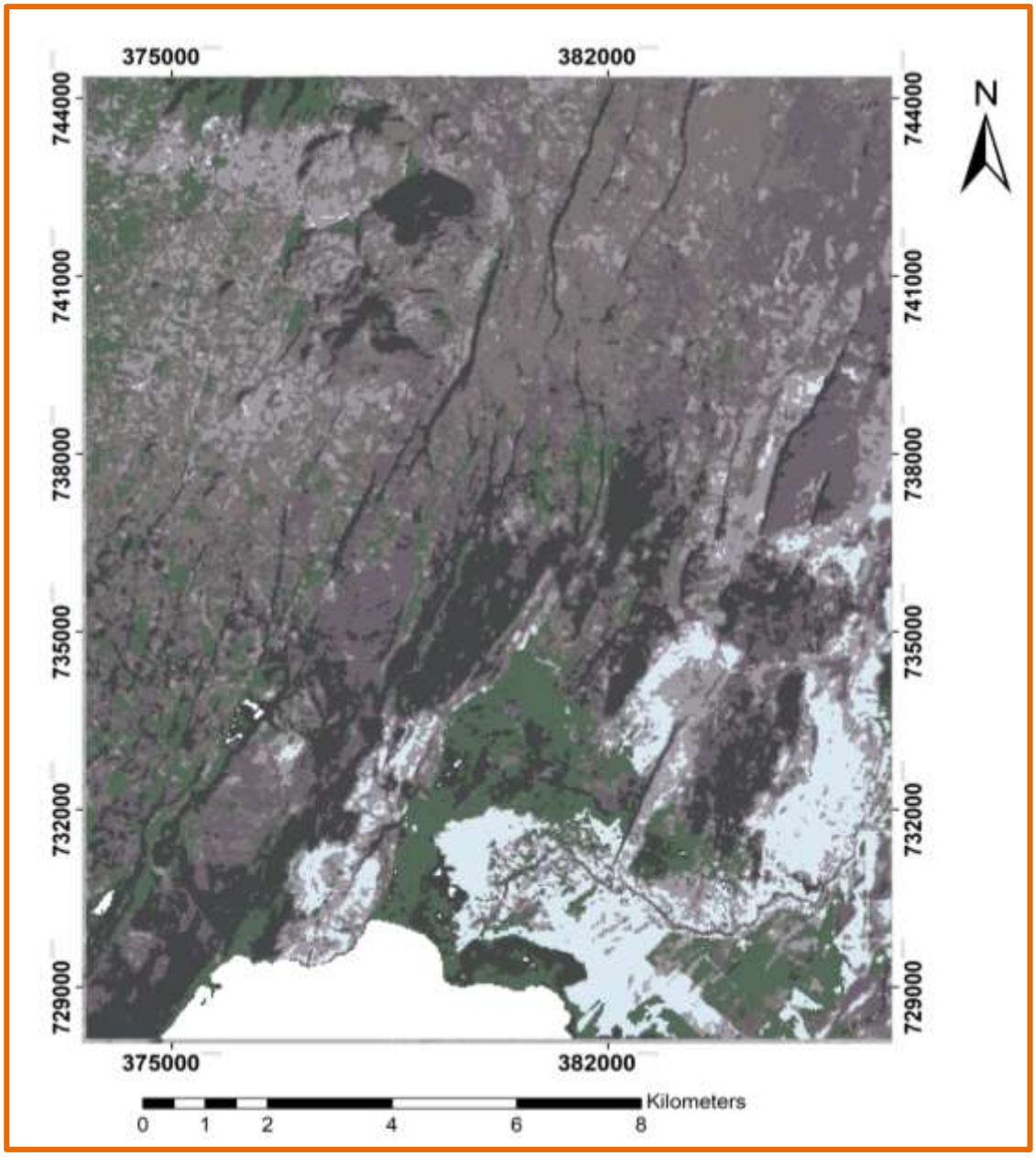

***FIGURE 4.30**: unsupervised classification of the Landsat 8 OLI imagery*

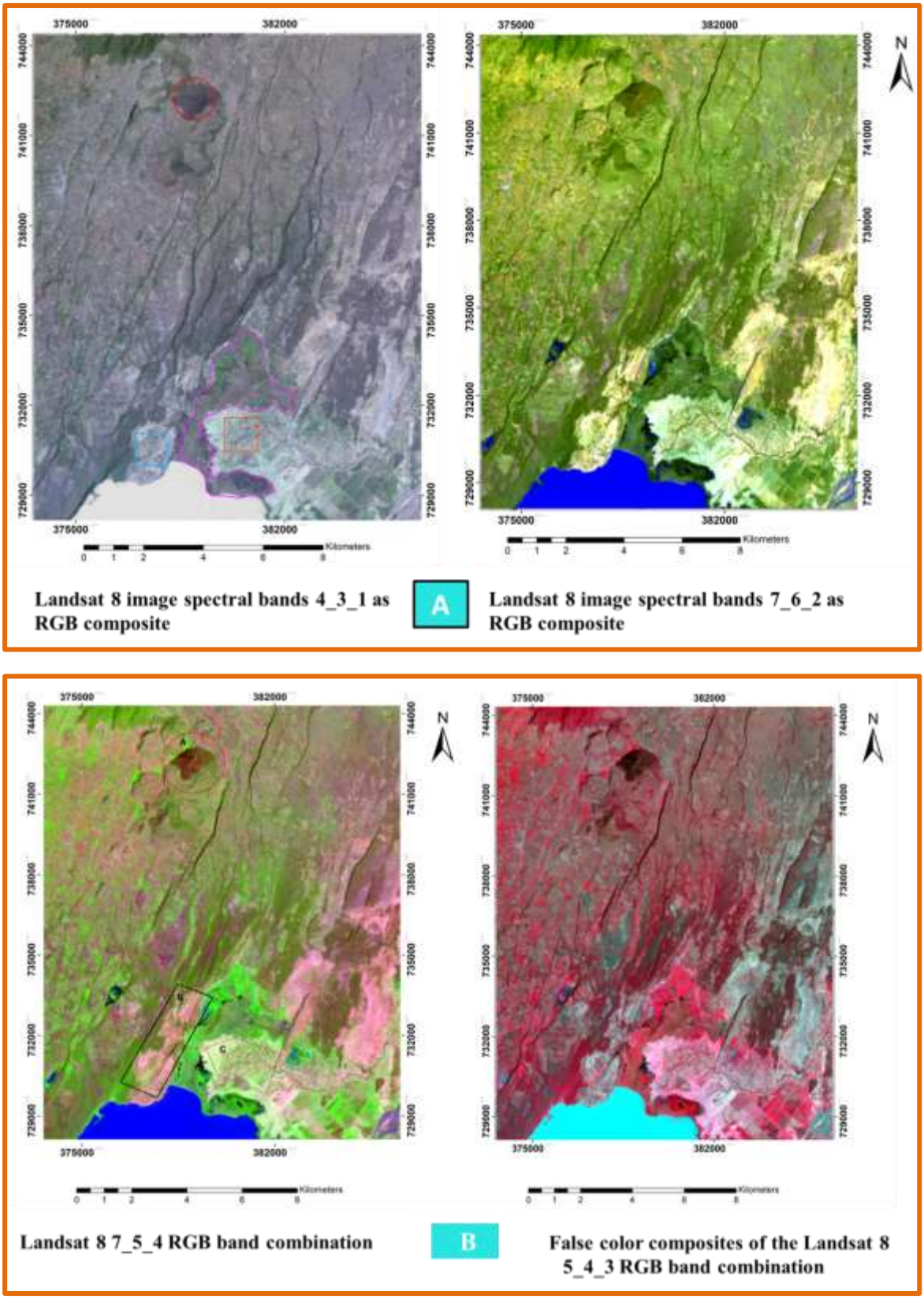

***FIGURE 4.31**: A. Landsat 8 image spectral bands 4_3_1 (left) and 7_6_2 as RGB composite (right). B. Landsat 8 7_5_4 RGB band combination (left) and False color composites of the Landsat 8 5_4_3 RGB band combination (right)*

4.4.1.4. Band Ratios and their composite images

Band ratioing is a technique where brightness values (digital numbers) of one band are divided by that of another band (Pour et al., 2015). Surface topography shadows may cause useless information in raw data of the satellite image like a false earth's surface. Band ratioing techniques help in improving the contrast and enhancement of compositional information through overpowering this useless information by allowing highlight some features that cannot be seen in raw data (Ali & Pour 2014).

Different band ratios were tested in this study, in order to enhance hydrothermally altered rocks and lithological units. The selection of bands is related to the spectral reflectance and position of the absorption bands of the mineral or assemblage of rocks to be mapped. Different authors refer the several types of band ratios for geological use important to enhance lithological features; Pour et al. (2015) refer to RGB image (4/2, 6/7, 6/5) band ratio for identification of hydrothermal alteration minerals and identification of lithology. Similarly for the same purpose, RGB image (7/5; 5/4; 6/7) band ratio was also used (Ali and Pour, 2014).

In the current study the band ratio method is used to create the RGB band combinations of the image using various efficient band ratio values. Different ratios have enabled to identify different features hydrothermal alterations, pyroclastic deposits, basaltic units, lacustrine sediments silicic centers and geologic structures. In this section, the different types of ratios calculated are also set in RGB color composite in order to improve the discrimination of mapped features found in the study area. The main features detected by band ratios and band combinations are then simply delineated using polygons.

In Landsat 8 OLI, band ratioing helped in different feature identification. In band ratio 5/7 image (Figure 4.32A), dark colours show hydrothermally altered ignimbrite and pumiceous pyroclastic rock (represented in circle). Lacustrine and alluvium sediments appear white (represented in polygon). Band ratio 4/2 image (Figure 4.32A) shows hydrothermally altered ignimbrite and pumiceous pyroclastic rocks appear both white (represented in rectangle). Dark colors represent silicic centers (represented in circle). Numerous fault densities of the study area are also clearly seen. Band combination into red, green and blue channels were also made to produce a false color composite imagery. Those images were

obtained using different band ratios. The RGB color composites of 7/5, 5/4, 6/7 band ratio depicts different features (Figure 4.32B). Here dark brown color show water, orange color show pyroclastic deposits (pumice and ash), purple color show basaltic outcrops and vegetation is represented by cyan color. Some pinkish colored areas (pink color in an orange as a background) can be related to the hydrothermal alteration. In the RGB color composites of 4/2, 6/7, 6/5 band ratio image (Figure 4.32B), outcrops are represented in light blue-light pink colour, vegetation in green and water in dark red. Strong blue represent young silicic centers and light pink altered rocks**.** The RGB color composites of 6/5, 6/5, 4/2 band ratio (Figure 4.32C) represent outcrops as light yellow to yellow (pumiceous pyroclastic rocks and hydrothermal alterations), vegetation in dark green and water in blue-dark blue. Dark black represents swamp area. In the RGB color composites of 6/5, 6/5, 6/7 band ratio (Figure 4.32C), outcrops are represented in light yellow-yellow, vegetation in blue – light blue and water in dark green.

The band ratio 6/7, 6/5, 4/2 as RGB colour composites image (Figure 4.32D), display outcrops in light green color and cyan, vegetation in red and water in blue. In RGB color composites image of 3/2, 5/7, 3/5 band ratio (Figure 4.32D), Outcrops are represented in light orange (lake sediment), dark blue (rhyolitic dome) and dark red (hydrothermal alteration and pyroclastic deposits), vegetation in light green-green and water in pink. The distinctive spectral colors and tones for the different lithological units found in each of the Landsat 8 images of the study area is presented in appendix VII.

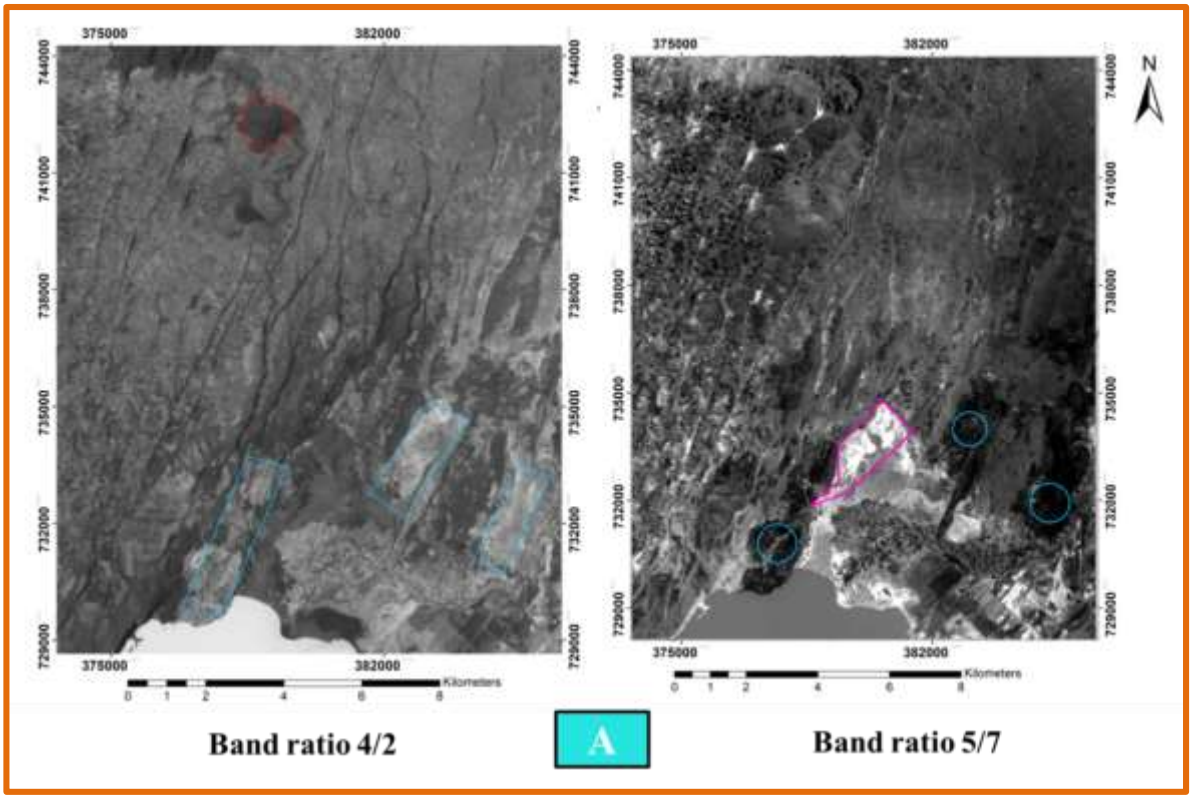
375000
382000
744000
741000
738000
735000
732000
729000
Kilometers
0 1 2 4 6 8
N
Band ratio 4/2
A
Band ratio 5/7

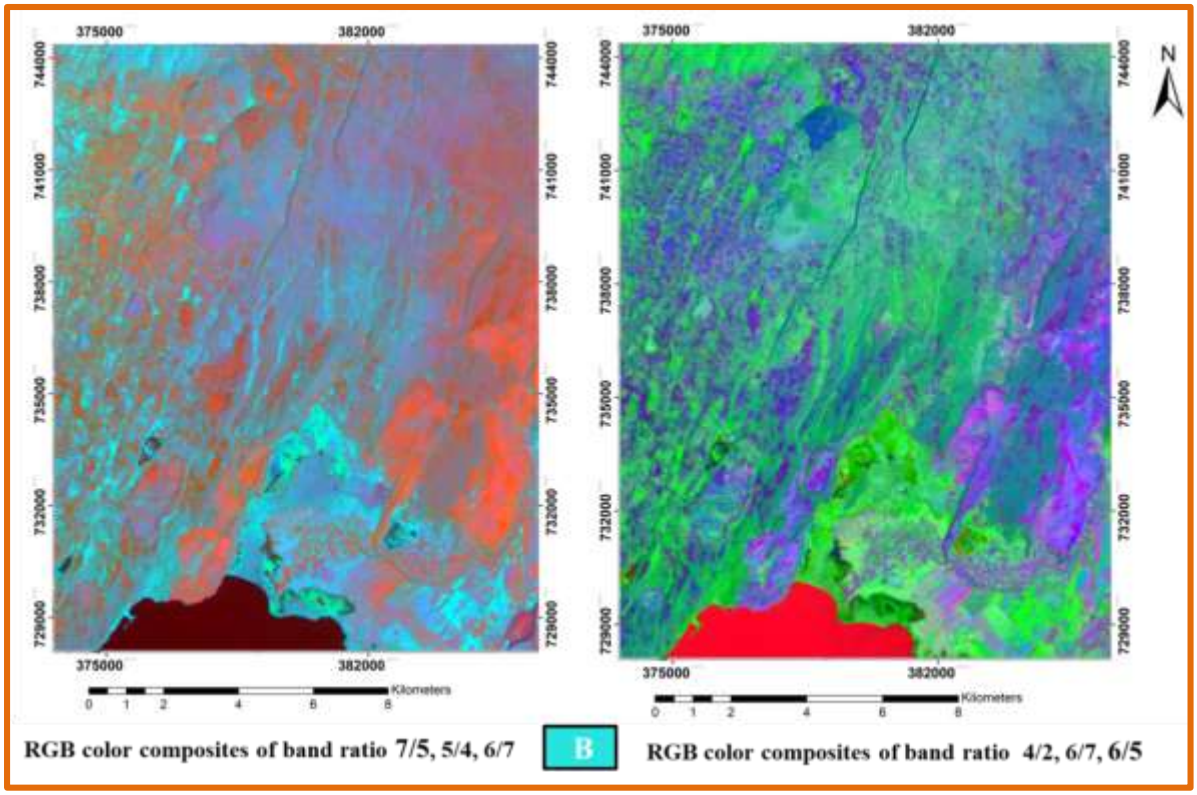

RGB color composites of band ratio 7/5, 5/4, 6/7 **B** RGB color composites of band ratio 4/2, 6/7, 6/5

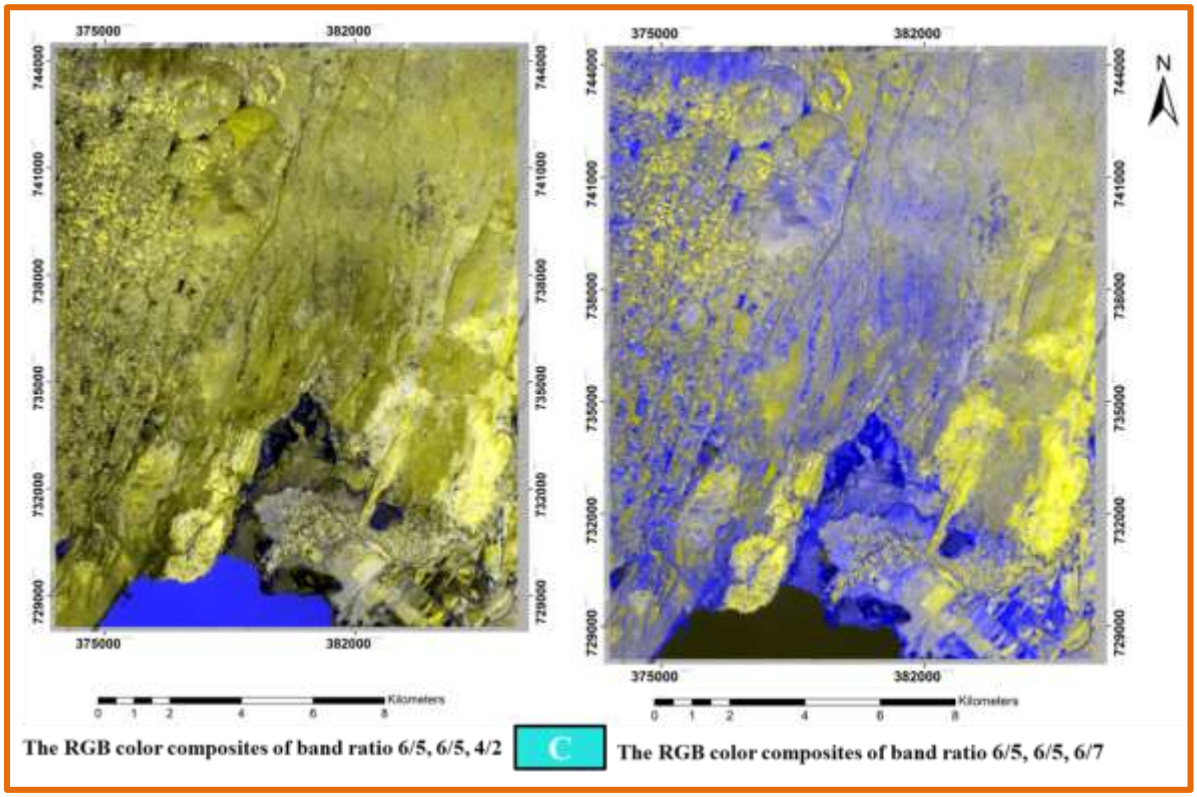

The RGB color composites of band ratio 6/5, 6/5, 4/2 **C** The RGB color composites of band ratio 6/5, 6/5, 6/7

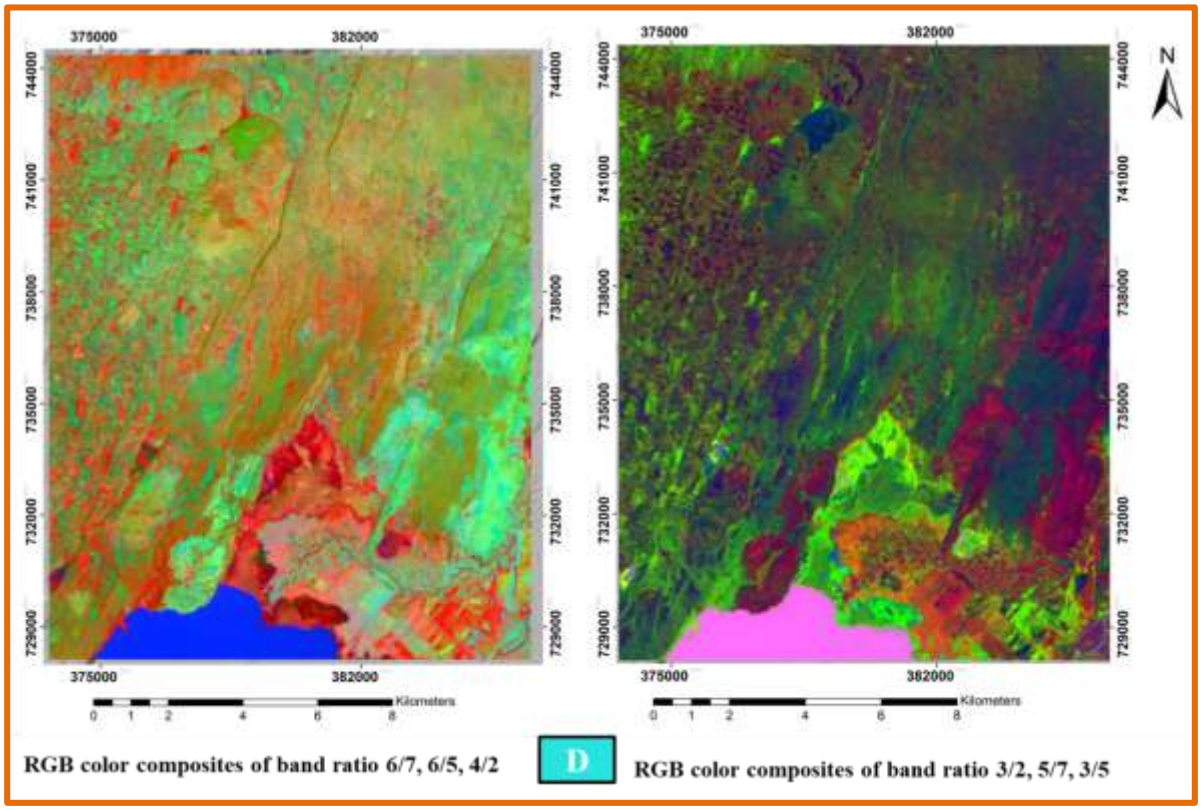

***FIGURE 4.32**: **A.** Landsat 8 band ratio 5/7 and 4/2 **B.** Landsat 8 OLI Images of the RGB color composites of band ratio 7/5, 5/4, 6/7 and 4/2, 6/7, 6/5 **C.** Landsat 8 OLI Images of the RGB color composites of band ratio 6/5, 6/5, 4/2 and 6/5, 6/5, 6/7 and **D.** Landsat 8 OLI Images of the RGB color composites of band ratio 6/7, 6/5, 4/2 and 3/2, 5/7, 3/5*

4.4.1.5. Manual extraction of volcanic cones and structures from SRTM DEM

Morphological analysis of topographic features from remotely sensed image, in particular lineaments, has long been applied in structural and tectonic studies (Hobbs, 1912; Frisch, 1997; cited in Jordan et al., 2005). The study of the Earth's surface using DEM-generated products such as applications of shaded-relief images, aspect and slope maps, profiling and contouring; combined with geological maps provides information that is very useful for structural analysis (Konon and Smigielski, 2006). Drawing a topographic profile is related to slope and understanding the shape of the land surface. It is helpful to visualize the shape of the land as if it had been sliced through. This in turn helps to draw conclusions about the strike and dip of the geology beneath the surface.

Aspect and slope are properties of a plane tangent to a point on a surface. The aspect is an azimuth of a slope line (line of locally greatest rate of altitude change). The slope is the angle between the slope line and the horizontal plane (Hodgson, 1998; Jones, 1998; zhou and Liu, 2004 cited in Konon and Smigielski, 2006).

In this study, slope map produced with arc GIS has been found helpful in extraction of morphotectonic features existed in the area. Scoria and pumice cones and geological structures have been mapped manually (Figure 4.33). Slope map-generated contours enable a precise location of structures. To avoid mistakes in interpreting slope maps, especially when the slope angles change only slightly, strongly contrasting colour scales have been applied.

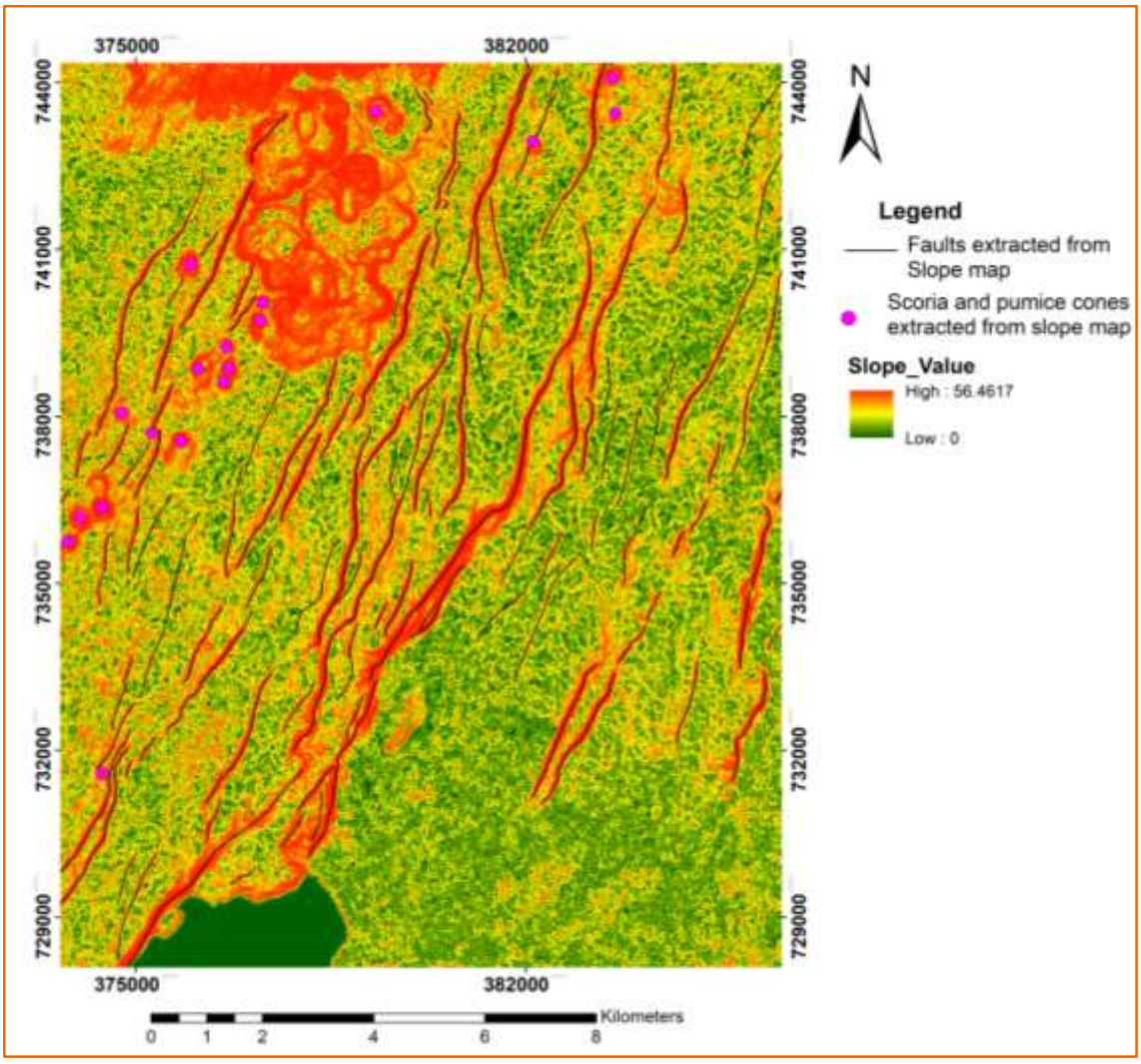

***FIGURE 4.33**: The slope map from DEM used to extract scoria cones and faults of the study area*

4.4.1.6. Thermal Imagery Using a Drone

Drones are now routinely used for collecting aerial imagery and creating digital elevation models (Harvey, 2016). Lightweight thermal sensors provide another payload option for generation of very high resolution aerial thermal orthophotos (an aerial photograph or image geometrically corrected such that the scale is uniform from edge to edge). This technology combined with light weight thermal sensors; provide a new method for mapping volcanic and geothermal areas at high resolution (Harvey et al., 2016).

As it is discussed in section 1.5.2, on the second phase of field work; primary data of thermal and RGB imageries of the study area was captured with drone having thermal camera on it. Here, a 13.4 km^2 georeferenced orthophoto of thermal ground within the study area is presented. Figure 6.5D shows, for example, thermal images showing a comparison of the same area mapped at 8:30 AM on the left and at 7:30 AM on the right. The area in the left picture has already heated up significantly whereas the area on the right shows only the heat from geothermal activity.

Georeferenced RGB orthomosaic created from the RGB images taken from the thermal camera shows areas of fault scarps (Figure 4.34C). The thermal orthomosaic of the area shows the absolute temperature (Figure 4.34A). This thermal image also shows footprints of the flights with the flight start times. A known geothermal area has been easily distinguished from the effects of sunlight at 7:30 AM. Whereas an area imaged at 11:45 AM, shows bedrock being heated by the sunlight.

Thermal images from the individual thermal flights have proven useful for making a comparison of the same area mapped in different time. This in turn helps to distinguish areas which have been heated up by sunlight during the day, and which might show consistently hot spots (potential geothermal activity at the surface) by overlapping these individual fights (Figure 4.34D).

Generally, areas imaged prior to 8 AM seem to show geothermal surface heat quite well but after 8 AM sunlight has too much of an effect on the ground temperatures so geothermal heat and latent heat due to sun irradiation cannot longer be distinguished as this was tested in an area which was known to have geothermal heat in the SE corner of the mapping area.

The thermal imagery dataset aided in the extraction of interesting locations that indicate areas which potentially show geothermal activity at the surface (Figure 4.34B). These are hotspots or areas of thermal anomaly that cannot be explained by the effect of sunlight. These hotspots were identified using both the thermal orthomosaic and the individual fights. Ground truthing of these hotspots has been carried out through field observation which shows that there are some false anomalies associated with fire burning for local charcoal use. Field observation also revealed that the true hotspots of the thermal imagery have a close relation with the steam vent, hot springs and fumaroles found in the Chewckare graben, south most part of the study area close to the Lake Abaya.

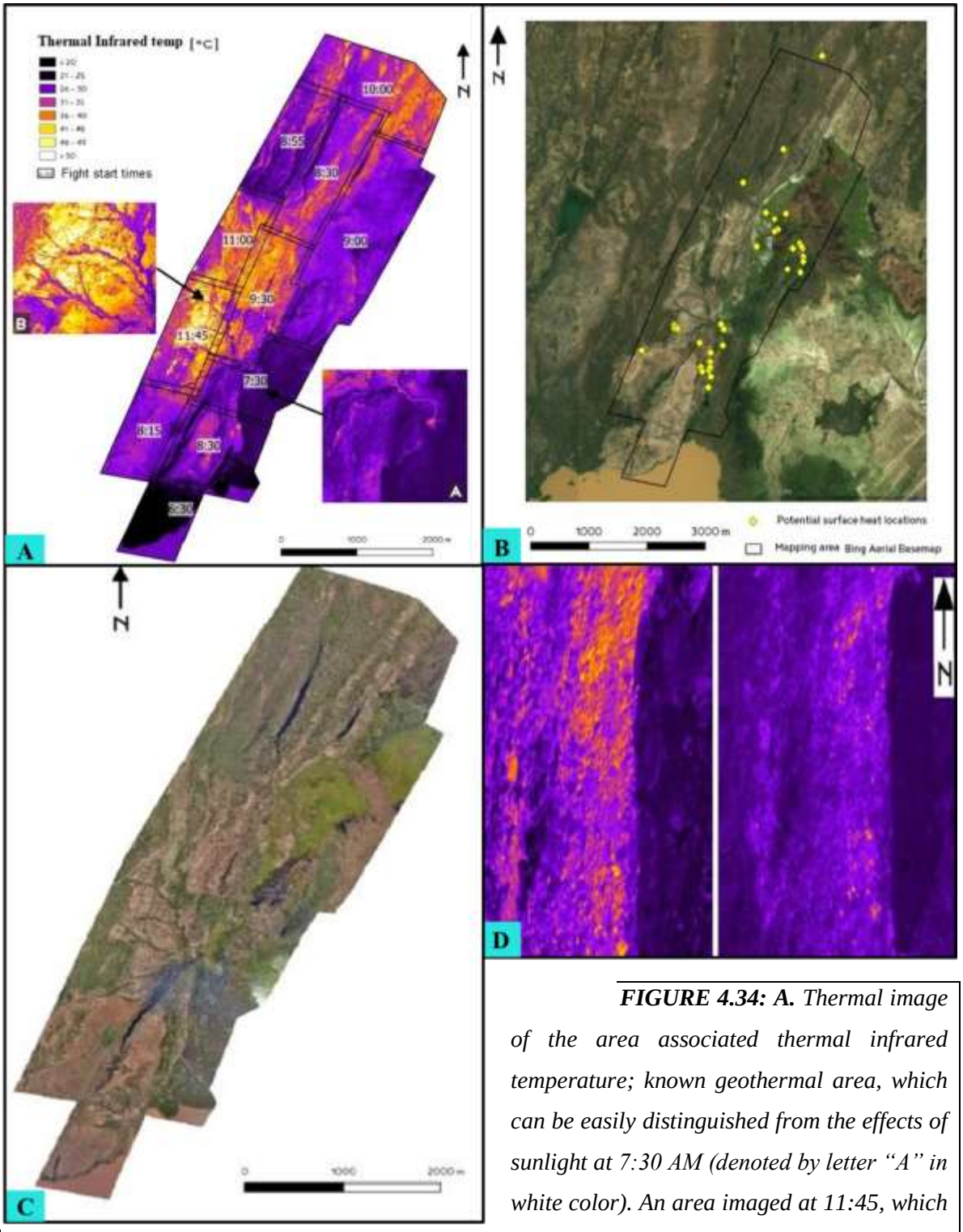

FIGURE 4.34: A. *Thermal image of the area associated thermal infrared temperature; known geothermal area, which can be easily distinguished from the effects of sunlight at 7:30 AM (denoted by letter "A" in white color). An area imaged at 11:45, which shows bedrock being heated by the sunlight (denoted by letter "B" in white color* ***B.*** *Temperature anomalies in the study area encountered from the thermal data sets (depicted by yellow rectangles)* ***C.*** *Georeferenced RGB orthomosaic of the area* ***D.*** *Image from single flights of the same area at different period of time (Source: RG Geothermal)*

4.4.2. Soil CO_2 flux measurement and distribution

The study of the soil CO_2 gas flux and temperature distribution has proven to be important methods to identify vertical zones of high permeability. These methods can give important and vital information for field development and exploitation. Carbon dioxide (CO_2) is the major component of typical geothermal gases, and is readily detectable (Harvey et al., 2015).

The present study on the CO_2 degassing is basically relying on the in situ soil CO_2 flux measurement undertaken during the third and fourth phase of the field work. The soil gas and temperature survey was focussed on the Salewa Dore-Hako graben (SD-H graben) and the Abaya thermal area (Figure 4.36). The SD-H graben is characterised by large number of scoria cones and large central volcanic complex (Hako and Salewa Dore). The volcanic formations all bear indications of being the most recent eruptive formations in the area. The Abaya thermal area is characterised by many surface manifestations in the form of fumaroles, springs and hydrothermally altered surface. The spring temperatures range from 40 °C to 90 °C and sound of boiling groundwater at shallow depths. Some of the springs have high gas flux that can be observed. The survey area is partitioned in to four sites for the purpose of easy analysis of data (Figure 4.36). Site-1 is the measurement stations north of the Salewa Dore; Site-2 is measurement points at the south of Hako graben; Site-3 is found at the southwest part of the study area and Site-4 is the CO_2 flux measurement stations at the main thermal manifestations (Abaya spring area). The number of stations and area covered are listed in Table 4.13. All soil CO_2 flux measurement data is presented in appendix III.

After measurements are completed, processing of the data is started firstly, by identification of the biological background component of CO_2 flux, so this is not confused with the geothermal signal. The approaches used for the identification of background flux are the Statistical methods that partitions separately distributed populations using log-probability plots. By applying the procedure proposed by Sinclair (1974), a combination of two overlapping populations can be identified in the probability plot of the flux values (Figure 4.35). This bimodal distribution suggests the existence of two sources (biogenic and volcanic-geothermal) feed overall soil CO_2 diffuse degassing. The CO_2 flux data were then converted from mol m^{-2} d^{-1} to g m^{-2} d^{-1} to see the data correlation with the regional work

(Hutchison et al., 2015). A multiplication factor of 44.0095 is used for conversion since mole is the international system of units (SI) for amount of substance hence 1 mole is equal to one mole of CO_2 or 44.0095 grams.

The measured CO_2 flux ranges between 0.223 - 2000 (g m^{-2} d^{-1}), with one value 6020 (g m^{-2} d^{-1}) and here considered an outlier and excluded from the analysis. The CO_2 flux distribution of the collected data is depicted in cumulative percentage in Figure 4.36, where 90% of the points have flux value lower than 47.4 g m^{-2} d^{-1}. The flux values below 16.1 g m^{-2} d^{-1} (the 75% lowest values) are considered a background value. The measurement values between 16.1 g m^{-2} d^{-1} to 47.4 g m^{-2} d^{-1} (75% - 90%) are considered as a transitional value and the flux values greater than 47.4 g m^{-2} d^{-1} (the 90% greater values) as geothermal anomaly (Table 4.14).

Mathematical analyses of the soil CO_2 flux data make it possible to calculate the total volume of CO_2 in the study area. The total CO_2 releases were calculated by multiplying the arithmetic mean value of CO_2 fluxes by the surveyed areas called Sichel‘st estimator (David, 1977, Chiodini et al., 1998). The calculation is for all population. Accordingly, the CO_2 emission from site-1 is amounted to be ~ 4 t d^{-1}, site-2 is estimated to have ~ 22 t d^{-1}, and site-3 is amounted to be ~ 12 t d^{-1}. The highest CO_2 emission is from an active geothermal area (Abaya hot spring) adjacent to the major fault scarp that is amounted to ~ 282 t d^{-1}. Table 4.15 shows the input values and results of soil CO_2 emission from the studied area. The total CO_2 released in site – 4 for each population is estimated where the geothermal anomaly source takes the major proportion and other populations are presented in Table 4.16.

The soil CO_2 flux data was gridded for contour maps using Oasis Montaj software. Interpolation between data points is made to yield spatial distribution and finally degassing structural pattern is identified. A dashed line linking the CO_2 flux anomalies is used to depict interpolated fault in the areas of thermal manifestation around the Abaya hot springs.

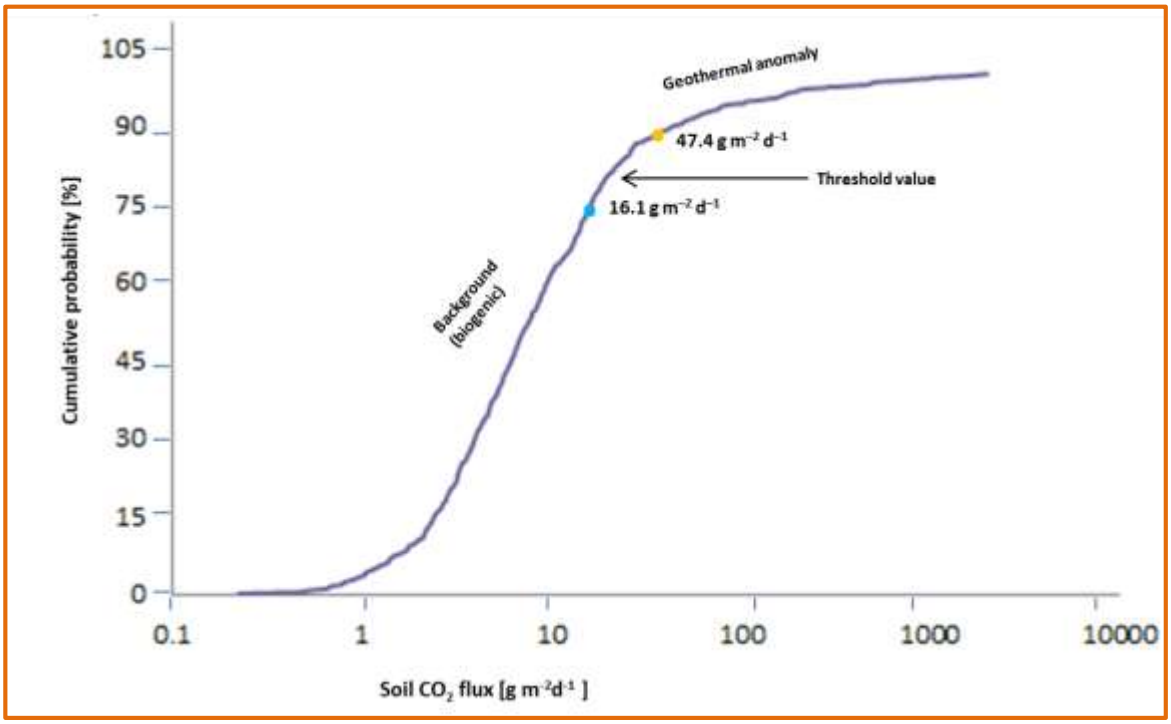

FIGURE 4.35: *Cumulative log-probability plot for soil CO_2 flux*

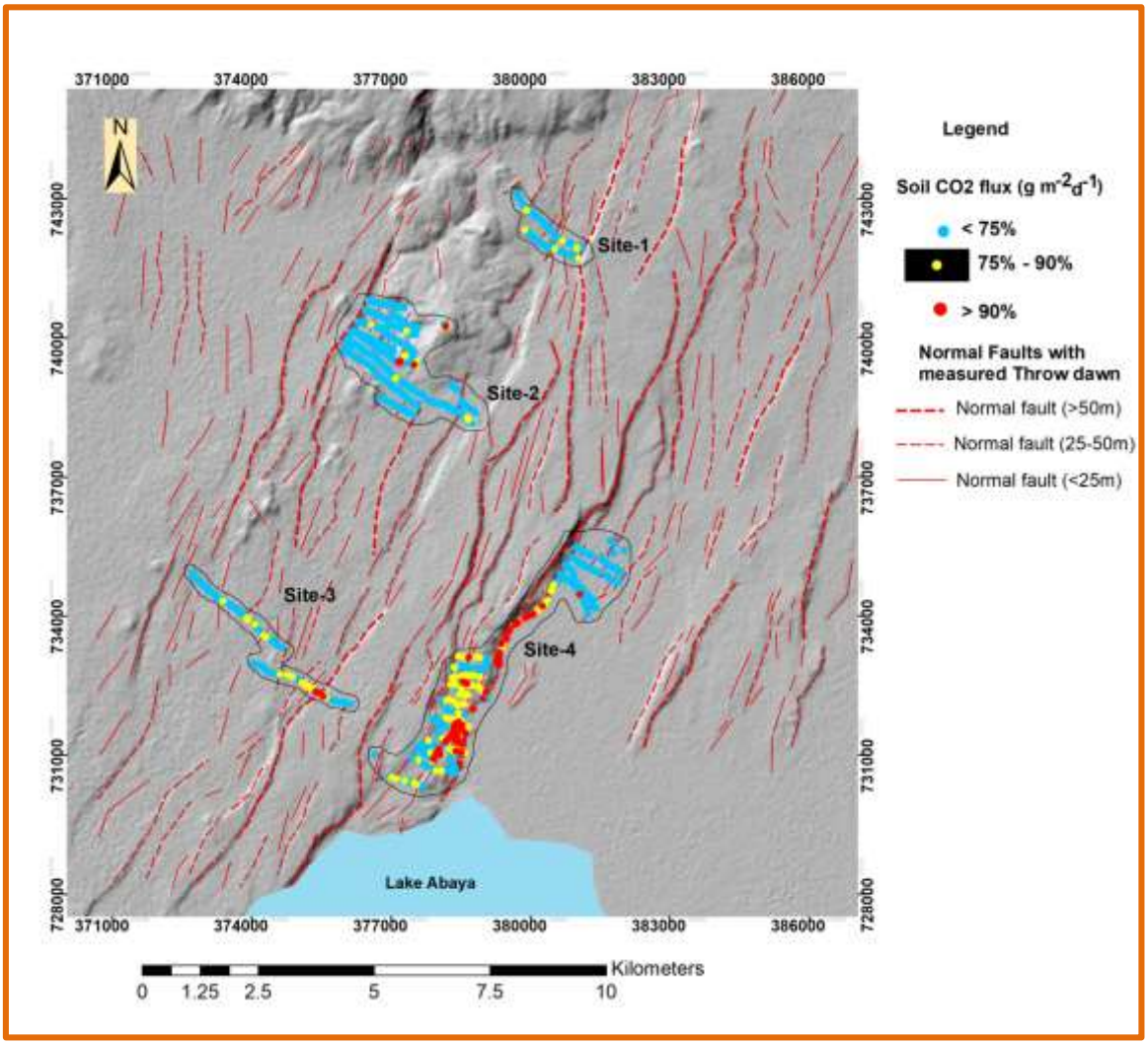

FIGURE 4.36: *Location/sites and spatial distribution of soil CO_2 flux in the Abaya. The measurment stations are in the area around Salewa Dore-Hako rhyolitic complex, a profile crossing the SD-H graben and in the Abaya springs. Spatial distribution of soil CO_2 flux is reported in cumulative percentage, with blue circles representing a background value, yellow representing a transitional value and red representing a geothermal anomaly*

***Table 4.13**: Soil CO2 flux and temperature measurement stations in the study area*

Study fields In Abaya	**Number of measuring stations**	**Total profile length (km)**	**Area covered (km^2)**
Site-1	60	~ 1.87	~ 0.497
Site-2	272	~ 3.28	~3.041
Site-3	80	~ 4.54	~0.969
Site-4	344	~ 6.31	~3.672

***Table 4.14:** The measured backround, transitional and geothermal anomalies values of the soil CO2 flux and temperature from the study area*

Populations	**Cumulative (%)**	**Temperature(°C)**	**Flux CO_2 ($g\ m^{-2}d^{-1}$)**
Background	< 75	< 36.7	< 16.1
Transitional/Treshold	75 - 90	36.7- 40.1	16.1 – 47.4
Anomaly	> 90	> 40.1	> 47.4

***Table 4.15:** Calculation of total gas emission from the study area*

Study fields In Abaya	**Artimetic mean (CO_2 flux [$g\ m^{-2}\ d^{-1}$])**	**Area covered (m^2)**	**Total gas emission (ton d^{-1})**
Site-1	8.31	497,176	4.132
Site-2	7.18	3,041,262	21.837
Site-3	13.36	969,738	12.956
Site-4	76.86	3,672,359	282.274

***Table 4.16**: Calculation of the total gas emission for site- 4 from each CO_2 flux population*

Populations	**Cumulative (%)**	**Mean CO_2 flux [$g\ m^{-2}\ d^{-1}$]**	**Area covered (m^2)**	**Total gas emission (ton d^{-1})**
Background	75	6.738	3,672,359	24.745
Transitional	15	25.877	3,672,359	95.031
Anomaly	10	44.244	3,672,359	162.481
Total				282.274

4.4.3. Soil temperature survey

Soil temperature was measured in the same locations as the soil gas flux during the same field trip. The temperature range at 50 cm soil depth is 18.3 – 98.5 °C. The temperature distribution of the collected data is shown on a cumulative percentage in Figure 4.37, where 90% of the points have temperature level lower than 40.1 °C. The values below 36.7 °C, the 75% lowest values, are considered a background value. These temperature values are also close to the atmospheric temperature in shade during the field days, and therefore are in good agreement to be considered natural values, i.e. not affected by geothermal heat flow. The values between 36.7 °C to 40.1 °C are considered as a transitional value and the values greater than 40.1 °C as geothermal anomaly. All soil temperature measurement data is presented in appendix IV.

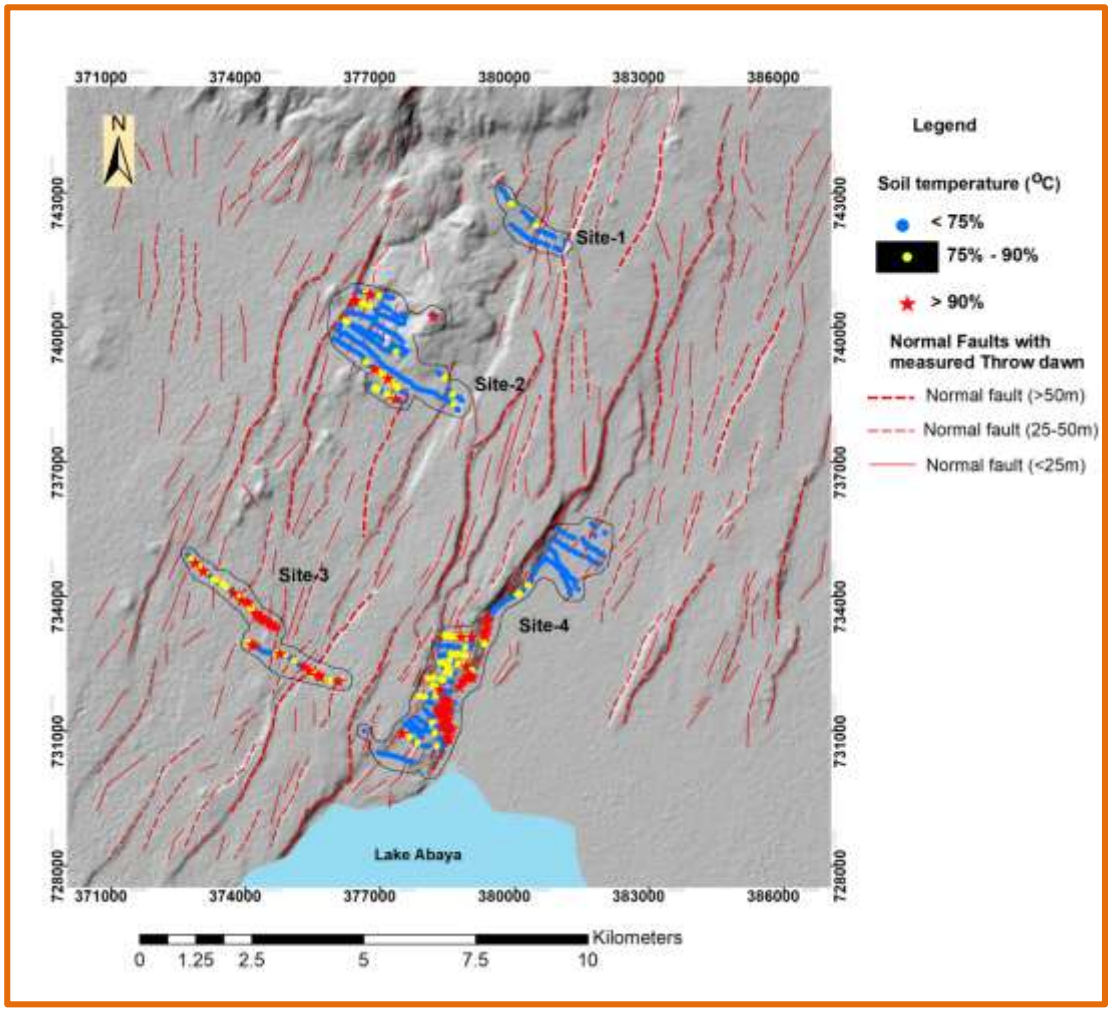

FIGURE 4.37: *Spatial distribution of temperature at 50 cm depth in the soil cover for the measured profiles. Temperatures measurments are represented in cumulative percentage, with blue circles representing a background value, yellow representing a transitional value and red representing a geothermal anomaly*

Mapping of temperature variations at or below the earth's surface is an essential geothermal exploration instrument (Zehner et al., 2012) The spatial variation of soil temperature at different sites of the study area is illustrated by counter maps (Figure 4.38, 4.39 and 4.40). Quite a number of temperature anomalies can be identified in relation to the major fault scarps.

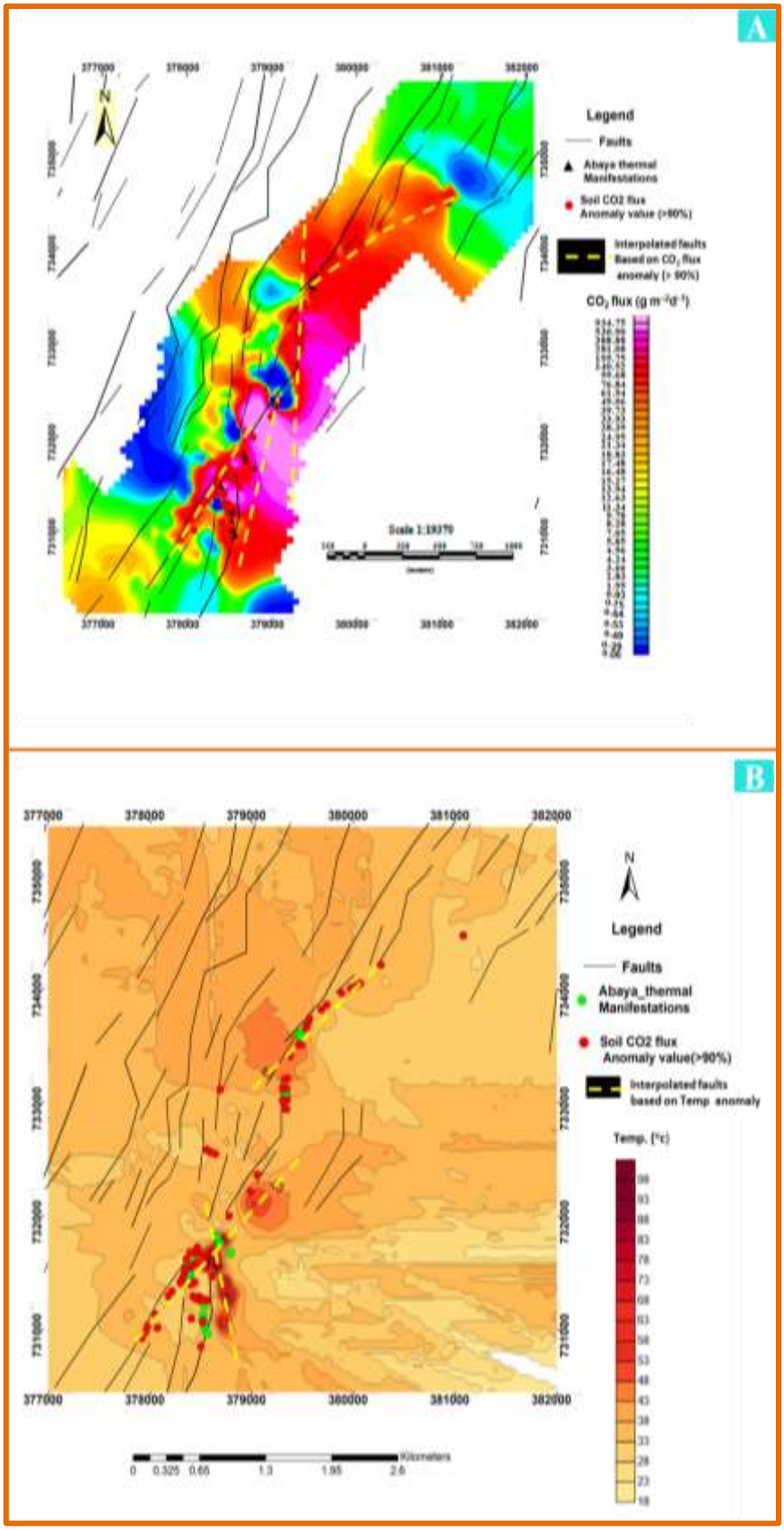

FIGURE 4.38: A. *Grid map showing soil CO_2 flux distributions and* ***B.*** *Soil temperature distribution map at 50 cm depth for the south eastern part of the study area (site -4 – Abaya thermal manifestations)*

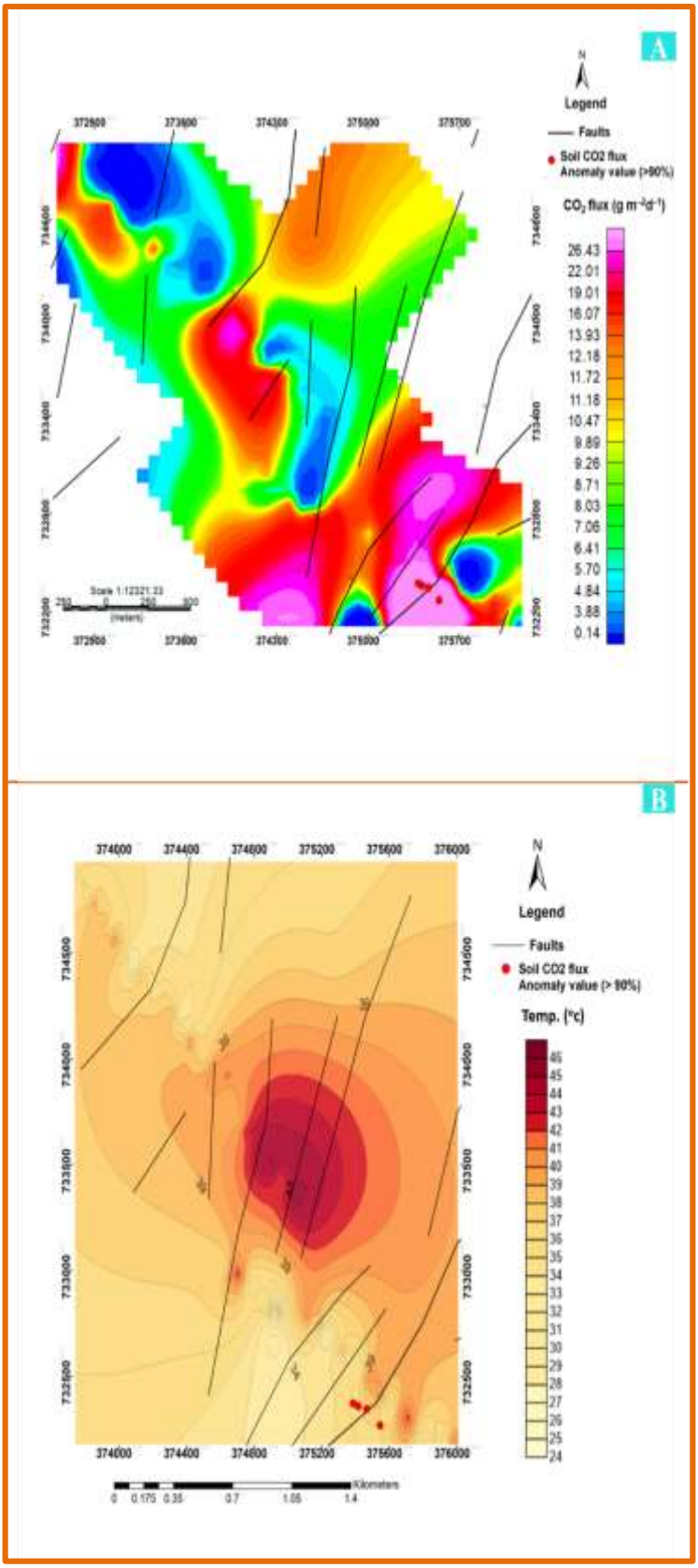

FIGURE 4.39: A. *Grid map showing soil CO_2 flux distributions and* ***B.*** *Soil temperature distribution map at 50 cm depth for the south west part of the study area (site -3 – fault line at the southern part of the H-SD araben)*

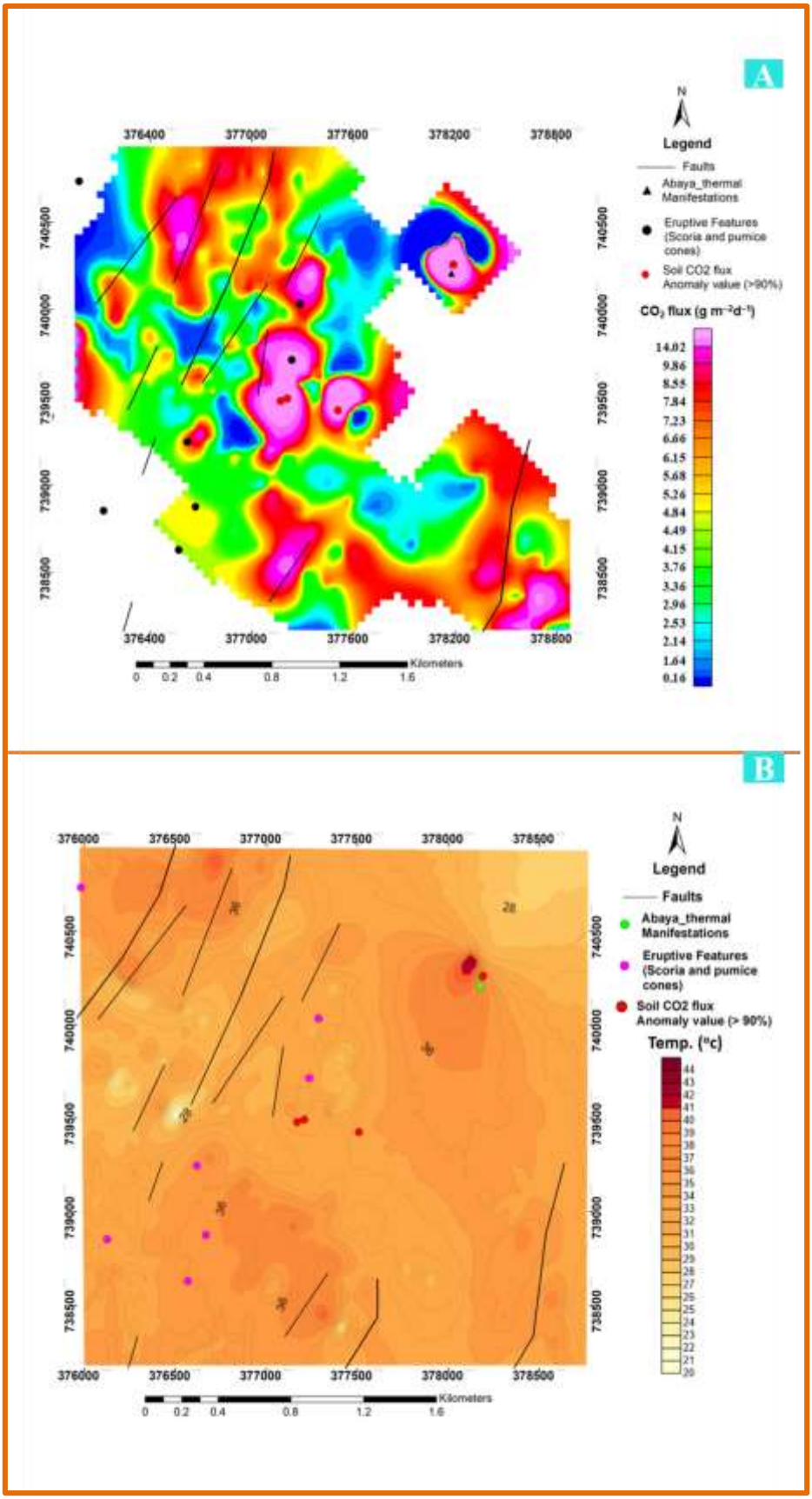

***FIGURE 4.40**: **A.** Grid map showing soil CO_2 flux distributions and **B.** contour map showing temperature distribution at 50 cm depth for the northern part of the study area*

5. Discussion

In this chapter, results of different methods adopted in the study to meet the proposed objective are presented. The results are found helpful to have the general characteristics of the geothermal resource and evaluation of structural permeability in the study area. Assessments of the major components of the geothermal system are presented. The heat source, the reservoir characteristics, the cap rocks, the recharge system and the geothermal fluid are discussed from different secondary and primary works. These studies are found helpful to establish a preliminary geothermal conceptual modeling.

5.1. Volcanic stratigraphy and tectonic structures

Information about the volcanic stratigraphy and tectonic structures is needed as a basis for interpreting results of geophysical and geochemical surveys and test drilling in geothermal exploration. The result of geological study shows that there exist different types of lithological units, many eruptive features with relatively young silicic centers, dense fault systems and active hydrothermal activity. The produced local stratigraphy shows that the dominant rock exposed in the area are of volcanic rocks. The geological and structural map shows that almost all rock units, except the very recent once, are intensely fractured by tectonic activity. The series of dense normal fault system with dominantly trending in NNE-SSW that is important as a passage way for geothermal aquifer was mapped.

The high density and length of faults and joints causes high degree of fracturing of rock formations. The presence of highly displaced fault system (180 m) is an implication of the effect of the faults to the crustal depth. This tectonic fracturing creates high degree of enhanced (secondary) permeability of geothermal reservoir.

5.2. Permeability of the rock units

The different rock units outcropping in the study area possess variable permeability. Those rocks intensely fractured by tectonic activity are highly permeable. This applies to almost all outcropping rock units except those which are younger than the last tectonic activity and have not or slightly been faulted. The variable permeability in the area is probably due to the fracturing and hydrothermal alteration processes. Volcanic rocks with variable permeability are governed by these contrasting processes where the hydrothermal alteration

processes decrease permeability while fracturing enhance the permeability (Ledesert et al., 2010). Tuffs and lavas locally undergo impermeability as a result of hot fluid circulation (Tonani, 1970). Previous permeable areas also may be sealed by this process depending upon the degree of alteration.

Ignimbrites are exposed in river valleys and by the normal faulting activities probably indicating that this rock unit could be the older outcropping unit which make the lowest stratigraphic position at Chewkare fault scarp. No clear centers of eruption are identified for these ignimbrites exposed in south and southeastern part of the study area but they could be related to a rather big silicic central volcano (Duguna) found outside the study area just north of 35 km (Zanettin and Mohr, 1988). The ignimbrites exposed at the Abaya fault have different characteristics with respect to grain shape and size, compaction, weathering and alteration process. The primary permeability of these rocks is affected to a great degree by tectonic fracturing as well as hydrothermal alteration at places. The net effect of this tectonic fracturing is an increased permeability of the study area except where alteration is dominant.

Field excursion on the way to Salewa Dore road cut came up with the identification of stratification of different rock units (Figure 4.14). The lowest layer of this stratigraphy is a 14m thick basaltic lava flow exposed by river cut (Figure 4.14B). This basaltic unit is probably being the oldest basalt that could correlate with the pre-rift basalt of the trap series (Zanettin et al., 1978).

The geological work also shows that there exist a variety of lacustrine sediments which may form an impermeable layer and therefore serve as a cap rock for the system. Previous works also suggests that these sediments are related to fluctuations of the present Lake Abaya level during the Holocene and form an important cap-rock for the hydrothermal system in the Lake Abaya geothermal fields as in the central MER (e.g., Tadiwos Chernet 2011).

The overall characteristics and distribution of hydrothermal activity is related to the different rhyolitic central volcanoes that reveals the existence of a heat source as well. These rhyolitic domes poorly or not affected by fracture are considered not to have enhanced permeability. The recent obsidian flows are compact and not faulted but are

intensively cracked by cooling contraction. It is therefore, unlikely that they fall into the impermeable Class.

The pattern and distribution of recent fracturing suggests that secondary permeability due to tectonism must have increased the bulk permeability of the underlying rocks. The alignment of surface thermal manifestations in the area shows that distribution of hydrothermal active zones is strongly controlled by tectonics and geological structures. For example, most thermal springs discharge within the study area, are in clear connection with the Abaya faults, a major NNE-SSW-trending faults (Figure 4.24) suggesting the geothermal fluid flow and degassing are controlled by faults (Figure 5.1).

5.3. Heat anomalies and sources

The chemical geothermometers from the current study shows high temperatures from all samples. This is somewhat expected with the cation geothermometers in regards to immature waters due high sodium concentration (Giggenbach, 1988). The high silica concentration measured in all springs result in estimated reservoir temperature of greater than 140 °C. The highest silica temperature estimation (AB-18-W08, 176°C) is in agreement with the average of estimated reservoir temperature (175.22°C) from cation (Na/K ratio) thermometer according to Fournier (1977). The results of the silica temperature estimation for AB-18-W04 are exactly in match with the cation temperature estimation where both show 152 °C. The results of AB-18-W02 are close to a match, with the silica temperature estimation at 149 °C and cation estimated temperature at 145°C. The clustering nature is observed between the silica temperature estimation of sample AB-18-W01 (147°C) and Sp-16 (RG Geothermal, 2011; 145°C). Another clustering also exists between AB-18-W02 (156°C) and Sp-15 (RG Geothermal, 2011; 159°C). The high estimated reservoir temperature based on silica and chemical geothermometer is in good agreement with the results of the CO_2 gas and Sulphate-water isotopic temperatures suggesting the presence of a sufficiently high temperature system underneath (Birhamu Gizaw, 1985). The hot water at depth probably flows to the north, northwest and northeast and mixes with shallow low chloride groundwater. The SiO_2 geothermometer (quartz) with no steam loss; has given 240ºC for Sp-5 (Asfaw Teclu, 2003). This might suggest that there is no sea water interference. Previous fluid geochemical studies in the Abaya area depicts that the silica concentration and temperature increase from north to south with springs 6

showing highest SiO_2 concentration as well as the highest temperatures (Asfaw Teclu, 2003, Salahadin Ali and Lemma Kassa, 2007, Reykjavík Geothermal, 2011). Analysis of data collected throughout time reveals that the waters of Lake Abaya have experienced an increase in salinity of 20% paralleled contemporaneously with a decrease in pH and δ18O and δD of water in the last 40 years (Mnissale et al., 2017). These changes do not appear to be related to climate change induced increases in temperature or evaporation at the global scale. This reveals that the geothermal activity is in active state being responsible for the change in water chemistry.

The plots of the stable isotope composition of most of the water samples collected in Abaya (Figure 4.25) show strong agreement to the meteoric lines (AddMWL). This is in good agreement with previous work (Abebe Ayele et al., 2002) were most of previous isotopic samples collected have □18O, □D values close to 9‰ and 3‰, perspectivley with the sample collected in SP-6 showing an oxygen shift of 2.3 ‰, suggesting high temperature subsurface. This shift is also seen in sample SP-6 (RG geothermal, 2011) as well as sample AB-18-W03 (in this paper) collected north of SP-6 from the high temperature spring.

Gas samples show very low H_2S concentrations and high concentrations of CO_2. This is in similar trend with other geothermal fields in Ethiopian (Tulu Moye and Corbetti, by RG Geothermal, 2017).The average of the geothermometers based on the the gas concentrations from this study suggest reservoir temperatures of greater 200 °C. It is in good agreement with the average of the cation thermometers.

The result of the soil CO_2 flux surveys in this study shows that the CO_2 degassing is generated from biogenic and volcanic-hydrothermal source. The natural CO_2 emission flux is mostly concentrated along the dense fault systems and the most recent eruptive mechanisms. The CO_2 flux anomalies within the study area are closely associated with the faults and surface manifestations. The result shows elevated fluxes (>>100 g m^{-2} d^{-1}) along major faults around Abaya hot springs and fumaroles suggesting that the CO_2 in that area travels mostly with rising hydrothermal steam. This is in good agreement with the CO_2 emission from Aluto geothermal field (Hutchison et al., 2015). Some distinct moderate to strong CO_2 flux anomalies are also found in the southern part of the central fault system of the SD-H graben and at the Hako silicic center (Figure 4.39 and 4.40). The presence of strong soil CO_2 flux anomalies nearby to the Abaya faults and young silicic center is consistent with the

geological and structural study in this work. All studies depicted the presence of obvious thermal activities and dense fault systems that explain as there are permeable zones at subsurface servings as a passageway for geothermal fluids flow. Areas which have highly affected by brittle structure will have high CO_2 flux measurement result. This is because those structures will act as a conduit and make the lithology plus the soil more permeable and finally enable us to get high value. These anomaly values of the CO_2 flux are used to map subsurface structures called diffuse degassing structures (Hutchison et al., 2015). The high CO_2 flux can be interpreted as sections of greater permeability causing accelerated gas diffusion from crustal magmatic sources. The anomaly may be attributed to presence of fault intersections which may have been reactivated to allow partial permeability. Alternatively, the anomaly may be in close proximity to an up flow zone (Harvey et al., 2016).

Significant variations in the CO_2 flux along the fault zones reflect differences in near-surface permeability caused by changes in topography and surface lithology (Tamiru Alemayehu and Vernier, 1997, Hutchison et al., 2015). The effect of the lithology is difficult to justify because it needs detail subsurface investigation at different spots. But some parts of the Hako graben showing significantly lower CO_2 flux value is probably due to thick pumiceeous pyroclastic rocks burial of their sources.

Calculation of the total CO_2 released for site-4 (the Abaya fault) from all populations indicates that the Abaya thermal area has a total degassing amount of 282.274 ton d^{-1} within 3.67Km^2. The CO_2 degassing from the hydrothermal source is coincident when it compares to Aluto volcano (57 ton d^{-1} within 0.8 Km^2; Hutchison et al., 2015).

The Abaya faults around the hot springs were transected numerous times (18 times). Strong soil CO_2 flux anomalies were found at these faults. This suggests that permeability extends over considerable distances (~ 4.5km). The CO_2 flux anomalies are coincident with the MT survey along profile line one (Mohammednur Desissa and Yohanes Lema 2006) which depicts that there exist very low resistivity value correlated with structurally weak zone. This provides additional evidence for the substantial flow of CO_2 and heat in the Abaya thermal area.

The results of soil temperature survey indicate that a higher temperature anomaly in the area is evident around the Abaya thermal manifestations (Abaya fault) with the fumaroles having the highest temperature of 98.5 ^{o}C. The other anomalous areas; according to contoured shallow soil temperature data are the southern end of the central faults of the SD-H graben and at the Hako silicic center associated with fumaroles. Similar to other soil surveys, soil temperature results in the south east part of the study area (the Abaya fault) gave higher anomaly confirming the geothermal potential of the area coinciding with the major faults of the area. The result of soil temperature is in good agreement with the absolute temperature (thermal infrared temperature) from the thermal imagery.
The temperature map produced from the survey shows that the highest anomaly is concentrated on two zones of the area; on the observed Abaya faults and the most recent eruptive mechanism (Hako silicic center).

Defusing degassing structural pattern with a general NNE-SSW direction are identified by interpolation between the soil temperature anomalies and the spatial distribution of CO_2 flux around the Abaya thermal manifestations (Figure 4.38). A dashed line linking the CO_2 flux anomalies for interpolated fault around the Abaya hot springs also links shallow temperature anomalies. This observation provides additional support for the existence of the permeable zone in the area.

Interpretation of the temperature anomalies at site-4 indicates the presence of NNE-SSW trending structure. This is also in good agreement with the detailed geological-structural study where the anomalies seem to coincide with the local as well as the regional structures. They are also parallel with the thermal manifestations of the area. The surface geothermal maifestations themselve are structurally controlled and are likey to occur parallell to the NNE-SSW direction. This appearance of temperture lineaments together with the manifestations can led us understand the precence of hidden fault along the flat lain in Abaya area which is parallel to the general NE-SW and NNE-SSW direction.

5.4. Preliminary Geothermal Conceptual Model

The conceptual model of the geothermal field is the synthesis of all the information collected, analysed and interpreted from surface studies and deep exploratory wells (Hochstein, 1990). It explains potential heat source, general geological setting of the area,

definition of the reservoir geometry in terms of areal extent (top and bottom), chemical characteristics of the reservoir fluids, and natural fluid flow patterns of a given geothermal field.

Data from remote sensing, geophysical, hydrogeological, geological and geochemical investigations have served as major inputs for the establishment of the preliminary geothermal conceptual modeling of the study area.

Hydrogeological study indicates that the study area has a regional recharge from different sources. These regional recharges are from the adjoining highland areas and seepage through fault fractures. Deep recharges are from the north, west and northwest mainly by infiltration of rainfall. The area gets high recharge from the major escarpments of Chencha and Fonko-Guraghe catchment regions to the west of the rift (Corti et al., 2014). A deep recharge from the east and northeast highland areas (within the Bilate River watershed) must also have come towards the topographic sink of the rift lowlands and finally towards Lake Abaya area. Underground water circulating at depth emerges along fault zones. Therefore, the groundwater system seems to be rather extensive as evidenced by the distribution of thermal springs throughout the area of Lake Abaya.

Geological mapping depicts the faulting or other permeable structures, as well as the present of alluvial and lacustrine sediments which could serve as the cap rock for the geothermal system. Soil gas measurement shows anomalous gas flow and therefore sub surface permeability and temperature soil survey shows anomalous heat flow and therefore permeability. The geophysical study along profile line one (MTL1-01 in figure 3.6) indicates that there exist very low vertical resistivity layer which could indicate the upflow zone through which hydrothermal fluids and gas migrate to the surface. Resistivity signature in this profile line below 1500m is relatively high, which could be due to volcanic intrusion. This indicates that there exists a heat source down depth.

Two Possibilities can be mentioned about the heat source for the geothermal system in the study area. The first possibility is that the quaternary tectonic activity in this area was such that the sub crustal magma rose very fast through deep and narrow fissures without stopping at shallow depth to undergo crystal fractionation. This assumption is based on the fact that numerious eruptive features are mapped and exposed following these tectonic structural

alignments. The only, but much localized, exception to this mechanism should be represented by the Holocene Salwa Dore and Hoko rhyolitic lava domes (Corti et al., 2014). In this case, the thermal supply of the geothermal fluids and gas along the Abaya fault would be represented by a small silicic magma body present beneath the Salewa Dore and Hoko domes. A possible minor contribution of heat could be also provided by the central silicic volcano (Duguna) located about 35 km to the NE of the study area (Zanettin and Mohr, 1988). This assumption is based on the fact that the heat source does not necessarily need to be directly beneath the thermal manifestations.

The groundwater from the recharge areas as it travels through the thermally anomalous zone is heated up and later comes out at the discharge area. The second possibility is that great quantities of subcrustal magma were trapped at a relatively shallow depth in many segments of the study area during the quaternary tectonic activity. The basaltic magma therefore had large possibilities of producing a much greater volume of differentiated products and not only had those now represented by the Salewa dere and Hoko silicic domes. This is reveal by geological mapping were most of the area of study is covered by basaltic lava flow and scoriaceous products. The occurrence of faulted-tilted blocks within the area also suggests the possibility of important tectonic traps at depth where magma may have stopped to undergo differentiation. In this case the heat storage at shallow depth should not be represented only by the presently cooling silicic magma beneath the Salewa dere and Hoko domes. Therefore, much greater volume of magma widely distributed and not necessarily extremely silicic is assumed to be the heat source for the geothermal system of the study area.

The existence of aquifer (reservoir) at depth is indicated by the escapes of thermal fluids and CO_2 flux occurring along the Abaya fault and in the vicinity of Hako rhyolitic dome. This is confirmed by the fluid geochemical study and CO_2 flux measurement. The isotopic data which shows an important oxygen shift may also be an evident suggesting that more than one aquifer (reservoir) exist at depth. The non-similarity between anion ratio (Cl/SO_4 and Cl/B ratio) of fluid samples may also strength the assumption. The study is in good agreement with the regional studies (e.g., UNDP, 1973). The large number of thermal areas in the Ethiopian rift and the high temperatures of the thermal fluids and gases issued, are all indications of a considerable flow of groundwater through the lower parts of the rift

volcanic series (UNDP, 1973). Based on the findings of the above surface and subsurface information, all the criteria for the geothermal system have been met in the study area.

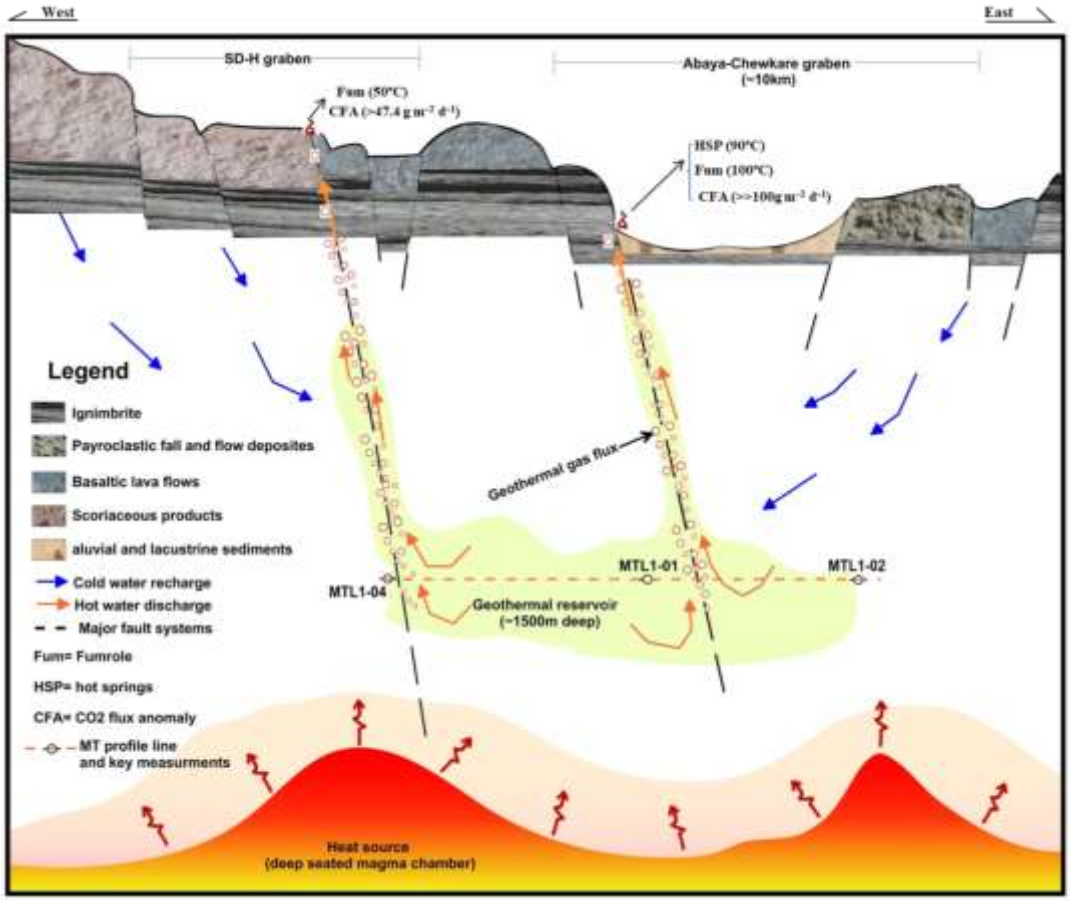

FIGURE 5.1: *Preliminary Geothermal Conceptual Model for the study area*

6. Conclusions and Recommendations

6.1. Conclusions

A combination of remote sensing, field mapping, structural analysis, petrographic and fluid analysis, Soil CO_2 flux measurement and temperature survey were employed to evaluate the structural permeability and to characterize the geothermal system in the Northern Lake Abaya Geothermal Field. The main outcomes of this study are listed in points below.

1. The geologic and structural map produced from integrated field work and remote sensing indicate that there are different lithological units, recent to very young eruptive features, series of dense normal fault systems and active geothermal activities. The major volcanic and sedimentary units are ignimbrite, trachyte, pumiceous pyroclastic flow and fall deposits, basalts, scoria, rhyolitic and obsidian lava flows and alluvial and lacustrine sediments. The geological structures observed include cracking, joints and normal fault system with dominantly trending in NNE-SSW that imitate the regional tectonic structure of the WFB in the Main Ethiopian Rift. The geothermal activities are in clear connection with these NNE-SSW-trending structures, suggesting the geothermal fluid flow and degassing are controlled by faults.

2. The fluid chemistry tells that the thermal waters are primarily of near neutral pH and are dominantly of sodium-bicarbonate types. The chemical and gas geothermometers shows that the geothermal system has high reservoir temperature. The high silica concentration measured in all springs result in estimated reservoir temperature exceeding 140°C. The average cation and gas geothermometers suggest reservoir temperatures of greater than 200°C.

3. The distribution of soil CO_2 flux has been established in accordance standard practice. The same applies for the temperature survey at 50 cm depth. A normal background value for the CO_2 flux and measured temperature was established and geothermal anomalies were mapped. The anomalies are centred on the Abaya faults where there are clear hydrothermal manifestations visible on the surface. The soil CO_2 flux measurement result shows elevated fluxes (>>100 g m^{-2} d^{-1}) along the major faults and

surface manifestations. The total CO_2 emission from the Abaya Fault has a total degassing amount of 282.274 ton d^{-1}.

4. The results of soil temperature survey indicate that a higher temperature anomaly up to 98.5 ℃. The temperature map produced from the survey shows that the highest anomaly is concentrated on two zones of the area; on the observed Abaya faults and on the recent eruptive centre (Hako rhyolitic dome). These temperature anomalies show a clear agreement with the flux of CO_2 anomalies. Not all mapped faults were found with anomalous heat or gas flow. The methods are therefore useful to identify the permeable fractures, a possible drilling target.

5. Areas of elevated CO_2 flux and elevated shallow (50 cm) subsurface temperature support the presence of mapped faults, and helped to identify other potential sub surface structural features that may be providing anomalous heat and gas flux. It is evident that the CO_2 soil flux anomalies are well defined and the shapes of the anomalies coincide with local structural directions that were mapped. The structural lineament and geothermal manifestations are parallel with the interpolated fault patterns from the soil CO_2 and temperature anomaly. This advocate's the precence of hidden structure associated with the general NNE-SSW direction of the flat lain Abaya area. The soil CO_2 and temperature survey has outlined the hidden structures along the flat plain.

6. The soil gas and temperature survey conducted in the Lake Abaya geothermal field showed that soil gas anomalies can be correlated to the permeability characteristics of structures. The combination of remote sensing, field mapping, structural analysis, petrographic and fluid analysis and Soil CO_2 flux and temperature survey all suggested that the area has deep seated permeable zones for the fluids and gases expulsion therefore the present of potential geothermal resources.

6.2. Recommendations

The key out come of the soil CO_2 and temperature survey has been to demonstrate the effectiveness of these methods as a powerful and relatively inexpensive geothermal prospecting tool. The soil CO_2 flux measurement has allowed identification of permeable structures and estimation of the total CO_2 through these permeable zones.

It is recommended that the priority target areas for future exploration by drilling of wells would be within the areas identified by the soil CO_2 and temperature measurements. Therefore, conducting geothermal test drilling toward the dense Abaya fault system around the thermal manifestations will be effective because the anomaly may be in close proximity to an up flow zone.

Closely spaced magnetotelluric (MT) stations geophysical investigation integrated with transit electromagmetic methods (TEM) should be conducted. This will be helpful to produce joint inversion model using detailed resistivity anomaly. It intern is used to get details information on the cap rock and heat source of the geothermal system in the study area.

REFERENCES

Abebaw Endeshaw (1988). Current status (1987) of geothermal exploration in Ethiopia. Geothermics, **17**(2): 477–488.

Abebe Ayele, Meseret Teklemariam and Solomon Kebede (2002). Geothermal Resource Exploration in the Abaya and Tulu Moye-Gedemsa Geothermal Prospects, Main Ethiopia Rift. Unpublished technical report, Geological Survey of Ethiopia, Addis Ababa, Ethiopia, 172 pp.

Ali, A., and Pour, A. (2014). Lithological mapping and hydrothermal alteration using Landsat 8 data: A case study in Ariab mining district, red sea hills, Sudan. International Journal of Basic and Applied Sciences, **3**: 199–208.

Amare Getahun (1978). Agricultural systems in Ethiopia. Agricultural Systems, **3**: 28-29.

Aquater (1996a). Tendaho Geothermal Project. Unpublished technical report, Addis Ababa, Ethiopia, 150 pp.

Aquater (1996b). Tendaho Geothermal Project. Unpublished final technical report, Addis Ababa, Ethiopia, 170 pp.

Arnórsson, S., Gunnlaugsson, E. and Svavarsson, H. (1983). The chemistry of geothermal waters in Iceland. Chemical geothermometry in geothermal investigations, Geochim. Cosmochim. Acta, **47**: 567-577.

Arnórsson, S. and Gunnlaugsson, E., (1990). New gas geothermometers from geothermal exploration – Calibration and application. Geochim. Cosmochim. Actta, **49**: 1307- 1325.

Arnórsson, S. (2000). Isotopic and chemical techniques in geothermal exploration, development and use. Sampling methods, data handling, interpretation. International atomic energy agency, Vienna, 351 pp.

Asfaw Teclu and Taffesse Gizaw (2001). Geochemistry of Tulu moye prospect area.GSE, unpublished report, GSE, 18 pp.

Asfaw Teclu (2003). Geochemical and Isotopic Study of North Lake Abaya geothermal Prospect. Unpublished report, GSE, Addis Ababa, Ethiopia, 5 pp.

Bertani, R. (2008). An Overview on Geothermal Resources and Potential. International Geothermal Days Slovakia Conference, Enel Green Power, Italy, 16 pp.

Bonini, M., Corti, G., Innocenti, F., Manetti, P., Mazzarini, F., Tsegaye Abebe and Pecskay, Z. (2005). Evolution of the Main Ethiopian Rift in the frame of Afar and Kenya rifts propagation. Tectonics, **24**: TC1007.

Bloomberg, S., Rissmann, C., Mazot, A., Oze, C., Horton, T., Gravley, D., Kennedy, B., Werner, C., Christenson, B. and Pawson, J. (2012). Soil gas exploration at the Rotokaw geothermal field and white Island, New Zealand. **In**: *proceeding of the thirty-sixth workshop on geothermal reservoir engineering*, Stanford University, Stanford, California.

Braile, L.W., Keller, G.R., Wendlandt, R.F., Morgan, P. and Khan, M.A. (1995). The East African Rift System. Olsen, K.H. (Ed.), Continental Rifts: Evolution, Structure, Tectonics. Developments in Geotectonics, **25**: 213–231.

Brhanu Gizaw (1985). The chemistry of geothermal fluids in geothermal areas of the Lakes District, Ethiopian Rift Valley. UNU geothermal training program Iceland.

Bruhn, R.L., Parry, W.T. Yonkee, W.A. and Thompson, T. (1994). Pure and Applied Geophysics, **142**: 609-644.

Charles Wanjie (2012). Overview of geothermal surface exploration methods. Presented at Short Course VII on Exploration for Geothermal Resources, organized by UNU-GTP, GDC and KenGen, at Lake Bogoria and Lake Naivasha, Kenya, 15 pp.

Chiodini, G., Cioni, R., Guidi, M., Raco, B. and Marini, L. (1998). Soil CO_2 flux measurements in volcanic and geothermal areas. Applied Geochemistry, **13**(5): 543-552.

Corti, G. (2008). Control of rift obliquity on the evolution and segmentation of the Main Ethiopian Rift. Nat. Geosci., **1**(4), 258–262.

Corti, G. (2009). Continental rift evolution: From rift initiation to incipient break-up in the Main Ethiopian Rift, East Africa. Earth-Science Reviews, **96**: 1–53.

Corti, G., Manetti, P., Tsegaye Abebe, Bonini, M. and Mazzarini, F. (2009). The volcano-tectonic activity of the Main Ethiopian Rift (East Africa): insights into the evolution of continental rifting.

Corti, G., Sani, F., Philippon, M., Sokoutis, D., Willingshofer, E. and Molin, P. (2013). Quaternary volcano-tectonic activity in the Soddo region, western margin of the Southern Main Ethiopian Rift. TECTONICS, **32**: 861–879

Corti, G., Sani, F., Minissale, A. and Montanari, D. (2014). Volcano-tectonic and hydrothermal activity in the Soddo area, western margin of the Southern Main Ethiopian Rift. **In**: *Proceedings 5th African Rift geothermal Conference,* Arusha, Tanzania.

Craig, H. (1963). The isotopic geochemistry of water and carbon in geothermal areas. Nuclear geology in geothermal areas, Spoleto, 17-53.

Craig, H. (1977). Isotopic Geochemistry and Hydrology of Geothermal Waters in the Ethiopian Rift Valley. Unpublished Report, Isotope Lab., Scripps Institution of Oceanography, Univ. of California at San Diego, USA, 140 pp.

D´Amore, F., and Panichi, C. (1980). Evaluation of deep temperatures in hydrothermal systems by new gas geothermometer, *Geochim. Cosmochim. Acta*, **44**: 549-556.

Darling, G.W. (1990). Rift Valley Gas Geothermometry Project. Unpublished technical report (WD/91/2R), British Geol. Survey, Keyworth, UK, 9 pp.

David, M. (1977). Geostatistical ore reserve estimation in developments of Geomathematics. Elsevier, New York, 364 pp.

De la Torre, I., Benito-Calvo, A., Mora, R., Martinez-Moreno, J., Moran, N. and Tibebu, Dejene (2007). Stone Age occurrences in the western bank of the Bilate River of the Southern Ethiopia. Nyame Akuma, **67**: 14–25.

Dickson, M. H. and Fanelli, M. (2004). Introduction to geothermal energy. Institute of Geosciences and Earth Resources, national resource council, Pisa, Italy, 61 pp.

Ebinger, C., Deino, A., Tesha, A., Becker, T. and Ring, U. (1993). Tectonic controls on rift basin morphology: evolution of the Northern Malawi (Nyasa) Rift. Journal of Geophysical Research, **98**(B10): 17821-17836.

Ebinger, C. J., Tilahun Yemane, Gidey Wolde Gabriel, Aronson, J. L. and Walter, R.C. (1993). Late Eocene recent volcanism and faulting in the Southern Main Ethiopian rift. Journal of the Geological Society of London, **150**: 99–108.

Ebinger, C. J. and Casey, M. (2001). Continental breakup in magmatic provinces: an Ethiopian example. Geology, **29**: 527–530.

Ebinger, C. (2005). Continental break-up: The East African perspective. Astronomy and Geophysics, **46**: 16–21.

Electric Power Research Institute (EPRI), (1978). Geothermal Energy Prospects for the Next 50 Years. Special report (ER-611-SR), Palo Alto, California.

Electroconsult (ELC), (2015). Consultancy Services for Geothermal Surface Exploration in Tendaho Alalobeda, Ethiopia. Unpublished report, Milano, Italy, 69 PP.

Elias Altaye (1984). Geology and surface alteration of Corbetti caldera, Ethiopia. Unpublished project report, Geothermal Institute, University of Auckland, New Zealand, 71 pp.

Ellis, A.J. and Mahon, W.A.J. (1964). Natural hydrothermal systems and experimental hot water/rock interactions. *Geochim. Cosmochim. Acta*, **28**: 1323-1357.

Energy and Geosciences Institute (EGI), (1997). The geothermal energy and its use. University of Utah, United States, 345 pp.

Engdawork Admassu and Selamawit Worku (2015). Characterization of Quaternary Extensional Structures: Tulu-Moye Geothermal Prospect, Ethiopia. GRC *Transactions*, **39**: 1-8.

Environmental Protection Authority (EPA), (2011). Ethiopia's Climate-Resilient Green Economy Strategy. Environmental Protection Authority, Addis Ababa, Ethiopia.

Ernst, L., Young, C. and ShinNihon, L. (2010). Study on geothermal power development project in the Aluto Langano Field, Ethiopia. Japan External Trade Organization (JETRO).

Fassil Teffera, Lemmens, P., Deriemaecker, A., Deckers, J., Bauer, H., Feleke Gamo, Brendonck, L. and De Meester, L. (2018). Why are Lake Abaya and Lake Chamo so different? A limnological comparison of two neighboring major Ethiopian Rift Valley lakes. Shallow lakes research, Springer Nature, Switzerland.

Fournier, R.O. (1977). Chemical geothermometers and mixing models for geothermal systems, Geothermics, **5**: 41-51.

Fournier, R.O. and Potter, R.W.II. (1982). A revised and expanded silica (quartz geothermometers). Geotherm. Res. Council Bull., **11**: 3-9.

Fridriksson, T. (2009). Diffuse CO_2 degassing through soil and geothermal exploration. Presented at "Short Course on Surface Exploration for Geothermal Resources", in Ahuachapan and Santa Tecla, El Salvador, Central America, 6 pp.

Fridriksson, T., Padrón, E., Óskarsson, F. and Pérez, N. M. (2016). Application of diffuse gas flux measurements and soil gas analysis to geothermal exploration and environmental monitoring: Example from the Reykjanes geothermal field, SW Iceland. Renewable energy, **86**: 1295-1307.

Frisch, W. (1997). Tectonic Geomorphology. **In**: *Proceeding of the Fourth International Conference on Geomorphology*, Supplementary Band, 118 pp.

Gad, S. and Kusky, T. (2006). Lithological mapping in the Eastern Desert of Egypt, the Barramiya area, using Landsat thematic mapper (TM). Journal of African Earth Sciences, **44**: 196-202.

Geological survey of Ethiopia (GSE), (2000). Geology, Geochemistry and Geophysics of the Abaya-Tulu moye geothermal prospects. Unpublished report, Addis Ababa Ethiopia.

Gezahegn Yirgu, Ebinger, C. and Maguire, P. (2006). The afar volcanic province within the East African Rift System: introduction. Geological Society, London, Special Publications **259**(1): 1-6.

Gibson, I. L. (1969). The structure and volcanic geology of an axial portion of the Main Ethiopian Rift. Tectonophysics, **8**: 561–565.

Gidey Woldegabriel, Aronson, J. L. and Walter, R. C. (1990). Geology, geochronology, and rift basin development in the central sector of the Main Ethiopia Rift. Geological Society of America Bulletin, **102**: 439–458.

Giggenbach, W.F. (1988). Geothermal solute equilibria, Geochim. Cosmochim. Acta, **52**: 2749-2765.

Giggenbach, W.F. and Goguel, R.L. (1989). Collection and analysis of geothermal and volcanic water and gas discharges. Unpublished report, department of scientific and industrial research, chemistry division, Petone, New Zealand.

Glover, R.B. (1976). Geochemical investigations in the Lakes District and Afar of Ethiopia

Gupta, R. (2003). Remote Sensing Geology, 2nd ed. Berlin Heidelberg: Springer-Verlag, 655 pp.

Harvey, M. C., Britten, K. and Schwendenmann, L. (2015). A review of approaches to distinguish between biological and geothermal soil diffuse CO_2 flux. School of Environment, University of Auckland and GNS Science, New Zealand, 6 pp.

Harvey, M. C. (2016). Geothermal Field Work Using a Drone with Thermal Camera: Aerial Photos, Digital Elevation Models and Heat Flow. GRC Transactions, **40**:1-6.

Harvey, M., Harvey, C., Rowland, J. and Luketina, K. (2016). Drones in geothermal exploration: thermal infrared imagery, aerial photos and digital elevation models. **In**: *Proceedings, 6th African Rift Geothermal Conference,* Addis Ababa, Ethiopia.

Heath, R.C. (1983). Basic groundwater hydrology. US Geological Survey, Reston, Verginia, USA, 86 pp.

Hobbs, W.H. (1912). Earth Features and their Meaning. Macmillian Co., New York.

Hochstein, M. P. (1990). Classification and assessment of geothermal resources. Geothermal Institute, University of Auckland, New Zealand.

Hutchison, J.W., Mather, T. A., Pyle, D. M., Biggs, J. and Gezahegn Yirgu (2015). Structural controls on fluid pathways in an active rift system: A case study of the Aluto volcanic complex. Geosphere, **11**(3): 1-21.

Hutchison, W., Fusillo, R., Pyle, M. D., Mather, A. T., Blundy, D. J., Biggs, J., Gezahegn Yirgu, Cohen, E. B., Brooker, A. R., Barfod, N. D. and Calvert, T. A. (2016). A pulse of mid-Pleistocene rift volcanism in Ethiopia at the dawn of modern humans. Nat. Commun. 7, 13192 doi: 10.1038/ncomms13192.

Hutchison, W., Pyle, D.M., Mather, T.A., Gezahegn Yirgu, G., Biggs, J., Cohen, B.E., Barford, D.N., and Lewi, E. (2016). The eruptive history and magmatic evolution of Aluto volcano: New insights into silicic peralkaline volcanism in the Ethiopian rift. Journal of Volcanology and Geothermal Research, **328**: 9–33.

Jordan, G., Meijninger, B.M.L., van Hinsbergen, D.J.J., Meulenkamp, J.E. and van Dijk, P.M. (2005). Extraction of morphotectonic features from DEMs: Development and applications for study areas in Hungary and NW Greece. International Journal of Applied Earth Observation and Geoinformation, **7**: 163–182.

Kazmin, V. (1980). Transform faults in the East African Rift system. Atti Convegni Lincei, **47**: 65-73.

Kazmin, V., Seife Mickael Berhe, Nicoletti, M. and Pertucciani, C. (1980). Evolution of the northern part of the Ethiopian rift. Atti Convegni Lincei, **47**: 275 – 292.

Keir, D., Ebinger, C.J., Stuart, G.W., Daly, E. and Amare Ayele (2006). Strain accommodation by magmatism and faulting as rifting proceeds to breakup: Seismicity of the northern Ethiopian rift. J.Geophysical Research, **11**(1): 1-17.

Keranen, K., Klemperer, S.L., Gloaguen, R. and Eagle working group (2004). Three dimensional seismic imaging of a protoridge axis in the Main Ethiopian Rift. Geology, **32**: 949–952.

Keranen, K and Klemperer, S.L. (2008). Discontinuous and diachronous evolution of the Main Ethiopian Rift: Implications for the development of continental rifts, Earth Planet. Sci. Lettt., **265**: 96–111.

Konon, A. and Smigielski, M. (2006). DEM-based structural mapping: examples from the Holy Cross Mountains and the Outer Carpathians, Poland. Acta Geologica Polonica, **56**: 1-16.

Ledesert, B., Hebert, R, Genter, A., Bartier, D., Clauer, N. and Grall, C. (2010). Fractures, hydrothermal alterations and permeability in the Soultz Enhanced Geothermal System. Comptes Rendus Geoscience, **342**: 607–615.

Levin, N. E., Quade, J., Simpson, S. W., Semaw, S. and Rogers, M. (2004). Isotopic evidence for Plio–Pleistocene environmental change at Oro Province, Gona, Papua New Guinea. Earth and Planetary Science Letters, **219**(1): 93-110.

Lewicki, J. L., Bergfeld, D., Cardellini, C., Chiodini, G., Granieri, D., Varley, N. and Werner, C. (2005). Comparative soils CO_2 flux measurements and geostatistical estimation methods on Masaya volcano, Nicaragua. Bull volcanology, **68**: 76-90.

Lloyd, E. F. (1977). Geological factors Influencing geothermal exploration in the Langano Region, Ethiopia. Unpublished report, NZ Geological survey, Rotorua, New Zealand, 73 pp.

Mackenzie, G., Thybo, H. and Maguire, P. (2005). Crustal velocity structure across the Main Ethiopian Rift: results from two-dimensional wide-angle seismic modeling. Geophysical Journal International, **162**(3): 994-1006.

Madani, A. (2014). Assessment and evaluation of band ratios, Brovey and HSV techniques for lithologic discrimination and mapping using Landsat ETM+ and SPOT-5 data. International Journal of Geosciences, **5**: 5-11.

Mahatsente, R., Jentzsch, G. and Jahr, T. (1999). Crustal structure of the Main Ethiopian Rift from gravity data: 3-dimensional modeling. Tectonophysics, **313**: 363–382.

Manzella, A. (2006). An introduction to geothermal energy. Institute of Geosciences and Earth Resources, national resource council, Pisa, Italy, 83 pp.

Marini, L. (2000). Geochemical techniques for the exploration and exploitation of geothermal energy. University of Genoa, Genoa, Italy, 82 pp.

Martina, K. (2009). Feasibility Study of Binary Geothermal Power Plants in Eastern Slovakia: Analysis of ORC and Kalina Power Plants. Solborg at Nordurslod, Akureyri, Iceland.

Martínek, K. (2018). Remote sensing data and analysis for geological mapping.unpublished report, Czech Geological Survey, Prague, Czech Republic, 56 pp.

Martin-Jones, C.M., Lane, C.S., Pearce, N.J.G., Smith, V.C., Lamb, H.F., Schaebitz, F., Viehberg, F., Brown, M.C., Frank, U. and Asfawossen Asrat (2017). Lake sediments provide the first eruptive history for Corbetti, a high-risk Main Ethiopian Rift volcano. Geophysical Research, **45** (12): 1127-1130, https://doi.org/10.1130/G39594.1.

Mazzarini, F., Rooney, T. and Isola, I. (2013). The intimate relationship between strain and magmatism: A numerical treatment of clustered monogenetic fields in the Main Ethiopian Rift. Tectonics, **32**: 49–64.

Meseret Teklemariam (1986). Petrography of the cores and cutting samples from wells LA-3, 4, 5 and 6. Aluto-Langano, Ethiopia. Unpublished report, Geological Survey of Ethiopia, Addis Ababa, Ethiopia.

Meseret Teklemariam, Battaglia, S., Gianelli, G. and Ruggieri, G. (1996). Hydrothermal alteration in the Aluto-Langano geothermal field, Ethiopia. Geothermics, **25**(6): 79-702.

Meseret Teklemariam and Kibret Beyene (2000). Geochemical monitoring of the Aluto-Langano geothermal field. Unpublished internal report, Geological Survey of Ethiopia, Addis Ababa, Ethiopia, 10 pp.

Meseret Teklemariam and Kibret Beyene (2005). Geothermal Exploration and Development in Ethiopia. **In**: Proceedings World Geothermal Congress, Antalya, Turkey.

Meseret Teklemariam and Solomon Kebede (2010). Strategy for geothermal resource exploration and development in Ethiopia. **In**: *Proceedings World Geothermal Congress*, Bali, Indonesia.

Minissale, A., Corti, G., Tassi, F., Darrahc, T. H., Vaselli, O., Montanari, D., Montegrossi G., Gezhagn Yirgu, Selmo, E. and Asfaw Teclu (2017). Geothermal potential and

origin of natural thermal fluids in the northern Lake Abaya area, Main Ethiopian Rift, East Africa. Journal of Volcanology and Geothermal Research, **336**: 1-8.

Mohammednur Desissa and Yohanes Lema (206). The Resistivity Structure of the Abaya Geothermal Field, (Southern Main Ethiopian Rift) Revealed by Magneto-telluric Imaging. Unpublished report, Geological Survey of Ethiopia, Addis Ababa, Ethiopia, 23 pp.

Mohr, P.A. (1962). The Ethiopian Rift system. Bull. Geophys. Obs, Addis Ababa, Ethiopia.

Mohr, P. (1987). Patterns of faulting in the Ethiopian Rift Valley. Tectonophysics, **143**: 169–179.

Mohr, P. and Zanettin, B. (1988). The Ethiopian food basalt province. Kluwer Academic Publishers, **45**: 63–110.

Molin, P. and Corti, G. (2015). Topography, river network and recent fault activity at the margins of the Central Main Ethiopian Rift (East Africa). Tectonophysics, **664**: 67-82.

Pour, A. and Hashim, M. (2015). Hydrothermal alteration mapping from Landsat-8 data, Sar Chesmeh copper mining district, south-eastern Islamic Republic of Iran. Journal of Taibah University for Science, **9**: 155-166.

Pürschel, M., Gloaguen, R. and Stadler, S. (2013). Geothermal activities in the Main Ethiopian Rift: Hydrogeochemical characterization of geothermal waters and geothermometry applications (Dofan-Fantale, Gergede-Sodere, Aluto-Langano). Geothermics, **47**: 1-12.

Reimer, G. (1980). Use of soil- gas helium concentrations for earthquake prediction: Limitations imposed by diurnal variation. Journal of Geophysical Research, Solid Earth **85**(B6): 3107-3114.

Reykjavík Geothermal (RG), (2017). Geological, Geochemical and Geophysical exploration in Tullu Moye, corbetti and Abaya geothermal fields. Unpublished internal report, Addis Ababa, Ethiopia.

Ring, U. (2014). The East African Rift System. Austrian Journal Earth Science, **107**(1): 132-146.

Rosendahl, B. L. (1987). Architecture of continental rifts with special reference to east Africa. Annual Reviews of Earth and Planetary Sciences, **15**: 445–503.

Salahadin Ali and Lemma Kassa (2007). Preliminary Geochemical Report of Abaya Geothermal Prospect. Unpublished report, GSE, Addis Ababa, Ethiopia, 16 pp.

Samrock, F., Kuvshinov, A., Bakker, J., Jackson, A. and Fisseha, S. (2015). 3-D analysis and interpretation of magnetotelluric data from the Aluto-Langano geothermal field, Ethiopia. Geophysical Journal International, **202**: 1923-1948.

Samrock, F., Grayver, A.V., Eysteinsson, H. and Saar, M.O. (2018). Magnetotelluric image of transcrustal magmatic system beneath the Tulu Moye geothermal prospect in the Ethiopian Rift. Geophysical Research Letters, **45**: 1-10.

Samson Tesfaye, Harding, D. J. and Kusky, T. M. (2003). Early continental breakup boundary and migration of the Afar triple junction, Ethiopia. Geol. Soc. Am. Bull, **115**: 1053-1067.

Seleshi Bekele (2001). Modern water level and Sediment accumulation changes of Lake Abaya, southern Ethiopia-A case study from the northern lake area.

Sladek, C., Coolbaugh, M.F., Penfild, R., Skord, J. and Williamson, L. (2012). The inflences of thermal diffusivity and weather on shallow (2-meter) temperature measurements. Geothermal Resources Council Transactions, **36**: 793-797.

Solomon Kebede and Mohammedberhan Abdulkadir (1987). Results of Shallow Wells Drilling and Geophysical Review of Corbetti Geothermal Prospect. Unpublished report, Ethiopian Institute of Geological Survey (EIGS), Addis Ababa, Ethiopia, 34 pp.

Solomon Kebede (2014). Country update on geothermal exploration and development in Ethiopia. Presented at Short Course on "Exploration for Geothermal Resources", at Lake Bogoria and Lake Naivasha, Kenya.

Solomon Kebede (2016). Country update on geothermal exploration and development in Ethiopia. I**n**: *Proceedings, 6th African Rift Geothermal Conference*, Addis Ababa, Ethiopia.

Tadesse Alemu (2012). Geology of Ethiopia. Unpublished report, GSE, Addis Ababa, Ethiopia.

Tadesse Mamo and Zewdu Abtew (2011). Report on results of near surface temperature measurments and associated hydrothermal alteration studies in Corbetti Geothermal Prospect. Unpublished report, Geothermal Resource Exploration and Assessment Core Process, Ministry of Mines, GSE, 54 pp.

Tadiwos Chernet (2011). Geology and hydrothermal resources in the northern Lake Abaya area, Ethiopia. Journal of African Earth Sciences, **61**: 129-141.

Takele Bassa (2017). Ethnobotanical Study of Medicinal Plants in Wolaita Zone, Southern Ethiopia. Journal of Biology, Agriculture and Healthcare, **7**: 2224-3208.

Tamiru Alemayehu and Tigistu Haile (2008). Geophysical exploration of the Boku geothermal area, Central Ethiopian Rift. Geothermics, **37**(6): 586-596.

Tester, J.W., Drake, E. M., Golay, M. W., Driscoll, M. J. and Peters, W.A. (2005). Sustainable Energy Choosing among options. Cambridge, MA, the MIT Press.

Tigistu Haile, Tamiru Alemayehu and Ranieri, G. (2000). Geophysical, Geological and Hydrogeological Investigations of Boku thermal field, Nazareth, Ethiopia. **In:** *Proceedings, 25th Workshop on Geothermal Reservoir Engineering*, California, USA, 8 pp.

Todd, D.K. and Larry, W.M. (2005). Groundwater hydrology. John Wiley and Sons, Inc., NY, 656 pp.

Tonani, F. (1970). Geochemical methods in prospecting for hot water. Geothermics, **2**: 492-5150.

Tonani, F. (1980). Some remarks on the application of geochemical techniques on the geothermal exploration. Proc. Adv. Eur. Geoth. Res., 2nd Sympo. , Strasbourg, 428-443.

Truesdel, A.H and Fournier, R.O. (1977). Procedure for estimating the temperature of the hot water component in mixed water using a plot of dissolved silica versus enthalpy, US geol. Survey J.Res, **5**: 49-52.

Tsegaye Abebe, Balestrieri, M.L. and Bigazzi G. (2010). The Central Main Ethiopian Rift is younger than 8 Ma: confirmation through apatite fission-track thermo-chronology. Terra Nova, **22**: 470–476.

United Nations Development Program (UNDP), (1973). Investigation of geothermal resources for power development, Geology, Geochemistry and Hydrogeology of hot springs of the east African Rift System within Ethiopia. Unpublished technical report, United Nations, New York, USA, 274 PP.

Varet, J., Tadiwos Chernet, Girma Woldetinsae and Arnason, K. (2012). Exploring for Geothermal Sites in Northern and Central Afar (Ethiopia). **In:** *Proceedings of the 4th African Rift Geothermal Conference*, Nairobi, Kenya.

Weiss, W. (2003). Solar Heating Systems for Houses: A Design Handbook for Solar Combisystems, London, James and James (science publishers), Ltd., London, England, 11 pp.

Westphal, E. (1975). Agricultural systems in Ethiopia. Centre for Agricultural Publishing and Documentation, Wageningen, Netherlands.

Yosef Mengistu Darge, Binyam Tesfaw Hailu, Ameha Atnafu Muluneh and Tesfaye Kidane (2019). Detection of geothermal anomalies using Landsat 8 TIRS data in Tulu -Moye geothermal prospect, Main Ethiopian Rift. Int. J. Appl. Earth Obs. Geoinformation, **74**: 16–26.

Younger, P. L. (2014). Missing a trick in geothermal exploration. Nature Geoscience, **7**: 479–480.

Zanettin, B., Justin-Visentin, E., Nicoletti, M. and Petrucciani, C. (1978). Evolution of the Chencha escarpment and the Ganjiuli graben (Lake Abaya) in the southern Ethiopian rift. Neues Jahrbuch fur Geologie und Palaontologie, Monatshefte, **8**: 473–490.

Zehner, R.E., Tullar, K.N. and Rutledge, E. (2012). Effectiveness of 2-meter and Geoprobe shallow temperature surveys in early stage geothermal exploration. Geothermal Resources Council Transactions, **36**: 835-841.

Appendix I

Field structural Data

Faults							
ID	**Orientation**		**Location**			**Down throw**	**Lithological Unit**
	Strike	**Dip**	**Easting**	**Northing**	**Elevation**		
F001	32	85SE	373468	736095	1393m	15m	Basalt
F002	10	80SE	375379	738719	1417m	35m	basalt
F003	15	85SE	379414	733645	1208m	180m	Ignimbrite
F004	005	65SE	378414	733159	1263m	25m	Basalt
F005	10	75SE	377069	732432	1296m	45m	Basalt
F006	30	85SE	374742	732686	1294m	20m	Basalt
F007	15	70SE	374676	732816	1303m	20m	Basalt
F008	25	75NW	372562	735099	1354m	20m	Basalt
F009	345	65NE	378535	731185	1457m	150m	Ignimbrite
F010	10	85SE	377116	742292	1452m	40m	Basalt
F011	005	80SE	376197	742239	1439m	10m	Basalt
F012	345	75SW	380202	743697	1428m	40m	Basalt
F013	340	65SW	380318	743710	1414m	30m	Basalt
F014	30	85SE	381368	744683	1387m	5m	Basalt
F015	005	70NW	382180	745033	1415m	18m	Basalt
F016	10	85NW	382082	744264	1393m	30m	Crystal rich basalt

F017	30	85NW	381951	744151	1377m	50m	Basalt
F018	340	75NE	377910	730967	1261m	15m	Ignimbrite
F019	20	65NW	382594	732306	1209m	85m	Ignimbrite
F020	005	35SE	382980	732269	1221m	35m	Ignimbrite
F021	10	35SE	383446	733184	1257m	40m	Ignimbrite
F022	15	35SE	385773	731826	1219m	30m	Ignimbrite
F023	005	55SE	385099	733593	1248m	10m	Vesicular Basalt
F024	005	25SE	385373	733972	1257m	5m	Ignimbrite
F025	20	60SE	378535	731185	1252m	25m	Vesicular Basalt
F026	005	65SE	380667	735001	1208m	210m	Ignimbrite
F027	005	35SE	384782	741167	1312m	25m	Basalt
F028	10	65SE	384155	741686	1354m	15m	Basalt
F029	20	20SE	383335	741847	1384m	10m	Basalt
F030	5	35SE	383193	742105	1397m	5m	Basalt
F031	20	65NW	382893	742314	1395m	20m	Basalt
F032	005	25NW	383783	741983	1381m	5m	Basalt
F033	10	35SE	384657	740807	1303m	8m	Basalt
F034	005	30NW	385474	740360	1284m	5m	Basalt
F035	005	45NW	385714	739724	1280m	6m	Basalt
F036	005	25SE	374449	735572	1345m	10m	Basalt
F037	10	35SE	374530	737210	1387m	20m	Basalt

F038	005	30NW	374870	737081	1382m	20m	Scoria
F039	005	55SE	375103	736956	1375m	35m	Basalt
F040	10	55SE	375204	737020	1365m	35m	Basalt
F041	10	35NW	376768	736973	1360m	5m	Basalt
F042	10	25NW	376911	736904	1366m	3m	Basalt
F043	10	40SE	377301	736058	1333m	10m	Basalt
F044	15	45NW	377523	736040	129m	5m	Basalt
F045	10	40SE	377552	735909	1332m	5m	Basalt
F046	10	40SE	378062	733817	1316m	10m	Basalt
F047	20	85SE	378405	733648	1276m	45m	Basalt
F048	005	25NW	378613	733628	1265m	5m	Basalt
F049	005	35NW	381391.8	734362.89	1194m	3m	Basalt
F050	320	25SW	381462.6	735015.29	1202	3m	Basalt
F051	320	30SW	381778.6	734805.75	1199m	4m	Basalt
F052	340	25SE	381636.2	735199.67	1209	3m	Basalt
F053	340	25NW	381421.7	735286.7	1204m	3m	Basalt
F054	10	65SE	381021.8	735580.57	1230m	120m	Basalt
F055	005	25NW	377931.2	731833.24	1276m	5m	Basalt
F056	005	25NW	378640.7	732266.08	1226m	10m	Ignimbrite
F057	005	25NW	378727.24	732554.35	1233m	5m	Ignimbrite
F058	005	75NW	376697	739621.51	1374m	10m	Basalt
F059	005	65SE	376071.64	740053.59	1372m	35m	Basalt
F060	002	65SE	376696.02	739874.38	1376m	13m	Basalt

F061	340	75SW	376819	739791	1378m	5m	Basalt
F062	340	35SW	377675.85	738784.42	1347m	5m	Basalt
F063	005	65SE	378464.62	738501.58	1342m	20m	Basalt
F064	005	65SW	378747.1	738217.02	1334m	25m	Basalt
F065	005	65SE	378509.36	738683.37	1342m	25m	Columnar Basalt
F066	350	35NE	380500.46	742240.81	1355m	5m	Basalt
F067	350	30SW	380628.28	742207.58	1347m	3m	Basalt
F068	005	65NW	381124.71	741962.14	1343m	100m	Basalt
F069	350	25SW	380652.11	741931.67	1357m	3m	Basalt
F070	350	65SW	380525.03	741956.72	1345m	3m	Basalt
F071	005	45SE	380442.98	741990.84	1350m	35m	Basalt
F072	350	65SW	377019.64	740093.55	1356m	5m	Basalt
F073	10	60SE	376872.52	740196.72	1341m	15m	Basalt
F074	320	60NE	376219.66	740342.16	1365m	35m	Basalt
F075	350	30NE	375978.09	739845.6	1389m	3m	Basalt
F076	340	10SW	376328.42	739609.3	1384m	2m	Basalt
F077	330	25SW	377555.3	738561.01	1356m	5m	Basalt
F078	005	65SE	378323.23	732737.13	1234m	15m	Basalt
F079	340	25SW	378531.9	732764.53	1231m	3m	Basalt
F080	330	55NE	378930.61	732280.04	1176m	35m	Ignimbrite
F081	330	35SW	375510.05	732375.92	1224	5m	Basalt
F082	300	25NE	376921.64	730591.96	1241	10m	Ignimbrite

Fracture							
ID	**Orientation**		**Location**			**Average spacing (m)**	**Lithological Unit**
	Strike	**Dip**	**Easting**	**Northing**	**Elevation**		
FR001	085	85S	380296	743933	1417m	6	Volcanic sediment
FR002	240	75S	383445	733704	1246m	3	Pumice
FR003	320	85S	384889	732380	1216m	5	Lake Sediment
FR004	005	68SE	381138.3	735465.88	1208m	5	Lake Sediment
FR005	320	35SW	378391.4	731884.18	1223m	3	Lake Sediment
FR006	315	45SW	378026.4	731632.46	1252m	4	Lake Sediment/pumice?
FR007	320	35SW	377943.3	731424.57	1257m	15	Pumice
FR008	340	30SW	378156.6	731385.84	1245m	15	Lake Sediment
FR009	280	25SE	377513.2	731155.3	1270m	2	Pumice
FR010	240	65SE	378182.1	732068.85	1240m	3	Lake Sediment/pumice?
FR011	300	55SW	378149.6	732282.31	1253m	10	Lake Sediment/pumice?
FR012	040	45SE	378296	732576.32	1235m	5	pumice
FR013	340	65SW	378833	732779.57	1234m	4	Pumice
Joint							

ID	Orientation		Location			Aperture (m)	Lithological Unit
	Strike	**Dip**	**Easting**	**Northing**	**Elevation**		
J001	**345**	65NE	378326	733055	1274m	10cm	Ignimbrite
J002	**030**	85SE	378468	738570	1359m	15cm	Basalt

Appendix II

Fluid Chemical Analysis Result

Sample ID	pH	T (°C)	SiO_2	Na	K	Ca	Mg	Fe	Al	B	CO_2	H_2S	SO_4^{2-}	HCO_3^-	CO_3^{2-}	Cl^-
AB-18-W01	6.39	41.4	119.1	219.5	30.55	39.45	43.29	0.092	0.127	0.140	542.8	N.a.	20.97	397.32	0.18	99.69
AB-18-W02	5.94	67	138.6	523.8	33.80	18.31	6.049	1.362	0.377	0.291	948.9	N.a.	16.79	422.77	0.08	55.33
AB-18-W03	5.4	88.1	116.8	5.987	9.301	2.235	0.544	0.079	0.063	0.007	10.2	N.a.	104.8	1.43	0	1.573
AB-18-W04	0	67.2	147.1	492.7	34.32	19.22	8.373	0.239	0.173	0.293	865.9	N.a.	18.45	571.43	0.22	50.63
AB-18-W05	5.94	67	142.9	533.5	34.20	16.51	5.857	0.088	0.074	0.286	N.a.	N.a.	14.51	0	0	54.52
AB-18-W06	6.23	67.3	142.9	526.6	33.60	16.66	5.603	1.278	0.186	0.291	1395.5	0	14.79	938.48	0.38	52.69
AB-18-W07	6.4	67.7	142.5	530.4	33.70	16.38	5.622	1.355	0.150	0.296	1356.7	0	14.17	1092.4	0.65	53.21
AB-18-W08	6.55	56.8	189.1	431.5	51.29	87.65	61.86	1.104	0.033	0.309	1730.4	0.1	11.07	1471.9	1.48	51.79
AB-18-W09	6.84	67.2	149.5	522.3	35.41	19.71	8.712	0.462	0.119	0.295	1294.7	0.1	14.00	1397.2	2.31	53.35

Stable Isotope Result

Sample	□ $^{18}O/^{16}O$	Stdev	□ $^{3}H_2/^{2}H_2$	Stdev	Date
AB-18-03	8.21	0.03	20.49	0.17	This paper
AB-18-04	-3.02	0.05	-7.34	0.38	This paper
AB-18-W06_1	-3.11	0.02	-6.9	0.71	This paper
AB-18-W06_2	-3.12	0.02	-7.7	0.57	This paper
AB-18-W09_1	-3	0.05	-7.48	0.81	This paper
AB-18-W09_2	-3.01	0.05	-6.86	0.36	This paper
Boloche-14	-0.13	N.a.	0.1	N.a.	2011
SP-15	-3.07	N.a.	-8.16	N.a.	2011
SP-16	-2.74	N.a.	-6.99	N.a.	2011
SP-6	-1.06	N.a.	-11.3	N.a.	2011
SP-8	-3.01	N.a.	-9.64	N.a.	2011

Gas sample analysis result

Sample name	H_2 [mmol/kg]	N_2 [mmol/kg]	CH_4 [mmol/kg]	O_2 [mmol/kg]	Ar [mmol/kg]	H_2S [mmol/kg]	CO_2 [mmol/kg]
AB-19-G04	N.a	N.a	N.a	N.a	N.a	1.19	11223
AB-19-G05	N.a	N.a	N.a	N.a	N.a	2.64	72414
AB-19-G06	N.a	N.a	N.a	N.a	N.a	3.40	106894
AB-19-G02	0.005	1.16	0.543	0.44	0.02	0.14	43560
AB-19-G04	0.005	2.83	0.0.15	1.37	0.06	0.14	13640
AB-19-G06	0.003	15.8	9.000	5.91	0.33	0.31	93148

Appendix III

Soil CO_2 Flux Data

Site	Easting	Northing	Elevation	CO_2 flux [g m^{-2} d^{-1}]
AB271	380245.8	742610	1407.66	10.4
AB272	380285	742560.6	1404.7	3.25
AB273	380321.5	742523.7	1411.75	1.46
AB275	380360.7	742483.5	1408.81	0.598
AB275	380400.8	742434.2	1413.76	2.41
AB276	380448.3	742394.3	1424.72	6.53
AB277	380486.3	742346.9	1398.33	4.72
AB278	380528.5	742238.8	1405.46	8.53
AB279	380581.2	742219.3	1422.93	6.19
AB280	380628.2	742210.8	1419.58	8.41
AB281	380699.5	742169.1	1412.76	18.1
AB282	380750.5	742150.6	1406.22	13.4
AB283	380789.6	742139.3	1407.19	6.69
AB284	380848.8	742129.4	1402.44	4.99
AB285	380899.8	742084.1	1401.55	7.82
AB286	380945.8	742060.6	1402.32	5.92
AB287	381008.6	742018.3	1195	18.7
AB288	381088	742017.3	1189.81	9.72
AB289	381135.4	742003.6	1187.53	5.3
AB290	381043.8	741776.4	1190.83	13.3
AB291	381039.6	741789.6	1186.08	18.3
AB292	380986.8	741810.5	1186.91	15.4
AB293	380940.4	741831.9	1184.45	1.04
AB294	380902.5	741853.8	1183.7	5.56
AB295	380802	741872.5	1185.27	14
AB296	380754.1	741898.8	1185.6	9.67
AB297	380695.3	741926.4	1184.82	7.89
AB298	380627.8	741942.1	1183.66	9.88
AB299	380583.5	741964.6	1184.69	3.67
AB300	380531.9	741980	1187.27	21.2
AB301	380487.4	742013.3	1186.55	5.91
AB302	380449.9	742033.6	1187.75	4.77
AB303	380399	742000.3	1187.62	16
AB304	380363.6	742025.6	1194.03	3.93
AB305	380298.4	742071.6	1193.45	1.74
AB306	380248.6	742110.6	1192.23	1.67
AB307	380203.3	742144.8	1191.65	6.41
AB308	380160	742183.2	1190.45	5.99
AB309	380118.5	742219.6	1191.51	4.38

AB310	380072.6	742250.2	1192	3.58
AB311	380028.7	742282.3	1194.57	0.498
AB312	379974.7	742320.4	1196.01	3.51
AB313	379927.2	742364.6	1194.52	7.59
AB314	379882.8	742398.9	1198.18	24.8
AB315	380222.9	742626.9	1190.14	4.63
AB316	380180.8	742663.6	1193.56	2.38
AB317	380145.2	742701.9	1200.24	11.3
AB318	380084.2	742729.1	1193.09	8.67
AB319	380033.3	742762.5	1199.7	15.8
AB320	379995.8	742787.7	1199.89	12.8
AB321	379932.7	742806.8	1206.45	14.2
AB322	379926.8	742822.6	1208.65	21.5
AB323	379924.2	742825.3	1203.89	37.2
AB324	379890	742871.3	1203.29	4.2
AB325	379859.5	742927.3	1197.37	1.15
AB326	379834.7	742976.3	1202.11	2.29
AB327	379807.8	743026.6	1197.68	1.05
AB328	379785	743086.1	1199.29	5.21
AB329	379745.4	743127.3	1195.09	1.77
AB330	379702.3	743168.6	1194.58	0.776
AB001	377393	739527	1188.67	2.58
AB002	377371	739537	1190.43	2.68
AB003	377342	739544	1198.66	2.17
AB004	377315	739553	11.6	3.12
AB005	377296	739564	766.52	1.38
AB006	377274	739576	1184.9	4.12
AB007	377255	739588	1202.76	2.35
AB008	377256	739588	1204.55	3.11
AB009	377298	739686	1189.89	24.4
AB010	377320	739676	1197.81	25.8
AB011	377340	739669	1175.67	8.8
AB012	377365	739652	1195.84	5.21
AB013	377383	739642	1207.01	9.08
AB014	377401	739632	1164.72	9.57
AB015	377425	739619	1031.33	1.13
AB016	377451	739606	1188.31	2.32
AB178	378251.5	740311.9	1203.71	18.1
AB179	378213.7	740342.2	1204.2	3.25
AB180	378192.9	740325.3	1204.44	165
AB181	378150.3	740367.6	1202	2.62
AB182	377107.7	739199.6	1209.92	17.2
AB183	377062.5	739240	11.6	2.78

AB184	377017.9	739285.2	11.7	1.92
AB185	376977.9	739331.8	539.81	0.898
AB186	376938.9	739376.1	1201.21	0.911
AB187	376902.8	739421.8	1208.45	2.36
AB188	376858.3	739458.8	1197.72	2.17
AB189	376813.1	739499.3	1207.81	0.845
AB190	376779.2	739541.8	1208.12	5.81
AB191	376741.9	739585.4	1223.02	2.17
AB192	376676.6	739627.8	1215.67	9.33
AB193	376637.6	739665.8	1263.53	5.59
AB194	376601.1	739703.6	1261.68	1.1
AB195	376546	739719.5	1256.59	2.13
AB196	376501.8	739748.3	1247.3	7.88
AB197	376456.7	739778.8	1245.19	0.775
AB198	376446	739786.6	1244.82	6.65
AB199	376406.4	739808.5	1259.2	6.16
AB200	376360.5	739843.8	1245.85	6.29
AB201	376305.9	739880.8	1245.14	1.54
AB202	376267.6	739927.6	11.9	2.12
AB203	376207.8	739948.8	1235.97	11.9
AB204	376127.7	739901.1	1247.81	0.757
AB205	376100.1	740004	1238.15	1.62
AB206	376060.4	740026.5	1257.14	1.43
AB207	376095.8	740085.4	1247.68	3.89
AB208	376130.9	740138.6	1279.75	7.26
AB209	376182.3	740222.9	1275.2	2.19
AB210	376231.3	740196.5	1276.11	3.86
AB211	376281.6	740170.3	1232.8	3.96
AB212	376329.2	740138.9	1222.13	3.18
AB213	376374.4	740104	1218.91	2.1
AB214	376418.7	740068.2	1254.71	2.63
AB215	376463.3	740035.9	1253.71	3.19
AB216	376506.4	740003.6	1252.69	1.39
AB217	376550.8	739977	1253.74	1.96
AB218	376590.1	739940.3	1251.28	2.15
AB219	376624.3	739907.3	1254.53	0.805
AB220	376723.4	739854.2	1254.91	0.506
AB221	376770.8	739820.4	1072.56	1.99
AB222	376813.3	739788.2	1265.59	1.47
AB224	377184.8	739156.4	1269.63	3.16
AB225	377220.8	739132.1	1263.64	3.21
AB226	377263.2	739112.9	1265.17	4.63
AB227	377302.4	739078.7	1255.2	3.27

AB228	377352.9	739054.4	1257.18	1.85
AB229	377386	739036.2	1261.42	2.64
AB230	377428.7	738999.8	1256.95	1.73
AB231	377479.8	738962.6	1255.67	3.09
AB232	377524.8	738931	1257.04	3.62
AB233	377564.8	738907.5	1260.8	6.09
AB234	377611.5	738881.6	1266.08	3.08
AB235	377654	738860.8	1271.51	1.46
AB236	377693.7	738840.1	1278.02	2.2
AB237	377742.9	738768.4	1273.51	2.36
AB238	377790.5	738739.6	1258.77	3.18
AB239	377833.4	738711	1252	1.73
AB240	377884.9	738695.4	1250.84	3.16
AB241	377944.1	738675.3	1256.54	0.65
AB242	378004	738668.7	1268.22	4.54
AB243	378077.6	738644.2	1277.35	3.34
AB244	378136.3	738638.6	1280.05	4.29
AB245	378201.5	738620.5	1281.02	4.98
AB246	378246.9	738593.2	1282.2	5.75
AB247	378274.4	738569	1267.77	7.07
AB248	378319.8	738518.9	1265.88	6.76
AB249	378368.3	738492.4	1273.21	12.2
AB250	378463.2	738493.4	1265.4	3.57
AB251	378501.2	738473.6	1265.22	14.7
AB252	378560	738403.5	1254.96	5.51
AB253	378592.3	738358.3	1222.8	1.32
AB254	378645.5	738350.3	1221.9	19.4
AB255	378678.4	738306.9	1213.23	21.1
AB256	378733.9	738240.5	1197.85	11.2
AB257	378748.4	738228.8	1216.15	9.5
AB258	378835.7	738442.7	1220.14	7.33
AB259	378789.7	738495.6	1222.03	9.08
AB260	378744.6	738531.3	1219.89	3.36
AB261	378684.7	738556.2	1230.12	6.71
AB262	378637.9	738590.9	598.35	6.93
AB263	378588.8	738630.8	1240.23	1.54
AB264	378554.2	738676.9	1240.69	3.13
AB265	378520.8	738696.5	1257.63	7.18
AB266	378448.9	738941.9	1256.08	7.43
AB267	378423.8	738969.9	1251.85	8.93
AB268	378367.8	739011.8	1247.31	3.27
AB269	378334.6	739039	1246.13	1.88
AB270	378311.5	739055.2	1242.1	7.6

AB359	376862.3	739766.8	1235.32	8.19
AB360	376908.4	739732.7	1227.68	2.89
AB361	376949.9	739704.1	1223.54	2.38
AB362	376989.7	739661.8	1226.35	3.22
AB363	377030.5	739623.8	1239.99	4.4
AB364	377069	739591.5	1237.85	13
AB365	377125.1	739567.9	1591.31	8.71
AB366	377172.1	739545.7	1605.97	55.5
AB367	377211.3	739559.6	1596.6	64.3
AB368	377243.1	739573.8	1583.81	5.33
AB369	377427.3	739512.7	1375.42	7.39
AB370	377470.5	739501.3	1378.29	9.24
AB371	377510.6	739492.4	1378.1	176
AB372	377545.8	739460.6	1383.35	25.8
AB373	377608.8	739549.8	1383.98	14.3
AB374	377573.8	739565.3	1379.46	27.5
AB375	377538.8	739588.8	1382.83	3.71
AB376	377491.1	739619.2	1386.95	4.22
AB377	377457.9	739629.2	1384.65	3.34
AB378	377510.6	739754.7	1392.2	2.4
AB379	377459.4	739800.8	1374.09	3.04
AB380	377425.2	739836.7	1380.13	4.75
AB381	377387.5	739878.7	1383.25	2.13
AB382	377350.6	739899.6	1382.11	2.79
AB383	377301.6	739936.8	1382.23	8.71
AB384	377237.3	739951.6	1380.28	5.15
AB385	377200.8	739975.4	1376.43	2.85
AB386	377153	739998.5	1373.2	4.67
AB387	377103.9	740032	1377.52	2.8
AB388	377061.6	740064.2	1374.41	4.04
AB389	377034.8	740083.1	1377.67	0.933
AB390	376971.8	740107.4	1378.25	9.2
AB391	376926.6	740143.4	1340.32	5.06
AB392	376894.1	740160.3	1379.76	7.04
AB393	376870.3	740174.8	1387.29	0.946
AB394	376911	740270.3	1382.06	6.51
AB395	376941.2	740382	1380.21	2.26
AB396	376987.9	740376.7	1375.73	2.53
AB397	377032.3	740353.1	1374.74	6.56
AB398	377080.4	740328.4	1372.75	6.38
AB399	377130.1	740311.8	1365.79	7.97
AB400	377178.8	740296.1	1369.92	2.61
AB401	377231.5	740273.9	1377.32	3.59

AB402	377292.3	740246.5	1374.36	7.04
AB403	377344.9	740218.4	1375.25	27.5
AB404	377399.2	740180.7	1372.34	10.3
AB405	377442.8	740167.9	1383.34	1.98
AB406	377496.5	740144.3	1384.3	2.09
AB407	377540.8	740153.9	1370.06	3.23
AB408	377574.3	740260.5	1369.18	2.79
AB409	377565.2	740313.4	1371.72	0.458
AB410	377506.3	740308.5	1387.52	6.69
AB411	377445.7	740314.2	1383.88	1.23
AB412	377372.6	740341.4	1389.87	2.32
AB413	377326.1	740371.9	1376.68	5.5
AB414	377266.7	740433.1	1379.74	1.91
AB415	377222.2	740466.1	1368.17	4.01
AB416	377174.3	740490.7	1374.54	5.72
AB417	377128.4	740515.6	1374.29	8.27
AB418	377082.3	740548.6	1370.19	2.16
AB419	377039.9	740578.7	1370.21	4.24
AB420	377103.3	740769.3	1372.35	8.49
AB421	377148	740748.3	1368.4	8.93
AB422	377192.1	740737.6	1353.69	6.82
AB423	377261.8	740733.2	1363.36	2.72
AB424	377298.5	740730.9	1364.24	5.55
AB425	377059.8	739791.4	1361.29	15.4
AB426	377019	739827.6	1361.47	1.39
AB427	376975.1	739861.1	1362.15	3.62
AB428	376930	739891.2	1362.99	3.64
AB429	376879.5	739896.6	1366.5	3.74
AB430	376837.2	739920.5	1367.07	2.37
AB431	376779.8	739936.4	1368.82	1.77
AB432	376767.2	739946.4	1367.43	1.76
AB433	376720	739964	1365.77	2.18
AB434	376668	739991	1362.29	7.85
AB435	376621.6	740016.2	1367.7	6.95
AB436	376576.6	740047.7	1341.31	9.51
AB437	376533.7	740070.9	1334.02	3.92
AB438	376470.3	740089.4	1344.83	4.79
AB439	376416.8	740115.8	1348.29	4.39
AB440	376374.8	740123.2	1349.63	6.77
AB441	376322.8	740152.8	1347.99	5.18
AB442	376266.5	740188.4	1336.48	3.43
AB443	376223.6	740215.6	1353.96	5.62
AB444	376194.2	740230.6	1350.71	4.3

AB445	376299.4	740420.8	1345.94	2.97
AB446	376345.8	740400	1349.34	0.964
AB447	376409.7	740393.1	1350.1	5.42
AB448	376463.4	740379.3	1347.14	7.11
AB449	376530.3	740375.6	1349.81	6.1
AB450	376574	740358.1	1347.7	19.7
AB451	376637.1	740336.7	1346.38	10.1
AB452	376688.5	740312.4	1372.99	3.87
AB453	376735	740299.4	1374.57	5.21
AB454	376791.3	740283.5	1373.8	8
AB455	376839.2	740271.4	1375.71	5.47
AB456	376928.5	740456.9	1375.82	5.5
AB458	376834.7	740512.5	1410.64	3.97
AB459	376791.3	740533	1396.28	6.54
AB460	376726.7	740561.5	1384.82	5.72
AB461	376659.7	740589.4	1397.27	10.4
AB462	376599.5	740625.7	1387.44	12.8
AB463	376544.1	740636.4	1389.11	4.85
AB464	376497.4	740651.7	1387.6	10.4
AB465	376455	740672.6	1368.92	6.4
AB466	376525.4	740884.8	1372.89	5.53
AB467	376577	740871.3	1368.16	6.43
AB468	376635.6	740853.6	1354.29	6.09
AB469	376692.3	740840.5	1362.25	4.75
AB470	376768	740810.8	1364.43	8.78
AB471	376819.8	740801.2	1362.52	10.1
AB472	376880.6	740796.6	1365.13	9.99
AB473	376935.8	740790.8	1359.51	6.08
AB474	376988.7	740783	1365.21	8.82
AB475	377045.5	740780.4	1344.92	3.75
AB476	375986.3	739815.1	1351.77	13.9
AB477	376031	739794.5	1368.37	6.09
AB478	376080.8	739759.4	1356.65	5.9
AB479	376135.2	739726.4	1362.96	2.9
AB480	376186.4	739692.3	1365.3	4.05
AB481	376235.4	739669.9	1364.26	2.82
AB482	376278.8	739642	1372.49	1.28
AB483	376320.9	739614.5	1371.77	5.83
AB484	376371	739584.6	1367.36	3.31
AB485	376416.6	739560.3	1362.08	5.07
AB487	376514.9	739511	1362.26	1.41
AB488	376558.1	739476.6	1355.54	4.39
AB489	376609.5	739435.3	1354.53	2.13

AB490	376609.5	739435.3	1358.23	2.13
AB491	376656.3	739341.2	1370.69	2.66
AB492	376701.6	739292.9	1376.58	15.9
AB493	376732.9	739235.3	1376.44	4.68
AB494	376843.7	739182.1	1376.11	1.76
AB495	376887.2	739146.9	1378.74	6.36
AB496	376929.7	739113.5	1377.98	3.5
AB497	376972.1	739077.1	1378.54	4.06
AB498	377011.2	739034.6	1385.31	3.2
AB499	377058.6	739002.5	1384.95	0.676
AB500	377097.1	738963.9	1386.15	10.3
AB501	377181.3	738933.3	1387.53	6.38
AB502	377220	738888.6	1389.61	7.47
AB503	377255.7	738847.5	1406.67	8.3
AB504	377296	738814	1406.23	4.9
AB505	377367.3	738757.4	1407.33	10.9
AB506	377410.6	738722	1417.18	7.88
AB507	377450.7	738678.6	1423.45	5.69
AB508	377487.4	738648.4	1427.68	4.49
AB509	377537.3	738621.9	1436.9	2.72
AB510	377574.4	738604.1	1431.09	10.5
AB511	377494.5	738401.7	1433.14	3.45
AB512	377441.8	738429.7	1438.32	7.63
AB513	377399.2	738458.3	1437.34	4.6
AB514	377350.2	738481.2	1437.44	3.81
AB515	377297.6	738508.6	1436.58	2.76
AB516	377248.5	738526.6	1436.8	15.9
AB518	377157.2	738585.6	1438.99	13.3
AB519	377115	738611.4	1441.3	6.91
AB520	377048.7	738646.2	1128.04	5.08
AB521	377003.6	738671.2	1221.99	3.71
AB522	376950.3	738692.2	1225.84	3.83
AB523	376884.8	738736.9	1244.74	2.65
AB524	376837	738763.4	1256.44	4.01
AB525	376791.3	738779.6	1251.25	4.86
AB652	372705.2	735012.6	1254.55	15.2
AB653	372752.2	734955.8	1268.22	14.2
AB654	372793.4	734908.1	1254.18	4.7
AB655	372825.2	734862.6	1251.04	5.47
AB656	372876.5	734818.5	1256.84	4.27
AB657	372925.1	734787.6	1249.36	3.94
AB658	372971.3	734733.9	1249.54	5.19
AB659	373018.3	734697	1255.49	14.2

AB660	373062.4	734643.9	1236.72	6.14
AB661	373112.8	734601.1	1225.58	6.87
AB662	373159.8	734560.8	1209.22	3.2
AB663	373206.8	734533.2	1202.9	8.48
AB664	373247.7	734489.9	1205.06	7.22
AB665	373289.3	734449.4	1206.38	7.86
AB666	373348.3	734443.4	1204.52	7.13
AB667	373386.1	734395.9	1182.7	19.3
AB668	373447.1	734376.8	1198.78	3.99
AB669	373489.8	734348.9	1198.78	4.75
AB670	373534.8	734314.5	1206.61	4.2
AB671	373580.1	734280	1195.85	4.16
AB672	373640.1	734261.7	1189.2	6.58
AB673	373680.9	734228.8	1392.28	2.09
AB674	373719.4	734189.1	1392.92	3.9
AB675	373739.1	734150.1	1398.47	2.28
AB676	373783.9	734120.3	1399.42	4.77
AB677	373854	734072.3	1399.5	10.2
AB678	373892.4	734025.8	1399.75	19.2
AB679	373922.5	733988.4	1420.74	26.3
AB680	374054.4	733048.2	1427.3	11
AB681	374097.8	733024.1	1431.09	8.92
AB682	374154.8	733001.8	1415.41	9.84
AB683	374197	732994.3	1402.36	12.9
AB684	374254.5	732973.9	1407.94	3.94
AB685	374315.2	732912.4	1417.11	5.92
AB686	374368.5	732862.6	1423.36	13.1
AB687	374443.4	732840.5	1436.04	12.5
AB688	374494.1	732826.9	1427.37	3.33
AB689	374543.7	732820.3	1412.57	3.74
AB690	374613.1	732808.3	1408.13	16.8
AB691	374688	732803.6	1399.39	13
AB692	374727.3	732795.6	1391.29	14.5
AB693	374776.6	732795.1	1390.75	26.2
AB694	374828.7	732777.1	1396.55	14.4
AB695	374885.9	732763.6	1384.48	16.7
AB696	374932.3	732731.7	1401.37	14.6
AB697	374981.4	732706.5	1404.25	9.86
AB698	375029.3	732688.5	1379.15	9.26
AB699	375095.8	732633.1	1374.43	16.3
AB700	375142	732604.4	1375.25	19.2
AB701	375195.3	732557.2	1366.63	23.9
AB702	375262.2	732529.5	1371.46	19.7

AB703	375312.4	732504.9	1357	26
AB704	375387.7	732438.4	1340.19	51.2
AB705	375417.6	732424.3	1340.99	49.6
AB706	375467.8	732410.9	1344.26	49.6
AB707	375505.4	732375.5	1351.68	22
AB708	375547.8	732334.9	1349.03	58.4
AB709	375613.6	732319.5	1352.31	46.9
AB710	375675.7	732294.7	1358.44	12.7
AB711	375751.3	732254.8	1349.72	15.8
AB712	375819.3	732240.8	1355.14	10.4
AB713	375900.9	732211.6	1355.49	12.1
AB714	375970.3	732203.8	1359.63	16
AB715	376025.7	732194.1	1360.81	15.1
AB716	376080.5	732185.3	1369.29	7.61
AB717	376128.6	732172.8	1382.75	5.35
AB718	374069.4	733945.8	1380.83	14.3
AB719	374073.5	733892.9	1373.76	23.1
AB720	374109.1	733826.6	1383.99	9.72
AB721	375011.8	734532.6	1382.67	10.7
AB722	374193	733738.1	1380.51	3.85
AB723	374238.1	733700.2	1377.38	4.63
AB724	374266.1	733653.4	1365.16	22.5
AB725	374315	733612.6	1374.45	17.3
AB726	374366.2	733585.7	1367.09	13.1
AB727	374413.6	733560.9	1361.4	4.63
AB728	374459.2	733533.9	1352.24	5
AB729	374537.3	733463.8	1347.77	2.94
AB730	374597.5	733432.6	1347.66	9.39
AB731	374658.2	733391.6	1347.05	3.57
AB017	380657.1	734970.1	1348.07	1.65
AB018	380709	734922.5	1348.41	3.2
AB019	380751	734889.1	1346.88	3.9
AB020	380785.4	734860.2	1345.98	7.7
AB021	380850.2	734828.6	1341.32	2.47
AB022	380896.1	734806	1350.49	4.71
AB023	380938.3	734745.6	1362.18	3.55
AB024	380980.6	734708.8	1400.46	7.66
AB025	381055.3	734617.7	1393.71	1.15
AB026	381080.4	734540.7	1382.88	200
AB027	381119.7	734482.3	1372.6	0.801
AB028	381149	734408.3	1355.28	4.8
AB029	381171.8	734366.7	1352.11	8.23
AB030	381207.7	734290.2	1358.79	1.76

AB031	381229.7	734240.9	1368.97	3.76
AB032	381239.8	734188.2	1387.94	4.02
AB033	381247.8	734116.4	1389.5	1.93
AB034	381422	734238	1388.83	4.4
AB035	381347	734350	1383.55	3.06
AB036	381375	734402	1386.39	2.43
AB037	381337	734446	1384.09	3.85
AB038	381260	734488	1380.89	1.33
AB039	381200	734547	1371.3	1.39
AB040	381171	734603	1370.63	2.27
AB041	381120.5	734671.5	1372.09	0.678
AB042	381075.3	734693.3	1371.08	0.537
AB043	381039	734753.4	1376.61	2.31
AB044	380979.4	734805.5	1359.8	2.67
AB045	380958.3	734880.6	1371.33	0.805
AB046	380948.3	734939.3	1375.3	0.308
AB047	380922	735007.1	1373.13	0.995
AB048	380889.9	735069.1	1370.08	1.4
AB049	380835.3	735100.6	1369.41	3.23
AB050	380807.3	735140	1358.65	1.61
AB051	380777.1	735188.7	1379.31	0.223
AB052	380892.6	735342.1	1383.44	6.86
AB053	380938.4	735316.5	1383.51	6.19
AB054	380987.5	735283.3	1381.77	2.21
AB055	381030.3	735250.2	1372.6	3.32
AB056	381085.3	735211.4	1370.05	2.5
AB057	381132.8	735201.1	1368.37	2.78
AB058	381170.8	735166.4	1371	2.89
AB059	381216.5	735129.6	1369.42	2.97
AB060	381265.1	735106.4	1362.01	1.28
AB061	381345.4	735070.6	1368.54	1.99
AB062	381390.1	735036.3	1372.41	1.22
AB063	381476.4	735005.3	1379.02	5.27
AB064	381721.3	735698.3	1374.9	6.49
AB065	381820.4	735624.2	1369.34	1.04
AB066	381639.3	734959.1	1366.07	2.57
AB067	381677.1	734903.9	1371.43	2.78
AB068	381736.3	734865.8	1360.64	2.45
AB069	381781.1	734836.7	1368.4	3.04
AB070	381851.8	734814.9	1370.98	0.856
AB071	381908.2	734799.6	1370.24	3.28
AB072	381968.5	734994.9	1375.58	5.9
AB073	381933.6	735021.4	1374.44	2.86

AB074	381875.1	735058.4	1398.64	1.38
AB075	381837.8	735117.5	1393.71	4.21
AB076	381788.8	735120.6	1390.03	1.07
AB077	381743.2	735148.1	1392.85	3.73
AB078	381690.4	735168.1	1391.25	1.2
AB079	381643.9	735191.1	1393.91	1.2
AB080	381610.8	735239.6	1390.93	7.71
AB081	381560.4	735278.4	1386.59	7.08
AB082	382018.1	735492.8	1393.49	3.34
AB083	381791.7	735428	1394.3	3.18
AB084	381533	735343.9	1395.13	5.42
AB085	381329	735373.7	1397.46	2.81
AB086	381281.3	735394.5	1407.5	1.01
AB087	381213.4	735427.4	1407.5	2.92
AB089	381102.1	735488.2	1408.47	6.33
AB090	381063.4	735514.8	1415.3	3.57
AB091	381018.8	735550.8	1395.44	4.54
AB092	381001.6	735570.3	1391.8	4.87
AB093	377811.9	731386.7	1388.46	18.2
AB094	377850.2	731349.3	1386.17	2.43
AB095	377891.2	731315	1381.09	3.75
AB096	377935.5	731281.2	1379.39	6.68
AB097	377980.3	731253.2	1381.03	1.04
AB098	378010.3	731236.3	1375.72	5.21
AB099	378051.8	731198	1375.32	366
AB100	378184.5	731360.6	1374.3	564
AB101	378217.1	731401.9	1370.76	452
AB102	376650.2	731087	1364.63	12.1
AB103	378119.5	731437	1369.92	16.6
AB104	378081.8	731479.4	1355.78	4.08
AB105	378046.9	731522.9	1358.36	8.43
AB106	378008	731544.1	1362.7	3.25
AB107	378046.4	731731.7	1362.35	2.86
AB108	378003.8	731833.5	1358.71	7.85
AB109	377915	731836.3	1365.13	3.83
AB110	377888.8	731843.3	1366.2	4.08
AB111	378093.4	731715.1	1367.35	3.15
AB112	378139.3	731694.4	1364.98	5.27
AB113	378196.1	731692.9	1368.83	5.99
AB114	377977.2	731097.9	1373.4	67.8
AB115	377920	730986.8	1369.99	60.8
AB116	377879.2	731027.8	1370.25	7.37
AB117	377832.2	731054.5	1367.41	11.1

AB118	377788.5	731083.1	1370.04	5.68
AB119	377734.1	731114.8	1370.97	0.655
AB120	377684.2	731140.2	1371.71	2.26
AB121	377700.1	731096.1	1372.26	2.94
AB122	377599.9	731209.3	1383.86	7.6
AB123	377554.7	731231.6	1230.15	2.83
AB124	377457.7	731049.9	1229.64	9.4
AB125	377496.8	731013.6	1231.94	6.19
AB126	377543	730985.6	1227.4	3.53
AB127	377597.2	730964.8	1233.42	17.9
AB128	377657.5	730919.3	1231.15	5.62
AB129	377704.9	730877.4	1240.92	4.7
AB130	377755.8	730848.3	1242.1	9.16
AB131	377799.9	730824.5	1230.89	5.51
AB132	377842.6	730815.6	1238.38	5.33
AB133	377905.6	730938.6	1248.64	33.3
AB134	377891.6	730787.1	1235.14	8.23
AB136	377978.8	730738.1	1237.42	18.4
AB137	378035.8	730736.6	1235.28	14
AB138	378089.3	730736	1237.93	30.5
AB140	378207	730741	1240.15	5.3
AB141	378265.5	730737.7	1251.46	2.51
AB142	378301.1	730960.3	1248.29	6.41
AB143	378271.4	730988.6	1241.43	2.64
AB144	378222.6	731015.2	1233	9.68
AB145	378174.1	731032.4	1240.58	15.3
AB146	378127.1	731057.6	1240.05	17.9
AB147	378075	731078.3	1220.28	50.7
AB148	378029.9	731104.3	1217.35	4.25
AB149	378173.3	731267.1	1205.78	1.04
AB150	378205.5	731230.9	1195.49	13.5
AB151	378254.8	731203.6	1176.92	30.7
AB152	378301	731185.9	1181.91	2.4
AB153	378356.3	731188.8	1178.6	36.2
AB154	378360.6	731686.3	1183.55	173
AB155	378341.6	731706.1	1179.94	25.6
AB156	378465.9	731785.8	1183.35	127
AB157	378527.2	731795.2	1222.75	43.3
AB158	378568.5	731954.3	1232.07	6.3
AB159	378504.3	731954.1	1246.04	10.1
AB160	378452.7	731971.1	1247.52	17.6
AB161	378404.1	731981.9	1244.73	14.6
AB162	378349	731999.3	1249.42	8.66

AB163	378593.7	730241.3	284.36	8.32
AB164	378228.5	732040	1255.23	11.6
AB165	378188.5	732071.5	1276.22	8.41
AB166	378077.9	732249.3	1265.06	11.5
AB167	378138.2	732260.6	1261.71	7.85
AB168	378199.2	732258.1	1301.69	18.5
AB169	378257.6	732261.9	1278.15	20.7
AB170	378313.8	732250.3	1257.55	14.3
AB171	378358.8	732235.3	1259.48	17
AB172	378409.5	732205.3	1258.74	15
AB173	378440.2	732146.4	1269.69	18.2
AB174	378601	732166.7	1263.8	33.4
AB175	378555.2	732184.4	1261.33	17.2
AB176	378665.1	732367.2	1255.28	26.1
AB177	378741.2	732565.1	1273.25	34.7
AB331	378362.4	730680.1	1273.76	13.7
AB332	378367.9	730676	1263.18	11.9
AB333	378385	730763.1	1226.29	4.66
AB334	378404.1	730865.3	1235.33	9.26
AB335	378363.7	730881	1243.25	13.8
AB336	378330	730918	1243.55	14.4
AB337	378310.9	730921.6	1250.84	9.53
AB338	378355.5	731148.6	1248.3	16.7
AB339	378406.3	731159.3	1252.99	78.2
AB340	378432.9	731139.4	1253.91	0.683
AB341	378435.6	731265.5	1235.99	41.5
AB342	378461	731333.2	1223.47	504
AB343	378443.8	731341.4	1219.09	379
AB344	378423.8	731356.4	1217.53	103
AB345	378487.8	731351.1	1214.49	197
AB346	378495.8	731323.6	1211.94	1000
AB347	378520.4	731325.7	1208.84	2000
AB348	378556.8	731321.5	1203.95	53.5
AB349	378537.3	731125.3	1227.25	21.4
AB350	378518	731129.1	1226.3	9.88
AB351	378518.4	731129.8	1230.44	81.8
AB353	378539.8	730923.6	1232.93	6.55
AB354	378522.2	730924.4	1236.42	20.3
AB355	378522.2	730924.4	1258.76	20.3
AB356	378501.1	730909.2	1252.76	247
AB357	378614.9	731531.2	1249.78	160
AB358	378676.5	731691.8	1250.36	27.2
AB526	378613.8	732372.8	1255.22	44.8

AB527	378566.3	732381.4	1253.55	42.4
AB528	378512.2	732380.4	1258.15	26.8
AB529	378483.6	732379.1	1262.65	26
AB530	378510.8	732494.4	1253.24	13.3
AB531	378527.4	732492.8	1256.73	16.3
AB532	378409.4	732506.8	1249.29	14.2
AB533	378298.7	732591.9	1258.8	22.9
AB534	378349.7	732600.6	1250.78	25.1
AB535	378398.8	732589	1233.54	26.5
AB536	378337.4	732745.6	1254.39	20.2
AB537	378375.8	732756.8	1242.35	21.2
AB538	378419.8	732765.9	1184.24	15.4
AB569	378473.4	732768	1190	15.1
AB540	378530.5	732774.7	1187.88	16.8
AB541	378580.2	732786.4	1185.11	16.3
AB542	378637.2	732785.6	1183.8	37.9
AB543	378691.5	732787.8	1192.53	17.8
AB544	378749.1	732790.8	1192.49	23.5
AB545	378806.3	732786.1	1191.23	21.8
AB546	378870.9	732762.1	1193.34	12.7
AB547	378920	732751.5	1194.11	22.1
AB548	378893	732538.4	1189.47	23
AB549	378926	732512.7	1190.64	26.2
AB550	378970	732452	1186.42	23.9
AB551	379055.7	732427.4	1186.57	75.8
AB553	379072.7	732278.1	1184.07	1.72
AB554	379032.9	732281.9	1195.11	13.9
AB555	378988.7	732281.1	1200	107
AB556	378938.9	732286.3	1200.55	12.9
AB557	378866.1	732197.3	1262.14	6020
AB558	378777.7	732064.7	1278.78	1070
AB559	378396.2	731745.9	1276.7	134
AB560	378438.3	731742.3	1270.46	117
AB561	378480.6	731741	1267.67	79.1
AB562	378531.3	731714.3	1260.77	1700
AB563	378563.2	731692.8	1260.48	14.1
AB564	378545.3	731606	1252.81	89.2
AB565	378613.5	731125.9	1250.2	28.5
AB566	378394.6	731610.6	1253.55	209
AB567	378353.4	731598.8	1252.73	1330
AB568	378347.2	731595.9	1123.23	23.3
AB569	378341	731563.2	1344.53	174
AB570	378323.6	731524.3	1334.51	500

AB571	378299.4	731484.1	1340.27	1800
AB572	378411.6	731617.4	1334.86	678
AB573	378437.8	731637.1	1337.04	105
AB574	378467	731652.3	1331.34	474
AB575	378474.4	731621.2	1331.04	17.8
AB576	378485.8	731605.1	1321.61	31.8
AB577	378471.9	731490.9	1326.02	26.9
AB578	378440	731480.9	1328.32	774
AB579	378403.4	731461.5	1321.06	1530
AB580	378357.5	731443.8	1321.64	13.1
AB581	378325.9	731454.3	1325.07	76.5
AB582	377957.8	731042.2	1326.86	52.5
AB583	377901.8	731081.7	1332.73	28.2
AB584	377859.5	731116.1	1326.44	16.4
AB585	377822.5	731152.9	1327.04	8.54
AB586	377781.7	731193.9	1321.82	9.2
AB587	377742.8	731236.2	1326.47	8.67
AB588	377702.5	731276.2	1330.13	9.07
AB589	377666.3	731315.1	1329.19	5.07
AB591	378131.8	731885.3	1333.98	9.67
AB592	378184.1	731875.7	1333.52	25.3
AB593	378241.5	731861.2	1331.33	24.1
AB594	378292.5	731856.4	1326.58	16.7
AB595	378355.6	731842.3	1326.95	22.6
AB596	378414.9	731837.6	1326.4	27.5
AB597	378467.6	731833.3	1306.33	31
AB598	378484.9	731822.3	1308.58	13.6
AB599	378745.5	732576.1	1309.55	40.6
AB600	378703.1	732589.1	1309.31	42
AB601	378643.7	732612.6	1307.68	155
AB602	378592.2	732630.8	1317.49	76.1
AB603	378559.3	732648.8	1320.39	49.2
AB604	378323.7	732961.3	1319.04	9.24
AB605	378373.3	732963.4	1323.84	17
AB607	378479.8	732969.2	1317.33	16.1
AB608	378538.5	732989.3	1305.68	12.3
AB609	378576.9	732974.8	1295.23	12.4
AB610	378623.3	732952.8	1292.02	16
AB611	378663.2	732945.7	1293.13	4.63
AB612	378730.8	732936.4	1288.43	11.4
AB613	378791.3	732939.3	1282.52	6.81
AB614	378860.8	732949.4	1279.54	5.58
AB615	378909.2	732931.6	1283.71	8.72

AB616	378962.6	732917.1	1281.48	8.76
AB617	378986	732922.9	1284.91	13.4
AB619	379035.5	732974.8	1281.93	13.2
AB620	379061	733021.6	1282.59	11
AB621	379080.2	733070.7	1282.4	7.28
AB622	379343.3	733007.9	1289.44	65.8
AB623	379322.5	733013	1285.1	803
AB624	379303	733083.9	1285.39	199
AB625	379351	733088	1284.63	62.1
AB626	379344.8	733193.1	1293.28	477
AB627	379303.4	733193.6	1280.62	69.9
AB628	379323.8	733269.8	1296.14	987
AB629	379352.4	733275.6	1299.14	105
AB630	379347.7	733376.1	1294.68	12.7
AB631	379396.2	733366.1	1299.43	40.9
AB632	379414.2	733475.4	1302.32	27
AB633	379382	733476.1	1295.51	57.3
AB634	379418.7	733570.6	1296.89	4.43
AB635	379465.6	733574.4	1295.22	60
AB636	379495.1	733577.6	1304.49	290
AB637	379532.4	733722.5	1326.81	215
AB638	379547	733753.4	1327.34	139
AB639	379570.8	733801.7	1323.56	280
AB640	379053.1	733172.1	11.6	5.76
AB642	378916.8	733175.8	1318.8	19
AB643	378874.1	733178.1	1321.61	16.2
AB644	378812.2	733180.9	1327.77	13.2
AB645	378748.6	733180.4	1325.61	18.1
AB646	378689.2	733179.7	1329.19	70.8
AB647	378628.3	733181.6	1321	14.1
AB648	378576.3	733181.9	1317.31	36.5
AB649	378527.1	733193.8	1306.06	8.4
AB650	378492.5	733197.7	1309.52	15.2
AB651	378457.9	733205.5	1307.41	32.7
AB732	376967.2	730590.9	1239.5	15.3
AB733	377021.9	730580	1242.33	19.8
AB734	377070.6	730565.6	1244.98	14.9
AB735	377129.3	730554.8	1248.07	19.2
AB736	377183.7	730546.8	1243.41	15.5
AB737	377236.6	730530.7	1242.51	15.5
AB738	377295.1	730516.3	1240.99	18.7
AB739	377344.9	730512.4	1239.38	14.8
AB740	377396.6	730492.1	1237.87	6.69

AB741	377451.4	730477.1	1236.39	11.6
AB742	377504.3	730461.5	1237.09	16.6
AB743	377552.9	730438.6	1240.61	21.2
AB744	377584.7	730416.3	1241.46	6.31
AB745	377632.4	730408.8	1245.32	9.13
AB746	377678.8	730397.9	1252.23	9.95
AB747	377709.3	730386.9	1259.73	6.86
AB748	379634.8	733851.8	1188.88	37.6
AB749	379685.9	733886.6	1187.9	84.6
AB750	379739.3	733927.6	1193.14	182
AB751	379794.3	733974.1	1194.6	11.7
AB752	379838.7	734007.9	1197.43	43.9
AB753	379884.1	734031.6	1194.95	166
AB754	379971.4	734073.4	1195.18	60.4
AB755	380026.2	734093.9	1192.54	156
AB756	380068.4	734114.9	1193.04	77.8
AB757	380117.6	734139.6	1197.32	11.2
AB758	380158	734176.6	1193.7	36.2
AB759	380196.3	734213.3	1193.25	38.5
AB760	380270.7	734280.6	1196.15	55.7
AB761	380309.9	734318.7	1196.54	30.3
AB762	380346.6	734356.9	1189.68	15.9
AB763	380380.3	734410.4	1186.17	19
AB764	380459	734603.4	1189.84	47.4
AB765	380488.5	734693.9	1191.53	21.7
AB766	380510.3	734753.9	1197.21	36.5
AB767	380565.7	734780.4	1191.28	14.3
AB768	380613.6	734838.3	1193.55	12.2
AB769	380670.3	734894.8	1204.3	13.4

Appendix IV

Soil Temperature Data at 50cm Depth

Site	Easting	Northing	Elevation	Soil Temp (°C, at 0.5m)
AB001	377393	739527	1407.66	28.68
AB002	377371	739537	1404.7	37
AB003	377342	739544	1411.75	33
AB004	377315	739553	1408.81	34
AB005	377296	739564	1413.76	34.5
AB006	377274	739576	1424.72	32
AB007	377255	739588	1398.33	31
AB008	377256	739588	1405.46	30.5
AB009	377298	739686	1422.93	32.7
AB010	377320	739676	1419.58	30
AB011	377340	739669	1412.76	31
AB012	377365	739652	1406.22	31
AB013	377383	739642	1407.19	30
AB014	377401	739632	1402.44	30.5
AB015	377425	739619	1401.55	31.5
AB016	377451	739606	1402.32	30
AB017	380657.0625	734970.0625	1195	34.4
AB018	380709.0313	734922.5	1189.81	32.2
AB019	380750.9688	734889.125	1187.53	27.8
AB020	380785.4063	734860.1875	1190.83	28.2
AB021	380850.2188	734828.5625	1186.08	29.8
AB022	380896.0625	734806	1186.91	36
AB023	380938.2813	734745.5625	1184.45	33
AB024	380980.625	734708.75	1183.7	27.3
AB025	381055.2813	734617.6875	1185.27	33.8
AB026	381080.4375	734540.6875	1185.6	31
AB027	381119.6563	734482.3125	1184.82	28.7
AB028	381149.0313	734408.3125	1183.66	27.5
AB029	381171.8125	734366.6875	1184.69	27.2
AB030	381207.6875	734290.1875	1187.27	28.5
AB031	381229.6875	734240.9375	1186.55	28.6
AB032	381239.75	734188.1875	1187.75	29.9
AB033	381247.7813	734116.4375	1187.62	29.5
AB034	381422	734238	1194.03	31.7
AB035	381347	734350	1193.45	29.1
AB036	381375	734402	1192.23	29.5
AB037	381337	734446	1191.65	30
AB038	381260	734488	1190.45	29
AB039	381200	734547	1191.51	27.6

AB040	381171	734603	1192	30.7
AB041	381120.5313	734671.5	1194.57	31.2
AB042	381075.25	734693.3125	1196.01	30.9
AB043	381039	734753.375	1194.52	33.5
AB044	380979.4063	734805.5	1198.18	32.5
AB045	380958.25	734880.625	1190.14	35
AB046	380948.3125	734939.25	1193.56	30.1
AB047	380922.0313	735007.0625	1200.24	32.9
AB048	380889.875	735069.0625	1193.09	35.5
AB049	380835.3438	735100.5625	1199.7	34.5
AB050	380807.25	735140	1199.89	32.5
AB051	380777.0625	735188.6875	1206.45	33.5
AB052	380892.5938	735342.125	1208.65	32.8
AB053	380938.4063	735316.5	1203.89	29.5
AB054	380987.5313	735283.25	1203.29	32.5
AB055	381030.25	735250.1875	1197.37	32.8
AB056	381085.3125	735211.375	1202.11	31.9
AB057	381132.8438	735201.0625	1197.68	33.8
AB058	381170.7813	735166.375	1199.29	33.5
AB059	381216.4688	735129.625	1195.09	34.5
AB060	381265.0625	735106.375	1194.58	34
AB061	381345.375	735070.625	1188.67	33.7
AB062	381390.0625	735036.25	1190.43	34.5
AB063	381476.4375	735005.3125	1198.66	33
AB064	381721.25	735698.25	11.6	28.1
AB065	381820.375	735624.1875	766.52	30.5
AB066	381639.2813	734959.0625	1184.9	32.5
AB067	381677.0938	734903.9375	1202.76	32
AB068	381736.2813	734865.75	1204.55	31
AB069	381781.0938	734836.6875	1189.89	32
AB070	381851.7813	734814.875	1197.81	33.5
AB071	381908.1563	734799.625	1175.67	31.7
AB072	381968.4688	734994.875	1195.84	30.5
AB073	381933.5938	735021.375	1207.01	32.2
AB074	381875.0938	735058.375	1164.72	30.5
AB075	381837.8438	735117.5	1031.33	32
AB076	381788.7813	735120.625	1188.31	30.1
AB077	381743.1875	735148.125	1203.71	30.5
AB078	381690.375	735168.125	1204.2	32.5
AB079	381643.875	735191.125	1204.44	30.5
AB080	381610.8125	735239.625	1202	34.5
AB081	381560.375	735278.4375	1209.92	29.1
AB082	382018.0938	735492.8125	11.6	33.5

AB083	381791.6563	735428	11.7	33
AB084	381533	735343.875	539.81	35.5
AB085	381329	735373.6875	1201.21	34.3
AB086	381281.2813	735394.5	1208.45	35
AB087	381213.375	735427.4375	1197.72	33.7
AB089	381102.0625	735488.1875	1207.81	31.5
AB090	381063.4375	735514.8125	1208.12	31.8
AB091	381018.8438	735550.75	1223.02	33.7
AB092	381001.625	735570.25	1215.67	35
AB093	377811.875	731386.6875	1263.53	32.1
AB094	377850.1563	731349.25	1261.68	29.4
AB095	377891.2188	731315	1256.59	33.9
AB096	377935.4688	731281.1875	1247.3	29.7
AB097	377980.3125	731253.1875	1245.19	32.7
AB098	378010.3438	731236.25	1244.82	30.7
AB099	378051.8125	731198	1259.2	31
AB100	378184.5313	731360.5625	1245.85	30
AB101	378217.125	731401.9375	1245.14	29.1
AB102	376650.2188	731087	11.9	29.6
AB103	378119.4688	731437	1235.97	31.3
AB104	378081.75	731479.4375	1247.81	31.2
AB105	378046.9063	731522.9375	1238.15	27.2
AB106	378008.0313	731544.0625	1257.14	33.1
AB107	378046.375	731731.6875	1247.68	33.3
AB108	378003.8125	731833.5	1279.75	37
AB109	377915.0313	731836.25	1275.2	34.5
AB110	377888.75	731843.3125	1276.11	36.7
AB111	378093.4375	731715.125	1232.8	35.7
AB112	378139.2813	731694.375	1222.13	34.2
AB113	378196.0938	731692.875	1218.91	32.4
AB114	377977.1875	731097.875	1254.71	27.9
AB115	377920	730986.75	1253.71	26
AB116	377879.1875	731027.75	1252.69	28.9
AB117	377832.1563	731054.5	1253.74	32.5
AB118	377788.5313	731083.125	1251.28	30.3
AB119	377734.0938	731114.8125	1254.53	30
AB120	377684.1875	731140.1875	1254.91	31
AB121	377700.125	731096.0625	1072.56	32
AB122	377599.875	731209.3125	1265.59	33.6
AB123	377554.7188	731231.625	1269.63	36
AB124	377457.6563	731049.9375	1263.64	33.7
AB125	377496.8438	731013.5625	1265.17	43.8
AB126	377543	730985.625	1255.2	36.9

AB127	377597.2188	730964.8125	1257.18	36
AB128	377657.5	730919.25	1261.42	38.4
AB129	377704.9375	730877.375	1256.95	35
AB130	377755.75	730848.25	1255.67	36.5
AB131	377799.9063	730824.5	1257.04	35
AB132	377842.5625	730815.5625	1260.8	37
AB133	377905.625	730938.625	1266.08	30
AB134	377891.5938	730787.0625	1271.51	33.5
AB136	377978.8125	730738.125	1278.02	32.8
AB137	378035.75	730736.5625	1273.51	32.5
AB138	378089.2813	730736	1258.77	34.8
AB140	378207	730741	1252	32.1
AB141	378265.5	730737.6875	1250.84	40
AB142	378301.0625	730960.3125	1256.54	34.2
AB143	378271.375	730988.625	1268.22	35.6
AB144	378222.5625	731015.1875	1277.35	40
AB145	378174.0625	731032.4375	1280.05	30.5
AB146	378127.125	731057.625	1281.02	34.2
AB147	378075	731078.3125	1282.2	34
AB148	378029.9375	731104.3125	1267.77	32.6
AB149	378173.25	731267.0625	1265.88	40
AB150	378205.4688	731230.9375	1273.21	31.9
AB151	378254.8125	731203.625	1265.4	33.8
AB152	378301	731185.9375	1265.22	31
AB153	378356.2813	731188.8125	1254.96	36.4
AB154	378360.5938	731686.25	1222.8	36
AB155	378341.625	731706.0625	1221.9	31.3
AB156	378465.9375	731785.75	1213.23	40.6
AB157	378527.2188	731795.1875	1197.85	36.4
AB158	378568.4688	731954.25	1216.15	32
AB159	378504.3438	731954.125	1220.14	35
AB160	378452.6563	731971.0625	1222.03	36.5
AB161	378404.125	731981.875	1219.89	34.5
AB162	378349	731999.25	1230.12	43.4
AB163	378593.6563	730241.3125	598.35	37.9
AB164	378228.4688	732040	1240.23	39
AB165	378188.5313	732071.5	1240.69	39
AB166	378077.9063	732249.3125	1257.63	37
AB167	378138.1875	732260.5625	1256.08	33.5
AB168	378199.2188	732258.125	1251.85	38.5
AB169	378257.5938	732261.9375	1247.31	36.2
AB170	378313.8438	732250.3125	1246.13	32.5
AB171	378358.8125	732235.3125	1242.1	38.4

AB172	378409.5	732205.3125	1235.32	37.7
AB173	378440.2188	732146.4375	1227.68	31
AB174	378601	732166.6875	1223.54	32.9
AB175	378555.1563	732184.4375	1226.35	33.4
AB176	378665.125	732367.1875	1239.99	34.4
AB177	378741.1875	732565.0625	1237.85	37.8
AB178	378251.4688	740311.9375	1591.31	31.5
AB179	378213.7188	740342.1875	1605.97	34
AB180	378192.9063	740325.3125	1596.6	46.4
AB181	378150.3125	740367.5625	1583.81	34
AB182	377107.7188	739199.5625	1375.42	32.5
AB183	377062.4688	739240	1378.29	31.2
AB184	377017.9063	739285.1875	1378.1	32.4
AB185	376977.9063	739331.75	1383.35	30.4
AB186	376938.875	739376.0625	1383.98	31.6
AB187	376902.8125	739421.8125	1379.46	31.5
AB188	376858.3438	739458.8125	1382.83	31
AB189	376813.125	739499.3125	1386.95	32.5
AB190	376779.1875	739541.8125	1384.65	29.1
AB191	376741.9063	739585.375	1392.2	34.5
AB192	376676.5625	739627.75	1374.09	27.3
AB193	376637.625	739665.75	1380.13	29.6
AB194	376601.125	739703.625	1383.25	31.7
AB195	376546	739719.5	1382.11	32
AB196	376501.75	739748.3125	1382.23	35
AB197	376456.6875	739778.8125	1380.28	27.5
AB198	376446	739786.625	1376.43	27
AB199	376406.375	739808.5	1373.2	31
AB200	376360.4688	739843.75	1377.52	33.5
AB201	376305.9375	739880.8125	1374.41	29.5
AB202	376267.5625	739927.5625	1377.67	31.9
AB203	376207.8125	739948.8125	1378.25	31.5
AB204	376127.6875	739901.125	1340.32	29.4
AB205	376100.0625	740004	1379.76	32.4
AB206	376060.4063	740026.5	1387.29	32
AB207	376095.8125	740085.375	1382.06	30.9
AB208	376130.875	740138.5625	1380.21	29.7
AB209	376182.25	740222.9375	1375.73	29.7
AB210	376231.25	740196.5	1374.74	29.5
AB211	376281.625	740170.3125	1372.75	29.4
AB212	376329.1875	740138.9375	1365.79	29.5
AB213	376374.4375	740104	1369.92	27.7
AB214	376418.6563	740068.1875	1377.32	31.5

AB215	376463.25	740035.875	1374.36	29.5
AB216	376506.4063	740003.625	1375.25	28.7
AB217	376550.7813	739977	1372.34	31.2
AB218	376590.0625	739940.3125	1383.34	31.3
AB219	376624.3438	739907.25	1384.3	30
AB220	376723.4063	739854.1875	1370.06	30.4
AB221	376770.8438	739820.375	1369.18	30.5
AB222	376813.3438	739788.1875	1371.72	31.6
AB224	377184.7813	739156.4375	1387.52	32.3
AB225	377220.75	739132.0625	1383.88	33
AB226	377263.1563	739112.9375	1389.87	31.9
AB227	377302.4375	739078.6875	1376.68	34
AB228	377352.9063	739054.375	1379.74	36.5
AB229	377386.0313	739036.1875	1368.17	36
AB230	377428.7188	738999.8125	1374.54	31.5
AB231	377479.8125	738962.625	1374.29	31.4
AB232	377524.75	738931	1370.19	31.3
AB233	377564.8125	738907.5	1370.21	33
AB234	377611.5	738881.625	1372.35	31.4
AB235	377654.0313	738860.75	1368.4	32
AB236	377693.6563	738840.125	1353.69	33
AB237	377742.9063	738768.4375	1363.36	34
AB238	377790.5	738739.625	1364.24	30.4
AB239	377833.4375	738711	1361.29	30.2
AB240	377884.9063	738695.375	1361.47	33.8
AB241	377944.125	738675.25	1362.15	29.4
AB242	378004.0313	738668.6875	1362.99	32.3
AB243	378077.5938	738644.1875	1366.5	30.5
AB244	378136.2813	738638.625	1367.07	33
AB245	378201.4688	738620.5	1368.82	34.9
AB246	378246.9375	738593.1875	1367.43	35
AB247	378274.4063	738569	1365.77	34.5
AB248	378319.75	738518.9375	1362.29	35
AB249	378368.3125	738492.375	1367.7	36.5
AB250	378463.1563	738493.4375	1341.31	34
AB251	378501.1563	738473.625	1334.02	34.5
AB252	378560.0313	738403.5	1344.83	35.5
AB253	378592.3125	738358.3125	1348.29	32.7
AB254	378645.4688	738350.25	1349.63	37.5
AB255	378678.4375	738306.875	1347.99	33.4
AB256	378733.875	738240.5	1336.48	35.4
AB257	378748.4375	738228.75	1353.96	33
AB258	378835.6875	738442.6875	1350.71	31.1

AB259	378789.7188	738495.5625	1345.94	31.8
AB260	378744.5938	738531.25	1349.34	31
AB261	378684.7188	738556.1875	1350.1	36
AB262	378637.9375	738590.875	1347.14	37
AB263	378588.8438	738630.8125	1349.81	35
AB264	378554.2188	738676.875	1347.7	31.5
AB265	378520.7813	738696.5	1346.38	35.5
AB266	378448.9063	738941.875	1372.99	37
AB267	378423.7813	738969.9375	1374.57	31.7
AB268	378367.8125	739011.75	1373.8	35.5
AB269	378334.5938	739039	1375.71	31.5
AB270	378311.5313	739055.1875	1375.82	35.5
AB271	380245.8438	742610	1410.64	32.3
AB272	380284.9688	742560.625	1396.28	35
AB273	380321.4688	742523.6875	1384.82	34.3
AB275	380360.7188	742483.5	1397.27	33.1
AB275	380400.8438	742434.1875	1387.44	33.5
AB276	380448.3125	742394.25	1389.11	36.5
AB277	380486.3125	742346.875	1387.6	37
AB278	380528.5313	742238.75	1368.92	35
AB279	380581.2188	742219.3125	1372.89	31.3
AB280	380628.1875	742210.8125	1368.16	33.6
AB281	380699.5	742169.0625	1354.29	36
AB282	380750.5313	742150.5625	1362.25	35.8
AB283	380789.625	742139.3125	1364.43	33.8
AB284	380848.75	742129.375	1362.52	31.9
AB285	380899.8125	742084.125	1365.13	34
AB289	381135.4063	742003.5625	1351.77	28.2
AB290	381043.8438	741776.4375	1368.37	35
AB291	381039.5625	741789.625	1356.65	30.9
AB292	380986.75	741810.5	1362.96	31.5
AB293	380940.375	741831.875	1365.3	35
AB294	380902.5313	741853.8125	1364.26	35
AB296	380754.0625	741898.8125	1371.77	32.5
AB297	380695.3125	741926.375	1367.36	35
AB299	380583.5313	741964.5625	1362.26	30
AB300	380531.9375	741980	1355.54	33.5
AB301	380487.375	742013.3125	1354.53	32.5
AB302	380449.9375	742033.625	1358.23	30.6
AB303	380399	742000.25	1370.69	36
AB304	380363.5938	742025.625	1376.58	33
AB305	380298.375	742071.5625	1376.44	32.5
AB306	380248.5938	742110.5625	1376.11	33.5

AB307	380203.3438	742144.8125	1378.74	36
AB308	380160	742183.1875	1377.98	35.5
AB309	380118.5	742219.5625	1378.54	34.5
AB310	380072.5938	742250.1875	1385.31	35.1
AB311	380028.6875	742282.3125	1384.95	35
AB312	379974.7188	742320.375	1386.15	32.6
AB313	379927.1563	742364.5625	1387.53	35
AB315	380222.875	742626.875	1406.67	31.1
AB316	380180.8438	742663.625	1406.23	35
AB322	379926.75	742822.5625	1431.09	36.2
AB323	379924.2188	742825.3125	1433.14	38.2
AB324	379890.0313	742871.25	1438.32	32
AB325	379859.5313	742927.3125	1437.34	30.3
AB326	379834.6875	742976.3125	1437.44	30.3
AB327	379807.8125	743026.5625	1436.58	30.2
AB328	379784.9688	743086.125	1436.8	30.5
AB329	379745.375	743127.3125	1438.99	31.2
AB330	379702.3438	743168.5625	1441.3	32.5
AB331	378362.4375	730680.0625	1128.04	33.5
AB332	378367.875	730676	1221.99	32.5
AB333	378384.9688	730763.0625	1225.84	33.5
AB334	378404.0938	730865.3125	1244.74	31.5
AB335	378363.6563	730881	1256.44	33.8
AB336	378330.0313	730918	1251.25	31.5
AB337	378310.9063	730921.5625	1254.55	29
AB338	378355.5313	731148.5625	1268.22	33.5
AB339	378406.3125	731159.3125	1254.18	40.6
AB340	378432.9063	731139.4375	1251.04	33.3
AB341	378435.625	731265.5	1256.84	35.2
AB342	378460.9688	731333.1875	1249.36	76.8
AB343	378443.75	731341.4375	1249.54	40.4
AB344	378423.75	731356.375	1255.49	40.6
AB345	378487.75	731351.0625	1236.72	39.2
AB346	378495.7813	731323.625	1225.58	86
AB347	378520.4375	731325.6875	1209.22	90
AB348	378556.8125	731321.5	1202.9	39.9
AB349	378537.3438	731125.25	1205.06	84
AB350	378518	731129.0625	1206.38	47
AB351	378518.4375	731129.75	1204.52	98.5
AB353	378539.7813	730923.625	1182.7	43
AB354	378522.1875	730924.4375	1198.78	72
AB355	378522.1875	730924.4375	1198.78	94.8
AB356	378501.0625	730909.1875	1206.61	77

AB357	378614.875	731531.1875	1195.85	36
AB358	378676.4688	731691.75	1189.2	34.5
AB359	376862.25	739766.75	1392.28	31.3
AB360	376908.375	739732.6875	1392.92	30.4
AB361	376949.875	739704.0625	1398.47	31.6
AB362	376989.6875	739661.75	1399.42	30.6
AB363	377030.5	739623.75	1399.5	30.5
AB364	377069.0313	739591.5	1399.75	30.6
AB365	377125.125	739567.9375	1420.74	34
AB366	377172.0625	739545.6875	1427.3	35
AB367	377211.3125	739559.5625	1431.09	33.4
AB368	377243.0938	739573.75	1415.41	29
AB369	377427.3438	739512.6875	1402.36	31.8
AB370	377470.5313	739501.25	1407.94	31.4
AB371	377510.625	739492.375	1417.11	32.7
AB372	377545.8438	739460.625	1423.36	33.7
AB373	377608.8125	739549.8125	1436.04	33.4
AB374	377573.8125	739565.25	1427.37	33.6
AB375	377538.8125	739588.75	1412.57	31.6
AB376	377491.125	739619.1875	1408.13	27.8
AB377	377457.875	739629.1875	1399.39	30.3
AB378	377510.5625	739754.6875	1391.29	32.4
AB379	377459.375	739800.75	1390.75	28.2
AB380	377425.1875	739836.6875	1396.55	29.1
AB381	377387.4688	739878.6875	1384.48	32.5
AB382	377350.5938	739899.5625	1401.37	34.3
AB383	377301.5938	739936.8125	1404.25	30.4
AB384	377237.3125	739951.5625	1379.15	31
AB385	377200.7813	739975.375	1374.43	32.7
AB386	377152.9688	739998.5	1375.25	30.7
AB387	377103.9375	740032	1366.63	33.2
AB388	377061.5625	740064.1875	1371.46	32.1
AB389	377034.75	740083.125	1357	30.2
AB390	376971.8125	740107.375	1340.19	33.8
AB391	376926.5625	740143.4375	1340.99	32.4
AB392	376894.0938	740160.3125	1344.26	31.9
AB393	376870.25	740174.75	1351.68	31.5
AB394	376911.0313	740270.25	1349.03	32.9
AB395	376941.1563	740382	1352.31	28.5
AB396	376987.875	740376.6875	1358.44	28.9
AB397	377032.2813	740353.125	1349.72	30.5
AB398	377080.4063	740328.375	1355.14	31.5
AB399	377130.125	740311.8125	1355.49	31.3

AB400	377178.8438	740296.0625	1359.63	33.5
AB401	377231.5	740273.9375	1360.81	33.2
AB402	377292.25	740246.5	1369.29	32.3
AB403	377344.9063	740218.4375	1382.75	32.1
AB404	377399.2188	740180.6875	1380.83	30.5
AB405	377442.75	740167.875	1373.76	30.6
AB406	377496.5313	740144.3125	1383.99	33.4
AB407	377540.75	740153.875	1382.67	32.9
AB408	377574.2813	740260.5	1380.51	33.1
AB409	377565.2188	740313.375	1377.38	33.5
AB410	377506.2813	740308.5	1365.16	34
AB411	377445.7188	740314.1875	1374.45	35
AB412	377372.5938	740341.4375	1367.09	35
AB413	377326.125	740371.9375	1361.4	35.3
AB415	377222.2188	740466.125	1347.77	30.5
AB416	377174.3125	740490.6875	1347.66	29.4
AB417	377128.375	740515.5625	1347.05	30.2
AB418	377082.25	740548.625	1348.07	29
AB419	377039.875	740578.6875	1348.41	30.8
AB420	377103.3125	740769.25	1346.88	32.5
AB421	377148.0313	740748.25	1345.98	35
AB422	377192.0938	740737.625	1341.32	30.9
AB423	377261.8438	740733.1875	1350.49	32
AB424	377298.5313	740730.875	1362.18	33
AB425	377059.8438	739791.375	1400.46	30.8
AB426	377019.0313	739827.5625	1393.71	29.9
AB427	376975.125	739861.125	1382.88	31.6
AB428	376929.9688	739891.1875	1372.6	32.6
AB429	376879.4688	739896.625	1355.28	30.4
AB430	376837.1875	739920.5	1352.11	29.6
AB431	376779.75	739936.4375	1358.79	28.8
AB432	376767.1563	739946.4375	1368.97	31.5
AB433	376720	739964	1387.94	30.1
AB434	376668	739991	1389.5	27.4
AB435	376621.625	740016.1875	1388.83	30.7
AB436	376576.5938	740047.6875	1383.55	26.7
AB437	376533.6563	740070.875	1386.39	34.6
AB438	376470.3438	740089.375	1384.09	32.1
AB439	376416.7813	740115.8125	1380.89	30.9
AB440	376374.8125	740123.1875	1371.3	29.6
AB441	376322.8125	740152.75	1370.63	30.6
AB442	376266.5	740188.375	1372.09	39.7
AB443	376223.5625	740215.5625	1371.08	38.5

AB444	376194.1875	740230.625	1376.61	36.5
AB445	376299.4375	740420.8125	1359.8	34.8
AB446	376345.8125	740400	1371.33	32.5
AB447	376409.6875	740393.125	1375.3	32.5
AB448	376463.375	740379.3125	1373.13	36.5
AB449	376530.25	740375.625	1370.08	33.2
AB450	376573.9688	740358.0625	1369.41	33.2
AB451	376637.0625	740336.6875	1358.65	31.2
AB452	376688.5	740312.4375	1379.31	33.5
AB453	376735	740299.4375	1383.44	31.3
AB454	376791.25	740283.5	1383.51	30.9
AB455	376839.1875	740271.4375	1381.77	32.5
AB456	376928.5	740456.875	1372.6	32
AB458	376834.6563	740512.5	1370.05	35.9
AB459	376791.25	740533	1368.37	38.5
AB460	376726.6563	740561.5	1371	36.5
AB461	376659.7188	740589.375	1369.42	38
AB462	376599.4688	740625.6875	1362.01	37.8
AB463	376544.0938	740636.4375	1368.54	37.6
AB464	376497.375	740651.6875	1372.41	33.6
AB465	376454.9688	740672.5625	1379.02	40.2
AB466	376525.4375	740884.8125	1374.9	33.1
AB467	376577.0313	740871.3125	1369.34	32
AB468	376635.5625	740853.5625	1366.07	36.5
AB469	376692.25	740840.5	1371.43	39.5
AB470	376768	740810.8125	1360.64	41.5
AB471	376819.8438	740801.1875	1368.4	36.6
AB472	376880.625	740796.625	1370.98	35.1
AB473	376935.7813	740790.75	1370.24	33.7
AB474	376988.6875	740783	1375.58	38.2
AB475	377045.5	740780.4375	1374.44	35.3
AB476	375986.3125	739815.0625	1398.64	29.4
AB477	376031.0313	739794.5	1393.71	32.8
AB478	376080.8125	739759.375	1390.03	33.3
AB479	376135.2188	739726.375	1392.85	32.3
AB480	376186.4375	739692.3125	1391.25	23
AB481	376235.375	739669.875	1393.91	30.2
AB482	376278.8438	739642	1390.93	26.5
AB483	376320.9063	739614.5	1386.59	29.9
AB484	376371.0313	739584.5625	1393.49	33
AB485	376416.625	739560.25	1394.3	36.5
AB487	376514.9063	739511	1395.13	18.3
AB488	376558.0625	739476.625	1397.46	31.8

AB489	376609.4688	739435.3125	1407.5	32
AB490	376609.4688	739435.3125	1407.5	33.1
AB491	376656.25	739341.1875	1408.47	33.8
AB492	376701.5625	739292.875	1415.3	38
AB493	376732.9375	739235.3125	1395.44	33.9
AB494	376843.6875	739182.125	1391.8	34.1
AB495	376887.1563	739146.9375	1388.46	40.5
AB496	376929.6563	739113.5	1386.17	34.7
AB497	376972.125	739077.125	1381.09	37
AB498	377011.1563	739034.5625	1379.39	35
AB499	377058.625	739002.5	1381.03	38.6
AB500	377097.125	738963.9375	1375.72	37.5
AB501	377181.2813	738933.25	1375.32	40.3
AB502	377219.9688	738888.625	1374.3	34.9
AB503	377255.7188	738847.5	1370.76	36.8
AB504	377295.9688	738814	1364.63	35.9
AB505	377367.25	738757.375	1369.92	38.9
AB506	377410.625	738722	1355.78	38.7
AB507	377450.6563	738678.5625	1358.36	33.3
AB508	377487.4063	738648.375	1362.7	33.3
AB509	377537.3125	738621.875	1362.35	34
AB510	377574.4063	738604.0625	1358.71	35.4
AB511	377494.4688	738401.6875	1365.13	34.4
AB512	377441.8125	738429.6875	1366.2	23
AB513	377399.1875	738458.3125	1367.35	36.5
AB514	377350.1563	738481.1875	1364.98	41.1
AB515	377297.625	738508.625	1368.83	39.4
AB516	377248.4688	738526.625	1373.4	36.2
AB518	377157.1563	738585.5625	1369.99	38.9
AB519	377115	738611.4375	1370.25	34.7
AB520	377048.6563	738646.1875	1367.41	32
AB521	377003.5938	738671.1875	1370.04	36
AB522	376950.25	738692.1875	1370.97	37.6
AB523	376884.8125	738736.875	1371.71	37
AB524	376837	738763.4375	1372.26	34.8
AB525	376791.25	738779.5625	1383.86	36
AB526	378613.75	732372.75	1230.15	33.5
AB527	378566.3125	732381.4375	1229.64	38.3
AB528	378512.1563	732380.375	1231.94	35.8
AB529	378483.625	732379.125	1227.4	36.8
AB530	378510.75	732494.375	1233.42	37.2
AB531	378527.4375	732492.75	1231.15	36.7
AB532	378409.4063	732506.75	1240.92	34.5

AB533	378298.6875	732591.875	1242.1	28.3
AB534	378349.6875	732600.625	1230.89	37.8
AB535	378398.8438	732589	1238.38	36.9
AB536	378337.4063	732745.625	1248.64	35.6
AB537	378375.7813	732756.8125	1235.14	34.9
AB538	378419.8125	732765.875	1237.42	33.9
AB569	378473.4375	732768	1235.28	35.5
AB540	378530.5	732774.6875	1237.93	36.2
AB541	378580.1563	732786.4375	1240.15	36.7
AB542	378637.1875	732785.625	1251.46	37.5
AB543	378691.5	732787.75	1248.29	37
AB544	378749.0938	732790.8125	1241.43	38.5
AB545	378806.25	732786.125	1233	35.4
AB546	378870.875	732762.125	1240.58	38.8
AB547	378920.0313	732751.5	1240.05	36.9
AB548	378893.0313	732538.375	1220.28	38.9
AB549	378926.0313	732512.6875	1217.35	40.4
AB550	378970.0313	732452	1205.78	32
AB551	379055.6563	732427.375	1195.49	37.2
AB553	379072.6875	732278.0625	1176.92	40.8
AB554	379032.875	732281.9375	1181.91	40.7
AB555	378988.6563	732281.125	1178.6	44.2
AB556	378938.9063	732286.3125	1183.55	40.4
AB557	378866.0938	732197.25	1179.94	50
AB558	378777.6875	732064.6875	1183.35	55
AB559	378396.2188	731745.875	1222.75	38.3
AB560	378438.3125	731742.25	1232.07	85
AB561	378480.5625	731741	1246.04	73.6
AB562	378531.25	731714.25	1247.52	70.3
AB563	378563.1563	731692.75	1244.73	37.8
AB564	378545.25	731606	1249.42	42
AB565	378613.5313	731125.875	284.36	42.8
AB566	378394.5938	731610.5625	1255.23	82
AB567	378353.4375	731598.8125	1276.22	78.5
AB568	378347.2188	731595.9375	1265.06	59.3
AB569	378340.9688	731563.1875	1261.71	84.6
AB570	378323.625	731524.25	1301.69	52.9
AB571	378299.4375	731484.125	1278.15	58.8
AB572	378411.625	731617.4375	1257.55	60.7
AB573	378437.75	731637.0625	1259.48	51.3
AB574	378466.9688	731652.25	1258.74	44.4
AB575	378474.4375	731621.1875	1269.69	46.3
AB576	378485.7813	731605.125	1263.8	38.9

AB577	378471.9375	731490.9375	1261.33	43.3
AB578	378439.9688	731480.9375	1255.28	93.4
AB579	378403.4375	731461.5	1273.25	94.3
AB580	378357.5	731443.75	1273.76	40.4
AB581	378325.9063	731454.25	1263.18	36.7
AB582	377957.8438	731042.1875	1226.29	32.7
AB583	377901.75	731081.6875	1235.33	35.5
AB584	377859.4688	731116.0625	1243.25	33.8
AB585	377822.5313	731152.9375	1243.55	34.4
AB586	377781.7188	731193.9375	1250.84	36.1
AB587	377742.7813	731236.1875	1248.3	35.8
AB588	377702.5	731276.1875	1252.99	34
AB589	377666.3438	731315.0625	1253.91	34.1
AB591	378131.8438	731885.3125	1235.99	24.1
AB592	378184.125	731875.6875	1223.47	34.5
AB593	378241.4688	731861.1875	1219.09	37.8
AB594	378292.5313	731856.4375	1217.53	33.6
AB595	378355.625	731842.25	1214.49	35.7
AB596	378414.875	731837.5625	1211.94	25.6
AB597	378467.5938	731833.25	1208.84	35.4
AB598	378484.9375	731822.3125	1203.95	35.6
AB599	378745.5313	732576.125	1227.25	38.9
AB600	378703.0938	732589.125	1226.3	18.5
AB601	378643.6875	732612.5625	1230.44	33.4
AB602	378592.1875	732630.75	1232.93	32.7
AB603	378559.2813	732648.8125	1236.42	39.8
AB604	378323.7188	732961.25	1258.76	33
AB605	378373.25	732963.375	1252.76	35.2
AB607	378479.75	732969.1875	1249.78	35
AB608	378538.5	732989.3125	1250.36	31.6
AB609	378576.9375	732974.75	1255.22	32
AB610	378623.3125	732952.8125	1253.55	33.1
AB611	378663.2188	732945.6875	1258.15	32.9
AB612	378730.75	732936.375	1262.65	32.2
AB613	378791.3125	732939.3125	1253.24	33.5
AB614	378860.7813	732949.4375	1256.73	34
AB615	378909.1563	732931.625	1249.29	37.5
AB616	378962.625	732917.0625	1258.8	33
AB617	378985.9688	732922.9375	1250.78	33
AB619	379035.5	732974.8125	1233.54	33.1
AB620	379061.0313	733021.625	1254.39	34.3
AB621	379080.1563	733070.6875	1242.35	33
AB622	379343.25	733007.875	1184.24	37.4

AB623	379322.5	733013	1190	36.5
AB624	379302.9688	733083.9375	1187.88	38
AB625	379350.9688	733088	1185.11	36
AB626	379344.7813	733193.0625	1183.8	43
AB627	379303.4375	733193.5625	1192.53	40
AB628	379323.8438	733269.75	1192.49	43.5
AB629	379352.375	733275.625	1191.23	30.28
AB630	379347.7188	733376.125	1193.34	39
AB631	379396.2188	733366.0625	1194.11	42
AB632	379414.1563	733475.375	1189.47	38.5
AB633	379382	733476.125	1190.64	44
AB634	379418.6875	733570.5625	1186.42	42
AB635	379465.5625	733574.375	1186.57	32
AB636	379495.0938	733577.625	1184.07	30.34
AB637	379532.4375	733722.5	1195.11	30.92
AB638	379546.99	733753.39	1200	35.5
AB639	379570.75	733801.6875	1200.55	35.5
AB640	379053.0938	733172.125	1262.14	42
AB642	378916.7813	733175.75	1278.78	38
AB643	378874.0938	733178.0625	1276.7	40
AB644	378812.1875	733180.875	1270.46	41
AB645	378748.625	733180.4375	1267.67	38.5
AB646	378689.1563	733179.6875	1260.77	39
AB647	378628.25	733181.5625	1260.48	38
AB648	378576.2813	733181.9375	1252.81	37
AB649	378527.0938	733193.75	1250.2	38.7
AB650	378492.5	733197.6875	1253.55	39.5
AB651	378457.9375	733205.5	1252.73	40
AB652	372705.2188	735012.625	1123.23	34.3
AB653	372752.1875	734955.8125	1344.53	36.3
AB654	372793.4063	734908.0625	1334.51	37.8
AB655	372825.1563	734862.5625	1340.27	33.9
AB656	372876.4688	734818.5	1334.86	40.1
AB657	372925.125	734787.5625	1337.04	36.8
AB658	372971.3438	734733.9375	1331.34	39.4
AB659	373018.3438	734697	1331.04	35.4
AB660	373062.4375	734643.9375	1321.61	40.1
AB661	373112.75	734601.125	1326.02	38
AB662	373159.75	734560.8125	1328.32	36.5
AB663	373206.7813	734533.1875	1321.06	32.1
AB664	373247.7188	734489.9375	1321.64	33.5
AB665	373289.2813	734449.375	1325.07	38.5
AB666	373348.3125	734443.375	1326.86	37.1

AB667	373386.125	734395.875	1332.73	36.2
AB668	373447.0938	734376.8125	1326.44	36.1
AB669	373489.8438	734348.875	1327.04	37.7
AB670	373534.8438	734314.5	1321.82	37.4
AB671	373580.0938	734280	1326.47	39.2
AB672	373640.0938	734261.6875	1330.13	33.3
AB673	373680.9375	734228.75	1329.19	36.1
AB674	373719.4063	734189.125	1333.98	34.7
AB675	373739.125	734150.125	1333.52	40.1
AB676	373783.9375	734120.3125	1331.33	37.8
AB677	373854.0313	734072.25	1326.58	37.1
AB678	373892.375	734025.75	1326.95	38.4
AB679	373922.5	733988.375	1326.4	40.8
AB680	374054.4375	733048.1875	1306.33	37.3
AB681	374097.8125	733024.0625	1308.58	39.9
AB682	374154.8125	733001.75	1309.55	43.2
AB683	374197.0313	732994.3125	1309.31	40.4
AB684	374254.4688	732973.9375	1307.68	34.7
AB685	374315.1563	732912.375	1317.49	35.8
AB686	374368.5313	732862.5625	1320.39	36.6
AB687	374443.4375	732840.5	1319.04	36.4
AB688	374494.0625	732826.9375	1323.84	22
AB689	374543.6875	732820.25	1317.33	35.4
AB690	374613.0938	732808.3125	1305.68	35.5
AB691	374688.0313	732803.5625	1295.23	38.5
AB692	374727.25	732795.625	1292.02	38.7
AB693	374776.5625	732795.0625	1293.13	41
AB694	374828.7188	732777.0625	1288.43	37.5
AB695	374885.9375	732763.625	1282.52	39.5
AB696	374932.3125	732731.6875	1279.54	31.5
AB697	374981.4375	732706.5	1283.71	33.6
AB698	375029.2813	732688.5	1281.48	35
AB699	375095.8125	732633.0625	1284.91	39.3
AB700	375141.9688	732604.4375	1281.93	33.6
AB701	375195.25	732557.1875	1282.59	36
AB702	375262.1875	732529.5	1282.4	34.7
AB703	375312.4375	732504.9375	1289.44	41.1
AB704	375387.6875	732438.4375	1285.1	38.8
AB705	375417.625	732424.3125	1285.39	41.5
AB706	375467.7813	732410.9375	1284.63	38.2
AB707	375505.4063	732375.5	1293.28	33.6
AB708	375547.7813	732334.9375	1280.62	36.7
AB709	375613.625	732319.5	1296.14	41

AB710	375675.7188	732294.6875	1299.14	42.9
AB711	375751.3438	732254.75	1294.68	37.8
AB712	375819.3125	732240.75	1299.43	34.6
AB713	375900.9375	732211.625	1302.32	37.6
AB714	375970.25	732203.75	1295.51	36.5
AB715	376025.7188	732194.0625	1296.89	33.5
AB716	376080.5313	732185.3125	1295.22	43.2
AB717	376128.5938	732172.75	1304.49	37.5
AB718	374069.4375	733945.8125	1326.81	41.4
AB719	374073.5	733892.9375	1327.34	39
AB720	374109.0625	733826.625	1323.56	39.5
AB721	375011.8125	734532.625	11.6	37.3
AB722	374193	733738.125	1318.8	39.8
AB723	374238.125	733700.1875	1321.61	43.4
AB724	374266.0938	733653.375	1327.77	42
AB725	374314.9688	733612.5625	1325.61	44
AB726	374366.2188	733585.6875	1329.19	45
AB727	374413.5938	733560.9375	1321	44.6
AB728	374459.1875	733533.9375	1317.31	45.5
AB729	374537.3125	733463.8125	1306.06	42
AB730	374597.4688	733432.5625	1309.52	43
AB731	374658.1875	733391.625	1307.41	46
AB732	376967.1875	730590.875	1239.5	31.4
AB733	377021.9063	730580	1242.33	31
AB734	377070.625	730565.625	1244.98	31.3
AB735	377129.3125	730554.8125	1248.07	31
AB736	377183.6875	730546.8125	1243.41	30.1
AB737	377236.5938	730530.6875	1242.51	28.8
AB738	377295.0625	730516.25	1240.99	29.7
AB739	377344.9063	730512.375	1239.38	29.7
AB740	377396.625	730492.0625	1237.87	29
AB741	377451.4063	730477.125	1236.39	28
AB742	377504.3438	730461.5	1237.09	29.8
AB743	377552.9375	730438.625	1240.61	30.2
AB744	377584.7188	730416.3125	1241.46	31.7
AB745	377632.375	730408.8125	1245.32	29.9
AB746	377678.7813	730397.875	1252.23	29.9
AB747	377709.2813	730386.875	1259.73	31.4
AB748	379634.7813	733851.8125	1188.88	35.8
AB749	379685.9375	733886.625	1187.9	32.5
AB750	379739.3125	733927.5625	1193.14	29.7
AB751	379794.25	733974.0625	1194.6	34.7
AB752	379838.6563	734007.9375	1197.43	33.5

AB753	379884.125	734031.625	1194.95	35.3
AB754	379971.4375	734073.4375	1195.18	36.3
AB755	380026.2188	734093.875	1192.54	35
AB756	380068.375	734114.875	1193.04	38
AB757	380117.625	734139.5625	1197.32	36.7
AB758	380157.9688	734176.625	1193.7	34.2
AB759	380196.2813	734213.25	1193.25	30.9
AB760	380270.7188	734280.625	1196.15	35.1
AB761	380309.9375	734318.6875	1196.54	37.6
AB762	380346.625	734356.875	1189.68	35.1
AB763	380380.25	734410.4375	1186.17	36.4
AB764	380459.0313	734603.4375	1189.84	36.1
AB765	380488.5313	734693.875	1191.53	36
AB766	380510.3438	734753.875	1197.21	35
AB767	380565.6875	734780.4375	1191.28	35.6
AB768	380613.5625	734838.25	1193.55	35.9
AB769	380670.2813	734894.8125	1204.3	35

Appendix V

Description of Spectral Bands of Landsat 8 satellite image

Bands	Spatial Resolution	wavelength	Subsystem
1	30	0.433–0.453	VNIR (Coastal Aerosol)
2	30	0.450–0.515	VNIR (Visible Near Infrared)
3	30	0.525–0.600	VNIR (Visible Near Infrared)
4	30	0.630–0.680	VNIR (Visible Near Infrared)
5	30	0.845–0.885	VNIR (Visible Near Infrared)
6	30	1.560–1.660	SWIR (Visible Near Infrared)
7	30	2.100–2.300	SWIR (Visible Near Infrared)
8	15	0.500–0.680	Panchromatic (Visible Near Infrared)
9	30	1.360–1.390	TIR (Thermal Infrared)
10	100	10.30–11.30	TIR (Thermal Infrared)
11	100	11.50–12.50	TIR (Thermal Infrared)

Appendix VI

Raw Landsat 8 data with path 169 and row 056

Appendix VII

Distinctive spectral colors and tones for the different lithological units found in each of the Landsat 8 images of the study area

Lithology	RGB band combination and band ratio	Spectral color and tones
Basalt	432 (percent clip histogram stretch)	
	431(natural color)	
Hydrothermal alterations	754	
	762	
	5/7	
Lacustrine sediments	754	
	762	
	5/7	

Rhyolitic lava flow	**754**	
	432 (percent clip histogram stretch)	
	8 3/2, 5/7, 3/5	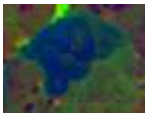
Pumice fall	**Unsupervised classification**	

Appendix VIII

The coordinates for the MT survey lines and points (Mohammednur Desissa and Yohanes Lema 2006)

Site No.	Easting	Northing	elevation	Remark
004	375389	732990	1257	**Profile line 1**
001	379425	733560	1190	
002	382923	729973	1182	
003	385682	728580	1207	
005	376782	742857	1440	**Profile line 2**
007	379494	742768	1438	
006	386480	741402	1294	